AD-A008 777

MECHANISMS OF ADHESION FAILURE BETWEEN POLYMERS AND METALLIC SUBSTRATES: ALUMINUM 2024-T3 AND TITANIUM 6A1-4V WITH HT424 ADHESIVE

Tennyson Smith, et al

Rockwell International Corporation
Thousand Oaks, California

June 1974

NOTICE

When Government drawings, specifications, or other data are used for any purpose other than in connection with a definitely related Government procurement operation, the United States Government thereby incurs no responsibility nor any obligation whatsoever; and the fact that the Government may have formulated, furnished, or in any way supplied the said drawings, specifications, or other data, is not to be regarded by implication or otherwise as in any manner licensing the holder or any other person or corporation, or conveying any rights or permission to manufacture, use, or sell any patented invention that may in any way be related thereto.

Copies of this report should not be returned unless return is required by security considerations, contractual obligations, or notice on a specific document.

This final report was submitted by Science Center, Rockwell International, 1049 Camino Dos Rios, Thousand Oaks, California 91360 under Contract F33615-72-C-1641, Job Order Nr. 73420204, with the Air Force Materials Laboratory, Wright-Patterson Air Force Base, Ohio. E. A. Arvay (AFML/MBC) was the laboratory project monitor.

This report has been reviewed and cleared for open publication and/or public release by the appropriate Office of Information (OI) in accordance with AFR 190-17 and DODD 5230.9. There is not objection to unlimited distribution of this report to the public at large, or by DDC to the National Technical Information Service (NTIS).

This technical report has been reviewed and is approved for publication.

E A Arvay

E. A. Arvay
Project Monitor

FOR THE COMMANDER

T. J. Reinhart Jr

T. J. Reinhart, Chief
Composites and Fibrous Material Branch
Nonmetallic Materials Division
Air Force Materials Laboratory

ACCESSION for
NTIS White Section ☑
DDC Buff Section ☐
UNANNOUNCED ☐
JUSTIFICATION ....
....
BY ....
DISTRIBUTION/AVAILABILITY CODES

Dist.	AVAIL. and/or SPECIAL	
A		

UNCLASSIFIED
SECURITY CLASSIFICATION OF THIS PAGE (When Data Entered)

REPORT DOCUMENTATION PAGE		READ INSTRUCTIONS BEFORE COMPLETING FORM
1. REPORT NUMBER AFML-TR-74-73	2. GOVT ACCESSION NO.	3. RECIPIENT'S CATALOG NUMBER AD-A008 777
4. TITLE (and Subtitle) MECHANISMS OF ADHESION FAILURE BETWEEN POLYMERS AND METALLIC SUBSTRATES: Aluminum 2024-T3 and Titanium 6Al-4V with HT424 Adhesive		5. TYPE OF REPORT & PERIOD COVERED Final Report June 1, 1972 - Feb. 1, 1974
		6. PERFORMING ORG. REPORT NUMBER SC534.23FR
7. AUTHOR(s) Tennyson Smith D. H. Kaelble		8. CONTRACT OR GRANT NUMBER(s) F33615-72-C-1641
9. PERFORMING ORGANIZATION NAME AND ADDRESS Science Center, Rockwell International 1049 Camino Dos Rios Thousand Oaks, Calif. 91360		10. PROGRAM ELEMENT, PROJECT, TASK AREA & WORK UNIT NUMBERS 7342
11. CONTROLLING OFFICE NAME AND ADDRESS Air Force Materials Laboratory Air Force Systems Command Wright-Patterson Air Force Base, Ohio 45433		12. REPORT DATE June 1974
		13. NUMBER OF PAGES 216 + xxi
14. MONITORING AGENCY NAME & ADDRESS (if different from Controlling Office)		15. SECURITY CLASS. (of this report) Unclassified
		15a. DECLASSIFICATION/DOWNGRADING SCHEDULE

16. DISTRIBUTION STATEMENT (of this Report)

Approved for public release; distribution unlimited

17. DISTRIBUTION STATEMENT (of the abstract entered in Block 20, if different from Report)

18. SUPPLEMENTARY NOTES

Reproduced by
NATIONAL TECHNICAL
INFORMATION SERVICE
US Department of Commerce
Springfield, VA. 22151

PRICES SUBJECT TO CHANGE

19. KEY WORDS (Continue on reverse side if necessary and identify by block number)

wettability, ellipsometry, surface potential difference, Auger electron spectroscopy, microscopy (electron, scanning electron, optical), adhesive joints, metal-polymer bonding, bond strength, failure mechanisms, mapping of surface characteristics.

20. ABSTRACT (Continue on reverse side if necessary and identify by block number)

This report describes a study of aluminum 2024-T3 alloy and titanium 6Al-4V alloy adherends, adhesively bonded with an epoxy HT424 adhesive. The adherend surface properties, after standard surface preparation treatments, were characterized with a number of surface tools. Ellipsometry was used to estimate oxide film thickness and optical properties, surface potential difference (SPD) measurements were made to characterize the outer surface dielectric properties, Auger electron spectroscopy (AES) was used to establish chemical analysis of the outer surface and chemical profiles during ion-sputter-back-etching. Topography and morphology

continued--

UNCLASSIFIED
SECURITY CLASSIFICATION OF THIS PAGE (When Data Entered)

were established with electron, scanning electron and optical microscopy and electron and X-ray diffraction. Wettability parameters were established by making contact angle measurements with a series of liquids with different surface tension. A study of bond strengths after adherend aging and bond aging in humidity chambers has been correlated with surface character. Comparison of surface character with bond failure has revealed probable failure mechanisms.

It is demonstrated that mapping of surfaces prior to bonding can reveal areas that will have a predisposition to fail interfacially and how the mapping technique can be used as an non-destructive testing (NDT) tool for monitoring surfaces.

PREFACE

This report covers the work conducted from 1 June 1972 to 1 February 1974 under the direction of Dr. Tennyson Smith, Manager and Principal Investigator, and Mr. D. H. Kaelble, Co-investigator. Those assisting were P. J. Dynes and L. W. Crane, Research Assistants, C. Rhodes, Electron Microscopy and X-ray Diffraction, R. Spurling, Principal Metallographer, and J. M. Harris, Auger Spectroscopist.

SUMMARY

This report describes a study of aluminum 2024-T3 alloy and titanium 6Al-4V alloy adherends, adhesively bonded with an epoxy HT424 adhesive. The adherend surface properties, after standard surface preparation treatments, were characterized with a number of surface analysis techniques. Ellipsometry was used to estimate oxide film thickness and optical properties, surface potential difference (SPD) measurements were made to characterize the outer surface dielectric properties, Auger electron spectroscopy (AES) was used to establish chemical analysis of the outer surface and chemical profiles during ion-sputter-back-etching. Topography and morphology were established with electron, scanning electron and optical microscopy and electron and X-ray diffraction. Wettability parameters were established by making contact angle measurements with a series of liquids with different surface tension. The effect of humid aging upon the measured parameters were determined after various periods of exposure.

Bonded joints using unaged and aged adherends were prepared and evaluated. Similar bonded joints were prepared and aged for various periods prior to evaluation. Joint strengths and faying surface appearance have been correlated to the measured surface parameters on both an averaged and point by point mapping basis.

It has been ascertained that correctly prepared surfaces, using standard surface preparation solutions, vary considerably on a point to point basis as shown by ellipsometry and SPD measurements. Areas with a predisposition to fail interfacially (adhesive failure) can be identified. Probable failure mechanisms can be delineated for certain substrate-polymer systems under specific conditions.

Preceding page blank

TABLE OF CONTENTS

LIST OF FIGURES

Figure No. | Page No.

Figure No. Page No.

Figure No. Page No.

Figure No. | Page No.

LIST OF TABLES

Table No. — Page No.

LIST OF SYMBOLS

Nomenclature for Wettability Parameters

θ	liquid solid contact angle
γ_{LV}^{d}, γ_{LV}^{p}	respective dispersion (d) and polar (p) parts of liquid surface tension $\gamma_{LV} = \gamma_{LV}^{d} + \gamma_{LV}^{p}$
γ_{SV}^{d}, γ_{SV}^{p}	respective dispersion (d) and polar (p) parts of solid-vapor surface tension $\gamma_{SV} = \gamma_{SV}^{d} + \gamma_{SV}^{p}$
α_L, β_L	respective square roots of γ_{LV}^{d}, γ_{SV}^{p}
α_S, β_S	respective square roots of γ_{SV}^{d}, γ_{SV}^{p}
W_a	nominal value of interfacial work of adhesion
σ_c, σ_I	critical crack propagation stress defined by Griffith theory
E	Young's modulus
c	crack length
γ_G	Griffith surface energy
α_1, β_1	adhesive surface properties
α_2, β_2	surface properties of environment
α_3, β_3	adherend surface properties
S_L	liquid (or adhesive) spreading coefficient

R_o R H K	wettability parameters related to α's and β's

Nomenclature for Surface Tools

Δ	ellipsometry phase shift of the parallel component with respect to perpendicular component of polarized light
ψ	arctan of the amplitude ration
p	polarizer azimuth
a	analyer azimuth
n_s	real part of the complex refractive index of the substrate
κ_s	imaginary part of the complex fractive index of the substrate
$\hat{n}_s$	complex refractive index of the substrate $\hat{n}_s = n_s (1 - i \kappa_s)$
n_f	real part of the complex refractive index of the film
κ_f	imaginary part of the complex refractive index of the film

μ	dipole moment of adsorbate molecules
μ_o	component of μ normal to the surface
α	polarizability of the adsorbate molecules
q	charge density of adsorbate
F	natural surface field
ξ	dielectric constant of the adsorbate

Adhesive Joint Parameters

ϕ'_c	fraction of bond area that failed in the adhesive
ϕ_I	fraction of bond area that failed at the interface
ϕ_v	fraction of bond area that failed in voids
ϕ_g	fraction of bond area that failed in the glass carrier
ϕ_c	fraction of bond area that failed in the adhesive and glass
σ'_c σ_I σ_v σ_g σ_c	bond strength in region corresponding to the ϕ values

$\hat{n}_f$	complex refractive index of the film, $\hat{n}_f = n_f (1 - i \kappa_f)$
d	film thickness
λ	light wave length
θ	angle of incidence
$\tan \beta_0$	roughness factor

Auger Electron Spectroscopy (AES)

E	retard voltage
$\frac{dN(E)}{dE}$	derivative of the energy distribution for secondary electrons
APPH	auger peak to peak height in the auger spectrogram $dN(E)/dE$ vs E

Surface Potential Difference (SPD)

$\Delta\phi$	change in work function
i	electrical current
R	resistance of the air gap
r	resistance of the electrometer
Γ	adsorbate concentration

Section I

INTRODUCTION

A. The purpose

To improve adhesive joints, the investigator concentrates his efforts on the weakest link. If failure occurs primarily in the adhesive, emphasis is placed on a search for a stronger adhesive or means to strengthen a given adhesive. If failure occurs primarily at a weak boundary layer consisting of surface contamination or oxide, emphasis is placed on cleanliness or surface preparations. Since new applications demand stronger and stronger adhesive joints, the tendency will be to continue improvement of the weakest link as it shifts from one locus to another. This study is primarily concerned with the nature of the adherend surface after preparation for bonding and the relationship between the nature of the surface and bond strength and reliability. Two important benefits will follow this type of intensive study; first, new knowledge about the physical and chemical nature resulting from surface preparations will point the way to improved surface preparations, and second, the correlation between surface characteristics and bond strength can be used to develop non-destructive testing (NDT) tools for monitoring assembly line parts that are to be adhesively bonded. Even if it is impractical to monitor all areas of every part, automatic spot checking of specific areas of a few parts would be valuable with respect to verification that surface preparations and storage procedures are acceptable or not.

B. The Problem

All metals, except gold, are thermodynamically unstable at room temperature when in contact with oxygen at atmospheric partial pressure, and hence should tend to form oxide surface layers. The thickness of this oxide may vary from a few atomic layers to many microns. Water, as vapor or liquid, is usually available to any surface and many metals such as aluminum and titanium are sufficiently active to displace hydrogen from this water to form hydroxyl groups. However, these reactions often fail to occur at any appreciable rate. The actual film formed on such metals is protective and usually is found to be a thin, nonporous film of insoluble oxide. The Wagner theory of oxidation[1] at the metal/oxide interface is the prevailing theory for describing the formation of protective films in refractory metals. The stoichiometry of the oxide formed is of importance because the relative diffusion rates of the metal or oxygen ions depends on the number of cation or anion vacancies. Studies by Smith,[2] Kofstad[3] and others have shown that, for gas-phase oxidation, zirconium and titanium tend toward a slight anion deficiency. Few detailed experiments of this type in the presence of moisture have been made.

In Fig. 1, a schematic representation of water and oxide layers on a metal surface is shown. The illustration, taken from a recent review by Bolger and Michaels,[4] is based on the results of a number of prior studies of adherend surfaces. The three basic assumptions of the model are: (1) that the oxide film is thick enough so that the underlying metal substrate exerts no influence on reactions or electrostatic interactions at the surface, (2) that, while the oxide surface can be dehydrated at elevated temperatures, at normal ambient bonding conditions the outermost surface oxygens hydrate to form a high density of hydroxyl groups, and (3) the hydroxyl adsorbs and retains several molecular layers of water. The spacing and the activity of the hydroxyl groups will depend in general on the spacing and valency of the metal atoms in the oxide. The use of oxidizing acids to clean metal surfaces might be expected to remove these hydrated oxides, oxidize and remove surface impurities, and increase the valence of the surface metal ions. Few detailed studies of surfaces before and after etching are to be found in the literature and, in most instances, the information obtained is inferential rather than direct observation. As discussed next, the structure of the surface layers on two of the most commonly used metals (Al and Ti) are not well established and it becomes an important part of this program to attempt to clarify this situation.

Keller[5] found that the structures of the films formed in sulfuric, chromic, phosphoric acid electrolytes, after anodizing, are basically similar. The oxide is found to consist of hexagonal cells whose outer and inner surfaces bulge into the solution and metal, respectively. Films formed in concentrated sulfuric acid are believed not to be pure Al_2O_3. For example, films formed in 10% H_2SO_4 at temperatures around 20°C were reported by Liechti and Treadwell[6] to contain 13% SO_3 as well as a few percent of bound H_2O. The films formed in the oxidizing acids often are porous, and have to be sealed to increase corrosion resistance. It is standard practice to seal films formed in sulfuric acid by immersion in boiling neutral water for 20 minutes. Electron diffraction

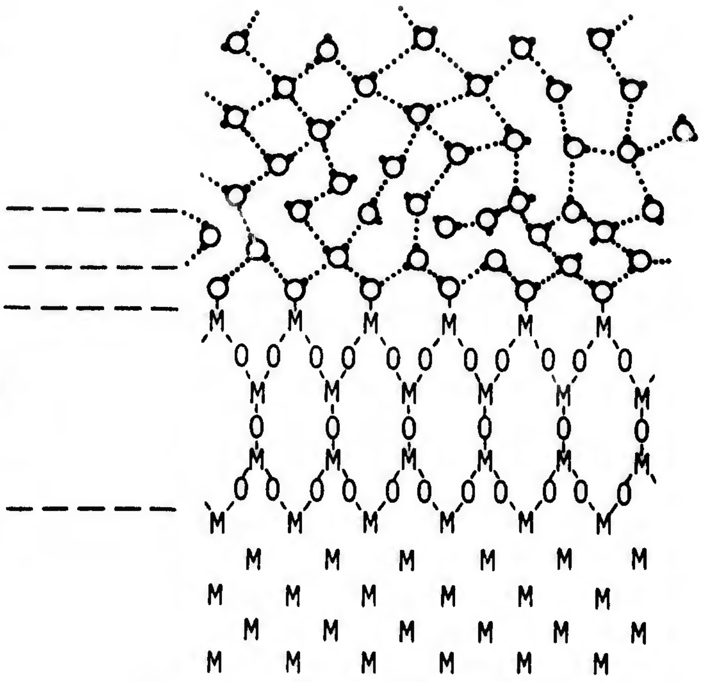

Additional H_2O surface layers. Thickness depends on temperature and relative humidity. Dots indicate hydrogen bonds

First H_2O surface layers tightly bound

Surface hydroxyl groups

Metal oxide layers. Actual thickness and structure depend on metal substrate

Crystalline metal substrate

Key:

M = Metal Atom, O = Oxygen, - $O^{\bullet}$ = -OH, $O^{\bullet}_{\bullet}$ = H_2O

Figure 1. Schematic Representation of Water and Oxide Layers on Metal Surface.

studies by Harrington and Nelson[7] and Phillips[8] showed that boehmite [α-AlO(OH)] is produced in the film. Since abrasion removed the boehmite pattern, they concluded that the boehmite must have been on the surface. There is considerable controversy in the literature as to the necessity of aluminum metal being present to convert the oxide portion to boehmite.

The oxide film formed on titanium has been reported to be anatase (tetragonal TiO_2) by Burghers[9] and Harrington and Nelson.[7] Other investigators[10] have found brookite (orthorhombic TiO_2) on stripped films. Rutile (tetragonal TiO_2), anatase, and hydrated oxides have been identified[11] on anodized surfaces. On the other hand, Brusilovdskii, Boguslauskaya, and Nasovich[12] reported that no hydrates are formed, but that the oxides simply hold water by adsorption. Recent work has been reported by Hamilton and Lyerly[13] concerning the characterization of Ti and Al alloy surfaces during selected stages of prebonding treatments. They suggest that bonding differences with the variously treated titanium alloys were caused by variations in the crystalline structure of the titanium oxide, whereas bonding differences with the aluminum alloys were caused by variations in the surface hydration, film thickness and surface morphology.

For adhesive joints with weakest link at the adherent-adhesive boundary, the problem lies in identifying the locus or loci of failure, e.g. in the primer, at the primer-oxide interface, in the oxide, at the oxide metal interface, and learning enough about the various interface phases to determine the cause of the weakness. In addition to the condition and properties of these phases immediately after surface preparation, one must be concerned with the stability or degradation of these properties in environments expected under factory conditions. That is, what changes will occur due to aging in humid atmospheres, what changes can occur due to inadvertent processing malfunctio such as contaminated etching solutions, incorrect formulations and applications, etc.

C. The Solution

Once having established the locus and cause of failure or degradation, a corrective procedure can be designed into the process to remove the problem, or at least improve the process. In this study we correlate the properties of the metal adherend and adhesive (after a specific preparation but prior to bonding) with subsequent initial bond strength and bond strength retention for various periods under varying environmental conditions. Characterization of the surface of metal samples is made with a variety of techniques. For example, the thickness and index of refraction of surface films is measured by ellipsometry. Chemical analysis of the surface layers and the chemical profile of films is made with Auger spectroscopy in conjunction with sputter-back etching by ion bombardment. Surface dielectric properties are determined by surface potential difference measurements (SPD) and surface topography and morphology are determined by optical, electron and scanning electron microscopy techniques. Electron diffraction is used to study the crystal structure of surface films. The sample surfaces and adhesives are characterized by contact angle measurements which delineate the surface tension properties. This allowed predictions of the wettability requirements between the adhesive and adherend to define strong adsorption bonding.

After preparation and characterization of the surfaces of the adherend and the adhesive, joints were fabricated and tested immediately after curing as well as after aging in environmental chambers. Examination of the fracture surfaces were made by optical and scanning electron microscopy and Auger spectroscopy to determine the region of failure (metal-oxide interface, oxide, oxide-adhesive interface or adhesive) and the chemical constituents at the fracture interface.

Some of the metal samples that have been characterized were subjected to the same aging environments without any adhesive in order to follow the morphologies and chemical changes of the surface films that might be expected if the metal surfaces were exposed for some time or if the bonds were permeable to the environment.

EXPERIMENTAL

A. Materials

1. Adherends: The metal adherends are bare 2024-T3 aluminum alloy sheet and Ti-6Al-4V titanium alloy sheet. Specimens were cut from 0.063" sheet with dimensions slightly larger than 4" x 1" and then milled to precisely 4" x 1".

2. Adhesives: The adhesive, used for most of the work reported here, was an epoxy-phenolic (HT424) from American Cyanamid. This adhesive has a glass fabric carrier and standard weight 0.135 ± 0.005 lbs/sq. ft. It was shipped in dry ice and stored at -10°C. Unfilled primer with parts A and B were used with the HT424 adhesive. The primer composition was 10 pbw HT424 part A, 10 pbw HT424 part B and 30 pbw HT424 primer-thinner. Another adhesive was used in the initial stages of this study with Ti-6Al-4V alloy. The adhesive was FM-34B-32 with BR-34 primer.

3. Surface Preparations: As has been shown[14] and as will be seen, every step of the surface preparation may be of significance with respect to bond strength. It is of the utmost importance that procedures be followed in every detail if experimental results are to be compared from laboratory to laboratory. Table 1 identifies the various surface preparation treatments for Al 2024-T3. Most of the work on Al was done with the dichromate cleaning process in 2 of Table 1, often referred to as the FPL etch. Table 2 identifies the various surface preparations for Ti-6Al-4V. Most of the work on Ti was done with the phosphate-fluoride cleaning process (No. 1 of Table 2). Approximate compositions of the aluminum and Ti alloys are given in Table 3.

B. Surface Characterization Techniques

1. Ellipsometry

Film thickness and film optical constants can be measured by ellipsometry. A good description of the principles of ellipsometry is given by McCrackin et al.[15] In brief, when plane-polarized light is reflected from a surface the light becomes elliptically polarized. That is, the surface

TABLE 1: DETAILS OF SURFACE PREPARATIONS

1) Vapor Degrease (VD)

   a. Vapor degrease for 1 minute in a vapor degreaser containing trichloroethylene.

2) Sulfuric Acid-dichromate (FPL etch)

   a. Samples are cleaned ultrasonically for 15 minutes in trichloroethylene.
   b. Samples are cleaned ultrasonically again for 5 minutes in fresh trichloroethylene.
   c. The samples are alkaline cleaned for 10 minutes at 66°C in a stirred solution 06 TURCO 4215 cleaner (31.2 g/liter in distilled water).
   d. The samples are rinsed with distilled water and then rinsed ultrasonically for 5 minutes in distilled water.
   e. Check for water break.
   f. The samples are immersed in a sulfuric acid-chromate solution for 13 minutes at 66°C. This solution is made as follows from reagent grade chemicals: This solution has been reacted with Al metal previously to give a dark brown color to it -

Sodium dichromate	28.5 gms.
Sulfuric acid	285.0 gms.
Distilled water	to make 1 liter

   g. The samples are spray rinsed with cold water (below 23°C).
   h. The samples are immersed in cold water and the spray rinse repeated.
   i. The samples are checked for water break and dried in a vented oven for 15 minutes at 40°C.

3) Glow Discharge (Plasma) Treatment of Al 2024-T3

   Vapor Degreased Sample (VD)

   a. wiped with TCE.
   b. cleaned ultrasonically 15 min. in TCE.
   c. Alkaline cleaned 10 min. at 66°C.
   d. D.I. H_2O rinse (water break test).
   e. air dry.

   Plasma Conditions

   gas = argon 150 μ

Continued--

TABLE 1: (Continued)

4) Glow Discharge (Plasma) Treatments of Al 2024-T3

For Wettability

a. Clean 1" x 4" samples ultrasonically in trichloroethylene for 15 min.

b. Place samples in plasma chamber and pump to 10^{-5} torr for 15 min.

c. Adjust the plasma treatment variables to the following values and start plasma and maintain these settings:

1)	Pressure	100 μ
2)	Flow	2ℓ/min argon
3)	Power	100 watts
4)	Time	20 min.

d. Plasma is turned off and chamber is pumped to 10^{-5} torr.

e. 1) Open the chamber to a source of O_2 gas and adjust to atmospheric pressure for O_2 post-treatment for 1 hour.

2) Open the chamber to a source of H_2O vapor for 1 hour; H_2O post-treatment.

f. Remove samples and perform contact angle measurements within 20 min.

5) For Plasma Treatment for Al 2024-T3 Bonding (Oxygen and Water Vapor Post-Treatment)

a. TCE wipe.

b. Ultrasonic clean in TCE for 15 min.

c. Place samples in plasma chamber and pump to 1μ for 15 min.

d. Purge chamber with argon for 10 min.

e. Start plasma with following constants:

1)	Pressure	300 μ
2)	Flow	0.4ℓ/min argon
3)	Power	100 watts
4)	Time	20 min.

f. Turn off plasma and pump to 1μ.

g. Bleed in flowing oxygen at just below atmospheric pressure for 20 hours.

h. Seal off chamber, place in glove box, pump to ~ 10 μ.

i. Flood with argon to ambient pressure.

j. Primer coupons with HT424 primer parts A & B.

k. Remove coupons from glove box, cure primer in vacuum oven, and bond with HT424 adhesive.

l. Perform shear test in Instron.

Continued--

TABLE 1: (Continued)

6) For Plasma Treatment for Al 2024-T3 Bonding (No Post-Treatment)

a. Wipe 12 Al-2024-T3 coupons with trichloroethylene (TCE) soaked cloth.

b. Alkaline-clean 10 min. at 66°C in TURCO alkaline cleaner (4215).

c. Place samples in plasma chamber and pump down to 1μ for 15 min.

d. Purge chamber with argon 10 min.

e. Start plasma with the following constants:

1)	Pressure	300 μ
2)	Flow	0.4ℓ/min. argon
3)	Power	100 watts
4)	Time	20 min.

f. Turn off plasma and seal chamber still at 300 μ.

g. Place sealed chamber in glove box and pump down to ~ 10 μ.

h. Flood with argon to ambient pressure.

i. Primer coupons with HT424 primer parts A & B.

j. Remove coupons from glove box, dry primer in vacuum oven, and bond with HT424 adhesive.

k. Perform shear test in Instron.

TABLE 2: DETAILS OF SURFACE PREPARATIONS FOR Ti-6Al-4V

1) Phosphate-Fluoride Surface Treatment

a. Wipe metal with acetone soaked cloth, followed by a 10 min. ultrasonic cleaning in acetone.

b. Emulsion clean in TURCO 3878 for 15 min. at 54-60°C.

c. Water rinse-spray and overflowing dip.

d. Water-break test.

e. Pickle 1 min at 23°C in the following solution:

$70\%\ HNO_3$

10 oz/gal NH_4HF_2

f. Deionized water rinse for 2 min at 23°C.

g. Dip in the following stirred solution for 1/2 min at 27°C:

7.3 oz/gal $Na_3PO_4 \cdot 12\ H_2O$

1.5 oz/gal NaF

7.3% by volume HF (60% solution).

h. Deionized water rinse - 15 min.

i. Deionized water blast to remove film.

j. Dry samples under ambient air conditions.

2) Nitric Acid-Fluoride Treatment

a. Solvent trichloroethylene (TCE) wipe metal with cloth.

b. 10 minute TCE - ultrasonic cleaning.

c. 10 minute cleaning in TURCO 4215 alkaline cleaner at 66°C.

d. Rinse in distilled water.

e. Pickle in the following distilled water solution at room temperature for 5 min.

Nitric acid 15% by weight

Hydrofluoric acid 3% by weight.

f. Rinse in distilled water at room temperature.

Continued---

TABLE 2: (Continued)

3) PASA-JELL Treatment

a. thru e. same as No. 2 but add:

f. Apply PASA-JELL 107 liquid to the titanium surface by dip or with an acid resistant brush. Cover the entire surface by cross brushing.

g. Allow to dry for 20 min.

h. Rinse thoroughly with water.

i. Dry 15 min. at 40°C in dry N_2.

4) TURCO Treatment (LAD Modification)

a. Wipe metal with acetone-soaked cloth, followed by a 10 min. ultrasonic cleaning in acetone.

b. Emulsion-clean in TURCO 3878 for 15 min. at 54-60°C.

c. Deionized water rinse.

d. Etch in TURCO 5578 for 10 min. at 66°C.

e. Deionized water rinse.

f. Dry in air.

TABLE 3: ALLOY COMPOSITIONS

Percentage Al (2024-T3) Alloy Composition

Cu	Mg	Si	Fe	Zn	Cr	Mn	Ti
3.8-4.9	1.2-1.8	0.5	0.5	0.25	0.1	0.3-0.9	---

Percentage Ti-6Al-4V Alloy Composition

Al	V	Fe	C	N	H	O
5.5-6.7	3.5-4.5	0.3	0.08	0.05	0.015	0.2

renders a phase shift (Δ) in the normal and parallel component of the polarized light as well as a change in the ratio of the amplitudes (tan ψ) of these components. The experimental arrangement is shown in Fig. 2. Monochromatic light is polarized and then compensated with a quarter wave plate (compensator) such that after reflection the light is plane polarized and can be crossed out by the analyzer. Values of Δ and ψ are obtained from the polarizer and analyzer azimuths at which the analyzer extinguishes the light. The experimental parameters measured with the ellipsometer are the polarizer azimuth p and analyzer azimuth a, which are directly related to Δ and ψ; $\Delta = 2p + \pi/2$ and $\psi = a$ where (Δ and ψ) = f (n_s, κ_s, n_f, κ_f, d, λ, θ, tan β_o). Subtracting 360° from Δ does not change its relationship to f( ), e.g., if Δ is 50°, it can just as well be expressed as -310°. The complex refractive index of the substrate is $\hat{n}_s = n_s\ (1-i\kappa_s)$ and the film $\hat{n}_f = n_f\ (1-i\kappa_f)$, where n_s and n_f are the refractive index and κ_s and κ_f are the absorption index. The other parameters are film thickness d, light wave length λ, angle of incidence θ and tan β_o is the mean slope of undulations due to surface roughness. The angle of incidence was 70° and the wave length of the He-Ne laser used was 6328 Å. The optical constants for Al at this wave length are approximately $n_s \approx 1.43$ $\kappa_s \approx 5.17$, some measurements were also made at λ = 5461 Å for which $n_s \approx 1.0$, $\kappa_s \approx 6.7$.

The computer program of McCrackin[16] was used. Given p and a this program searches for solutions of d and n_f for a specified range of κ_f. The search for solutions covered n_f = 1.0 to 3.0, for κ_f from 0 to 1.0 in increments of 0.1. Fenstermaker and McCrackin[17] have shown that surface roughness can seriously affect the ellipsometer parameters, therefore, the p and a or Δ and ψ values are recorded and the computer solutions are considered to be only approximate. Unless two of the parameters d, n_f, κ_f and tan β_o are known from independent measurements, unambiguous solution set (d, n_f, κ_f, tan β_o) cannot be established by ellipsometry. However, order of magnitude values can be obtained and most probable values estimated. Since values of n_f for bulk oxides are known and since bulk oxides are usually transparent ($\kappa \approx 0$) to 6328 or 5461 Å light, the most probable solution set is for a minimum value of κ_f and n_f value near the bulk values. The minimum values of κ_f is an effective value which may reflect the unknown roughness parameter tan β_o. The values for n_f for oxides of titanium[18] are reported between 2.6 and 2.9 and for oxides of aluminum[19] between 1.5 and 1.8.

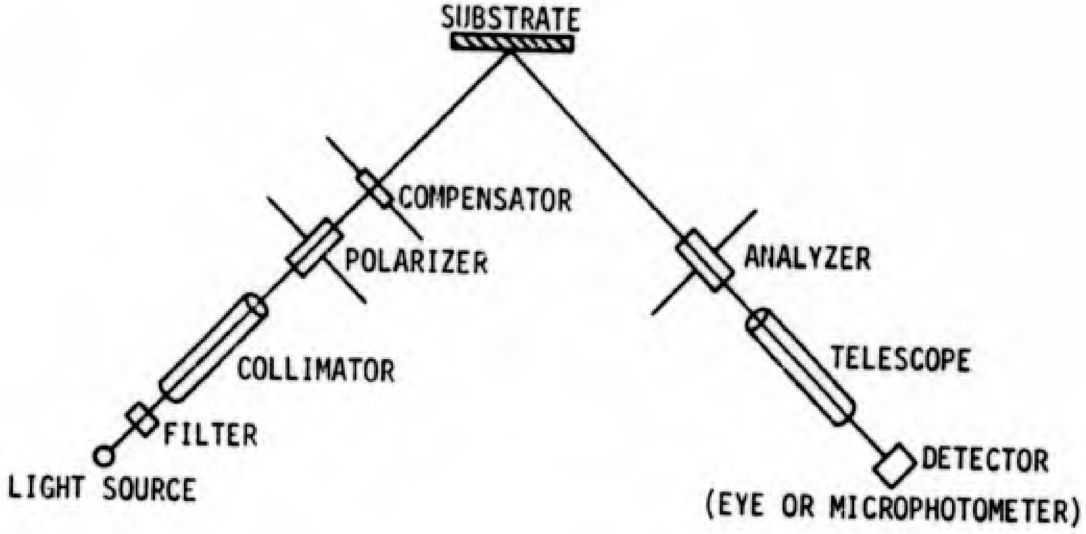

Fig. 2. Schematic representation of the optical arrangement of the ellipsometer.

2. Auger Spectroscopy

Auger spectroscopy involves the analysis of secondary electrons that are emitted from a surface that has been bombarded with a monochromatic electron beam. The Auger electron spectrogram (AES) reveals the elements that are present in the first three or four atom layers at the surface. A good description of Auger spectroscopy can be found in a paper by Simmons.[20] An example of an AES is given for Al 2024-T3 that had the FPL etch treatment (No. 2 of Table 1) in Fig. 3. Figure 4 shows the AES after ion sputtering the oxide film away. The abscissa E is the retarding voltage and the ordinate $dN(E)/dE$ is the derivative of the energy distribution curve for secondary electrons. Although progress is being made[21] in the interpretation of the AES with respect to the quantitative chemical composition of a surface, at present only semi-quantitative interpretation can be made. Comparison of Auger peak to peak height (APPH) for a given peak is significant with respect to changes of surface composition after various surface treatments. The significance of the APPH for different peaks of a given spectrum is not known at this time.

3. Chemical Profiles

Monitoring the chemical composition of a surface as the film is sputter-etched by ion bombardment is a very powerful tool. However at present the interpretation of these profiles are only semi-quantitative. To yield quantitative chemical profiles much has yet to be learned. As a first approximation the Auger peak to peak height (APPH) of the derivative $dN(E)/dE$, for a particular Auger transition, is proportional to the concentration of the particular element, subject to the validity of the following assumptions:

1. The mean electron escape depth is small compared to the film thickness.
2. APPH is directly proportional to the Auger current.
3. The electron beam does not change the atomic ratios at the surface.
4. The ion beam does not change the atomic ratios at the surface.
5. The electron beam diameter is small compared to the ion beam diameter.

The mean escape depth for metals and oxides[22] range from 5 to about 30 Å for electron energies to about 2 KeV. Therefore, AES monitors the outer four or five monolayers and assumption 1 is good for films > ~ 100 Å. Tarng and Wehner[23] give a detailed analysis of the relationships and parameters involved.

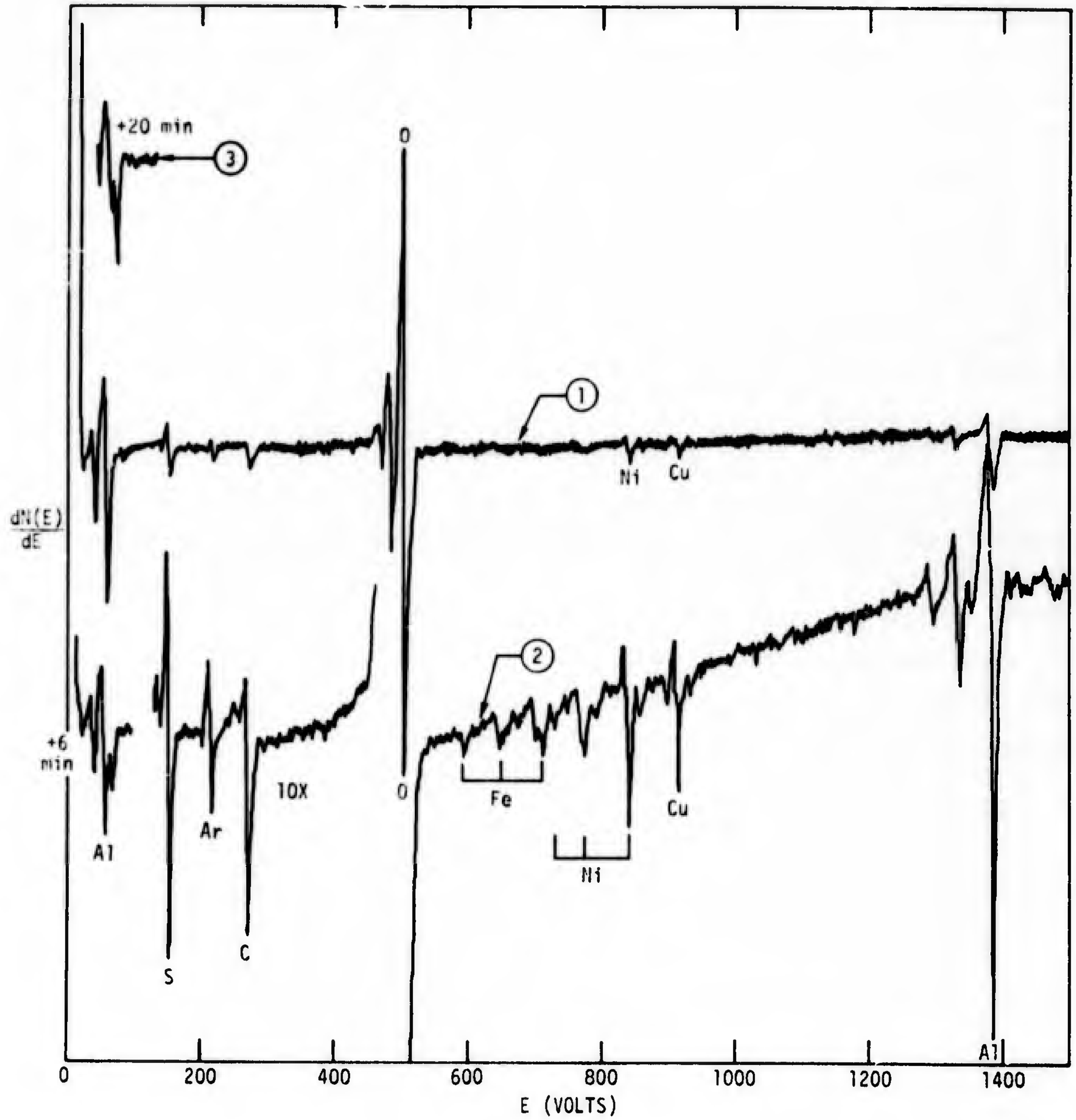

Fig. 3. An Auger Electron Spectrogram of an FPL etched Al 2024-T3 Sample.

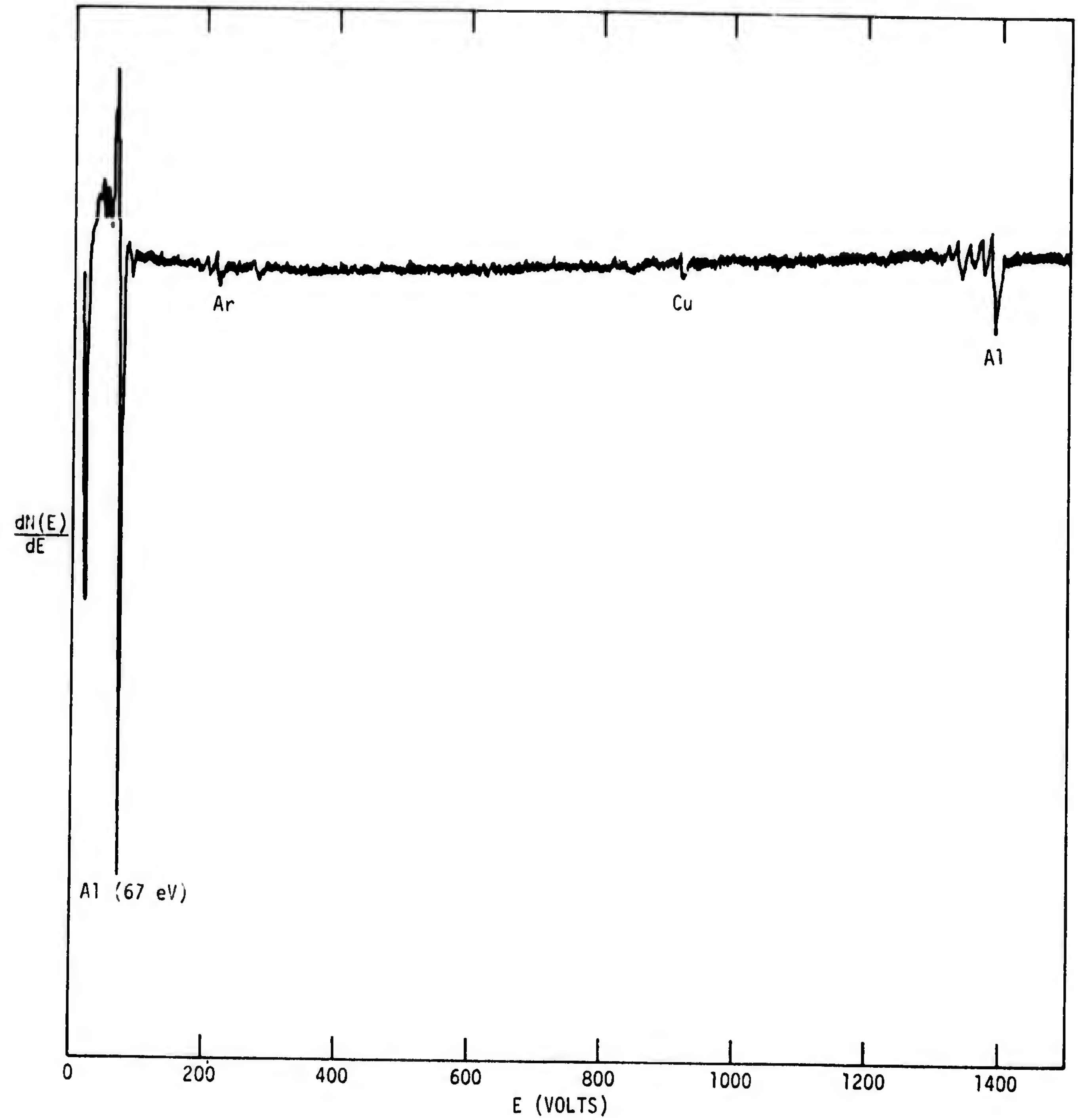

Fig. 4. An Auger Electron Spectrogram of an FPL etched Al 2024-T3 sample after ion sputter etching through the oxide film.

Although assumption 2 has generally been accepted, Grant et al[24] have shown that in some cases assumption 2 is not valid due to the shape of the Auger derivative peaks. They show that this problem can be overcome by integration of the AES and measuring the currents directly from the area under the integrated peaks.

We have discovered assumption 3 to be invalid for electron currents usually used for AES (20-100 μa). This is demonstrated in Fig. 3 for curves 1, 2 and 3. Curve 1 is for the initial spectrum which took about 6 minutes. It will be noted that the low energy aluminum peak in curve 1 is at 55 eV. This 55 eV peak is associated[25] with a transition between oxygen and aluminum and therefore is related to aluminum oxide and not pure aluminum. After 6 min. of electron gun current (at 90 μa) the 55 eV peak has diminished and the 67 eV peak appears. The 67 eV peak is associated[25] with pure aluminum and not the oxide. After 20 minutes of electron current, curve 3 shows that the 55 eV peak has further diminished and the 67 eV peak has increased. Experiments on pure single crystal α alumina showed the same trends. It can only be concluded that the electron beam is transforming the outer layers of the oxide to pure aluminum. This effect was not discovered until after most of the Auger work reported in this report was done. Experiments have shown that the use of gun currents between 1 and 10 μa greatly reduces this problem. Although some loss in sensitivity results, Auger measurements with minimum electron exposure should increase the validity of assumption 3 to an acceptable level. Assumption 3 should be approximately valid for AES results near zero sputter time in the profile figures since the surfaces had been exposed to very little electron current.

Shimizu et al[26] have shown that unless the ion yield is the same for each element, some changes will occur in the composition of the outer layers during ion sputter-etching. We have observed that the ion sputter yields are much closer for metal and oxygen than the electron beam yield, however, this problem may be more important than the electron yield problem because one cannot lower the ion current and still etch through the film. Very little is known about the validity of assumption 3 at this time.

Assumption 5 is easily made valid since the ion beams can be large >1 cm diameter and the electron beams very small <0.05 cm diameter. In our system the electron beam was ~ 0.05 cm diameter and the ion beam ~ 1 cm diameter and the position of the beam on the sample could be observed with a telescope mounted on the UHV system.

In spite of the problems mentioned the AES is a very powerful tool for semi-quantitative analysis of surfaces and will become increasingly more powerful as more is learned about Auger processes and sputter-etching.

4. Surface Potential Difference (SPD)

The surface potential difference is the potential between a reference electrode and the sample to be studied. It arises from the work function difference ($\Delta\phi$) of the two surfaces. If the reference electrode is inert, any changes in SPD will be due to changes that occur on the sample surface. Any process that will change the work function of the sample surface will affect SPD. Therefore, the SPD is related to the structure and dielectric properties of the surface film. Due to the large number of property changes that can affect SPD, its usefulness is quite limited if measured by itself. However, if the SPD is measured in conjunction with other measurements such as ellipsometry, AES, SEM, etc., it can add valuable information for the interpretation of the structural and chemical properties of films.

Figure 5 is a schematic current diagram used for the measurement of SPD. The current i flowing in the circuit can be expressed by Ohms law

$$i = \Delta\phi/(R+r) = e/r \tag{1}$$

where $\Delta\phi$ is the SPD, R is the air gap resistance between the sample surface and reference electrode, r is the electrometer resistance and e is the electrometer voltage reading. A radioactive substance sealed behind a metal foil on the reference electrode is used to provide ionization of the gas between the electrodes, thus reducing R such that $R \ll r$. In this case

$$i = \Delta\phi/r = e/r \tag{2}$$

and $\Delta\phi = e$. That is, the electrometer yields SPD directly. To demonstrate that $R \ll r$, e is measured with increasing distance d between the electrodes; as long as e is independent of d, $R \ll r$. Our reference electrode has Am^{241} sealed behind gold foil and e proves to be constant with distance between 8 and 3 mm (see Fig. 6). Our measurements were made with about 5 mm between the

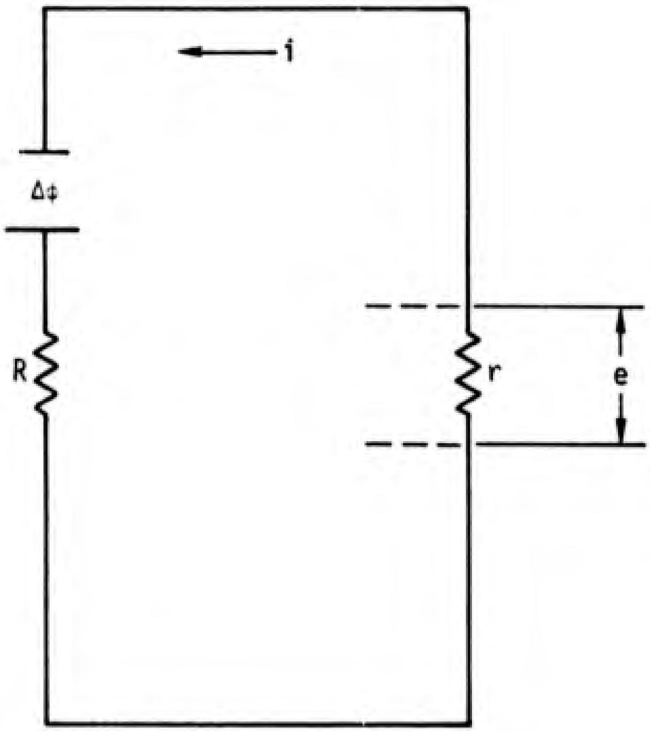

Fig. 5. Schematic equivalent circuit diagram of the ionization technique for measuring the surface potential difference (SPD)

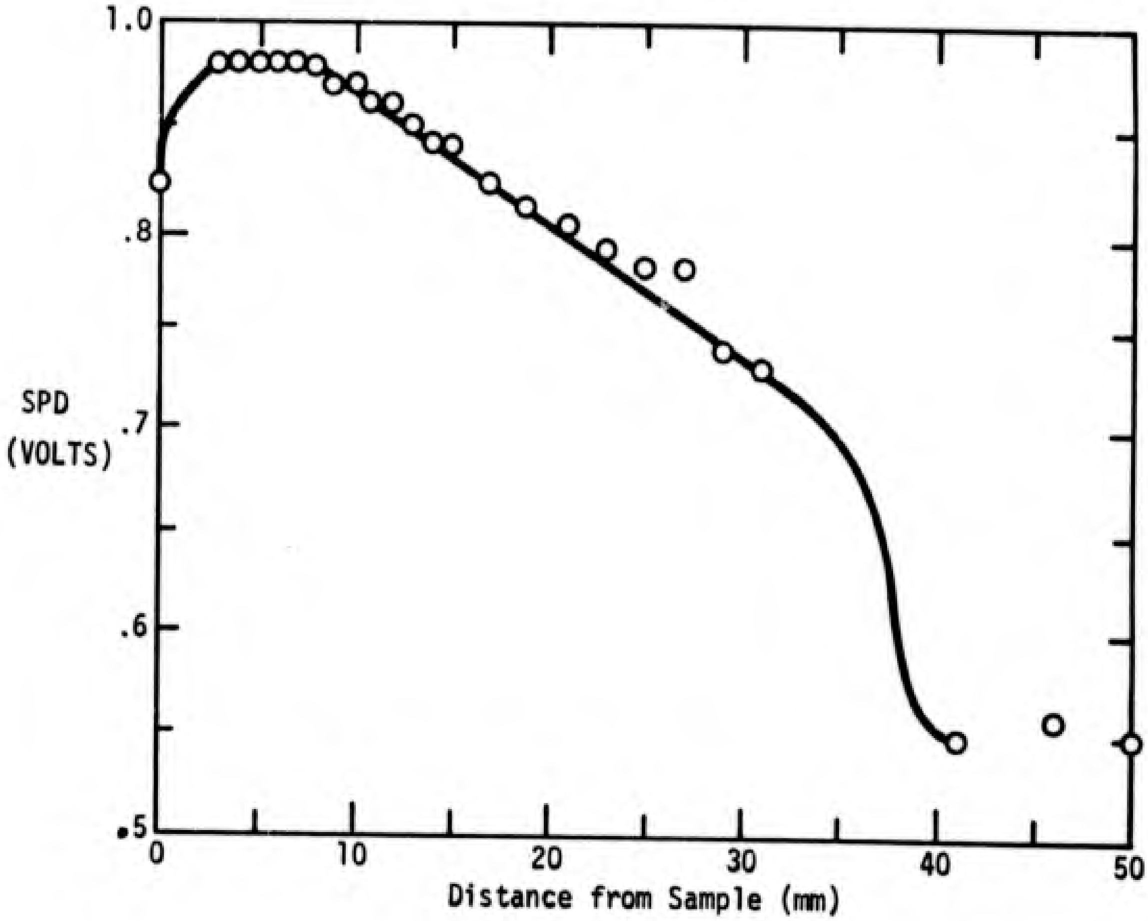

Fig. 6. Variation of SPD with electrode distance from an FPL etched aluminum sample.

reference electrode and sample. The gold foil was sprayed with a thin layer of Teflon to maintain its inertness.

The most comprehensive analysis of the relationship of the measured values of the surface potential difference ($\Delta\phi$) to the molecular adsorbed state has been given by MacDonald and Barlow.[27,28] Elementary electrostatics applied to a continuous dipole sheet leads to the Helmholtz equation[29]

$$\Delta\phi = \pm 4\pi\mu\Gamma \qquad (3)$$

where μ is the dipole moment and Γ is the adsorbate surface concentration. This equation was modified to account for the polarizability of real dipoles and their discrete nature. A depolarizing field at the position of a given dipole arises from all surrounding dipoles. The modification to Eq. 3 is

$$\mu \approx [\alpha(4\pi q+F) + \mu_0]/\varepsilon \qquad (4)$$

where q is the charge density of the adsorbate, F is the natural surface field, α is the polarizability of the adsorbate, μ_0 is the component of the permanent dipole moment normal to the surface and ε is the dielectric constant of the adsorbate film. The sign is positive if the positive end of the dipole is pointed away from the surface. The effect of oxide films on SPD is discussed by Boggio and Plumb.[30]

Because the SPD is relative to the reference electrode the absolute values reported here are not of significance. However, the values of SPD for one surface treatment relative to another is of significance, the change being due to differences in the work function of the two samples.

5. Microscopy

Optical, scanning electron, transmission electron and interference microscopy are used in this study. These microscopy studies allow morphology, topography and structure of films to be revealed. The electron microscope is a Philips Model 300, the SEM is an ETEC autoscan and the interference microscope is a Zeiss.

6. Contact Angles

This section will introduce and briefly discuss the concepts currently applied to the analysis of liquid-solid contact angle measurements. Zisman and coworkers[31] developed detailed procedures for experimental measurement of liquid-solid contact angles θ_{LS}. Zisman showed that a plot of cos θ versus liquid surface tension γ_{LV}, for a homologous liquid series against a common solid tends to produce a linear curve of cos θ versus γ_{LV}. Extrapolation of cos θ versus γ_{LV} curve to cos θ = 1.0 defines a critical surface tension for wettability γ_C for the solid with the prediction that when $\gamma_{LV} < \gamma_C$ the liquid will spontaneous wet and spread (with $\theta = 0$). A number of refinements in the analysis of contact angle data have been more recently introduced to define surface energetic criteria for adhesive bonding and fracture. Recent reviews of this subject by Kaelble[32,33] provide details of the surface energy analysis applied to the wettability measurements conducted in this study.

Present theory provides an equation for work of adhesion which states:[34]

$$\frac{W_a}{2} = \alpha_L \alpha_S + \beta_L \beta_S \tag{5}$$

where

$$\gamma_{LV} = \gamma_{LV}^d + \gamma_{LV}^p = \alpha_L^2 + \beta_L^2 \tag{6}$$

$$\gamma_{SV} = \gamma_{SV}^d + \gamma_{SV}^p = \alpha_S^2 + \beta_S^2 \tag{7}$$

$$W_a = \gamma_{LV} (1 + \cos\theta) \qquad [\theta \geq 0] \tag{8}$$

A new basis for designing wettability experiments which becomes evident by rearranging Eq. 5 as follows:

$$\frac{W_a}{2\alpha_L} = \alpha_S + \beta_S (\beta_L/\alpha_L) \tag{9}$$

Equation 9 points out that a plot of $W_a/2\alpha_L$ versus (β_L/α_L) defines α_S as the intercept at $\beta_L/\alpha_L = 0$ and β_S as a slope. Thus by selecting test liquids with varied values of surface tension γ_{LV} and (polar/dispersion) = β_L/α_L character a means becomes available to isolate two solid-vapor surface tension properties as defined by Eq. 7.

Based on the detailed knowledge of solid surface properties, as defined by Eq. 7, new and more detailed surface energetic criteria for adhesive bonding becomes available. The concept of the adherend "wettability envelope" was introduced in our work to define the equilibrium conditions under which an adhesive phase will spontaneously wet and spread over an adherend surface to displace the ambient air phase and eliminate interfacial cavities. The wettability envelope represents a critical function of γ^d_{LV} and γ^p_{LV} which can be generated by introducing polar coordinates T and θ defined by

$$T = \left[\left(\gamma^d_{LV}\right)^2 + \left(\gamma^p_{LV}\right)^2\right]^{\frac{1}{2}} \tag{10}$$

$$\tan \theta = \gamma^p_{LV} \Big/ \gamma^d_{LV} \tag{11}$$

Substituting Eq. 10 and Eq. 11 into the equation for the liquid (or adhesive) phase spreading coefficient:

$$S_L = W_a - 2\gamma_{LV} \tag{12}$$

it follows that for spontaneous spreading to occur where $S_L \geqslant 0$ that the wettability envelope for the adherend surface is defined by the region of γ^d_{LV} versus γ^p_{LV} bounded by the following function:

$$T(\theta) = \left[\frac{(\gamma^d_{SV} \cos \theta)^{\frac{1}{2}} + (\gamma^p_{SV} \sin \theta)^{\frac{1}{2}}}{\cos \theta + \sin \theta}\right]^2 \tag{13}$$

If a combined value of γ^d_{LV} and γ^p_{LV} for the liquid (or adhesive) phase falls within the region enclosed by Eq. 13 that adhesive is predicted to spread. Conversely, if the surface energy properties of the adhesive are outside the wettability envelope non spreading and weak bonding with interfacial cavities is predicted.

Environmental effects on adhesive joint strength have recently been defined in terms of the critical Griffith surface energy γ_G for crack propagation. The new definition of γ_G appears in the following special relation for the critical stress σ_c for crack opening under normal stress loading:

$$\sigma_c = \left(\frac{2E\gamma_G}{\pi C}\right)^{\frac{1}{2}} = \left(\frac{2E}{\pi C}\right)^{\frac{1}{2}} (R^2 - R_o^2)^{\frac{1}{2}} \tag{14}$$

where:

$$R_o^2 = 0.25\,[(\alpha_1-\alpha_3)^2 + (\beta_1-\beta_3)^2] \tag{15}$$

$$R^2 = (\alpha_2-H)^2 + (\beta_2-K)^2 \tag{16}$$

$$H = 0.50\ (\alpha_1 + \alpha_3) \qquad (17)$$

$$K = 0.50\ (\beta_1 + \beta_3) \qquad (18)$$

where the subscripts relate respectively to 1 = adhesive, 2 = environmental immersion phase, and 3 = adherend and $\alpha = (\gamma^d)^{\frac{1}{2}}$ and $\beta = (\gamma^p)^{\frac{1}{2}}$ of these phases. Equation 14 provides a means of predicting the suppression of the critical Griffith stress σ_c which may be induced by modifying the surface energy properties of the environment as defined by $\alpha_2 = \beta_2 = 0$ for dry air to $\alpha_2 = 4.67\ (\text{dyn/cm})^{\frac{1}{2}}$ and $\beta_2 = 7.14\ (\text{dyn/cm})^{\frac{1}{2}}$ for water immersion.[34]

C. Adhesive Primer Procedures

1. Applications and Cure Cycles

a. Priming procedure for Al 2024-T3 and Ti-6Al-4V with HT-424 A&B primer: Freshly treated coupons are spray primed to an approximate thickness of 0.001" using an atomizer operated on low pressure, clean, dry (argon) gas. The primer has the following composition:

10 pbw HT-424 part A
10 " " " B
30 " " primer-thinner

The primed coupons are dried for 30 min. under ambient laboratory conditions. The primed coupons are then oven dried for 60 min at 66°C. This priming procedure is recommended[35] by the manufacturer and was followed throughout the program.

b. BR-34 primer application for bonding Ti-6Al-4V:

1) Thin and spray on 2 mil dry coating,
2) 30 min air dry,
3) 30 min oven dry at 220°F (104°C),
4) 45 min oven dry at 410°F (210°C).

c. BR-34 primer for contact angle analysis:

1) 1 part primer diluted with 5 parts BR34-2 thinner,
2) coated on glass slide by dipping,
3) 30 min air dry,
4) 30 min oven dry at 104°C in dry N_2 atmosphere,

5) 60 min oven dry at 210°C in dry N_2 atmosphere,
6) uncured samples given 20 hr air dry and 5 hr vacuum dry.

D. Bonding Procedures

1. Bonding Fixture

A 1" x 0.5" section of adhesive is tacked onto the treated and primed end of a 4.000" x 1.000" coupon to be bonded. This coupon is then positioned against one end of a 1.000" x 7.500" hole cut in a 0.126" thick aluminum or titanium sheet (see Fig. 7). Six such sections have been cut in this sheet allowing up to six bonds to be prepared at once. At the other end of the cut-out section a spacer is positioned as in Fig. 8. Then the other half of the bond which is also 4.000" long and 1.000" wide is placed against the other end of the cut-out section on top of the spacer. From Figs. 7 and 8 we see that by this arrangement the two coupons making up the bond are prevented from moving horizontally and the overlap between the two bonding coupons is maintained at the desired 0.500". Measurement of the glue line thickness showed that the glass carrier in the HT-424 adhesive maintains the glue line thickness at 0.008". As shown in Fig. 7, a 1/8" overcut around the bonding area allows for excess adhesive to flow out without bonding to the jig. A 0.063" thick aluminum sheet with an aluminum foil cover to prevent bonding to it by excess adhesive is then taped over the jig on each side. This assembly is then placed in a press at ~ 50 psi during the cure cycle.

2. Cure Cycles

The cure cycle for the HT424 system was that recommended by the manufacturers:[35]

a) Raise temperature to 340°F (171°C) in 60 min.
b) Cure for 60 min at 340°F (171°C),
c) Cool down in

For FM-34B-32 the cure cycle was:

a) Cut adhesive and store in desiccator prior to bonding.
b) Heat joint to 550°F (288°C).
c) Hold at 550°F for 90 min at 40 psi.
d) Cool to room temperature at 40 psi.

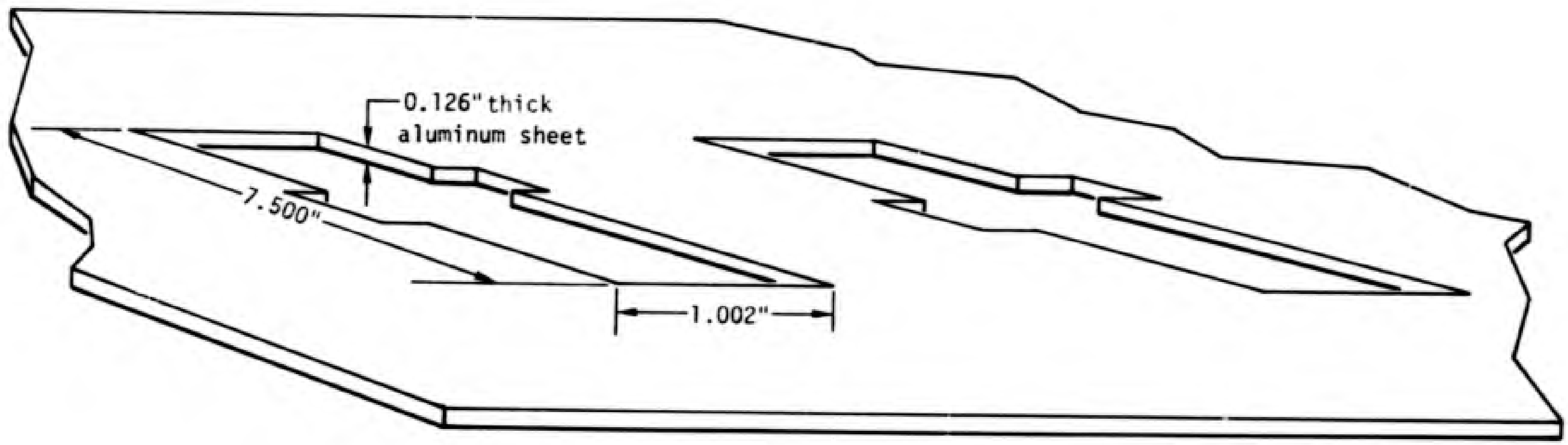

Fig. 7. Schematic drawing of cut out sections for the bonding jig.

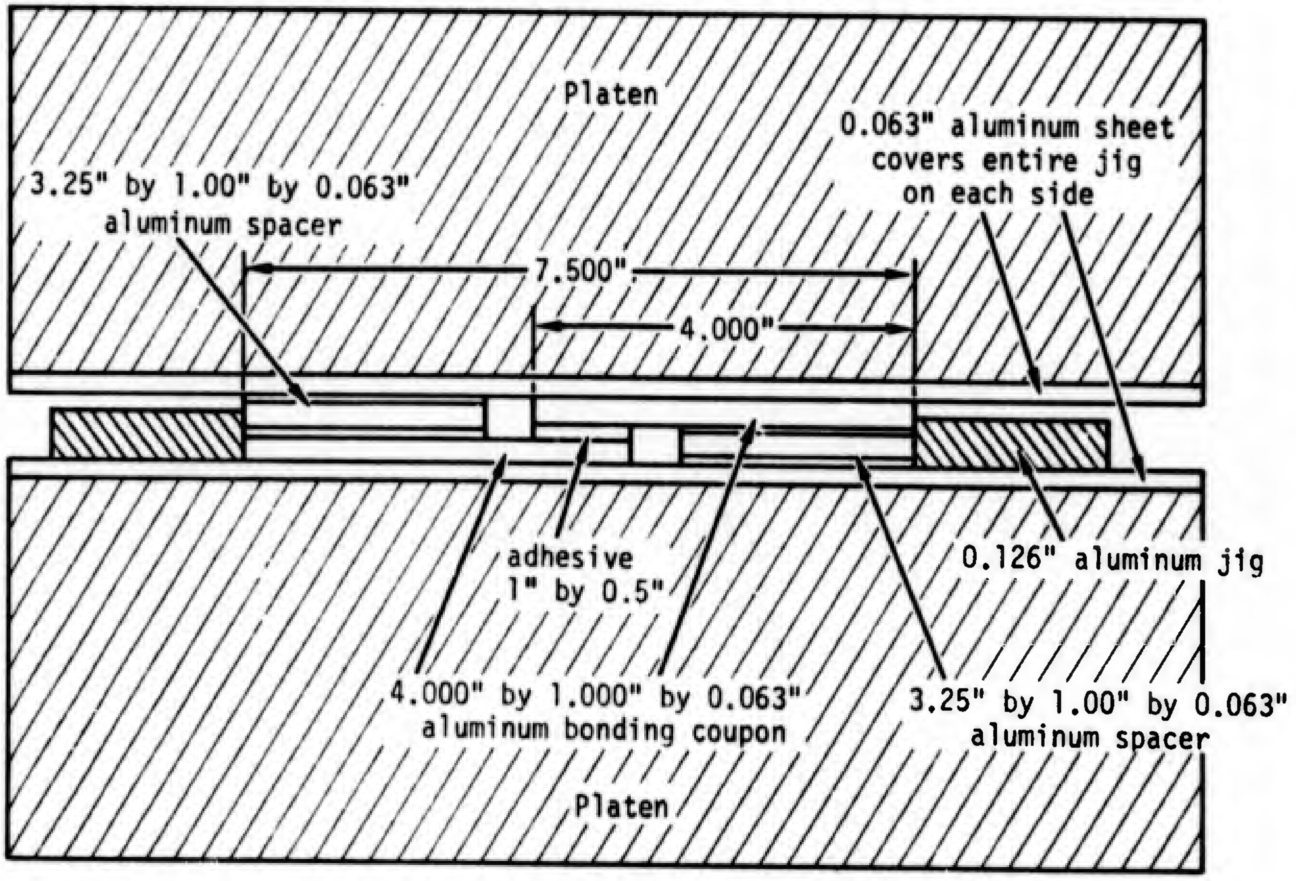

Fig. 8. Schematic drawing of bonding jig and press.

E. Tensile Lap Shear Testing

1) 1-1/2 inch x 1 inch x .063 aluminum shims are bonded to the inside (bonded side) ends of the bonded pieces.

2) Bonded pieces are clamped in 0-.25 inch jaws of floor model Instron testing machine leaving 4.5 inches jaw to jaw distance (2 inches from each glue-line).
3) Bonds are sheared at crosshead rate = 0.01 inch/min.
4) Strip chart recorder records stress in pounds versus strain (crosshead displacement).

F. Surface Aging (SET) Effects

SET refers to surface exposure time. For surface exposure experiments 4" x 1" x 0.063" samples of freshly treated Al 2024-T3 or Ti-6Al-4V are set in an 8" diameter glass chamber (usually used as a desiccator) which contains a dish of saturated K_2SO_4. The 1" wide samples just fit into holes in a ceramic bottom plate, which held them in approximately a vertical orientation. The lid is then secured on with tape as no stopcock grease is used. The desiccator is then placed in an oven at 55°C and the saturated salt solution provides a 95% R.H. condition. Samples are then withdrawn at various SET. For contact angle measurements 4" x 1" x 0.063" samples were cut into 4" x 0.12" x 0.063" strips and placed in the chamber. After SET these strips were then cut into 0.5" lengths.

G. Bond Joint Aging (BET) Effects

BET refers to bond exposure time. Bond exposure experiments at 54°C and 95% R.H. are also carried out in the glass chamber with a saturated K_2SO_4 solution to provide constant humidity.

Section III

EXPERIMENTAL RESULTS AND DISCUSSION

A. Aluminum Adherends

1. Surface Character vs. Joint Strength

a. Ellipsometry

The average value of Δ and ψ for 22 different samples with the FPL etch is 110.5 ± 2.5 and 37.6 ± 0.3, respectively. The wavelength was 6328 Å and angle of incidence 70°. Nomographs of Δ vs ψ are plotted in Figs. 9 and 10 for various film thickness and optical constants. Plotting the average values of Δ and ψ for the FPL etch on 2024-T3 aluminum fall outside the curves for reasonable values of n_f between 1.5 and 3.0 and d between 0 and 2000 Å for transparent films ($\kappa_f = 0$). The values of Δ and ψ for the FPL etch fall within reasonable limits if the effective value of κ_f is assumed to be ~ 0.3 as in Fig. 10. The best estimate of film thickness is obtained as ~ 200 Å if $n_f \approx 1.7$ as for bulk oxide.

According to the literature[36] anodized aluminum in borate solutions produces oxide films ~ 14 Å/volt with optical constants similar to bulk α aluminum ($n_f = 1.7$, $\kappa_f = 0$). To establish the reliability of our ellipsometric measurements for aluminum; samples were anodized at various voltages to yield films between 50 and 1000 Å. Our ellipsometric results were within 5% of the values predicted from the literature (i.e. 14 Å/volt, $n_f = 1.7$, $\kappa_f = 0$). The thickness of oxide on FPL etch aluminum has been estimated by another independent technique, i.e. photo-electron emission. Photo-electron currents from aluminum that had been anodized to thicknesses between 50-1000 Å) with light of $\lambda = 2500$ Å ($h\nu \approx 5$ eV), yielded a calibration curve. The photo-emission current from an FPL etched sample corresponded to 210 Å on the calibration curve.

Attempts to remove FPL-etch films by the methods of Hamilton and Lyerly[13] was not successful because the films appeared to grow in thickness. Lyerly (personal communication) confirmed they had observed the apparent film growth problem and report films of thicknesses from 650 (mμ) to 4500 (mμ), i.e. 6500 Å to 45,000 Å.

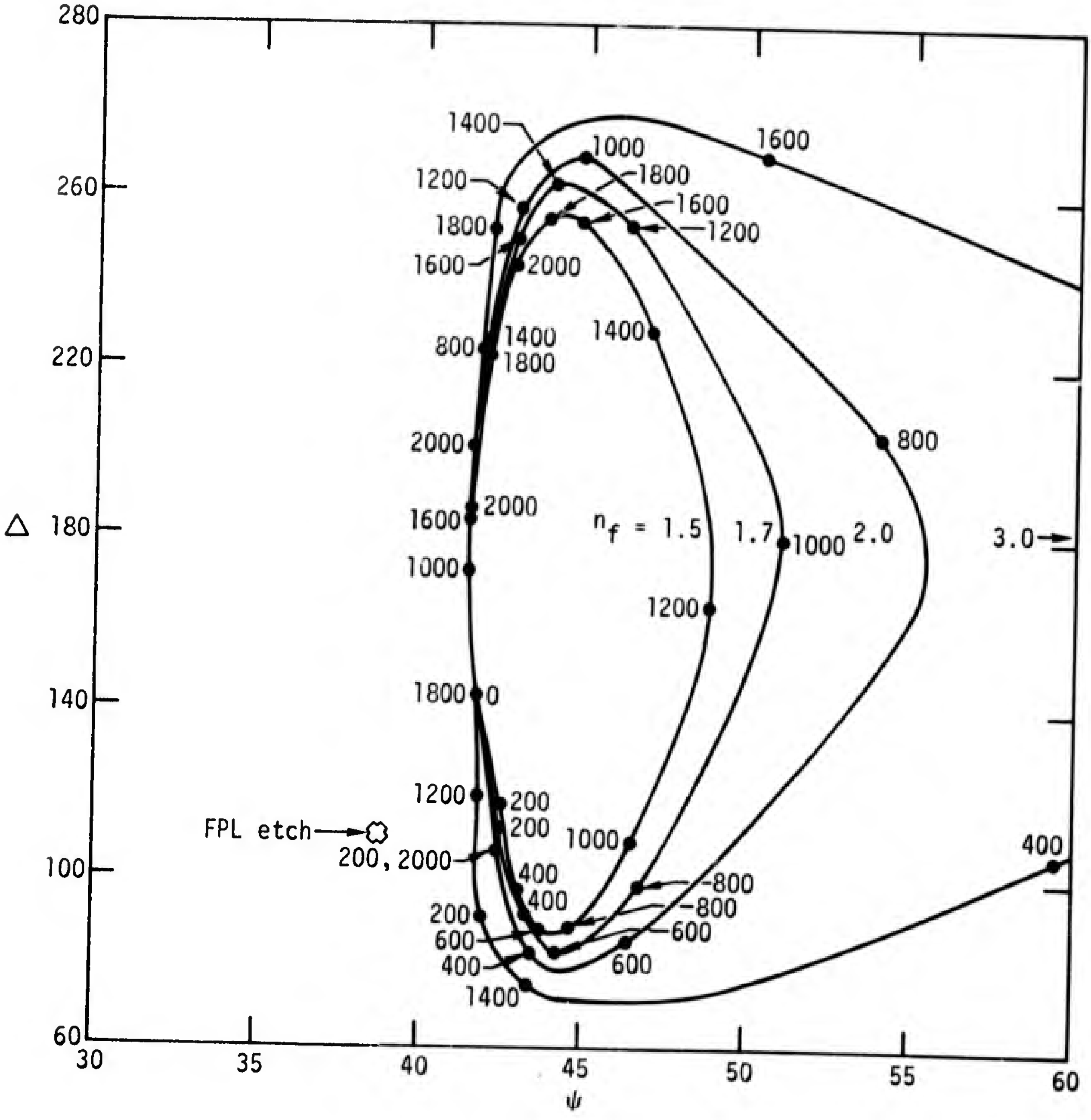

Fig. 9. Nomograph of Δ vs ψ for transparent films on aluminum (λ = 6328 Å, angle of incidence 70°, n_s = 1.43, κ_s = 5.17).

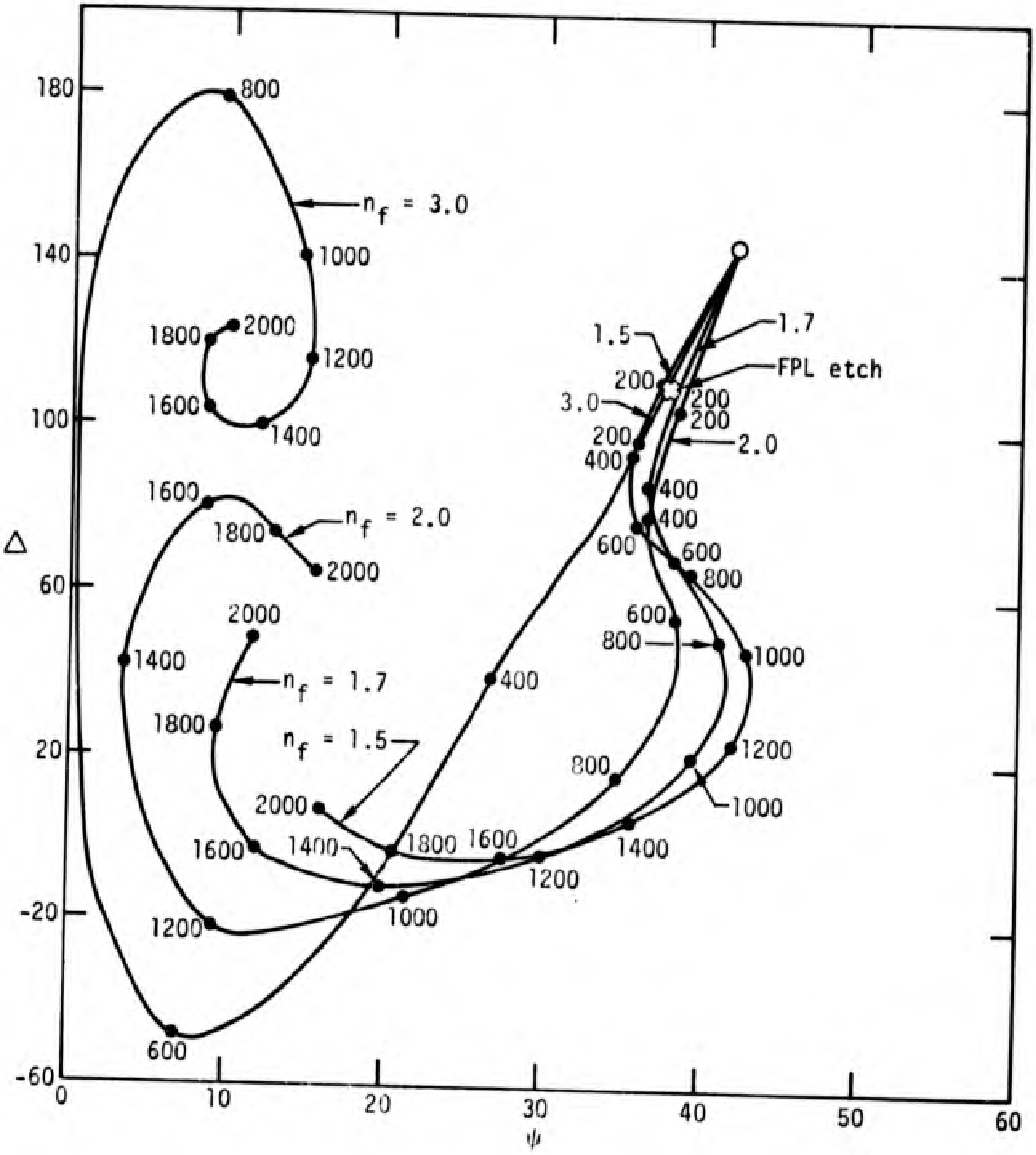

Fig. 10. Nomograph of Δ vs ψ for an absorbing (κ_f = 0.3) film on aluminum.

Bowen[37] observed oxide films (~ 2000 Å by ion sputter etching) on FPL etch aluminum but found the weak bonds resulting from these films was associated with aged etching solution in a lead lined etchant tank. Strong bonds were observed for samples etched in solutions contained in glass beakers as we are using. He had not measured the thickness of the FPL etch films that gave strong bonds.

It should be noted in Fig. 29 of the Picatinny report[13] that alkaline cleaned 2024-T3 aluminum produced a thick cracked film estimated from the protruding layer, to be about 1000 mμ (10,000 Å) thick. One might expect that films 4500 mμ thick from the FPL etch might also crack and be revealed by SEM. However, none of the SEM pictures in the Picatinny report or in our SEM pictures reveal such films. It is believed that FPL etch films were grossly thickened by the removal process reported in the Picatinny report[13] and that oxide films left on aluminum from the FPL etch (in glass beakers) are very thin (~ 200 Å).

The estimate of thickness of the oxide film on vapor degreased 2024-T3 aluminum is 280 Å and $\kappa_f \approx 0.5$ if $n_f = 1.7$ and Table 4 shows ellipsometric data for plasma treated 2024-T3 aluminum. These experiments were carried out in a glass chamber in order to control the atmosphere during and after the plasma treatment. The purpose of the plasma treatment was to remove surface layers prior to bonding. In order to make ellipsometric measurements through the glass chamber, it was necessary to provide birefringent free windows. The first two rows of data in Table 4 indicate that the presence of the windows had a very small effect on Δ and ψ. For these experiments the angle of incidence was 60° and the wavelength 5461 Å. A one-half hour plasma treatment removed approximately 23 Å of the film and the next half hour only removed about 2 Å more. The surface pretreatment was an alkaline clean process. A similar small decrease in film thickness and saturation effect is noted in Table 5 for the vapor degrease pretreatment, whereas continued plasma exposure continues to remove film from an FPL etch treated surface. From the experiments reported in Table 5, the samples were removed from the plasma chamber to make the ellipsometric measurements. The plasma etching rates were much lower than had been hoped for but it is expected that outer surface contamination is removed by the process. Values for estimated film thickness and optical constants for the various surface treatments are reported in Table 6.

TABLE 4

Ellipsometer Study of Plasma Treated* Al2024-T3

λ = 5461 Å ϕ = 60°

Time in Plasma (min)	Power (watts)	Δ	ψ	n_f	κ_f	Thickness d(Å)	δd (Å)
0	No Windows	116.8	34.50	1.8	0.6	310	0
0	Windows	117.0	34.85	1.7	0.6	315	0
10	50	117.5	34.65	1.8	0.6	301	14
20	100	117.9	34.72	1.9	0.6	296	19
30	150	119.4	35.3	1.8	0.6	282	23
60	200	120.6	36.0	1.8	0.6	280	25

* See No. 3 of Table 1

TABLE 5

Surface Potential and Ellipsometric Study of Plasma Treated Al2024-T3*

(Measurements in Air)

Plasma Treatment Time (hrs)	Initial Treatment	Average Surface Potential Difference (Volts)	Average Thickness (Å)	δd (Å)
0	Vapor degrease	0.31	250	0
0.25		0.15	217	33
1.25		0.25	217	33
2.91		0.30	217	33
0	FPL Etch	0.26	250	0
0.25		0.02	220	30
1.25		-0.01	210	40
2.91		0.03	195	55

*See No. 1 and 2 of Table 1

TABLE 6

Surface Characterization of Al 2024-T3 Samples and Bond Strengths for Various Surface Preparations. Adhesive HT-424

	SURFACE CHARACTERIZATION																BOND STRENGTH
	Ellipsometry			SPD	γ_{SV}	Auger Spectroscopy											Tensile Shear Strength psi
						APPH											
Surface Preparation	Film Thickness Å	n	κ	ΔV Volts	$\frac{dyn}{cm}$	Al	Cu	Mg	Ni	Fe	Si	C	O	Cr	Cl	S	
Vapor degrease	280	1.7	0.5	0.56	45	5	0	29			14	65	100	0	12	6	2367 ± 50
FPL-Etch	200	1.7	0.3	0.48	80	38	4	0	4	0.7	0	0.5	87	0	0	0.5	3080 ± 250
Plasma	296	1.9	0.6	----	64												3130 ± 263

b. Auger Spectroscopy

The initial Auger peak to peak height (APPH) for various elements on the aluminum surface after the vapor degrease (No. 1 of Table 1) and the FPL etch (No. 2 of Table 1) are also recorded in Table 6. No Auger results were obtained for the plasma treated surface. Relative to the FPL etch, the vapor degrease treatment leaves considerably more Mg, Si, C, Cl and S at the outer surface. The aluminum peak on the vapor degreased sample is masked by the contamination. Other than aluminum and oxygen, Fe, Ni, Cu, C and S were detected on the FPL etch sample if the sample was placed in the vacuum chamber within an hour of treatment. It should be noted that no chromium is observed. Bowen[37] reports observation of Cr on the surface immediately after placing the sample in the vacuum system but that it is removed by the vacuum system in a few hours. Our samples were not measured with Auger for about 12-24 hrs after being placed in the vacuum system and this may be why no Cr was observed.

c. Chemical Profiles

Figure 11 shows chemical profiles of two identically treated 2024-T3 aluminum samples with the FPL etch which had been exposed to laboratory air for some hours. The solid points are for one sample and the open circles for the other. The reproducibility is excellent for the Auger peak to peak heights (APPH). The Ar^+ ion sputtering was done at about 10^{-5} torr, 2 kV, $\sim 100\ \mu a/cm^2$ over an area of $\sim 0.25''$ diameter. As pointed out previously, the interpretation of these profiles with respect to actual atomic concentrations is too difficult at present. The value of the profiles lies in qualitative and semi-quantitative analysis. The APPH for Cu, C, Ni, S and Fe have been expanded by a factor of 12.5 with respect to the APPH for Al and oxygen. The alloy elements Al, Cu and Fe (see Table 3) are observed in the oxide film and the substrate metal. The Cu has segregated to higher concentration in the oxide than in the metal and Fe is in the outer atom layers only. Within the resolution of the spectrometer, the alloy elements Mg, Si, Zn, Cr and Mn are not observed, whereas Ni is observed. Carbon contamination is probably from laboratory air or from adsorption of CO in the UHV system.

Figure 12 shows the profile of the back side of a sample that had the FPL etch and then exposed to 55°C and 95% R.H. for 48 hrs, bonded and

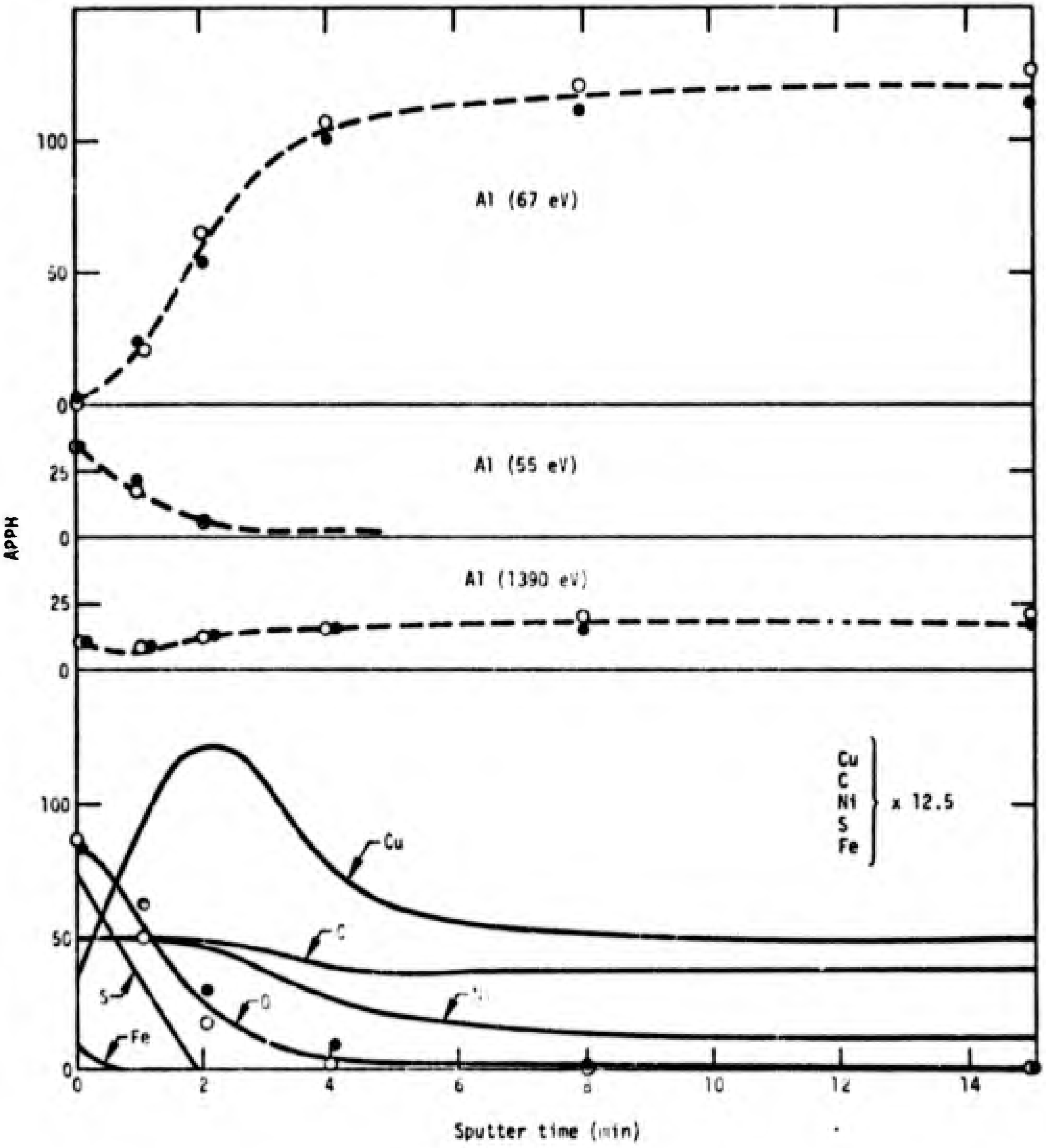

Fig. 11. Chemical profiles of oxide films formed on Al 2024-T3 by the FPL etch.

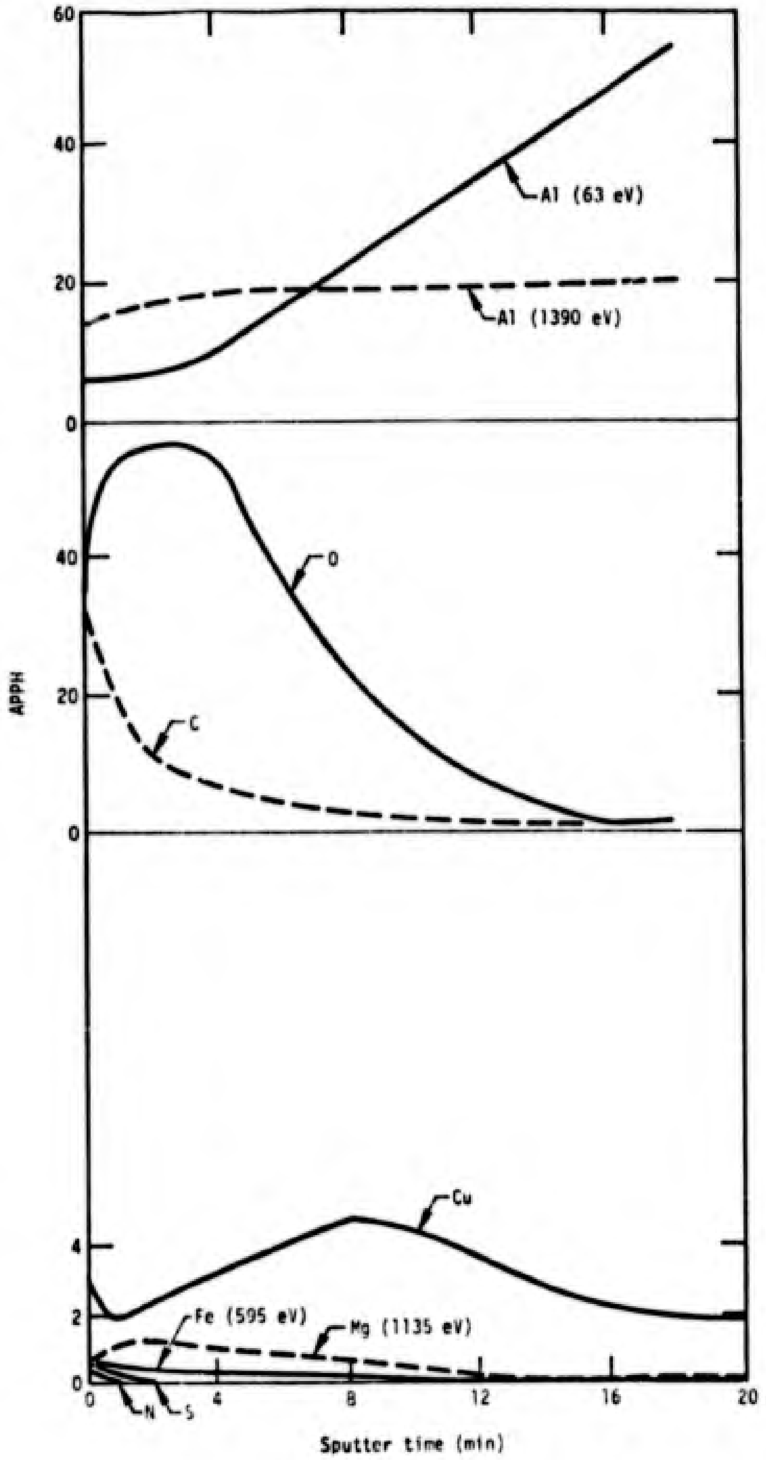

Fig. 12. Chemical profile for the unbonded side of a sample with the FPL etch and SET = 48 hrs at 54°C and 95% R.H.

fractured. The low energy Al (55 eV) and (67 eV) peaks were not resolved in these measurements, the curve labeled Al (63 eV) reflects mostly the Al (67 eV) peak. Initial carbon contamination was much greater for the 48 hr SET sample (e.g. APPH ~ 34) as compared to the fresh sample (APPH ~ 50/12.5 = 4). Cu, Mg and Fe was observed but no Ni was observed and S and N in addition to C was observed. Since the electron beam diameter was small ~ 0.04 cm^2, an attempt was made to profile the adhesive side of the fractured couple. Figure 13 is a profile in an area that interfacial failure occurred. The striking feature of Fig. 13 is the high APPH value for Si in the failure area. This may indicate that interfacial failure (weak oxide) is associated with areas that were contaminated by the carrier glass fibers or silicones from the atmosphere. Figure 14 shows profiles as the electron beam was moved slightly into the adhesive region. No Si is observed and as expected the C peak increased dramatically. It should also be noted that the sputter rate has been decreased by a factor of 10 for the adhesive side (Figs. 13 and 14).

d. Surface Potential Difference

If the reference electrode changes over a period of time, comparison of SPD becomes difficult. It is therefore useful to compare SPD values for a series of measurements made at one time; for example as in Table 5. The plasma treatment decreased SPD from 0.31 volts to 0.15 volts and then increased it to 0.3 again for the vapor degrease pretreatment. Plasma treatment of the FPL etch sample decrease SPD from 0.26 volts to ~ zero where it remained.

In a previous set of experiments SPD for a vapor degreased sample was 0.56 volts as compared to 0.48 volts after the FPL etch, a decrease of 0.08 volts. This decrease can be compared with a decrease of 0.31-0.26 = 0.05 volts in Table 5.

e. Microscopy

Figure 15 shows SEM pictures of a 2024-T3 aluminum surface after the FPL etch. The pitted nature of the surface is similar to that revealed by SEM in other laboratories. For example, Fig. 15 can be compared with Figs. 31 and 32 of the Picatinny report[13] and Figs. 10 and 11 of a paper by Patrick.[38] Figures 16 and 17 are optical microscope pictures of typical fractured bonds for 2024-T3 aluminum with HT-424 adhesive. The photographs are much more

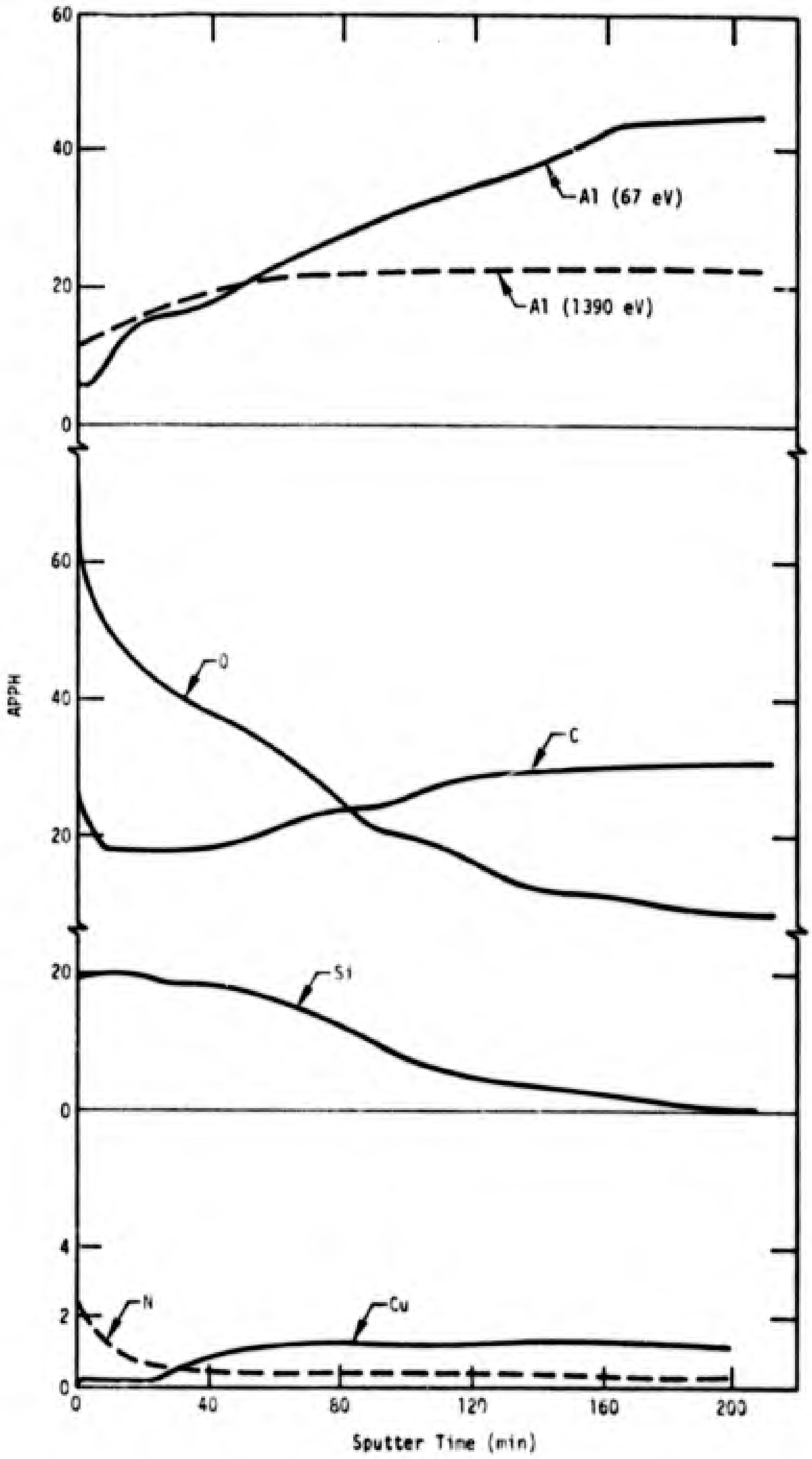

Fig. 13. Chemical profile in the interfacial failure area of an Al 2024-T3-HT424 joint. SET = 48 hrs, 54°C, 95% R.H.

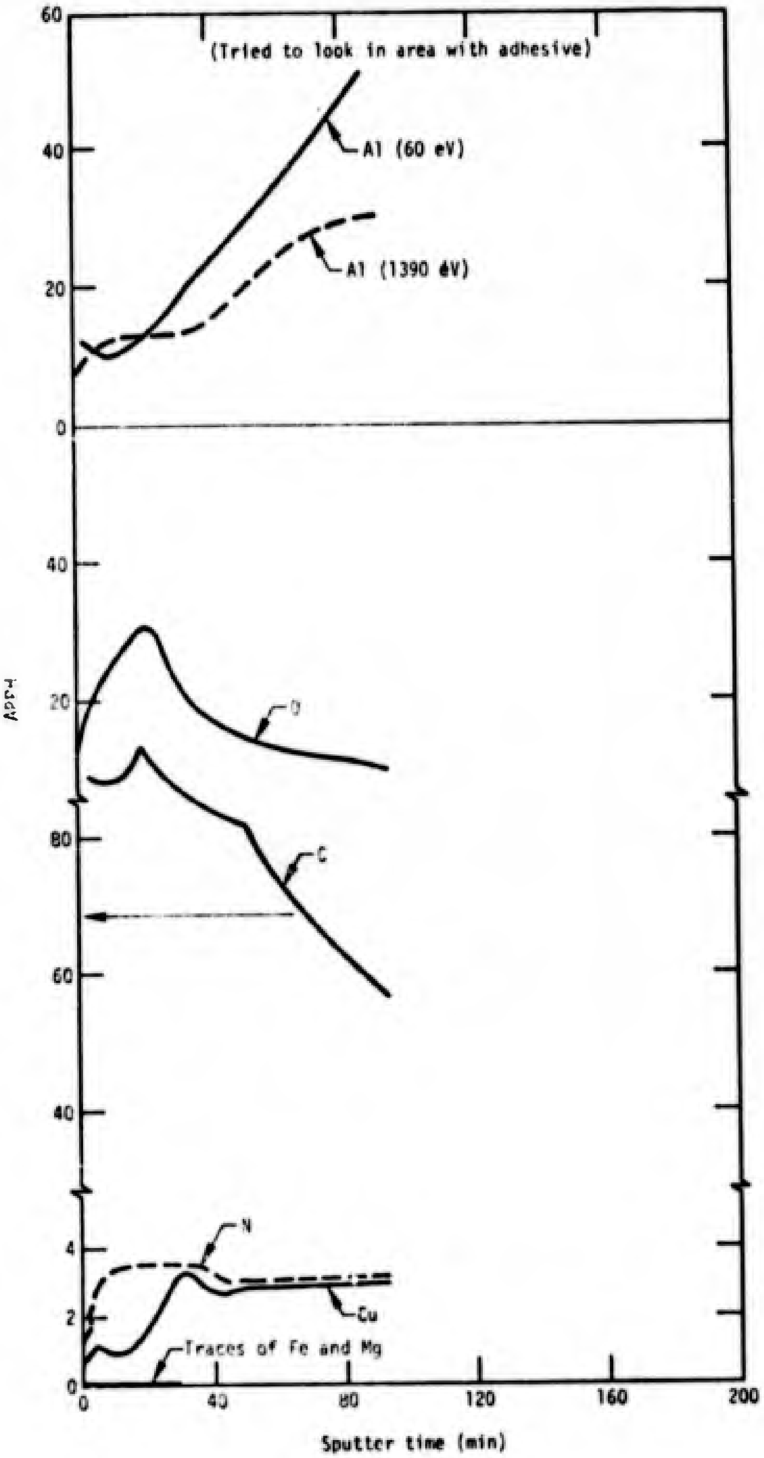

Fig. 14. Chemical profile in a region of cohesive failure for Al 2024-T3 - HT424, SET = 48 hrs, 54°C, 95% R.H.

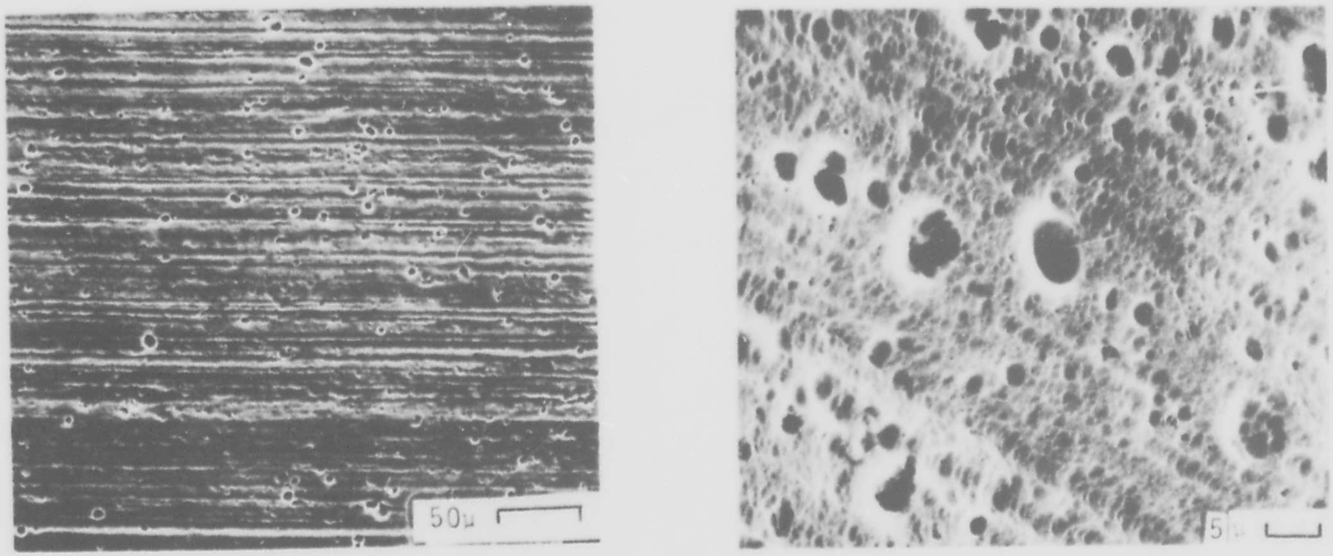

240X

1600X

Figure 15

Scanning electron micrographs (SEM) of an FPL etch Al 2024-T3 surface.

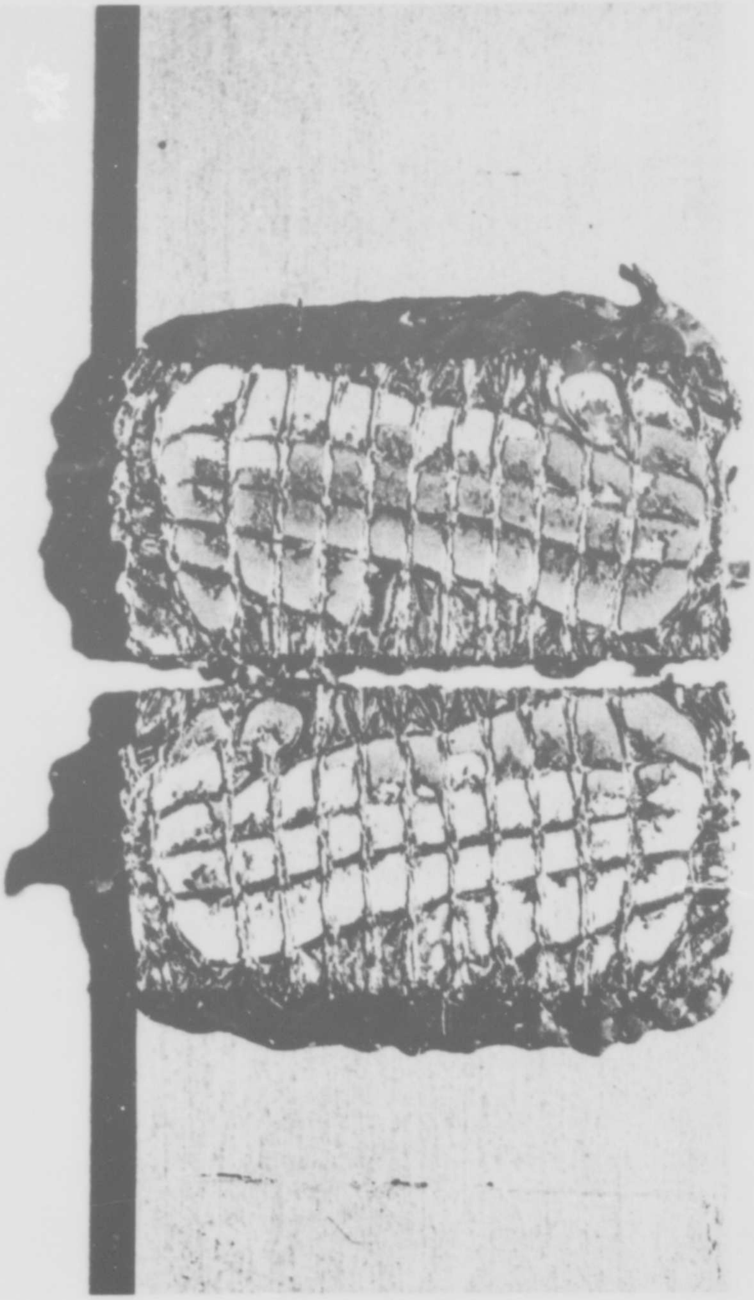

Fig. 16. Photograph of fractured bonds for Al 2024-T3 - HT424 joint after 808 hrs at 54°C and 95% R.H.

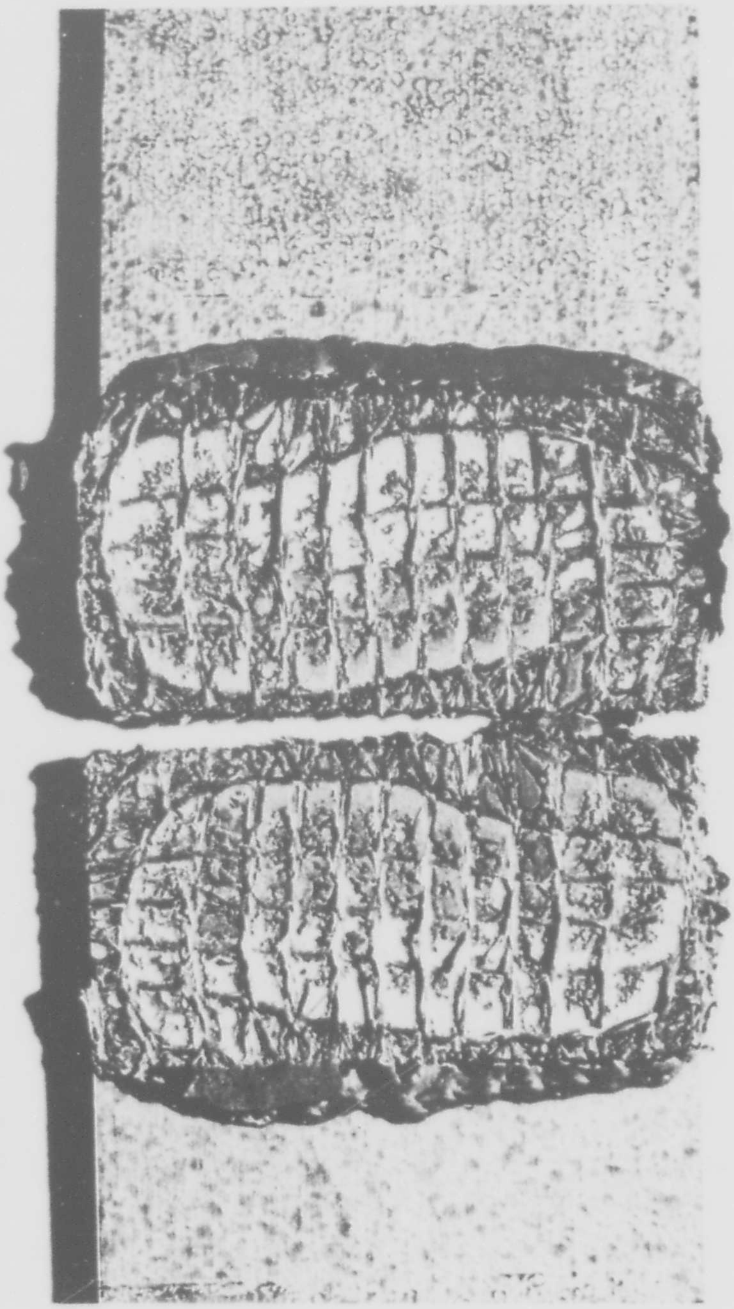

Fig. 17. Photograph of fractured bonds for Al 2024-T3 HT424 adhesive after 1023 hrs at 54°C and 95% R.H.

difficult to interpret than observation under the microscope. Low power microscopic observation reveals three failure modes in the 0.5" x 1" bond area. First the glass carrier network usually fails, with about half the fiber bundle on one adherend and half on the other, leaving the fiber net observed in Figs. 16 and 17. Second, most of the bond appears to fail at metal-adhesive interface leaving matching surfaces. The light areas between the fiber net is the metal interface, the darker more dull areas are the matching adhesive surface. Third, cohesive failure occurs in the adhesive revealing a large amount of natural porosity caused by water vapor bubbles formed during the cure. Details of the cure process with respect to this porosity can be found in a paper by Kaelble and Cirlin.[39] The failure mode is related to the stress distribution of the lap shear joint during the tensile test. The stress distribution is schematically represented in Fig. 18 (by Bolger[38]). The predicted pattern (Fig. 18) of interfacial failure, in the region farthest from the end of the metal coupon, was observed in general and is somewhat revealed in Figs. 16 and 17. Cohesive failure was generally more prevalent at the periphery of the bond area as for Fig. 16. Cohesive failure spread towards the center of the bond area for the bond with longer aging time (Fig. 17). In some instances failure occurred almost entirely at the metal-adhesive interface as shown in Fig. 19 for aging in 100% relative humidity.

It is of interest to investigate regions of different failure modes in more detail. Figures 20a and b are low magnification SEM pictures for a bond that had not been aged. The bright areas in these pictures are caused by removal of the metal over-layer used in the SEM process and charging of the dielectric substrate. Figure 20a shows a region of the adhesive surface that had mostly failed at the metal interface. An enlargement of the central part of Fig. 20a is seen in Fig. 20c. The fractured adhesive in Fig. 20c indicates that void regions in Fig. 20a penetrate to the opposite interface. There is considerable cohesive and interfacial failure in the region of Fig. 20a. Figure 20b shows interfacial failure in the top half of the picture and cohesive failure in the lower half. The enlargement of a region of the lower half of Fig. 20b, in Fig. 20d shows cohesive failure parallel to the metal surfaces in contrast to interfacial failure and cohesive failure perpendicular to the plane of the metal in Fig. 20c. The large pore regions revealed at the bottom of Fig. 20b are presumably also beneath the adhesive surface in the top of Fig. 20b.

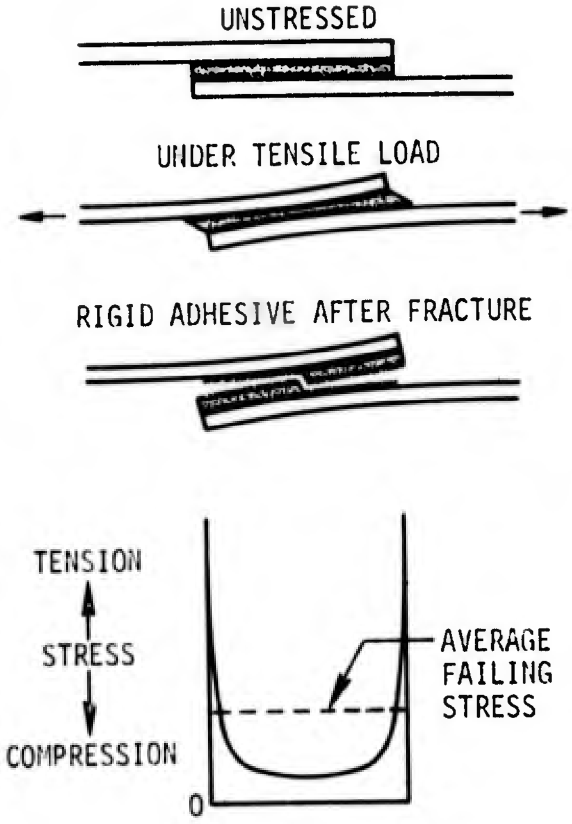

Fig. 18. Failure region in lap shear joint due to stress distribution (after Bolger[38]).

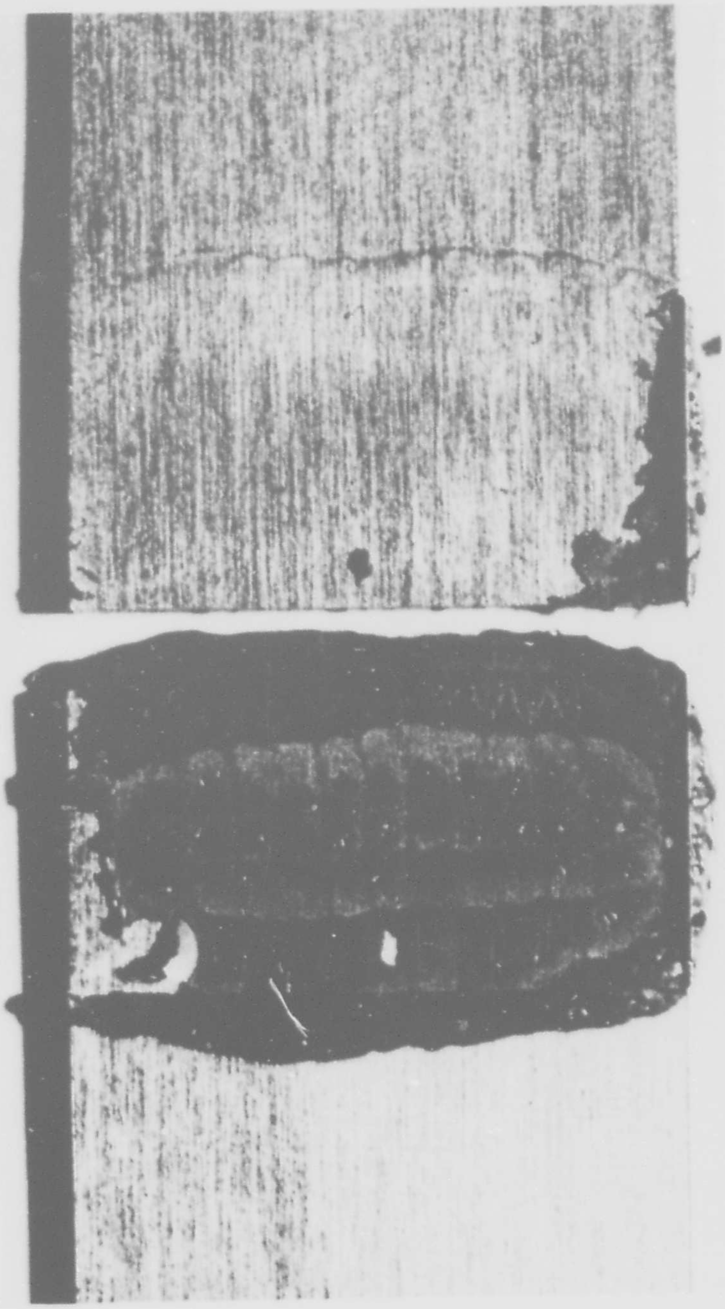

Fig. 19. Photograph of fractured bonds for Al 2024-T3 - HT424 after aging at 54°C and ~ 100% R.H.

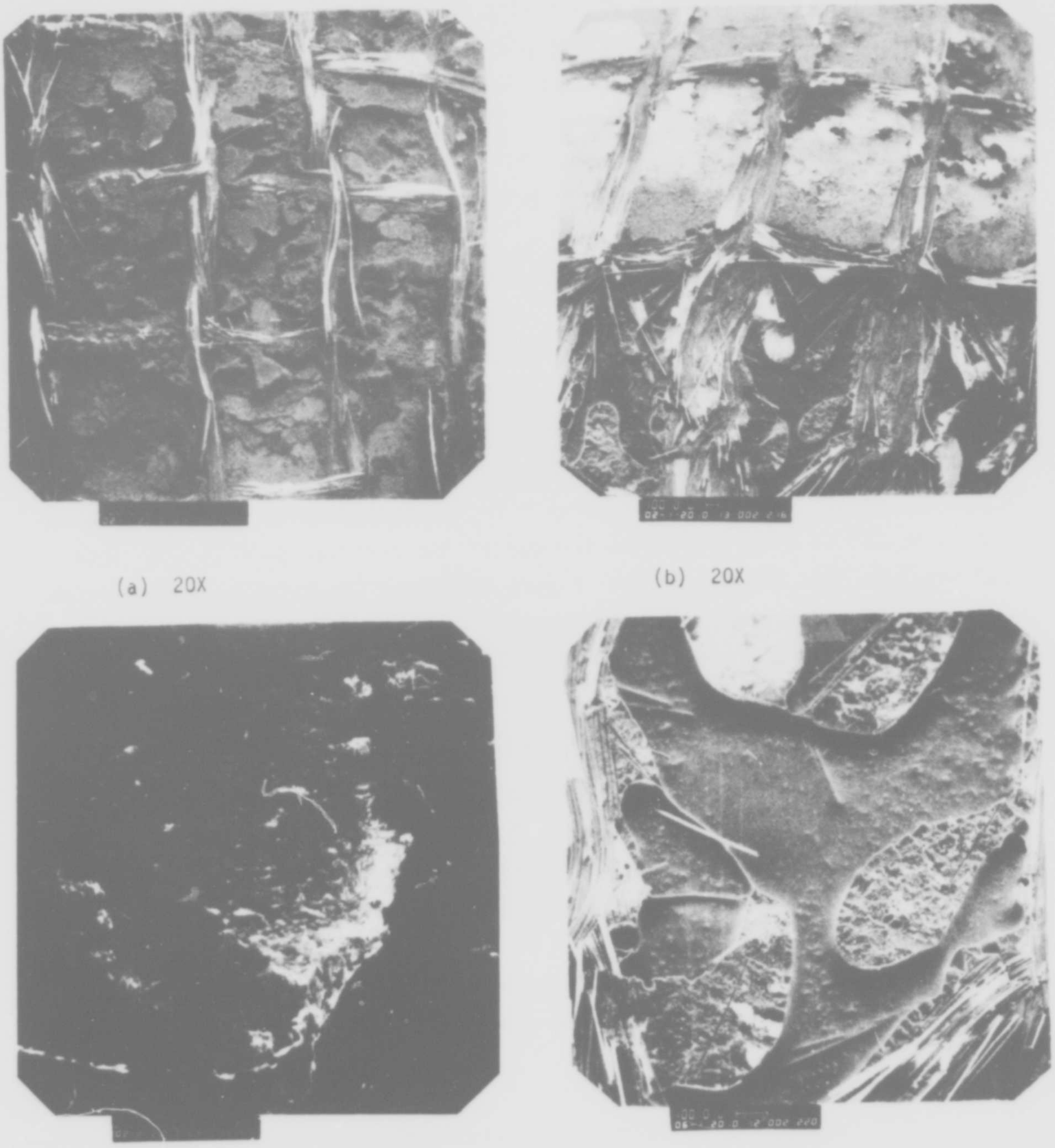

(a) 20X

(b) 20X

(c) 200X

(d) 60X

Fig. 20. SEM micrographs of an Al 2024-T3 - HT424 joint after fracture. SET = 0, BET = 0.

Figure 21a is a higher magnification of the adhesive surface in Fig. 20a. Figure 21b is a magnification of a region near the metal surface and reveals a region of primer layer that apparently did not adhere to the adhesive. The thin transparent nature of this region can be compared with the opaque pore region of Fig. 20d which is adhesive. Closer scrutiny of the edge of the primer film in Fig. 21c reveals small holes in the primer which will be shown, are due to penetration of primer into holes in the FPL etched surface (see Fig. 15). The region in the lower portion of Fig. 21b and c show that what might be interpreted from low power optical micrographs as interfacial failure includes a great deal of failure in the primer layer. The small voids within the primer (lower part of Fig. 21c) are elongated in a direction approximately perpendicular to the metal surfaces and probably nucleate and grow during fracture.

Figures 22, 23 and 24 are for a fractured bond that had been aged for 1000 hrs at 54°C and 95% R.H. Figure 22a is an optical micrograph of the adhesive surface and Fig. 22b is an SEM of the mating metal surface. Figure 22c is an SEM of a fiber bundle, the top of the adhesive surface (top left) and metal surface (bottom left). Figure 22d shows the metal area (left side) and adhesive pore area (right side) near a glass fiber bundle. Figure 23a is an enlargement of the adhesive surface after the 1000 hr (BET) and can be compared with Fig. 21a for 0 hr BET. Figure 23b shows a region of primer layer as for Fig. 21b and Fig. 23c is an enlargement of a region in Fig. 23b.

Figure 24a shows a region of adhesive pore surface (top, left), regions of cohesive failure (bottom left and top center), and regions of interfacial failure (bottom right). Figure 24b is an enlargement of the region designated by coordinates marked 1 in Fig. 24a. Holes in the primer can be associated with penetration of primer into holes in the metal substrate. Figure 24c is an enlargement of the region of interfacial and cohesive failure and Fig. 24d is an enlargement of the region with coordinates 2 in Fig. 24a.

f. Contact Angles

In order to evaluate the several methods of surface energy analysis, wettability studies were carried out on panels of Al 2024-T3 given the vapor degrease and FPL etch surface treatments. The results of liquid-solid contact angle measurements are summarized in Table 7. Contact angle measurements were conducted at 22°C in the B-100 environmental chamber of the NRL contact angle apparatus (Rame-Hart Inc.) using sessile drops. All liquids displayed stable

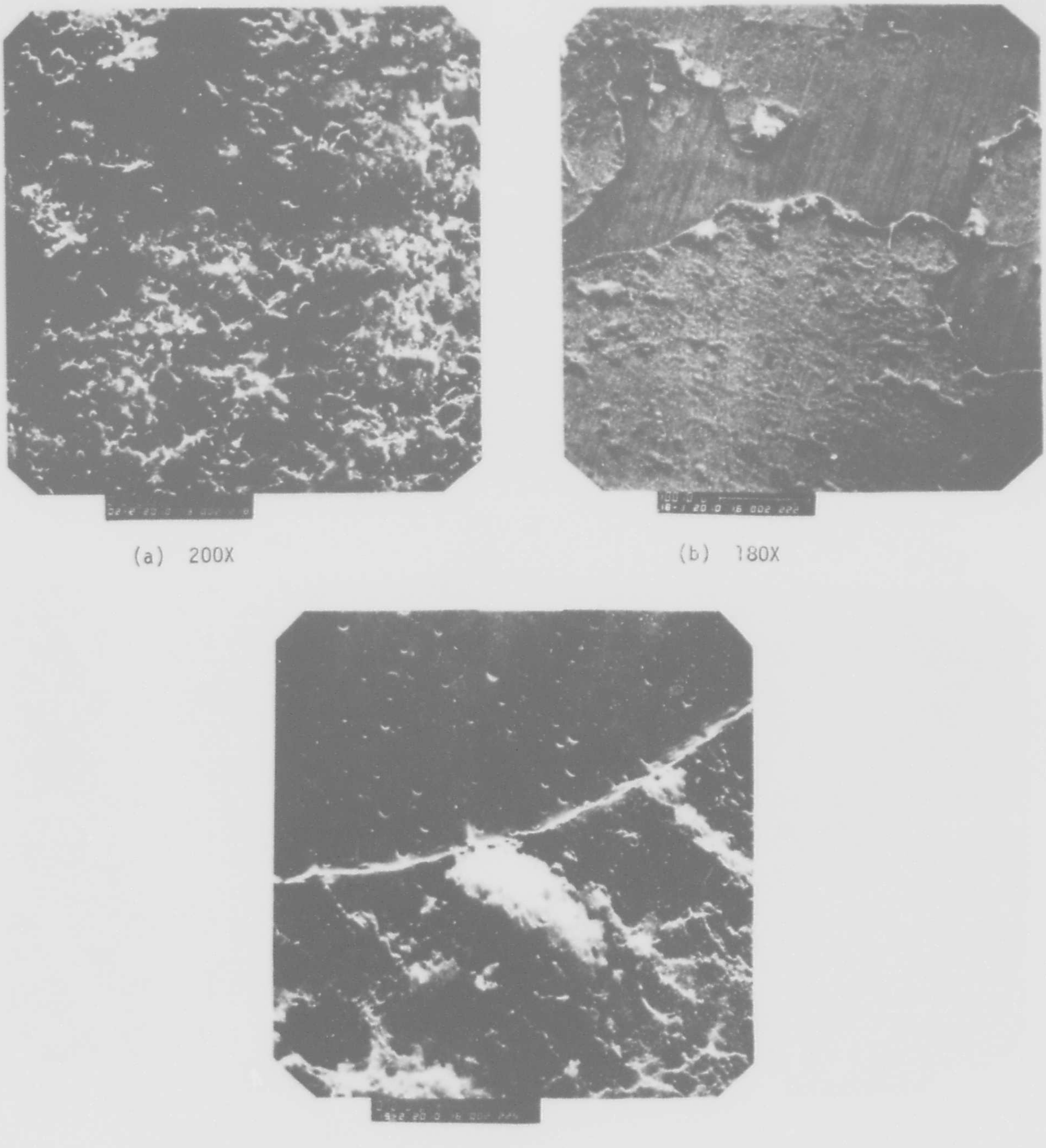

(a) 200X

(b) 180X

(c) 1900X

Fig. 21. SEM micrographs of an Al 2024-T3 - HT424 joint after fracture. SET = 0, BET = 0.

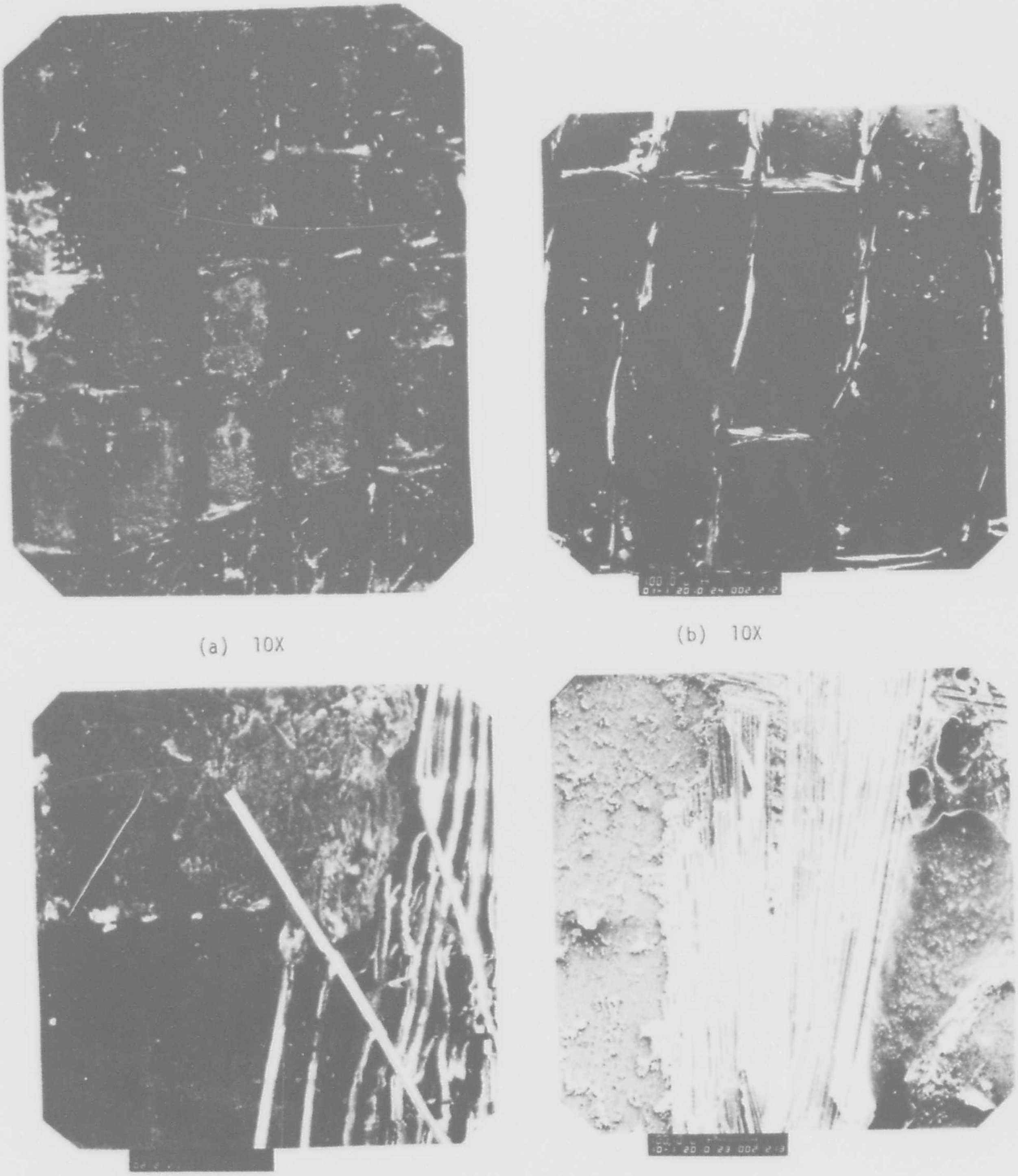

(a) 10X

(b) 10X

(c) 200X

(d) 100X

Fig. 22. a) Optical micrograph of Al 2024-T3 - HT424 joint after fracture. b,c,d) SEM micrographs. SET = 0, BET = 1000 hrs at 54°C, 95% R.H.

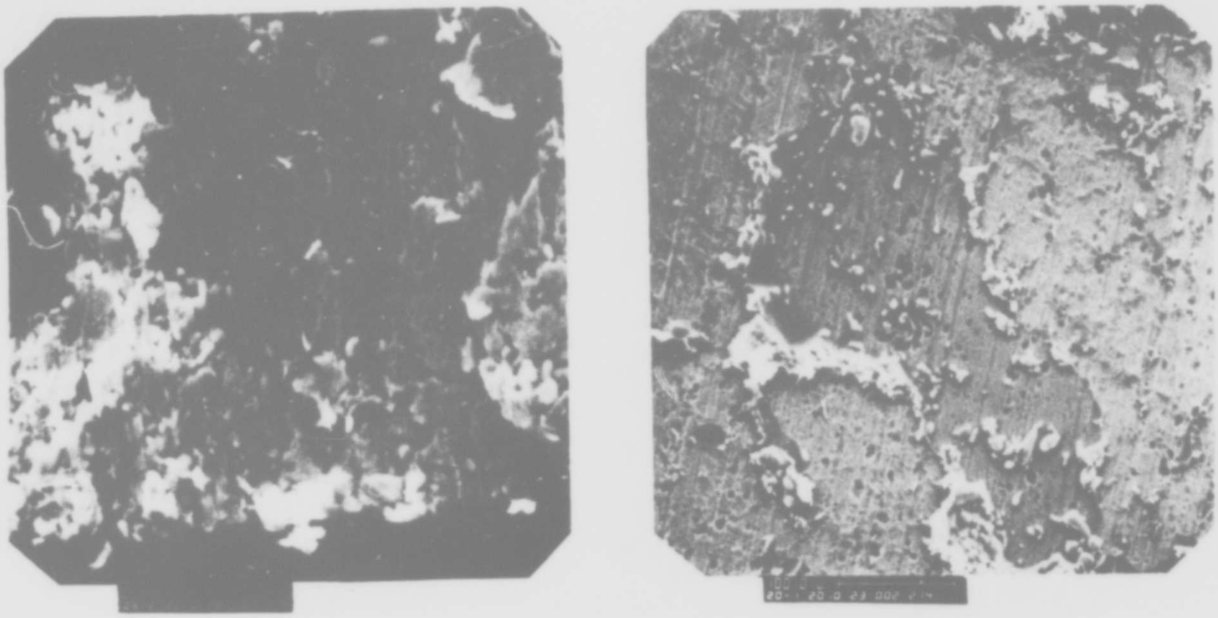

(a) 500X

(b) 200X

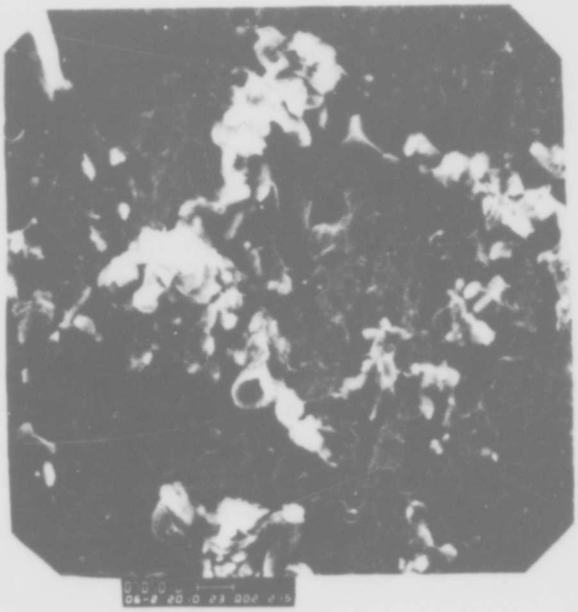

(c) 600X

Fig. 23. SEM micrographs of an Al 2024-T3 - HT424 joint after fracture. SET = 0, BET = 1000 hrs at 54°C, 95% R.H.

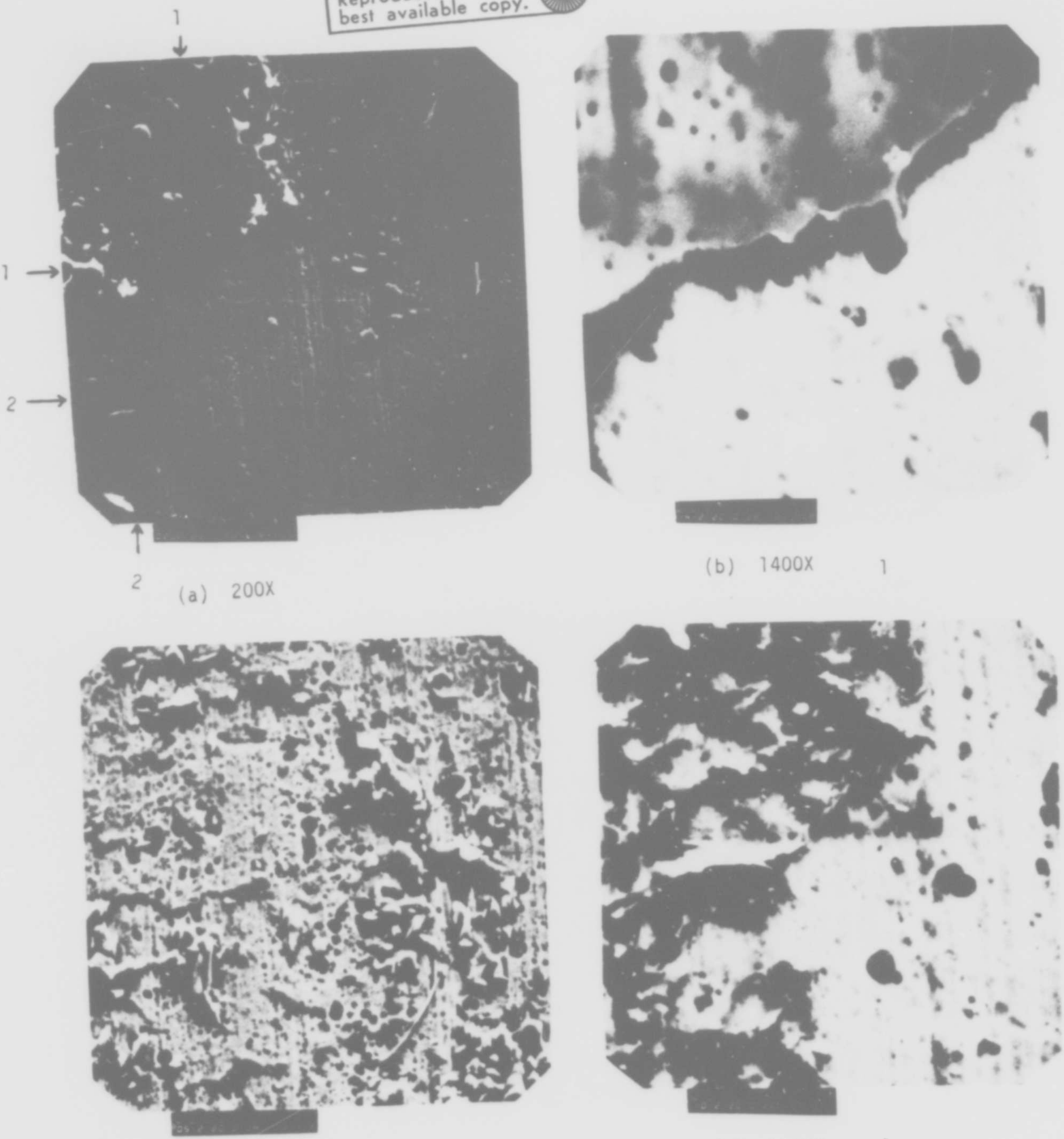

(a) 200X

(b) 1400X 1

(c) 500X

(d) 1000X 1

Fig. 24. SEM micrographs of an Al 2024-T3 - HT424 joint after fracture. SET = 0, BET = 1000 hrs at 54°C, 95% R.H.

TABLE 7 Experimental Values of Liquid Surface Tension (γ_{LV}) and cosine of Liquid-Solid Contact Angle (cos θ) at 22°C

Al 2024-T3 Surface Treatment		V.D.	FPL Etch	Plasma
Test Liquid	γ_{LV} (dyn/cm)			
water*	72.8	-.643 (≈0.94)	.998	1.00
glycerol	64.0	-.052	.998	0.98
1-br-napthalene	44.6	.616		0.84
tricresyl phosphate	40.9	.574	.996	0.99
polyglycol PG-1200	31.3	.829	.994	0.99

* All liquid-solid interactions display time invarient contact angles from $t \leq 10$ sec to $t \geq 10$ min except water on surface treatments 1, 2, and 3 where $t \leq 10$ sec values are without parenthesis and $t \geq 10$ min values are in parenthesis.

advancing contact angles over the time range $t \leq 10$ sec to $t \geq 10$ min except water on surface treatments 1, 2, and 3, as noted in Table 7. For the special case of water on surfaces 1, 2, and 3 one may suspect surface modification by interaction with water. The data of Table 7 may be plotted as cos θ versus γ_{LV}. When the data display a linear variation of cos θ versus γ_{LV} an extrapolation to cos $\theta = 1.0$ identifies the critical surface tension γ_c for the solid surface as shown by Zisman and coworkers.(31)

These data may be further analyzed by a more detailed model for interface interactions discussed in Section II.B.6. To apply this model the measured values of γ_{LV} and cos θ reported in Table 7 are introduced into the standard Young equation $W_a = \gamma_{LV}(1 + \cos\theta)$ to provide nominal values for the work of adhesion W_a. Table 8 organizes these data into the format defined by Eq. 9 of Section II.B.6. which describes a linear function of $W_a/2\alpha_L$ versus β_L/α_L whose intercept at $(\beta_L/\alpha_L) = 0$ is $\alpha_S = (\gamma_{SV}^d)^{\frac{1}{2}}$ and whose slope is $\beta_S = (\gamma_{SV}^p)^{\frac{1}{2}}$.

Computed average values γ_{SV}^d, γ_{SV}^p and γ_{SV} in conjunction with standard deviations $\pm\gamma^d$, $\pm\delta^p$, and $\pm\delta$ are summarized in Table 9 for the surface treatments. The calculations exclude the parenthesized data of Table 7 and Table 8. Quantitative conclusions concerning the effects of surface treatment on Al 2024-T3 wettability are automatically restricted by the magnitudes of the standard deviations shown in Table 9. Qualitative ranking would suggest the FPL etch to be the most wettable, followed by plasma treatment and then the vapor degrease when γ_{SV} is used as a wettability index. The results of this initial wettability experiment showed that the surface energy analysis discussed in Section II.B.6. was applicable to surface treated Al 2024-T3 plates.

Wettability studies combined with surface energy analysis were subsequently carried out for the surfaces which form the interfacial bond between HT424 adhesive and sulphuric acid-chromate etched Al 2024-T3. Films of HT424 primer were deposited from solution on glass microscope slides. Uncured primer films were dried, following manufacturer's recommendations, as follows:[35]

1) 30 min dry at 23°C,
2) 60 min dry at 66°C.

Primer films were dried then cured as follows:

1) 30 min dry at 23°C,
2) 60 min dry at 66°C,
3) 30 min cure under dry N_2 at 171°C.

TABLE 8: Analysis of Liquid-Solid Interactions

Al 2024-T3 Surface Treatment			V.D.	FPL	Plasma
γ_L dyn/cm	$2\alpha_L$ $(\text{dyn/cm})^{\frac{1}{2}}$	β_L/α_L		$W_a/2\alpha_L$ $(\text{dyn/cm})^{\frac{1}{2}}$	
72.8	9.34	1.53	2.78	15.6	----
64.0	11.66	.94	5.20	11.0	10.9
44.6	13.36	0	4.39		6.1
40.9	12.52	.21	5.14	6.50	6.5
31.3	9.90	.53	5.78	6.31	6.3

TABLE 9: Calculated Solid-Vapor Surface Tension Properties for Al 2024-T3 Surface Treatments by Application of the Determinant Method

Surface Treatment	$\gamma_{SV}^d \pm \delta^d$	$\gamma_{SV}^p \pm \delta^p$	$\gamma_{SV} \pm \delta$
FPL etch	14.8 ± 5.2	65.5 ± 14.0	80.3 ± 9.4
Plasma	28.8 ± 6.0	35.5 ± 18	64.3 ± 12.7
V.D.	40.3 ± 6.8	4.3 ± 2.1	44.6 ± 8.8

Steps (1) and (2) above follow adhesive manufacturer's recommended procedure for drying of primer films. Step 3 above correlates with curing conditions recommended for HT424 adhesive bonding. This last step is conducted under dry N_2 to minimize oxidative and hydrolytic degradation of the primer surface. Assuming the curing kinetics of HT424 primer follow results of prior curing studies(39) of HT424 structural adhesive film, it follows that steps (1) + (2) complete solvent removal without substantial crosslinking and that step (3) substantially completes the chemical curing of the HT424 primer films. Liquid-solid contact angle measurements were conducted at 20°C in the B-100 Environmental Chamber of the NRL contact angle apparatus (Rame-Hart Inc.) using sessile drops. The results of contact angle measurements, reported in terms of the cosine of the advancing liquid-solid angle θ, are summarized in Table 10. When the data of Table 10 are plotted as $\cos\theta$ versus γ_{LV} a linear variation of $\cos\theta$ versus γ_{LV} and extrapolation to $\cos\theta = 1.0$ identifies the critical surface tension γ_c of the adhesive film (ref. 31).

These data have also been further analyzed by a more detailed model for interface interactions discussed in Section II.B.6. To apply this model the measured values of γ_{LV} and $\cos\theta$ reported in Table 10 are converted to values of nominal work of adhesion by application of the Young equation. Table 11 presents these data in the format described by Eq. 9 of Section II.B.6.

Computed values of γ_{SV}^d, γ_{SV}^p, and γ_{SV} in conjunction with standard deviations $\pm\delta^d$, $\pm\delta^p$, and $\pm\delta$ obtained by a method of determinant calculations are summarized in Table 12. Both Table 11 and Table 12 indicate that the HT424 primer displays a well resolved polar component γ_{LV}^p to its total surface tension $\gamma_{SV} = \gamma_{SV}^d + \gamma_{SV}^p$. It is also evident that the dried and cured forms of HT424 primer have essentially equivalent wettability and surface tension properties. Figure 25 illustrates the wetting data in terms of $\cos\theta$ <u>vs</u> γ_{LV} while Figure 26 provides the experimental variation of $W_a/2\alpha_L$ versus β_L/α_L described by Eq. 9 of Section II.B.6. Earlier surface energy studies of HT424 structural adhesive film provide reference(34) values of $\gamma_{SV}^d \pm \delta^d = 30.3 \pm 4.5$ dyn/cm, $\gamma_{SV}^p \pm \gamma^p = 12.0 \pm 2.6$ dyn/cm and $\gamma_{SV} \pm \delta = 42.3 \pm 2.3$ dyn/cm. A close similarity between these literature values $\gamma_{SV} = \gamma_{SV}^d + \gamma_{SV}^p$ for HT424 adhesive and the values reported for HT424 primer films in Table 12 is evident.

TABLE 10: Cosine of Liquid-Solid Contact Angles cos θ of Test Liquids on Dried and Cured Films of HT424 Primer

HT-424 Primer Film Test Liquid	γ_{LV} (dyn/cm)	Dried cos θ	Cured cos θ
water	72.8	0.276	0.326
glycerol	64.0	0.515	0.469
ethylene glycol	48.3	0.743	0.669
tricresyl phosphate	40.9	0.987	0.982
poly glycol P-1200	31.3	0.981	0.982

TABLE 11: Analysis of Liquid-Solid Interactions

	HT-424 Primer		Dried	Cured
γ_L dyn/cm	$2\alpha_L$ $(\text{dyn/cm})^{\frac{1}{2}}$	β_L/α_L	$W_a/2\alpha_L$ $(\text{dyn/cm})^{\frac{1}{2}}$	$W_a/2\alpha_L$ $(\text{dyn/cm})^{\frac{1}{2}}$
72.8	9.34	1.53	9.94	10.33
64.0	11.66	.94	8.32	8.07
48.3	10.83	.81	7.77	7.44
40.9	12.52	.21	6.49	6.47
31.3	9.90	.53	6.26	6.26

TABLE 12: Calculated Solid-Vapor Surface Tension's Properties by the Determinant Method

HT424 Primer	Dried	Cured
$\gamma_{SV}^{d} \pm \delta^{d}$	28.7 ± 3.5	25.5 ± 3.8
$\gamma_{SV}^{p} \pm \delta^{p}$	10.3 ± 2.6	11.7 ± 2.4
$\gamma_{SV} \pm \delta$	39.0 ± 1.3	37.2 ± 1.5

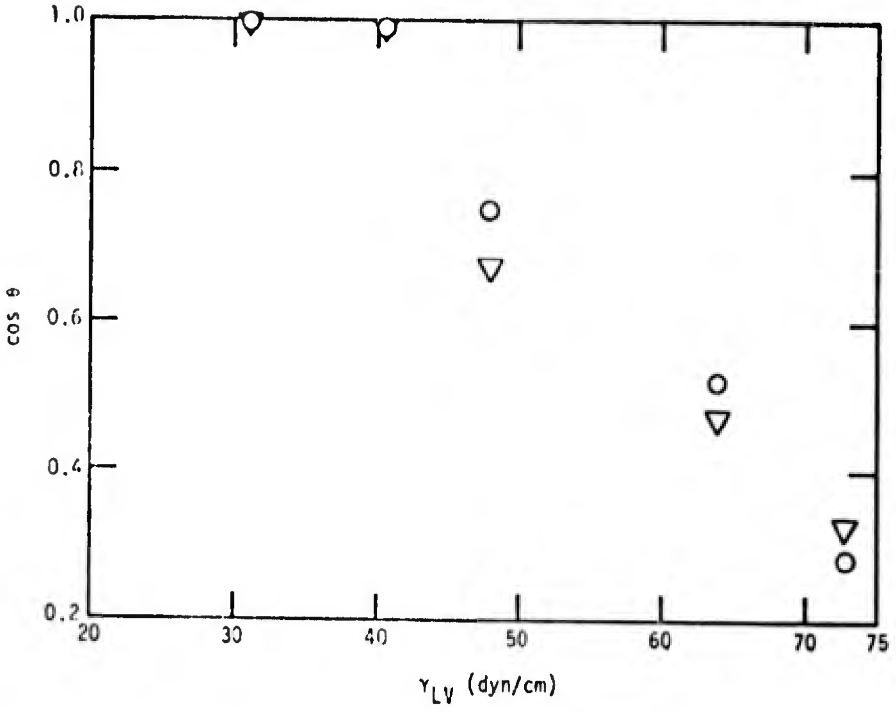

Fig. 25. Variation of cos θ vs γ_{SV} for dried (○) and cured (Δ) films of HT424 primer.

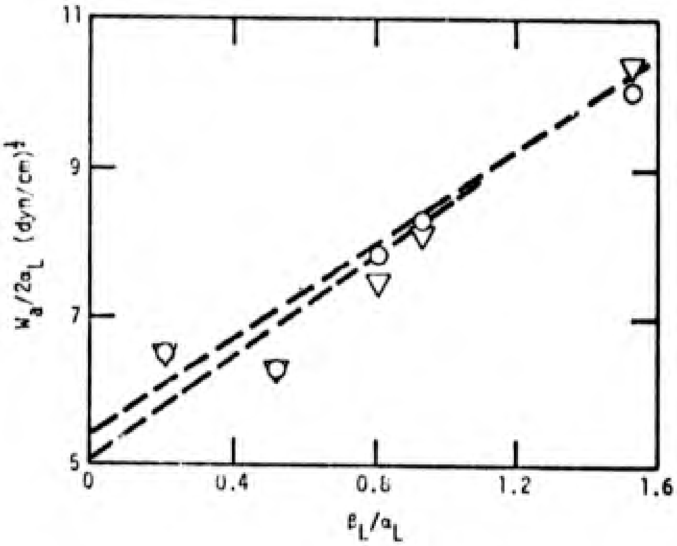

Fig. 26. Variation of $W_a/2\alpha_L$ vs β_L/α_L for dried (○) and cured (▽) films of HT424 primer.

The results of the surface energy analysis for HT424 primer and the FPL etch 2024-T3 aluminum can be combined in a "wettability envelope" diagram as defined by Eq. 13 of Section II.B.6. The diagram in Fig. 27 reveals that the HT424 primer and adhesive fall well within the envelope for freshly etched aluminum and therefore should, by this criterion, form strong adhesive bonds.

g. Joint Strengths

The last column of Table 6 gives average (of 6 bonds) bond strengths and the mean deviation from the mean, for comparison with surface preparation and surface character. The weakest bond results from the degrease only surface preparation. This preparation had the highest value of SPD, the lowest value of γ_{SV} (lowest wettability) and the most contamination. These results suggest that the low bond strength for the vapor degrease treatment results from a non-wettable weak boundary layer at the oxide-primer interface. The bond strength for the FPL etch and plasma treated surfaces are nearly the same. Although AES measurements were not made on the plasma treated surface, ion bombardment is shown to remove contamination (chemical profile section) and surface contamination is expected to be low as for the FPL etch. There does not appear to be any correlation between film thickness and bond strength for these thin films. However, it will be shown that for thicker films a correlation does exist.

h. Loci of Fracture

The optical and SEM micrographs reveal that for each particular bond, failure occurs in a non-uniform manner. Failure appears to occur in the adhesive, in the glass carrier bundles, in the primer and at the metal surface. The spacial distribution of the areas of different failure modes are determined by the stress profile during fracture and the exposure condition of the metal surface prior to bonding or exposure condition of the bond.

It is apparent that the surface after the FPL is not uniform in character and that surface aging accentuates this non-uniformity. Mapping of surfaces after surface treatment and aging reveals this to be true, as will be seen in the next section. It is clear that since failure occurs by different modes at different loci on the surface, an investigation of the mechanisms

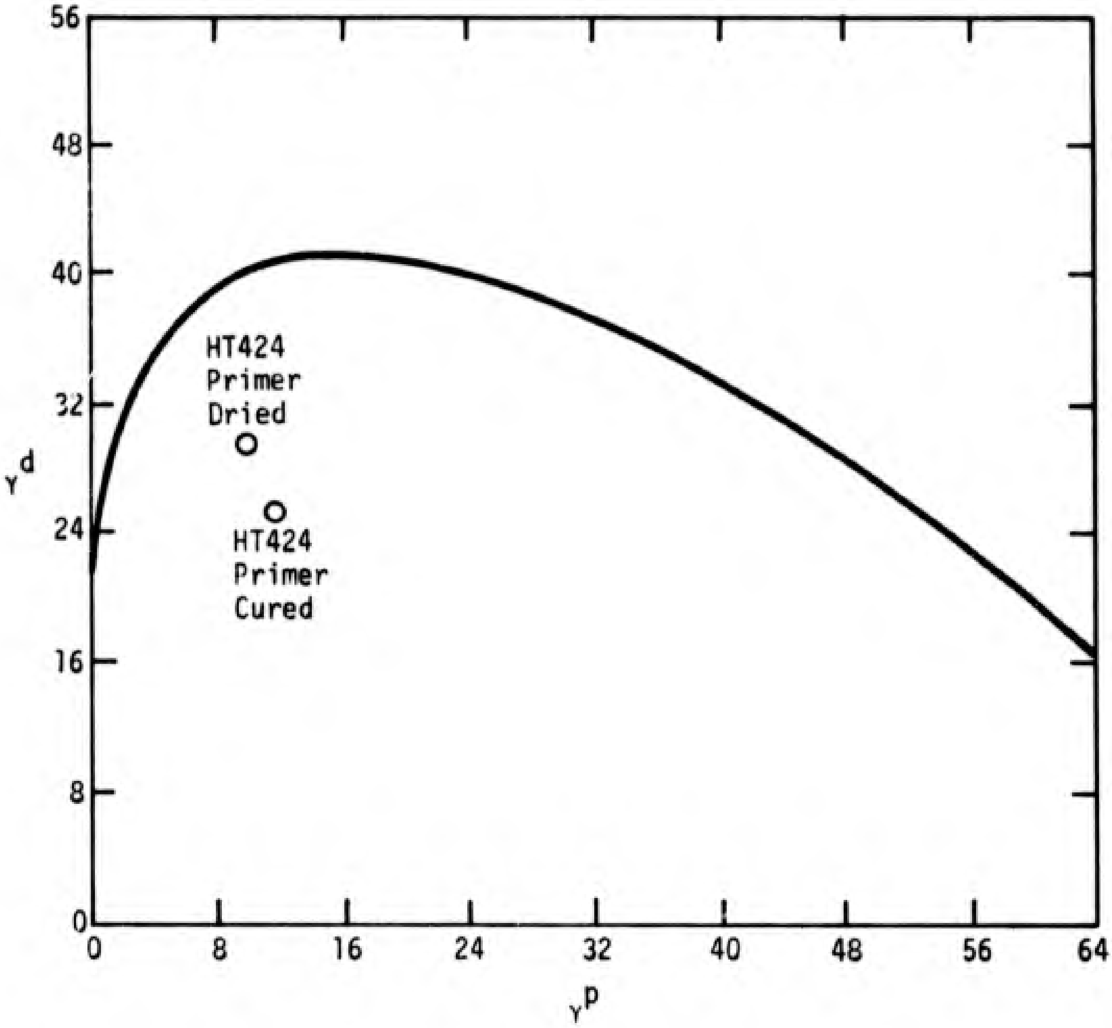

Fig. 27. Wettability envelope for freshly etched (FPL) Al 2024-T3.

of bond failure requires identification of these various regions prior to and after bond fracture. Identification prior to bonding is done by mapping the surface with respect to ellipsometry and SPD. Identification after fracture is done with a low power optical microscope. The area of regions that appeared to fail interfacially (at the metal-adhesive interface) are estimated by taking low power micrographs as in Fig. 16 but with about a factor of 10 larger magnification. A cellophane sheet with a grid (20 lines per inch) was placed over the photographs in order to keep track of each small area in the grid. An estimate of the fraction of each grid square that failed interfacially was recorded then the total fraction of the bond area that failed interfacially was computed and designated ϕ_I. The complimentary fraction is designated ϕ_C where $\phi_I + \phi_C = 1$. The average bond strength corresponding to these regions are designated σ_I and σ_C. Alternative techniques for estimating ϕ_I and ϕ_C were investigated and are reported in Appendix A.

We have referred to interfacial failure as failure at the metal-adhesive interface. However, one cannot determine by visual observation whether fracture occurred in the primer very near the oxide surface, at the primer-oxide interface, in the oxide or at the metal-oxide interface. To determine which of these is the locus of failure for the FPL etch surfaces, ellipsometric measurements were performed on the samples prior to bonding and in areas of interfacial failure after bond fracture. If the interfacial failure occurred in the primer near the oxide interface or at the oxide interface, the effective film thickness should be greater or approximately the same as before bonding. The results in Table 13 indicate that in each case the thickness of the oxide after fracture was substantially less than before. It is concluded that the aged FPL etched surfaces with thick oxide layers ~ 500 Å, fail in the oxide. It should be noted that solutions of n_f, κ_f and d could not be found for the Δ and ψ values, near $n_f = 1.7$ and $\kappa_f \approx 0.3$ as for unaged FPL etch films. The values reported in Table 13 are the minimum values of n_f and κ_f that correlate with the Δ and ψ values. This indicates that aging has caused a structural as well as thickness change in the oxide.

TABLE 13

Oxide Thickness Before and After Fracture
SET and BET were at 54°C, 95-100% R.H.
λ = 5461 Å, Angle of Incidence 70°

Bond History		Δ	ψ	n_f	κ_f	Thickness (Å)
FPL etch SET 24 hr BET 264 hr	Before bonding	- 9.6	21.2	2.4	0.3	623
	After fracture	-87.2	35.5	2.9	0.3	195
FPL etch SET 24 hr BET 0	Before bonding	-108	51.9	2.9	0.4	576
	After fracture	6.8	19.8	2.9	0.3	433
FPL etch SET 24 hr BET 0	Before bonding	90.5	16.7	2.5	0.7	550
	After fracture	88.0	35.9	2.5	0.3	273

2. Surface Aging Effects

a. Effect of Humidity

For the aging experiments, samples were placed upright in a glass chamber which contained saturated K_2SO_4. The glass chamber was placed in an oven that had temperature control. However, it was observed that some condensation occurred at the side of the desiccator nearest the door of the oven. This suggested that the relative humidity was more near 100% for some of the samples than others. To check this hypothesis, samples were placed side by side as couples at specific distances from the front of the desiccator to obtain a systematic gradient of R.H. and left for 23.6 hrs at 54°C. After SET the samples were characterized with respect to surface potential difference (SPD) and ellipsometry, then bonded and fractured.

The results in Table 14 show the effect of relative humidity (position in desiccator) on the surface characteristics as well as ϕ_c and the total bond strength σ_b. In Table 14, A and B refer to the two Al samples that were adjacent to each other at the various positions. The results in Table 14 also show that systematic trends in the surface characteristics exist as a function of relative humidity (position in the desiccator) between R.H. ~ 95 and 100%. Figure 28 shows that a definite correlation exists between the surface characteristics, SPD and film thickness, and the fraction of the surface that failed cohesively. The solid points in Fig. 28 are for the A sample of the couple, and the open circles are for the B sample. The samples in position 1 yielded ellipsometric values quite different from the other samples. No computer solution was found for sample A in position 1. The optical constants for sample B prove to be larger than for the other samples. This is probably due to the fact that condensation was observed to occur on the samples in position 1.

Figure 29 shows that except for the couple in positions 1 and 5 an excellent correlation exists between σ_b and ϕ_c. The values of σ_I and σ_c obtained from the intercepts of the line through the points are 1700 and 3800 psi, respectively. σ_c is close to the maximum value reported for the adhesive (3950 psi) by the manufacturer. Figures 28 and 29 show that a direct correlation exists between the surface characteristics and ϕ_c and thus the bond strength. The thicker the film the higher is the probability that fracture

TABLE 14

Effect of Humidity on Surface Characteristics and Bond Strengths of 2024-T3 Al after SET of 23.6 hrs 54°C

	Higher R.H. ←				Sample Position in Desiccator				→		Lower R.H.	
	1		2		3		4		5		6	
	A	B	A	B	A	B	A	B	A	B	A	B
SPD (Volts)	0.17	0.16	0.22	0.21	0.24	0.22	0.28	0.25	0.27	0.26	0.28	0.27
Δ (degrees)	143.8	90.5	81.7	83.5	85.2	84.8	86.5	88.8	89.3	89.3	94.4	93.6
ψ (degrees)	14.9	16.7	41.8	39.1	35.6	35.5	35.6	35.1	34.2	35.0	34.2	34.3
Film Thickness (Å)	----	550	350	350	277	282	260	----	240	258	216	224
n	----	2.47	1.8	1.8	2.04	2.0	2.1	----	2.2	1.96	2.2	2.1
κ		0.7	0.2	0.2	0.4	0.4	0.5	----	0.5	0.5	0.6	0.6
ϕ_c (Visual, with Stds)	0.1		0.45		0.55		0.65		0.65		0.75	
σ_b (psi)	2620		2640		2860		3050		2770		3290	

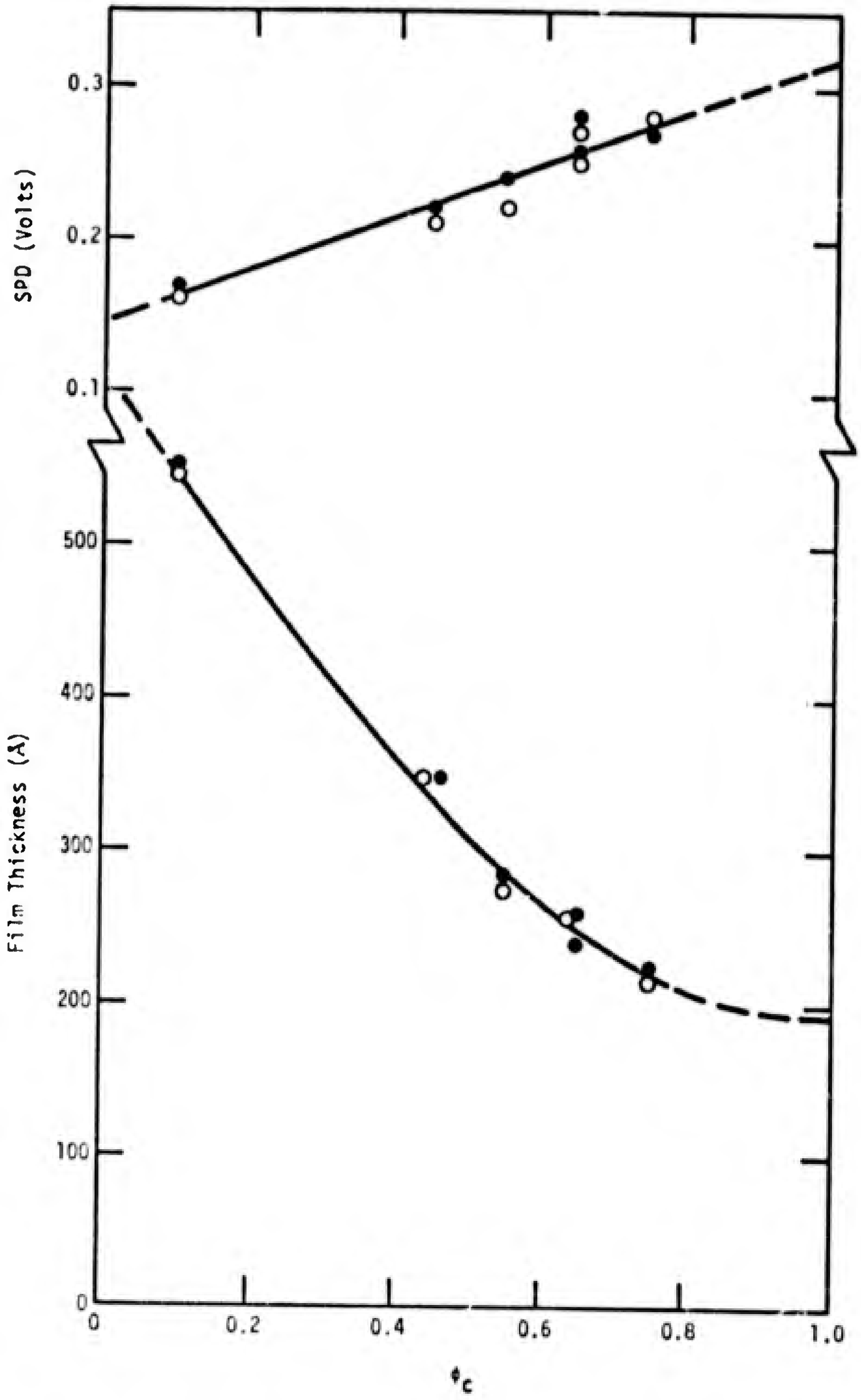

Fig. 28. Plot of film thickness and SPD vs ϕ_c.

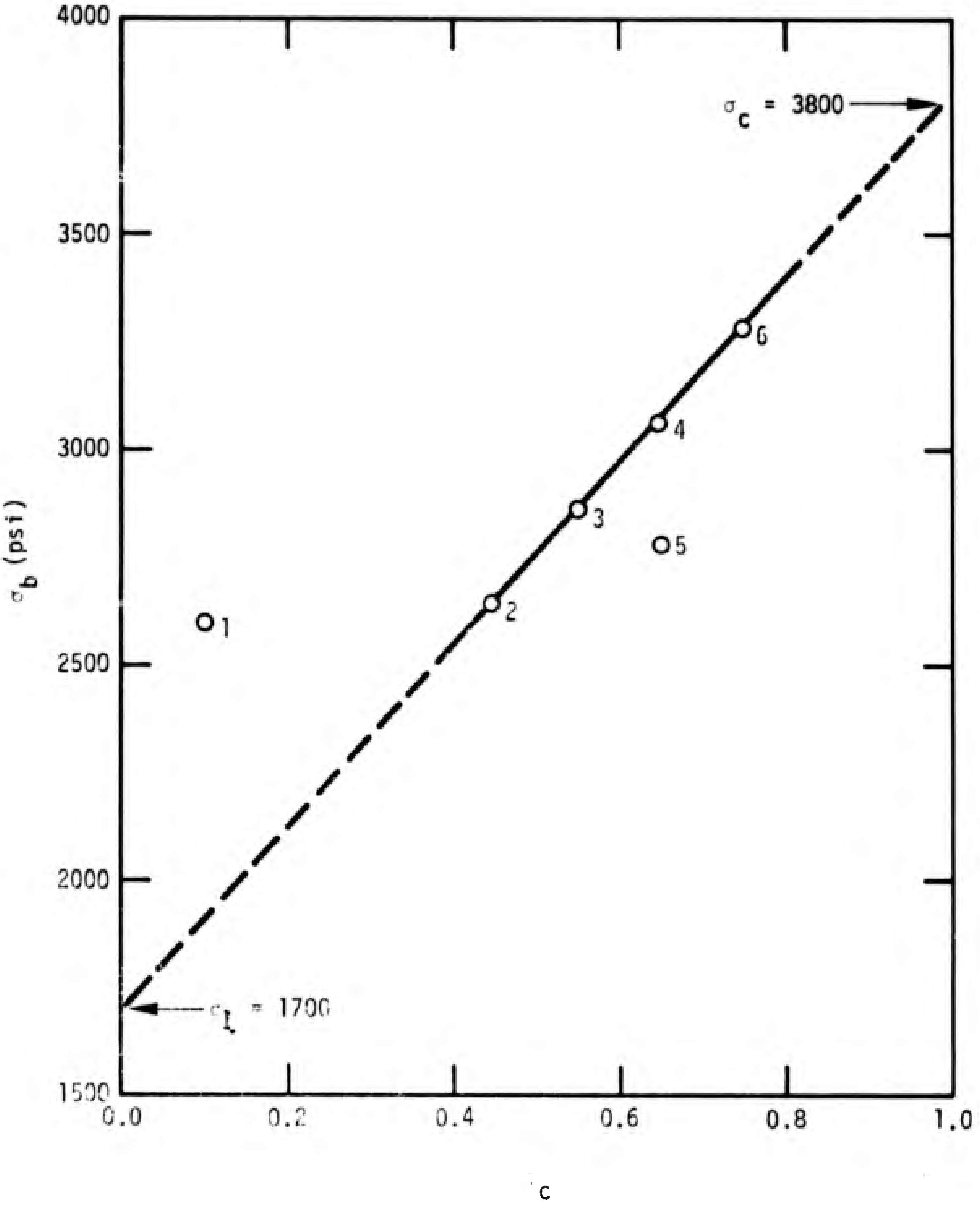

Fig. 23. Plot of σ_b vs ϕ_c for samples at various positions in the humidity chamber.

will occur at the interface. Figure 30 is a plot of SPD and film thickness vs σ_b, where σ_b is obtained from Fig. 29.

Table 14 shows that except for bond 1, n_f and κ_f tend to increase as the film becomes thinner. The values of the optical constants are related to film structure and may indicate stronger films for higher values of n_f and κ_f. Even though samples from position 1 have thicker films and would thus, from the line in Fig. 29, be predicted to fail at lower σ_b, the values of n_f and κ_f are larger indicating stronger structure. This may account for the larger value of σ_b for position 1. The reason for the deviation from the line for the point for position 5 is not known.

The straight line relationship in Fig. 29 indicates that films of approximately the same optical properties (structure) fail at the interface with about the same specific bond strength σ_I. However, the fraction of the bond area that fails at the interface ϕ_I is related to film thickness. These results are in accord with the results of Table 13, for those areas that fail interfacially fracture probably occurs in the oxide film rather than at the oxide-primer interface or in the adhesive very near to the interface.

b. Effect of Glow Discharge

Plasma (glow discharge) treatment of surfaces may remove surface contamination and weak boundary layers. Experiments were carried out to discover if plasma treated surfaces would produce better adhesive bonds. In order not to expose the plasma treated surfaces to air, the sealed plasma treating tube was opened in a glove box with controlled atmosphere. Five experiments were performed as follows:

1. Three samples (3 bond couples) were degreased (TCE) primed and bonded.
2. Twelve samples were plasma treated and immediately primed in the glove box.
3. Six samples were plasma treated then exposed to 1 atm of pure oxygen in the plasma tube for 20 hrs, then primed in the glove box.
4. Six samples were plasma treated then exposed exclusively to water vapor for 20 hrs by opening a valve between the plasma tube and a bulb containing water but no air.
5. Six samples were plasma treated then exposed to a mixture of pure oxygen and water vapor.

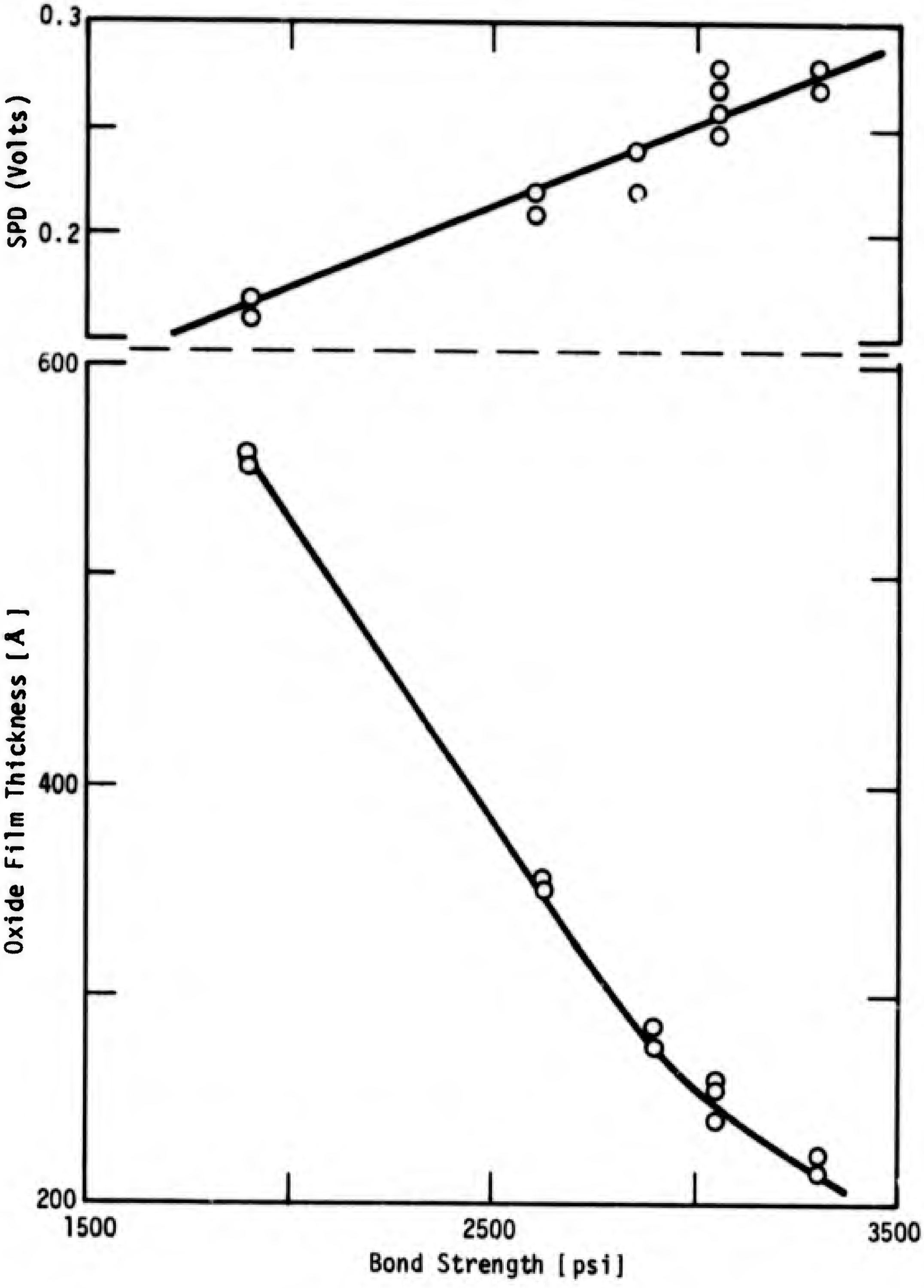

Fig. 30. Oxide Film Thickness and SPD vs bond strength.

The precise steps for these treatments are found in Table I. The results in Table 15 are plotted in Fig. 31. Comparison of the average values of σ_b for each treatment reveals that plasma-only yields the highest and plasma + H_2O + O_2 yields the lowest. Note that at $\phi_c \approx 0.1$ values of σ_b are above the line at the same position as for Fig. 29. That is, the σ_b and ϕ_c values are the same for samples exposed to water condensation at 54°C for 23 hrs and samples exposed to pure oxygen at RT after the plasma treatment. It can be concluded from Fig. 31 that except for the plasma + O_2 (open circles at lowest ϕ_c value) the strength of the oxide is $\sigma_I \approx 1700$ psi and the strength of the adhesive is $\sigma_c \approx 3800$Å as for the experiments recorded in Fig. 29.

Figures 32 and 33 show plots of bond strength σ_b vs ϕ_c for various SET aging. When these experiments were performed the variation in humidity (see (Fig. 29) within the glass chamber had not been discovered. Consequently the RH probably varied between ~ 95% and 100% but the position of the samples was not recorded. For the set of experiments presented in Fig. 32, interfacial failure (ϕ_I) increases and bond strength decreases as SET increases to 24 hrs, then ϕ_c and σ_b increase again. The fact that the data in Fig. 32 cluster around a straight line indicates that for this set σ_c is approximately constant (~ 3800 psi) for cohesive failure and σ_I is approximately constant but much lower (~ 800 psi) than for the plasma experiments reported in Fig. 31, or those reported in Fig. 29. The experiments reported in Fig. 33 do not cluster around a straight line, indicating that for these experiments, although σ_c may approximate a constant, σ_I does not.

c. Surface Mapping

Thus far we have reported average values for ϕ_c and surface properties averaged over a small area of the sample. No attention has been paid to non-uniformity over the surfaces to be bonded. However, as pointed out in Section III-A.1.e. the micrographs taken after fracture reveal that the mode of fracture is not uniform over the surface. The tendency to fail by a particular mode in a particular area must be built into the surface during the sample history, perhaps prior to bonding. It was thought that the scatter of the data in Fig. 33 may be related to non-uniformity. It follows that a map of the surface with respect to ellipsometry and SPD may reveal the areas of interfacial failure prior to bonding. To test this the following experiments were performed. Two Al samples that were contaminated with

TABLE 15

Effect of Plasma Treatment on Bond Strength, ϕ_I and ϕ_c

Bond Couple	Surface Treatment	ϕ_I	ϕ_c	σ_b psi
1	TCE only	0.40	0.60	3000
2		0.50	0.50	2650
3		0.70	0.30	2710
				avg. 2790 ± 140
1	Plasma only	0.25	0.75	3320
2	" "	0.35	0.65	2940
3	" "	0.30	0.70	3430
4	" "	0.45	0.55	2830
5	" "	0.50	0.50	2830
6	" "	0.20	0.80	3430
				avg. 3130 ± 263
1	Plasma + O_2	0.90	0.10	2540
2	" "	0.90	0.10	2560
3	" "	0.80	0.20	2490
				avg. 2530 ± 27
1	Plasma + H_2O vapor	0.60	0.40	2630
2	" " "	0.60	0.40	2960
3	" " "	0.50	0.50	2770
				avg. 2787 ± 116
1	Plasma + H_2O + O_2	0.85	0.15	2140
2	" " "	0.75	0.25	2330
3	" " "	0.75	0.25	2370
				avg. 2280 ± 93

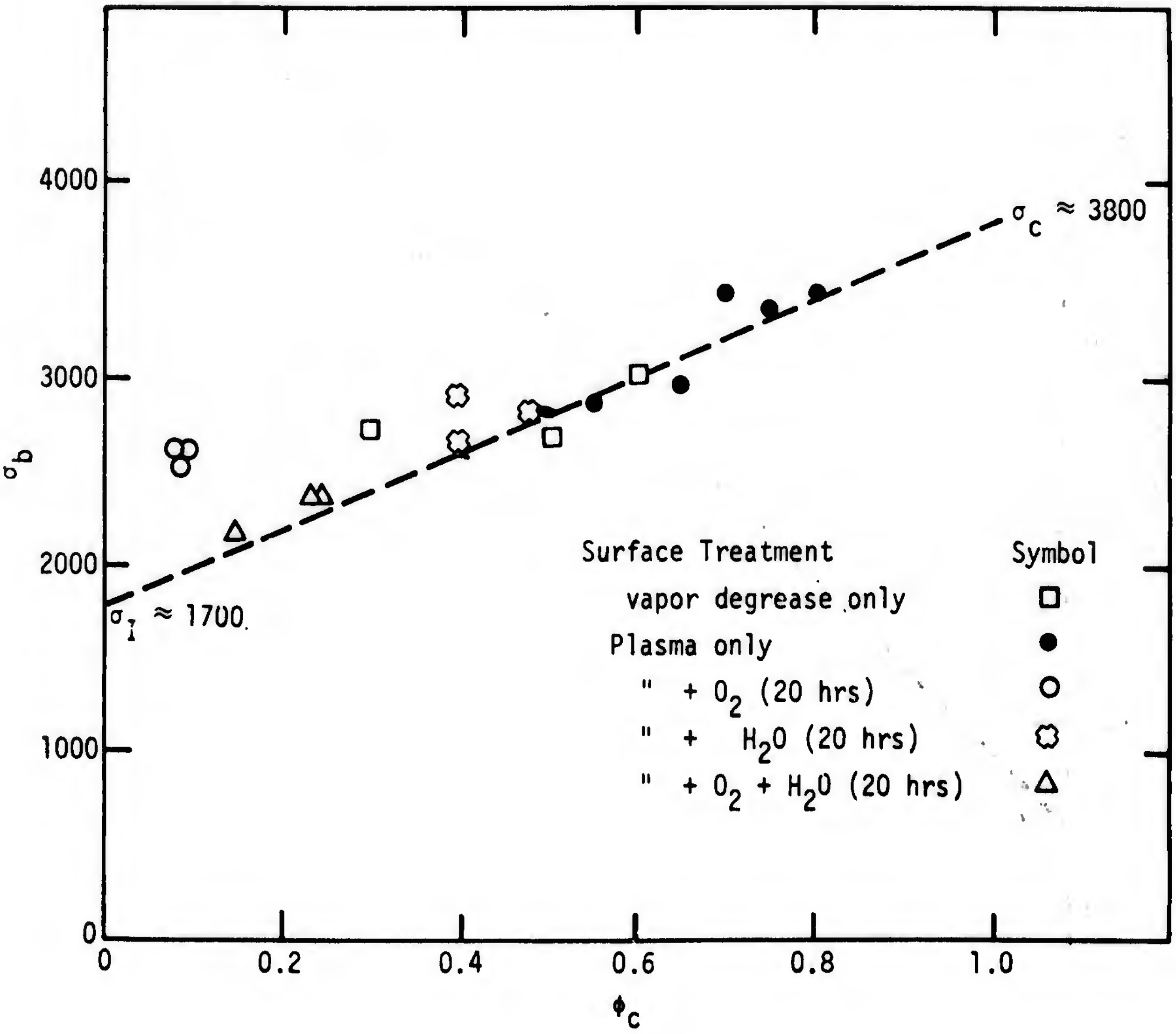

Fig. 31. Plot of σ_b vs ϕ_c for plasma treated surfaces of Al 2024-T3.

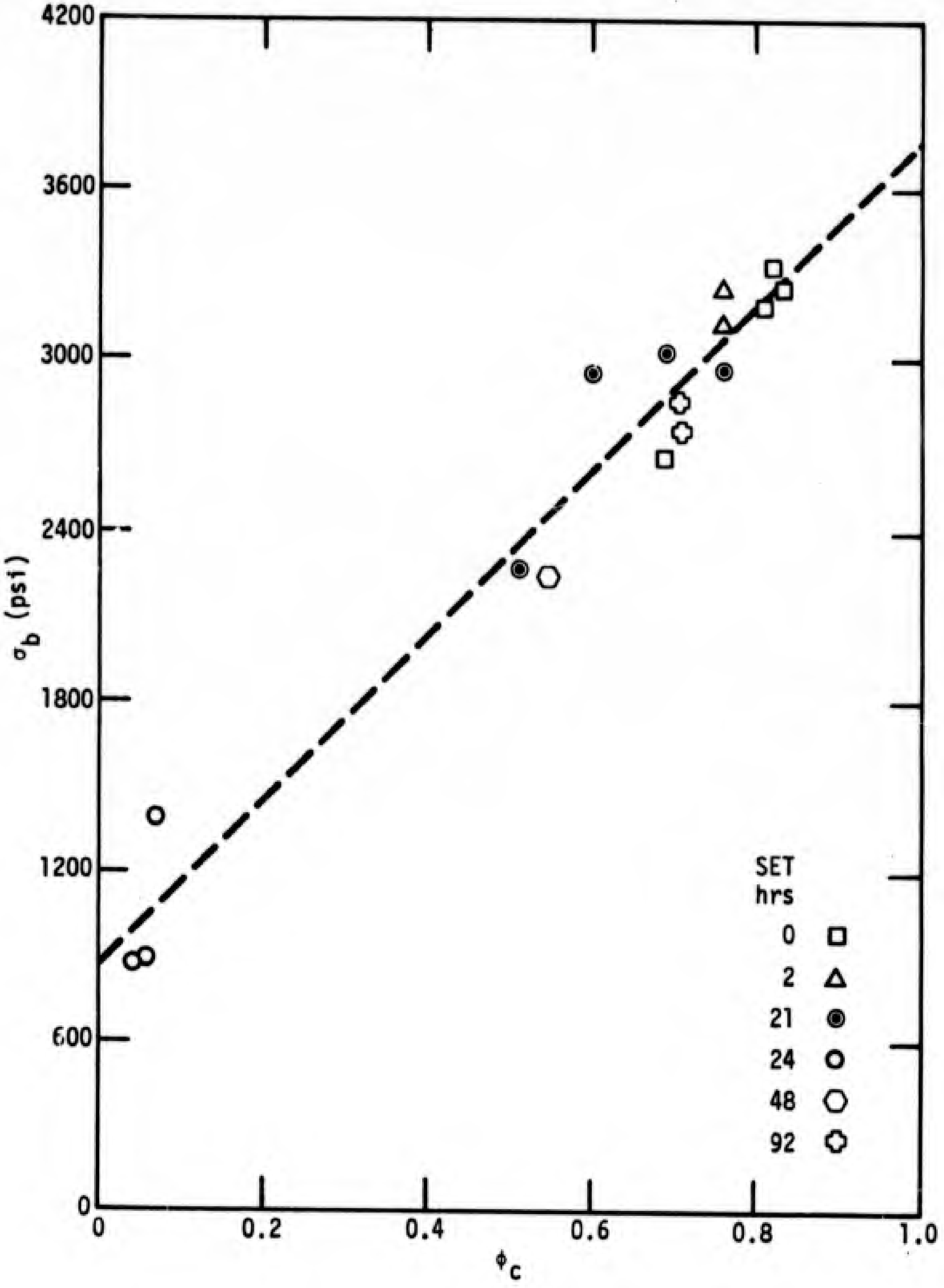

Fig. 32. Plot of σ_b vs ϕ_c for various SET.

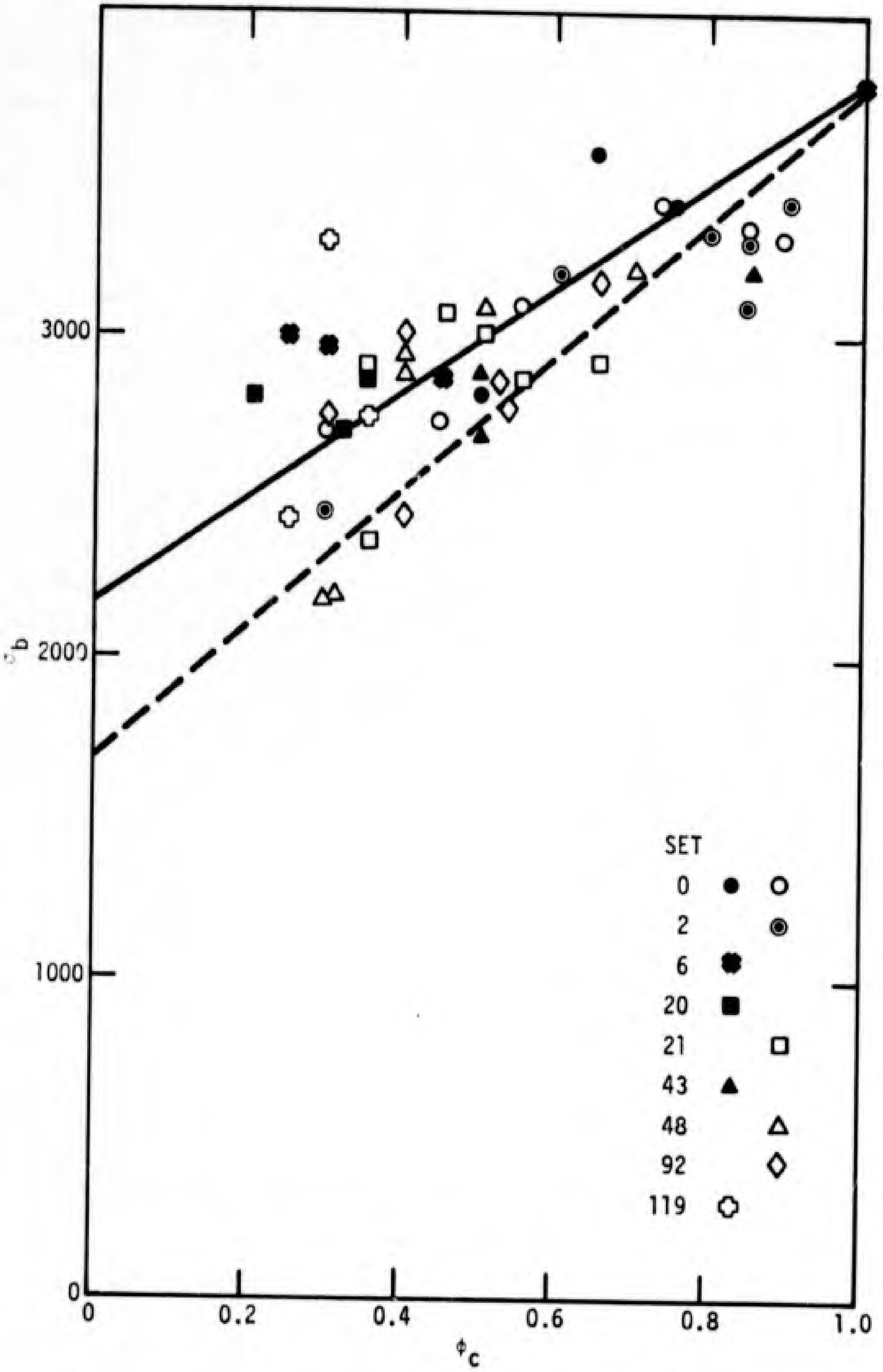

Fig. 33. Plot of σ_b vs ϕ_c for Al 2024-T3 after SET at 54°C and 95-100% R.H.

dichromate solution during aging at R.H. 95% at 54°C revealed stains at various positions across the areas to be bonded. Two other samples were aged with R.H. between 95 and 100% at 54°C for 24 hrs. Each of these samples were bonded with a freshly prepared sample so that the interfacial fracture would only occur on the stained and aged samples. Prior to bonding the aged and stained samples were mapped in the bond region with ellipsometry and SPD. The samples were then bonded and fractured and ϕ_I measured by photographing each map position under a low power microscope and counting interfacial fracture area squares with the cellophane grid. All of the bonds fractured at the aged and stained samples, as expected. The map positions are shown at the right of Fig. 34. Table 16 gives the ellipsometric parameter Δ and ψ as well as SPD and ϕ_I for the various sample positions. Samples 1 and 2 were the stained samples and 3 and 4 the aged samples. Figure 34 shows plots of ϕ_I (solid lines) and Δ (dashed lines) as a function of position. At the right of Fig. 34 estimates of film thicknesses are given for each sample. Figure 34 dramatically demonstrates that mapping of the surfaces by ellipsometry prior to bonding allowed prediction of the trend in ϕ_I in every case. Again it is observed that ϕ_I increases with film thickness. Although the range of film thickness for all of the samples is about the same (300-500 Å) the large differences in Δ and ψ for samples 1 and 2 as compared to 3 and 4 is due to differences in optical constants for the two sets. The optical constants for samples 1 and 2 are about $n_f \sim 2.8$, $\kappa_f \sim 0$ to 0.3, whereas for samples 3 and 4, $n_f \sim 1.8$, $\kappa_f \sim 0.1$ to 0.3. Note that the negative values of Δ in Table 16 can be expressed as positive values by adding 360°. Table 16 shows that a good correlation exists between SPD and ϕ_I for samples 1 and 2. The correlation is not as good for 3 and 4.

d. Effect of Time

Some of the aged samples were used to measure SPD and ellipsometry, others were used to measure contact angles, θ, for water and tricresylphosphate (TCP) and others were used to make adhesive joints with HT424. Figure 35 is a plot of Δ and ψ, SPD and θ_{H_2O}, θ_{TCP} with SET.

It is apparent from Fig. 35 that all parameters level off in about 20-30 hrs. The shape of curves SPD, ψ and θ_{TCP} indicate that a different process is occurring in the first 10 hrs than is occurring after 10 hrs. A clue as to the process during the first 10 hrs is given by the curve for ψ and SPD. Computer calculations show that growth of an oxide film of constant optical

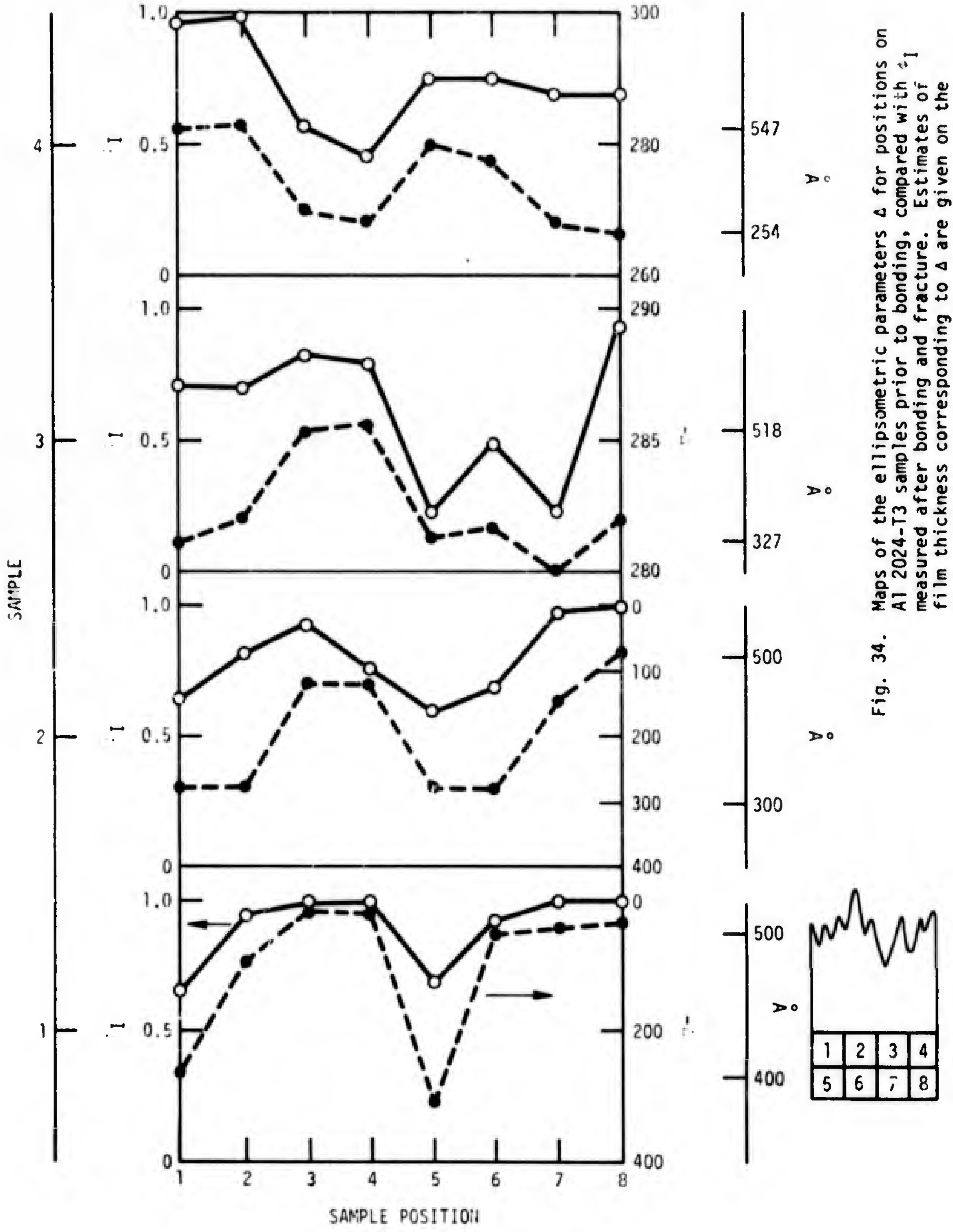

Fig. 34. Maps of the ellipsometric parameters Δ for positions on Al 2024-T3 samples prior to bonding, compared with Δ_I measured after bonding and fracture. Estimates of film thickness corresponding to Δ are given on the right ordinate.

TABLE 16

Mapping of Surface Characteristics and Comparison with ϕ_I

Position	Δ	ψ	SPD (volts)	ϕ_I	σ_b (psi)
Sample #1					
1	-260.8	58.4	-0.16	0.65	
2	- 98.8	50.6	-0.14	0.88	
3	- 18.0	11.5	+0.02	0.97	
4	- 22.2	14.2	+0.01	0.98	
5	-313.2	70.2	-0.16	0.68	
6	- 52.4	30.9	-0.20	0.84	
7	- 47.1	14.3	-0.05	0.99	
8	- 32.0	19.1	-0.05	0.97	
				avg. 0.87	2040
Sample #2					
1	-274.8	39.0	-0.07	0.66	
2	-275.8	46.0	-0.07	0.83	
3	-----		+0.02	0.93	
4	-107.6	71.8	+0.06	0.77	
5	-275.8	40.0	-0.04	0.59	
6	-278.0	45.5	-0.04	0.68	
7	-145.0	6.4	-0.01	0.97	
8	- 70.0	38.0	+0.04	0.99	
				avg. 0.80	2500
Sample #3					
1	-281.2	41.6	+0.23	0.71	
2	-282.0	45.1	+0.11	0.70	
3	-285.3	46.8	+0.12	0.82	
4	-285.6	41.8	+0.06	0.78	
5	-281.4	39.9	+0.04	0.23	
6	-281.6	44.9	-0.12	0.49	
7	-280.0	44.5	-0.11	0.22	
8	-282.0	46.8	-0.13	0.92	
				avg. 0.61	2770
Sample #4					
1	-282.4	41.9	-0.27	0.96	
2	-283.1	44.1	-0.28	0.98	
3	-270.2	38.4	-0.29	0.56	
4	-268.4	39.0	-0.26	0.47	
5	-279.8	40.3	-0.24	0.74	
6	-276.0	38.6	-0.27	0.74	
7	-267.8	38.4	-0.28	0.66	
8	-266.4	37.6	-0.27	0.65	
				avg. 0.72	2110

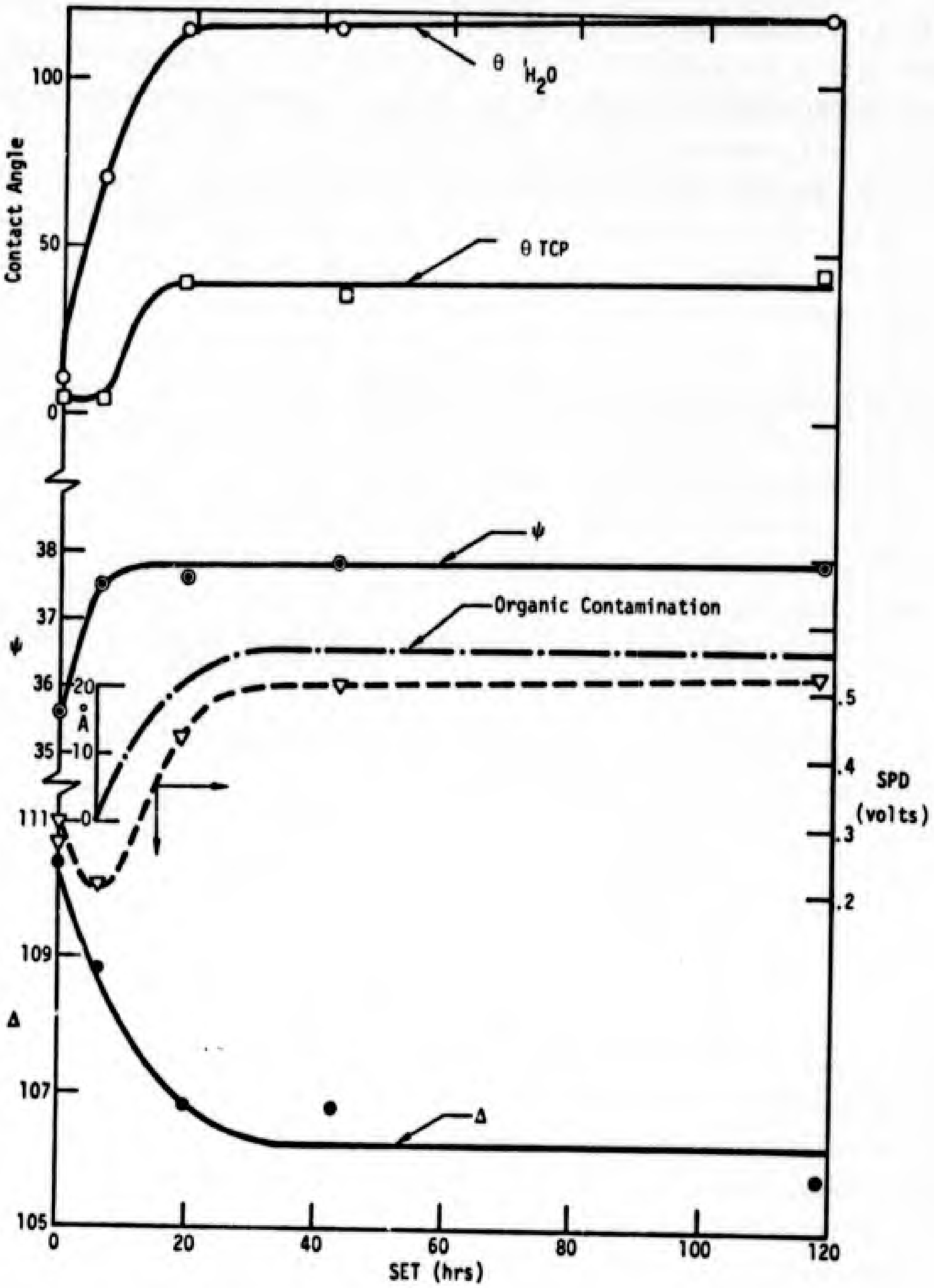

Fig. 35. Plot of Δ, ψ, SPD, θ_{H_2O} and θ_{TCP} vs SET for Al 2024-T3 at 54°C, 95% R.H.

properties will cause both Δ and ψ to decrease. The increase in ψ with SET can be interpreted in two ways, ψ can increase if the oxide is being transformed to one with smaller absorption coefficient (κ_f) and/or organic surface contamination is forming. The value of SPD in air 26 minutes after the dichromate treatment was 0.3 volts and 0.27 volts after 43 minutes. These two values are shown at SET = 0 in Fig. 35 and indicate that the initial process began before exposure to the humidity chamber. The results in Fig. 35 are best interpreted as oxide film transformation during the first 6 hrs, followed by organic contamination that continues to 20-30 hrs. The curve labeled "organic contamination is obtained from the ellipsometric data if one assumes that the total change in Δ and ψ after 6 hrs is due to formation of an organic film with refractive index 1.5 on the transformed oxide film, 200 Å thick with optical properties, $n_f = 1.7$ and $\kappa_f = 0.4$. At about 30 hrs the contamination reaches about 25 Å. The data between SET = 0 and 120 hrs can also be interpreted as transformation alone if the oxide changes from one of 195 Å with $n_f = 1.4$, $\kappa_f = 0.5$ to 223 Å with $n_f = 1.7$, $\kappa_f = 0.3$. The data cannot be interpreted in terms of organic contamination alone.

To estimate σ_I, it is assumed that σ_C is a constant and that the relation between σ_b, σ_I, σ_C, ϕ_C and ϕ_I is

$$\sigma_b = \phi_C \sigma_C + \phi_I \sigma_I \quad . \tag{19}$$

where $\phi_I = 1 - \phi_C$. Therefore

$$\sigma_I = (\sigma_b - \phi_C \sigma_C)/(1-\phi_C) \quad . \tag{20}$$

Figure 36 shows the average values of σ_b, σ_I and ϕ_C plotted vs SET. As for surface properties in Fig. 35, all parameters level off in 20-30 hrs indicating the relationship between the bond character and the surface character. Figure 37 shows average curves for Δ, ψ, SPD and water contact angle for aging in laboratory air at room temperatures (~ 23°C ~ 50% RH). The processes are probably the same as for the higher temperature, higher humidity experiment in Fig. 36 but slower. Note that ψ and SPD are still increasing at 300 hrs, as would be expected if they are both related to organic contamination. At this point it is uncertain as to which process, oxide transformation or contamination, degrades the adhesive bond. However, the results discussed under mapping tends to favor weak oxides and therefore oxide transformation. It should be noted that both σ_I and ϕ_C decrease (ϕ_I increases) with SET.

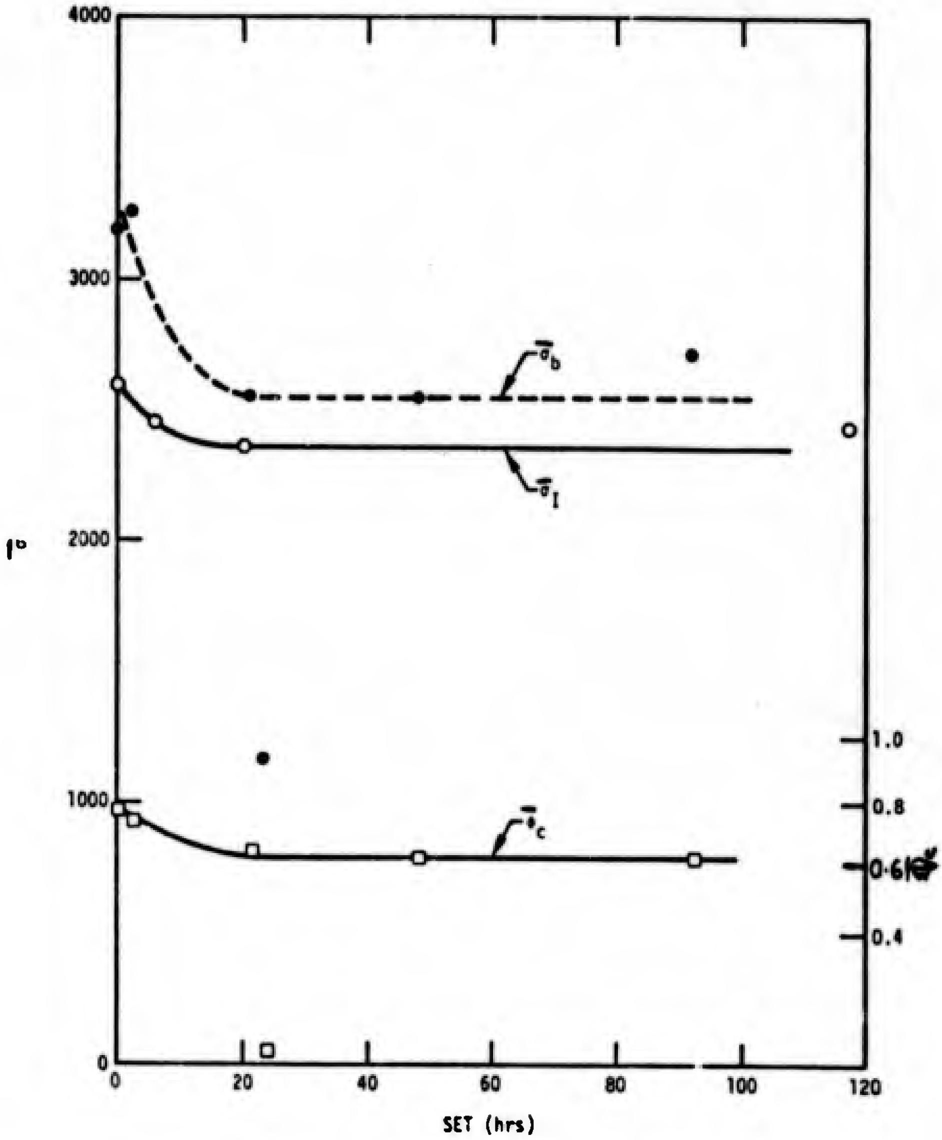

Fig. 36. Plot of σ_b, σ_I and ϕ_c vs SET at 54°C, 95% R.H.

Fig. 37. Plot of Δ, ψ, SPD and θ_{H_2O} vs SET at 23°C and 50% R.H.

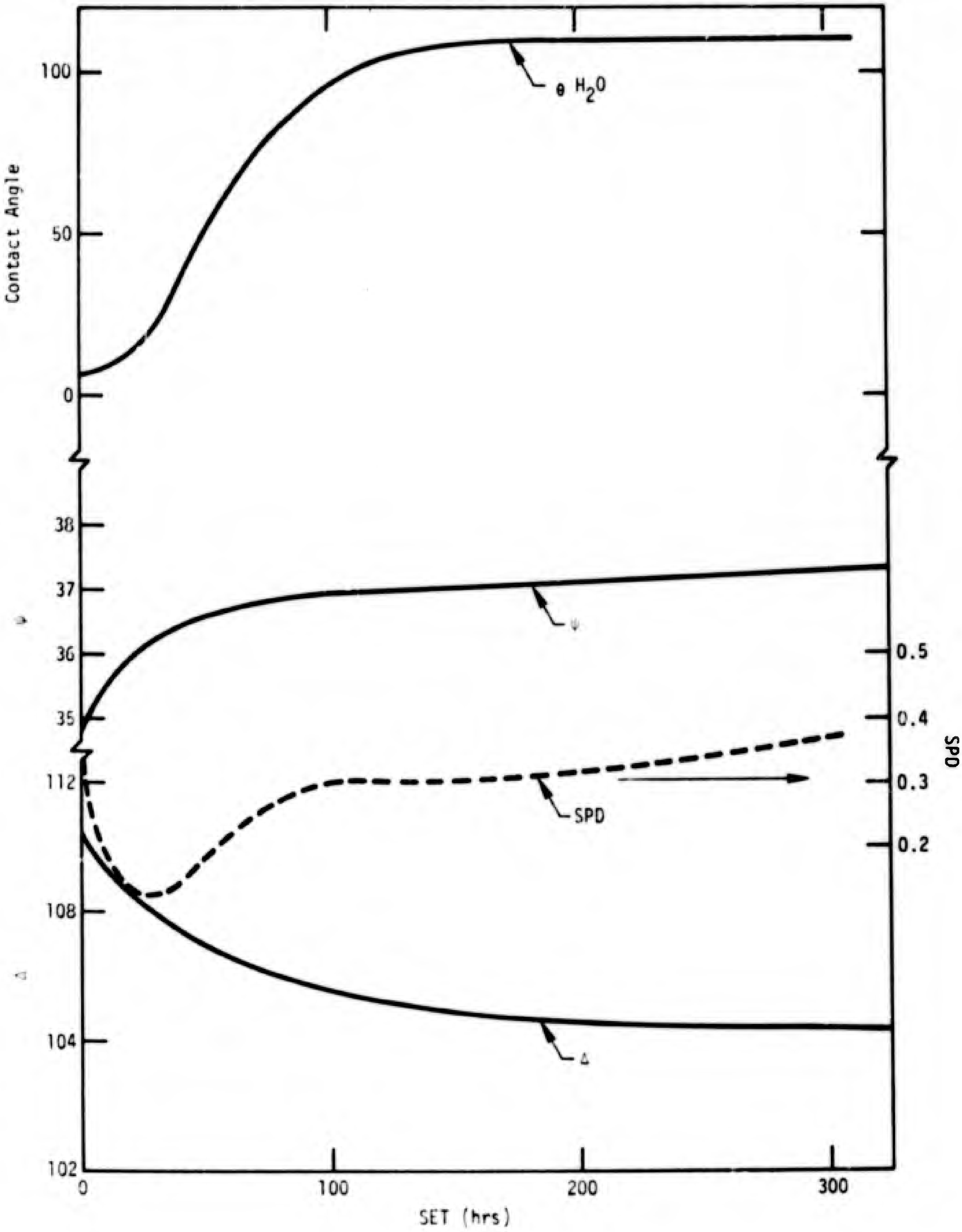

e. Effect of SET on Contact Angles

Wettability measurements and analysis identified notable variations in the surface properties of the FPL etched 2024-T3 aluminum which are functions of surface exposure time (SET) at 24°C and 54°C. To further define this phenomena with regard to interfacial bonding properties between Al 2024 and HT424 adhesive, a special study was conducted for the effects of SET at 23°C and 50 ± 5% R.H. The wettability measurement and surface energy analysis of Al 2024-T3 follow the methods already described for HT424 primer. Subsequent to the etching treatment the Al 2024-T3 specimens were stored under ambient laboratory air at 23°C and 50 ± 5% R.H. while protected from dirt and dust by tissue paper covers.

The results of contact angle measurements of five surface exposure times (SET) are summarized in Table 17. The results of analysis of liquid-solid interactions by Eq. 9 of Section II.B.6 are summarized in Table 18. Computed values of solid-vapor surface tension properties at various SET conditions are tabulated in Table 19.

Plots of cos θ versus γ_{LV} for various ambient SET conditions are shown in Figure 38. These curves show that increasing SET produces a dramatic reduction in cos θ values for liquids of higher γ_{LV} which are characterized as polar in surface tension properties. Figure 39 displays the variation in $W_a/2\alpha_L$ versus β_L/α_L for SET of $\leq$ 0.5 hr characteristic of a freshly etched surface of Al 2024-T3. The solid curve of Figure 39 represents the calculated values (see Table 19) of γ^d_{SV} = 14.8 dyn/cm and γ^p_{SV} = 65.5 dyn/cm while the dashed curves represent the standard deviations from these calculated averages. It is evident that ambient SET conditions provide a major shift in both γ^d_{SV} and γ^p_{SV} for the FPL etched surface of Al 2024-T3, as indicated by Table 19 which exceed the uncertainties reflected in the standard deviations $\pm\delta^d$ $\pm\delta^p$. Curves of average values of γ^d_{SV} and γ^p_{SV} versus ambient SET from the data of Table 19 are plotted in Fig. 40.

FPL etch treated Al 2024-T3 can be combined on a "wettability envelope" diagram, as defined by Eq. 13 of Section II.B.6, and shown in Fig. 41. The distance of γ^d_{LV} and γ^p_{LV} extending from the origin $\gamma^d = 0$, $\gamma^p = 0$ to a particular wettability envelope curve describes a condition of spreading cos θ = 1.0 for the liquid on the solid surface. The average values of γ^d and γ^p for HT424 primer, from Table 19, are represented in Figure 41. It may be noted that all the wettability envelopes for FPL etched Al 2024-T3 at

TABLE 17· Cosine of Liquid-Solid Contact Angle θ of Acid Etched Al-2024-T3 at various SET Conditions (23°C and 50±5% R.H.)

Surface Time	Exposure (hr)	0 to 0.5	23	51	126	219
Test Liquid	γ_{LV} (dyn/cm)	cos θ	cos θ	cos θ	cos θ	cos θ
water	72.8	.9976	.9848	.9455	.500	- 0.1392
glycerol	64.0	.9976	.7880	.9063	.2756	- 0.1737
ethylene glycol	48.3	.9998	.9962	.9986	.9903	0.8660
tricresyl phosphate	40.9	.9962	.9926	.9962	.9816	0.9848
poly glycol P-1200	31.3	.9945	.9877	.9926	.9816	0.9659

TABLE 18: Analysis of Liquid-Solid Interactions

Surface time		Exposure (hr)	0 to 0.5	23	51	126	219
γ_{LV}	$2\alpha_L$	β_L/α_L	$W_a/2\alpha_L$ (dyn/cm)$^{\frac{1}{2}}$				
72.8	9.34	1.53	15.57	15.47	15.16	11.69	6.71
64.0	11.66	.94	10.96	9.81	10.46	9.37	4.54
48.3	10.85	.81	8.92	8.90	8.91	8.88	8.32
40.9	12.52	.21	6.52	6.49	6.52	6.47	6.48
31.3	9.90	.53	6.31	6.28	6.30	6.26	6.22

TABLE 19: Calculated Solid-Vapor Surface Tension Properties by the Determinant Method

Surface Exposure time (hr)	$\gamma_{SV}^{d} \pm \delta^{d}$	$\gamma_{SV}^{p} \pm \delta^{p}$	$\gamma_{SV} \pm \delta$
0 - 0.5	14.8 ± 5.2	65.5 ± 14.0	80.3 ± 9.4
23	14.0 ± 5.6	59.1 ± 11.9	73.1 ± 6.5
51	14.9 ± 5.2	58.0 ± 11.4	72.9 ± 6.6
126	25.3 ± 5.3	20.4 ± 8.0	45.7 ± 3.7
219	47.7 ± 12.0	7.4 ± 2.4	55.2 ± 12.0

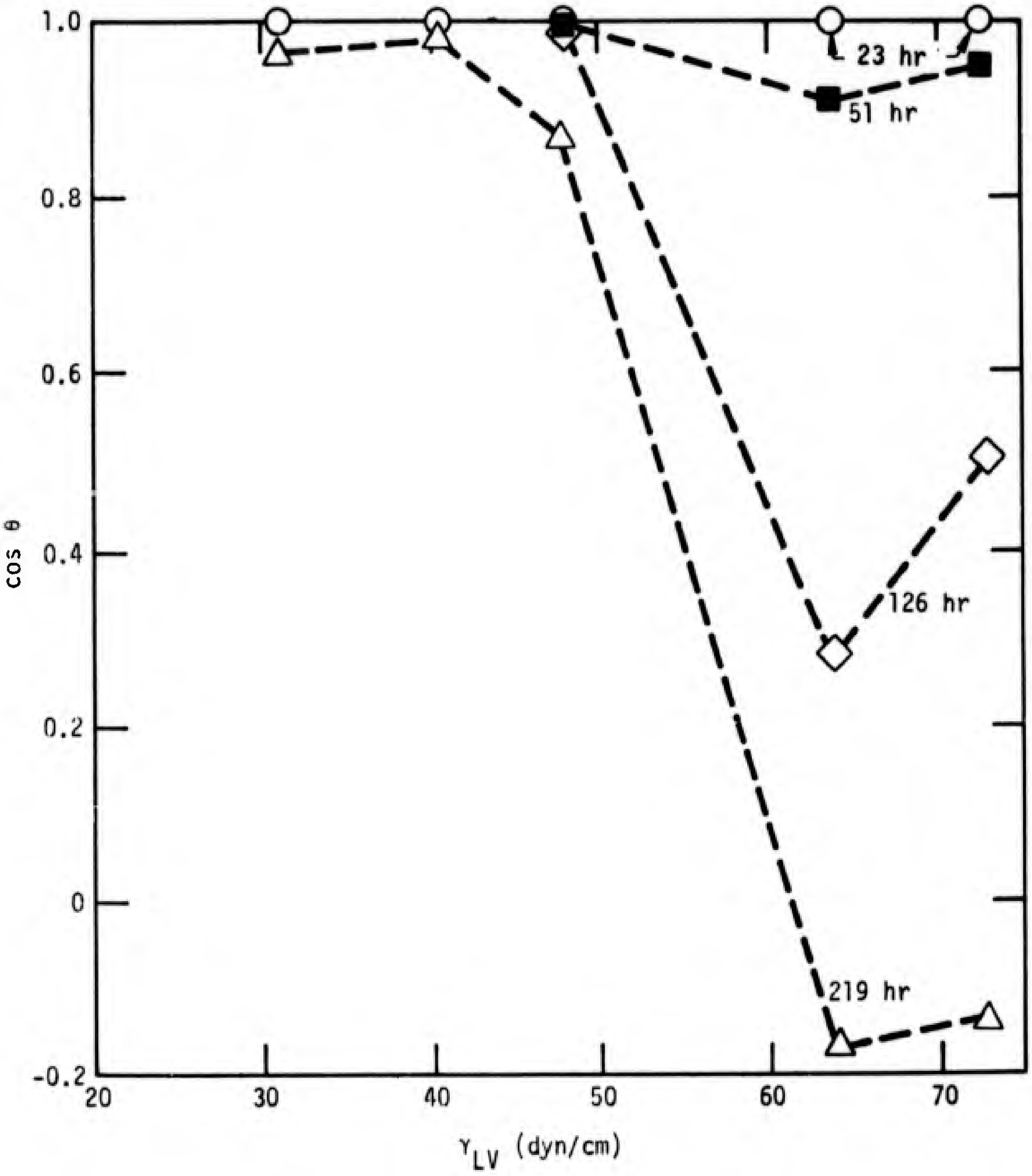

Fig. 38. Variation of cos θ vs γ_{LV} with SET for FPL etch Al 2024-T3.

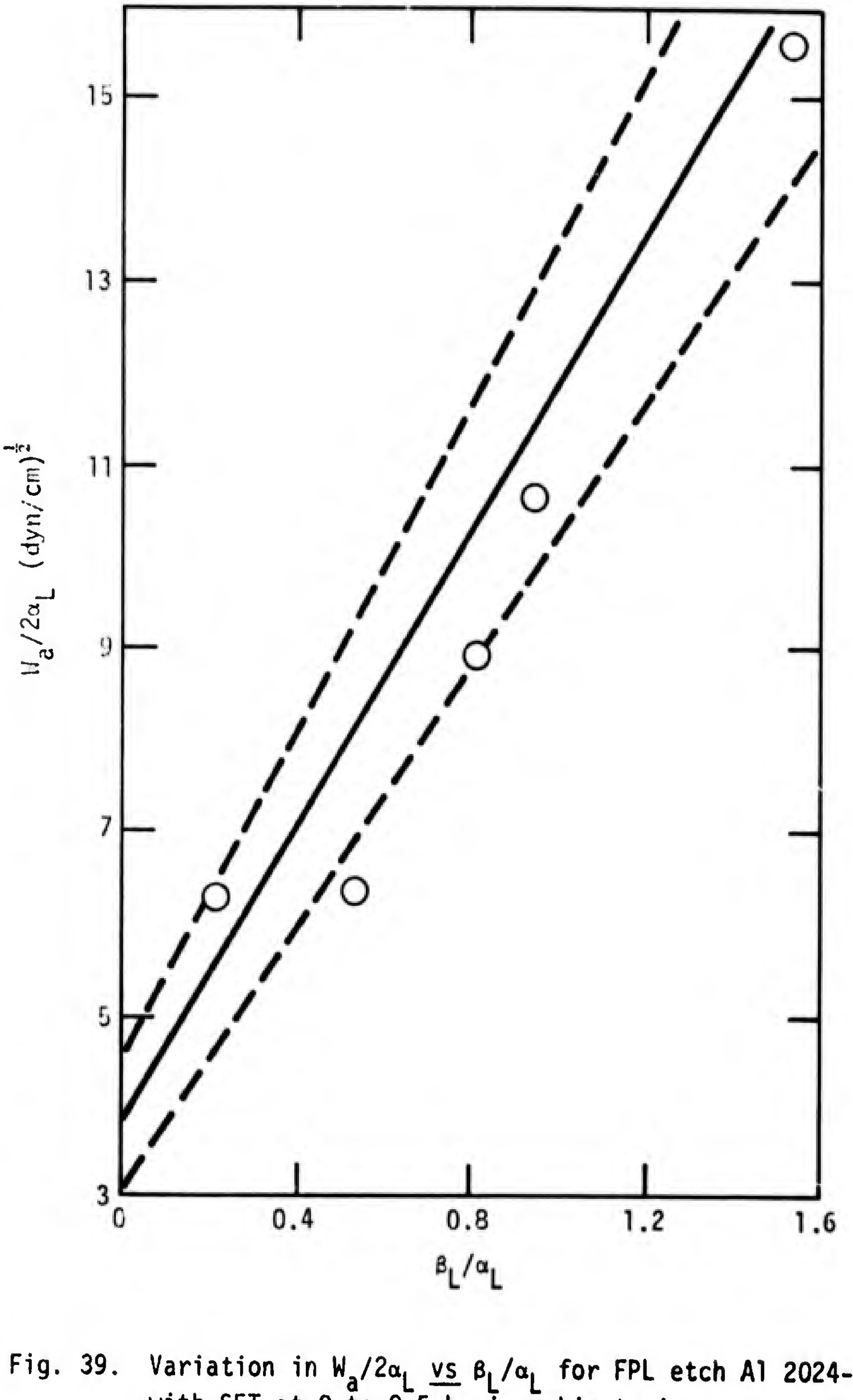

Fig. 39. Variation in $W_a/2\alpha_L$ vs β_L/α_L for FPL etch Al 2024-T3 with SET at 0 to 0.5 hr in ambient air.

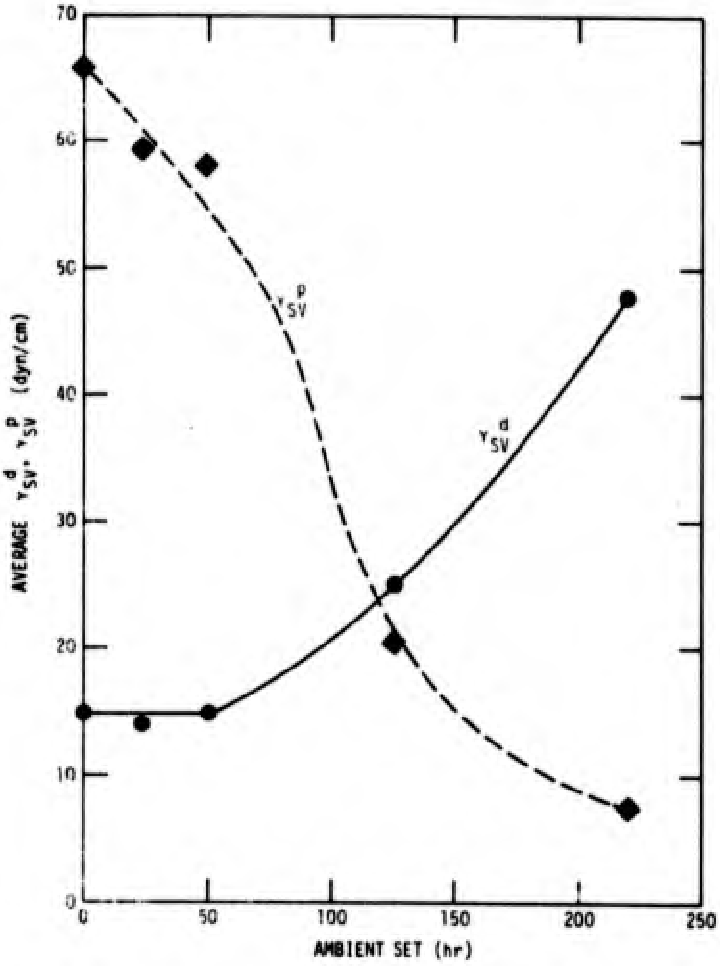

Fig. 40. Effect of SET at 23°C and 50 ± 5% R.H. on calculated values for γ_{SV}^d and γ_{SV}^p for FPL etch Al 2024-T3.

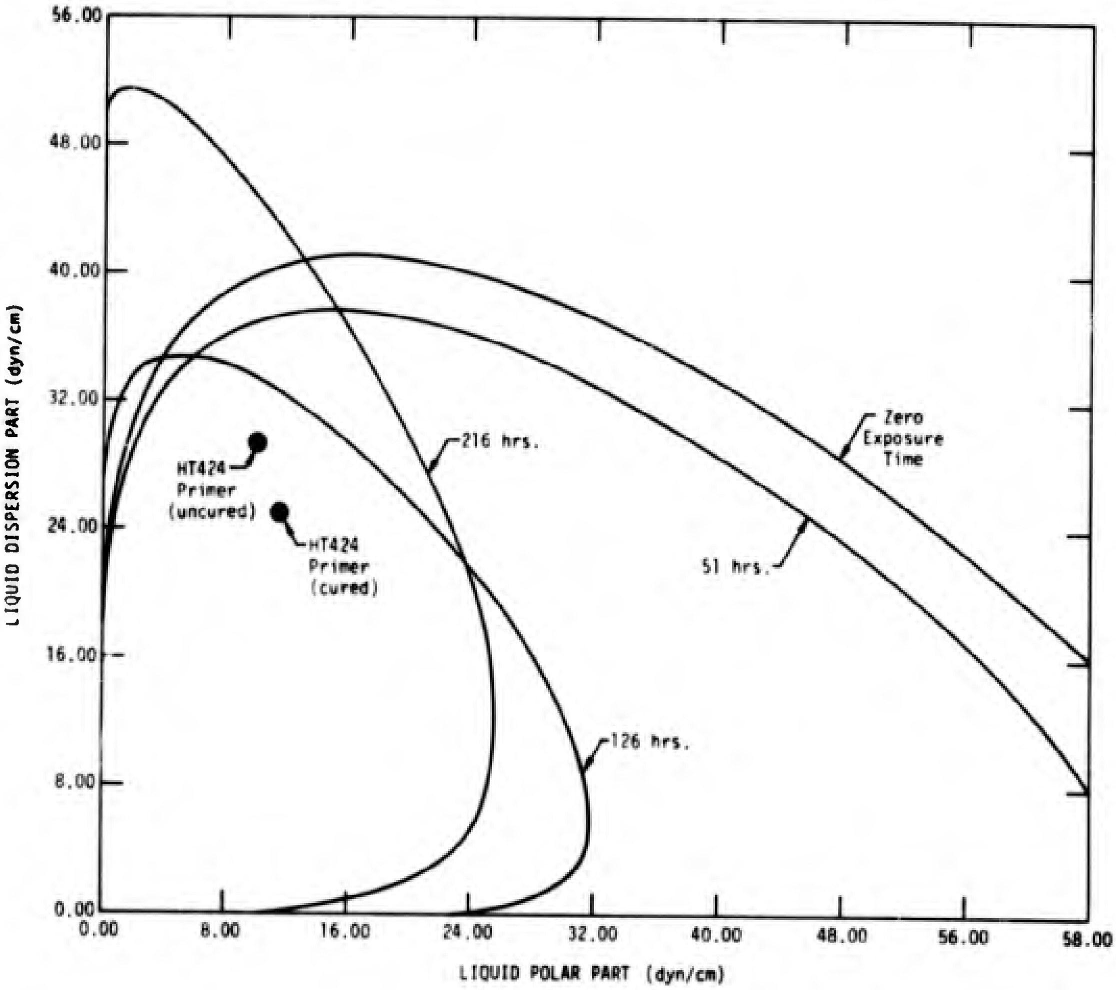

Fig. 41. Wettability envelopes for Al 2024-T3 with FPL etch and SET at 23°C, 50-60% R.H.

different ambient SET conditions enclose the surface tension properties of HT424 primer. Since the wettability envelopes of Figure 41 are based upon the average values of γ_{SV}^{d} and γ_{SV}^{p} from Table 19, the uncertainties inherently expressed by $\pm\delta^{d}$ and $\pm\delta^{p}$ are not illustrated.

These studies provide more detailed information than available previously concerning the effects of surface exposure time under ambient air atmosphere upon the wettability and interfacial bonding properties of etched Al 2024-T3. Despite the obvious complexities introduced by micro-roughness, adsorption layers, and possible ionic-covalent mechanisms of bonding, it is evident that the analysis summarized in Section II.B.6 is capable of resolving significant changes in the surface energies γ_{SV}^{d} and γ_{SV}^{p} surface treated Al 2024-T3.

A special set of integrated experiments were implemented to examine the relationship between metal surface properties and adhesive joint strength as a function of SET at 54°C and 95% R.H. The surface treatment applied to Al 2024-T3 is the FPL etch. Subsequent to the etching treatment the Al 2024-T3 specimens were stored in a closed environment at 54°C and 95% R.H. for varying degrees of surface exposure time.

After varying levels of SET at 54°C and 95% R.H. the Al 2024-T3 samples were withdrawn to ambient atmospheric (23°C and 50 + 5% R.H.) conditions. A portion of these samples were utilized in wettability studies and surface energy analysis. The remainder were conditioned briefly under ambient atmosphere then spray coated with HT424 primer solution and dried according to manufacturer's recommendations as follows:

1) 30 min dry at 23°C,
2) 60 min dry at 66°C.

The average thickness of the dried primer layer is 0.001. These primer coated surfaces were subsequently bonded into standard lap shear joints using HT424 structural adhesive film (0.135 lb/ft^{2}) and cured under 50 psi pressure for 60 min at 171°C.

Liquid-solid contact angles on the Al 2024-T3 samples after SET at 54°C and 95% R.H. were conducted at 20°C in the B-100 Environmental Chamber of the NRL contact angle apparatus (Rame-Hart Inc.) using sessile drops. The results of contact angle measurements, reported in terms of the cosine of the advancing contact angle θ, are summarized in Table 20. These data were converted to values for nominal work of adhesion and re-expressed in Table 21 in terms

Table 20: Cosine of the liquid-solid contact angle θ of sulfuric-chrome etched Al-2024T3 at various SET conditions (55°C and 95% R.H.)

Surface Exposure Time (hr)		0	2	8	21	92
Test Liquid	γ_{LV} (dyn/cm)	$\cos\theta$	$\cos\theta$	$\cos\theta$	$\cos\theta$	$\cos\theta$
water	72.8	.9976	.5592	-.1219	-.3584	-.5446
glycerol	64.0	.9976	.2079	.3305	.4384	-.2079
ethylene glycol	48.3	.9998	.9205	.7772	.4540	-.1219
tricresyl phosphate	40.9	.9962	.9703	.9598	.9945	.6293
polyglycol P-1200	31.3	.9945	.9816	.9744	.9782	.9744

Table 21: Analysis of Liquid-Solid Interactions

Surface Exposure Time (hr)			0	2	8	21	92
γ_{LV}	$2\alpha_L$	β_L/α_L	$Wa/2\alpha_L$ $(dyn/cm)^{\frac{1}{2}}$				
72.8	9.34	1.53	15.57	12.15	6.84	5.00	3.55
64.0	11.66	.94	10.96	6.63	7.30	7.90	4.35
48.3	10.83	.81	8.92	8.56	7.93	6.49	3.92
40.9	12.52	.21	6.52	6.44	6.40	6.52	5.32
31.3	9.90	.53	6.31	6.26	6.24	6.25	6.24

described by Eq. 9 of Section II.B.6. The results of determinant calculations which isolate averaged values of γ^d_{SV}, γ^p_{SV}, and γ_{SV} in conjunction with standard deviations from the mean $\pm\delta$, $\pm\delta^p$, and $\pm\delta^d$ are summarized in Table 22.

Plots of $\cos\theta$ versus γ_{LV} for various SET conditions at 54°C and 95% R.H. are shown in Figure 42. These curves illustrate that the polar liquids with $(\beta_L/\alpha_L) \geqslant 0.8$ display the most pronounced shift in $\cos\theta$ with SET. In Table 21 this result is expressed as a decrease in calculated values of $W_a/2\alpha_L$ with increased SET. The values of γ^d_{SV} and γ^p_{SV} summarized in Table 22 are plotted versus SET in the curves of Figure 43. The curves of Figure 43 display an initial rapid increase in γ^d_{SV} and concurrent decrease in γ^p_{SV} over the first 8 hr. period of SET at 54°C and 95% R.H. similar to that for longer SET at 23°C and 50 ± 5% R.H. (see Figure 40). A direct correlation of these two experiments is obtained by the time ratio:

$$a_{TC} = \frac{\text{SET(23°C, 50\% R.H.)}}{\text{SET(54°C, 95\% R.H.)}} \cong 58.5 \tag{21}$$

where a_{TC} is a dimensionless time shift factor that includes both the effects of increased temperature and humidity.

Figure 44 illustrates the superposition of the values of γ_{SV} (upper curve) and γ^d_{SV} and γ^p_{SV} (lower curves) and an SET characteristic of ambient surface exposure at 23°C and 50 ± 5% R.H. The data points represent the averaged values of γ_{SV}, γ^d_{SV}, γ^p_{SV} and the vertical bars identify the uncertainty represented by $\pm\delta, \pm\delta^d$, and $\pm\delta^p$, respectively. Figure 44 illustrates that Eq. 5 of Section II.B.6 provides an effective basis for representing SET effects over an extended time range at ambient aging conditions by shifting the data of Table 22 to longer times characteristic of slow aging at ambient SET. The reduced data represented in Figure 44 covers a time range 0.25 hr $\lesssim$ SET (23°C, 50% R.H.) $\leqslant$ 5250 hr (218 day).

The "wettability envelopes" for Al 2024-T3 with FPL etch and SET at 54°C and 95% R.H. are shown in Figure 45. The distance of γ^d_{LV} and γ^p_{LV} extending from the origin $\gamma^d = \gamma^p = 0$ to a particular envelope describes a condition of spreading $\cos\theta = 1.0$ for the liquid on the solid. The averaged values of γ^d and γ^p for uncured and cured HT424 primer fall within all of the wettability envelopes representing the SET conditions of Table 22.

The results of this wettability study shows that the surface energy $\gamma_{SV} = \gamma^d_{SV} + \gamma^p_{SV} = \alpha^2_S + \beta^2_S$ of FPL etched Al 2024-T3 surfaces undergoes a systematic

Table 22: Calculated Solid-Vapor Surface Tension Properties by the Determinant Method

Surface Exposure Time (hr)	$\gamma_{SV}^{d} \pm \delta^{d}$	$\gamma_{SV}^{p} \pm \delta^{p}$	$\gamma_{SV} \pm \delta$
0	14.8 ± 5.2	65.5 ± 14	80.3 ± 9.4
2	24.7 ± 5.0	25.6 ± 11.4	50.3 ± 7.2
8	45.6 ± 7.8	2.6 ± 1.1	48.2 ± 7.5
21	59.0 ± 17.1	7.2 ± 3.4	66.2 ± 19.5
92	40.1 ± 7.4	5.6 ± 2.7	45.7 ± 10.0

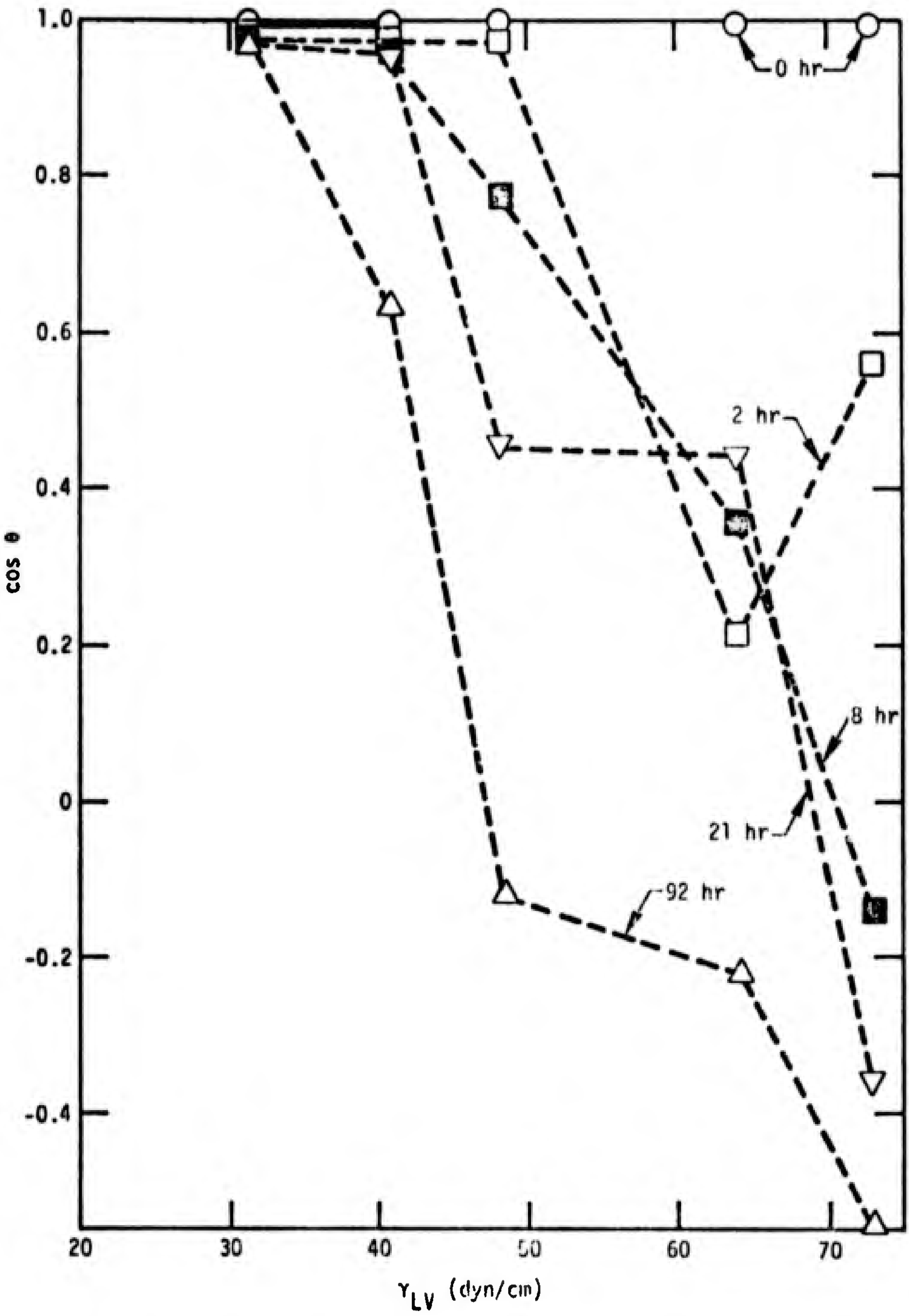

Fig. 42. Variation in cos θ vs γ_{LV} with SET at 54°C, 95% R.H.

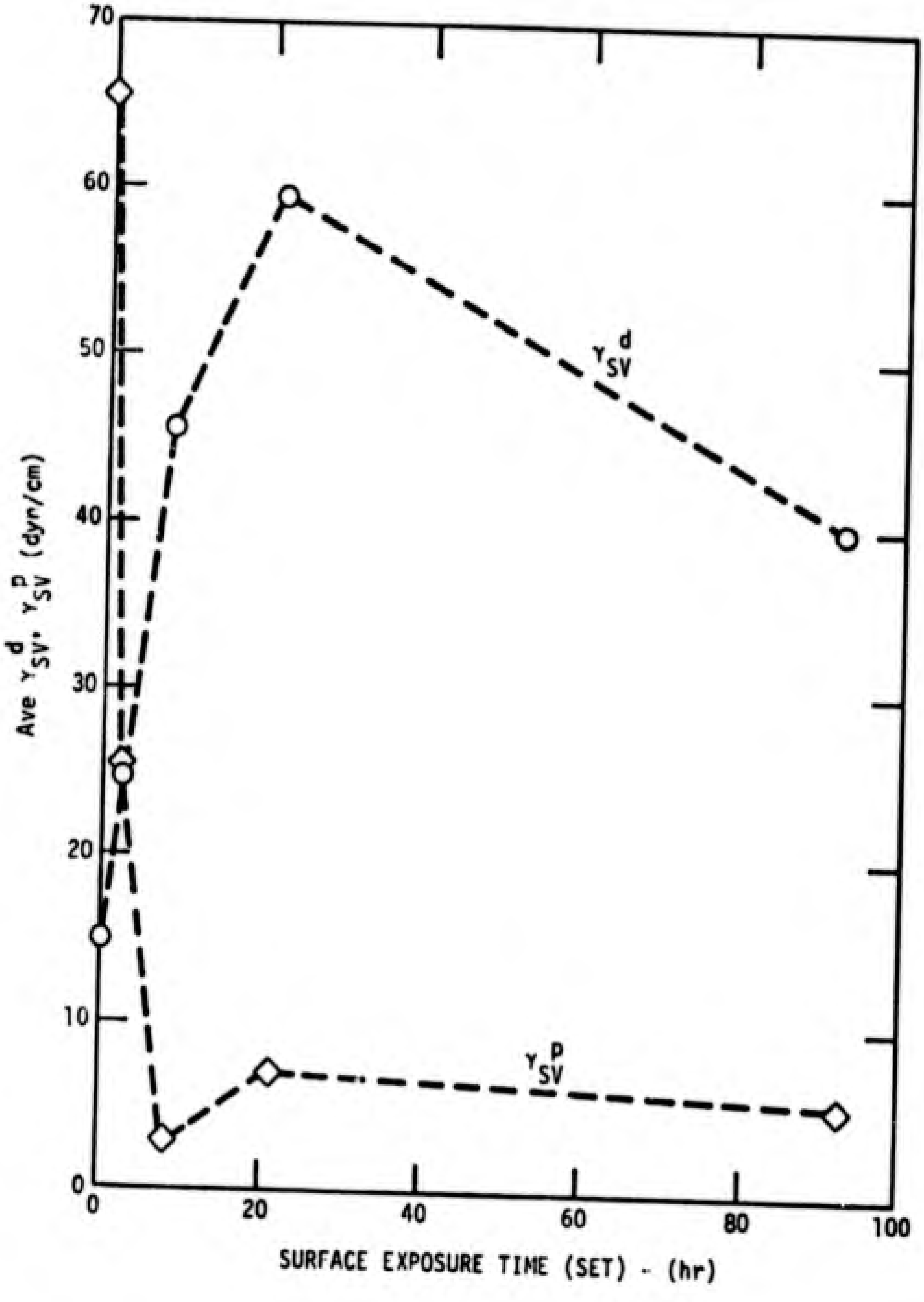

Fig. 43. Effect of SET at 54°C, 95% R.H. on calculated average values of γ_{SV}^{d} and γ_{SV}^{p}.

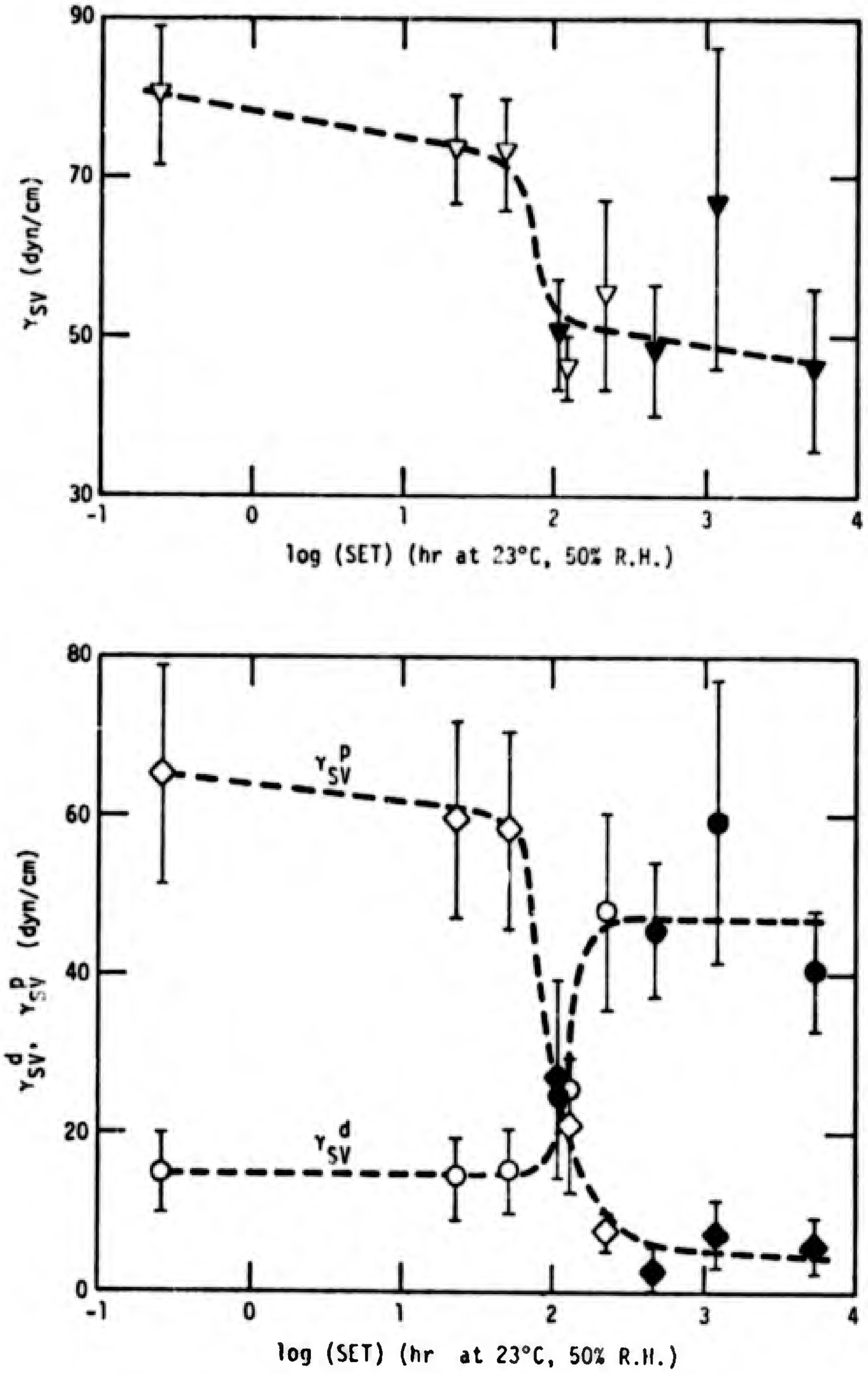

Fig. 44. Superposition of SET with $\gamma_{SV} = \gamma_{SV}^{d} + \gamma_{SV}^{p}$ at 23°C, 50% R.H. (open points) and SET 54°C, 95% R.H. (solid points) by the line shift factor $a_{T_c} = 58.5$.

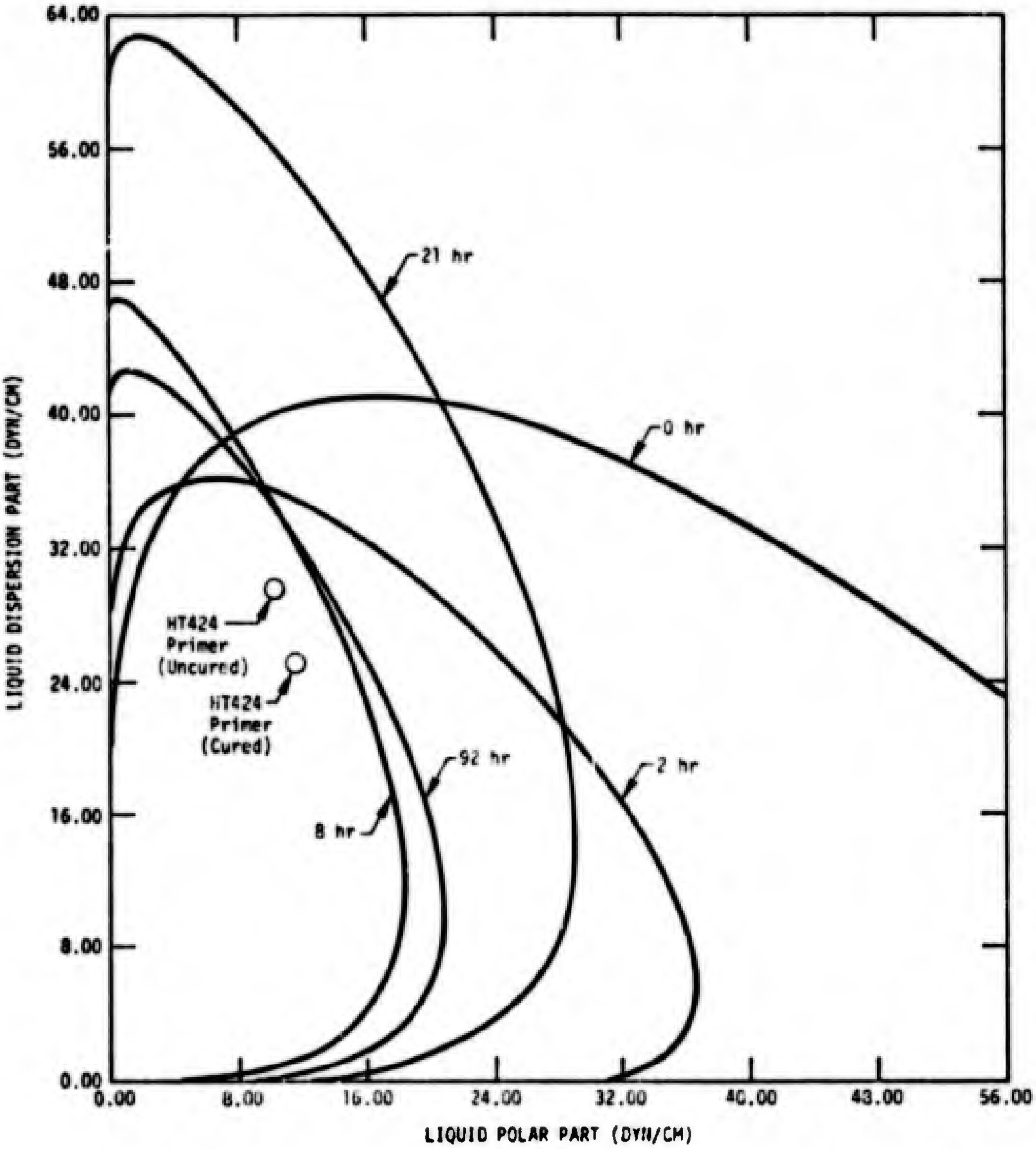

Fig. 45. Wettability envelopes for Al 2024-T3 with FPL etch and SET at 54°C, 95% R.H.

shift with surface exposure time (SET). It is of interest to examine the consequences of this transition in the wettability and surface energy of Al 2024-T3 as it relates to the mechanisms of interfacial bonding and fracture with the HT424 adhesive system utilized in lap shear tests for evaluation of performance and reliability.

The average values of the surface energy properties for HT424 (designated phase 1) and FPL etched Al 2024-T3 (designated phase 3) at varied conditions of SET are summarized in Table 23. The shift in the balance of α_3 versus β_3 for Al 2024-T3 with increasing SET is illustrated in the diagram of Figure 46. It may be noted in Figure 46 that all of the α_3, β_3 data points are farther removed from the origin $\alpha=\beta=0$ than the circled point for HT424 indicated as $\alpha_1 = 5.21$ (dyn/cm)$^{\frac{1}{2}}$ and $\beta_1 = 3.31$ (dyn/cm)$^{\frac{1}{2}}$. Figure 46 provides a compact graphic statement of the experimental result that the calculated values of the interfacial work of adhesion between adhesive and adherend W_{13} as defined by the following relation:

$$W_{13} = 2(\alpha_1\alpha_3 + \beta_1\beta_3) \text{ erg/cm}^2 \qquad (22)$$

exceeds the work of cohesion W_{11} for HT424 which is defined by the relation:

$$W_{11} = 2(\alpha_1^2 + \beta_1^2) = 76.2 \text{ erg/cm}^2 \qquad (23)$$

Calculated values of W_{13} are tabulated in the lower right columns of Table 23 and graphed as a function of SET at 54°C and 95% R.H. in the upper curve of Figure 47. The reduced SET time scale for the upper curve of Figure 47 combines previously reported data for SET at 23°C and 50% R.H. and SET at 54°C and 95% R.H. One notes that the calculated values of W_{13} diminish in a monotonic fashion with increasing SET over the first 10 hour period and then display an apparent time invariance. The lower curve of Figure 47 plots experimental data for the averaged values of lap shear bond strength σ_b as a function of SET time between FPL etch treatment and bond formation. It may be noted that the variation in σ_b with SET shows a close correspondence with the variation in W_{13} with SET as was noted in Figures 35 and 36 for other surface properties.

Based upon the correlation demonstrated in Figure 47 between the nearly equivalent effects of surface exposure time (SET) upon interfacial work of adhesion W_{13}, the lap shear bond strength σ_b and the interfacial bond strength σ_I, the propositions outlined by Eq. 14 through Eq. 18 of Section II.B.6 were applied. While the modified Griffith failure criteria defined by Eq. 14 of

TABLE 23

Surface Energy Analysis and Work of Adhesion Between HT424 (phase 1) and Sulfuric-Chromate Etched Al 2024-T3 (phase 3) at Varied Surface Exposure Times (SET)

A: Adhesive Surface Properties:

Material	α_1 $(\text{dyn/cm})^{\frac{1}{2}}$	β_1 $(\text{dyn/cm})^{\frac{1}{2}}$
Uncured HT424	5.36	3.21
Cured HT424	5.05	3.42
Averaged values:	$\alpha_1 = 5.21$	$\beta_1 = 3.31$

B. Adherend Surface Properties and Work of Adhesion W_{13}

SET (hr) (23°C-50% R.H.)	Reduced SET(hr) 54°C-95% R.H.	α_3 $(\text{dyn/cm})^{\frac{1}{2}}$	β_3 $(\text{dyn/cm})^{\frac{1}{2}}$	W_{13} (erg/cm^2)
0.25 ± .25	.0043	3.85	8.09	93.7
23	.39	3.74	7.69	89.9
51	.87	3.86	7.62	90.7
126	2.15	5.03	4.52	82.3
219	3.74	6.91	2.72	90.0
SET (hr) (54°C-95% R.H.)				
0	≈ 0 (.0043)	3.85	8.09	93.7
2	2	4.97	5.06	85.3
8	8	6.75	1.61	81.0
21	21	7.68	2.68	97.8
92	92	6.33	2.37	81.6

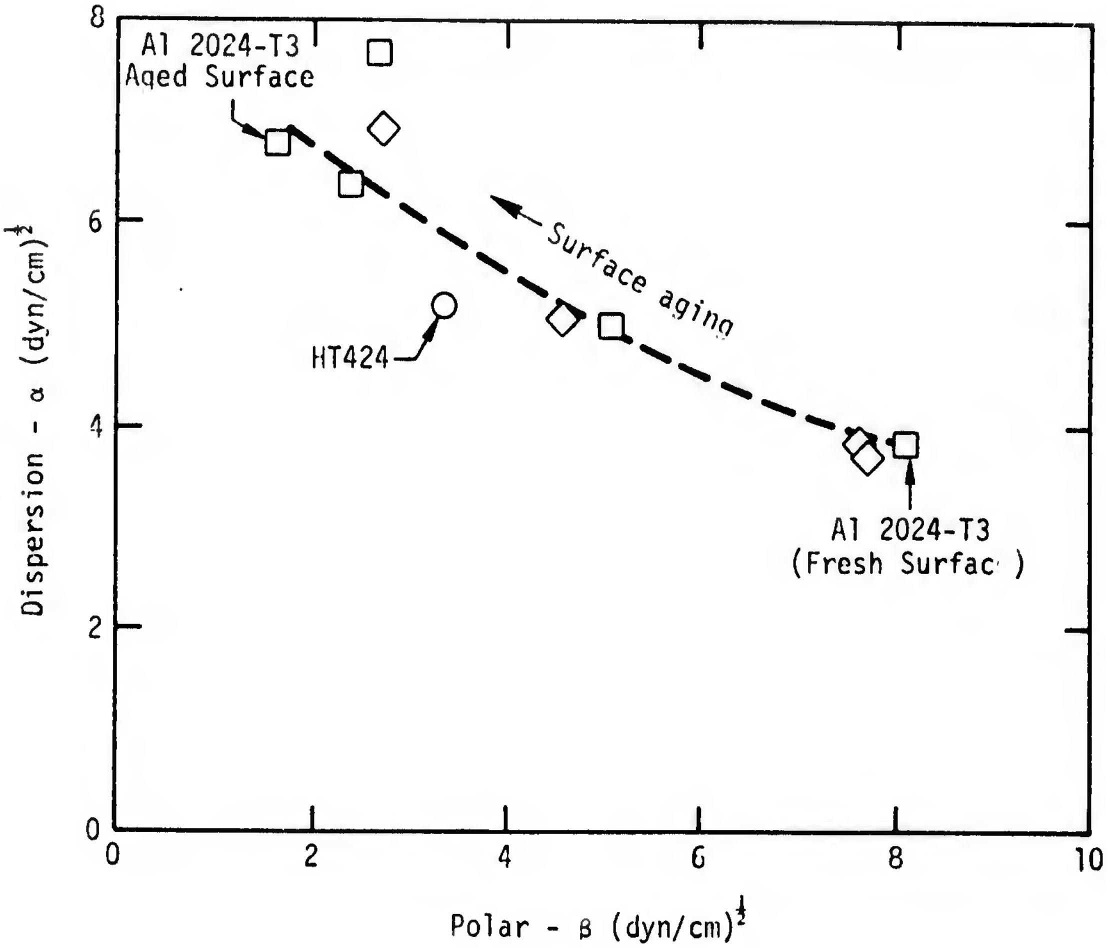

Fig. 46. Dispersion (α) and polar (β) components of the solid-vapor surface tension $\gamma_{SV} = \alpha_S^2 = \beta_S^2$ for HT424 primer (phase 1) and Al 2024-T3 adherend (phase 3).

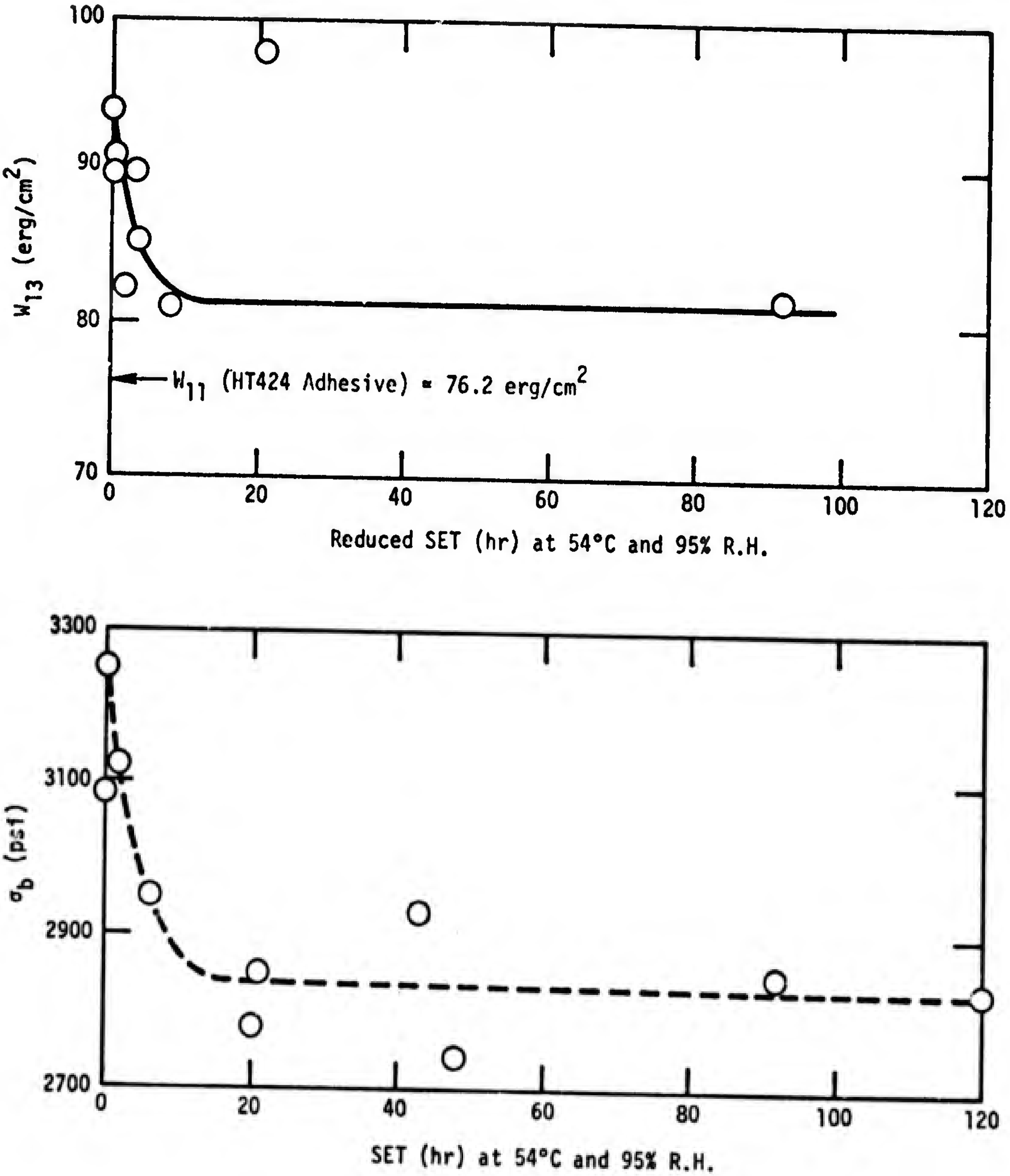

Fig. 47. Dependence of interfacial work of adhesion W_{13} (upper curve) and lap shear bond strength σ_b (lower curve) at varied SET.

Section II.B.6 represents a highly idealized boundary failure criteria it makes a useful simplified basis for correlating fracture mechanics and surface energetic arguments.

The averaged values of $\alpha_1 = 5.21\ (\text{dyn/cm})^{\frac{1}{2}}$ and $\beta_1 = 3.31\ (\text{dyn/cm})^{\frac{1}{2}}$ define the surface properties of HT424 primer as summarized in Table 12. For surface aged Al 2024-T3, surface energy analysis has defined the following values (see Table 23) as representing a fully aged surface at high SET:

SET (hr) at 54°C and 95% R.H.	α_3 $(\text{dyn/cm})^{\frac{1}{2}}$	β_3 $(\text{dyn/cm})^{\frac{1}{2}}$
21	7.68	2.68
92	6.33	2.37
averaged values:	$\alpha_3 = 7.00$	$\beta_3 = 2.52$

These surface energy parameters for HT424 and etched Al 2024 T3 are indicated in the α versus β diagram of Figure 48 (left view). The points H = 6.11 and K = 2.92 $(\frac{\text{dyn}}{\text{cm}})^{\frac{1}{2}}$ defined by Eq. 17 and Eq. 18 of Section II.B.6 represent the locus of the vectors R_0, R(air) and R(H_2O) where for air ($\alpha_2 = \beta_2 = 0$) and for H_2O [$\alpha_2 = 4.67\ (\text{dyn/cm})^{\frac{1}{2}}$ and $\beta_2 = 7.14\ (\text{dyn/cm})^{\frac{1}{2}}$] for interfacial failure, with $\phi_I = 1-\phi_c = 1.0$ between HT424 and Al 2024-T3. The right view of Figure 48 presents the function of $\gamma_G^{\frac{1}{2}} \propto (\propto_c)$versus R which may be generated from Eq. 14 of Section II.B.6 for the case where E, and c are assumed constant. The prediction from the Griffith surface energy analysis is that:

$$\frac{\sigma_I\ (H_2O)}{\sigma_I\ (\text{air})} = 0.644 \tag{24}$$

Equation 24 expresses the equilibrium ratio of $\sigma_I\ (H_2O)/\sigma_I$ (air)at exposure time $t = \infty$ and therefore is a minimum expected value where other factors of Eq. 14 of Section II.B.6 remain invariant.

The critical Griffith stress σ_c for cohesive failure in HT424, with $\phi_c = 1-\phi_I = 1.0$, may also be made for air and water immersion in similar fashion. In this case where the locus of failure is within phase 1, we make $\alpha_1 = \alpha_3 = H = 5.21\ (\text{dyn/cm})^{\frac{1}{2}}$ $\beta_1 = \beta_3 = K = 3.31\ (\text{dyn/cm})^{\frac{1}{2}}$ with $R_0 = 0$. The left view of Figure 49 shows the argument in terms of the α versus β coordinates. The right view shows the simple linear form for the Griffith function generated

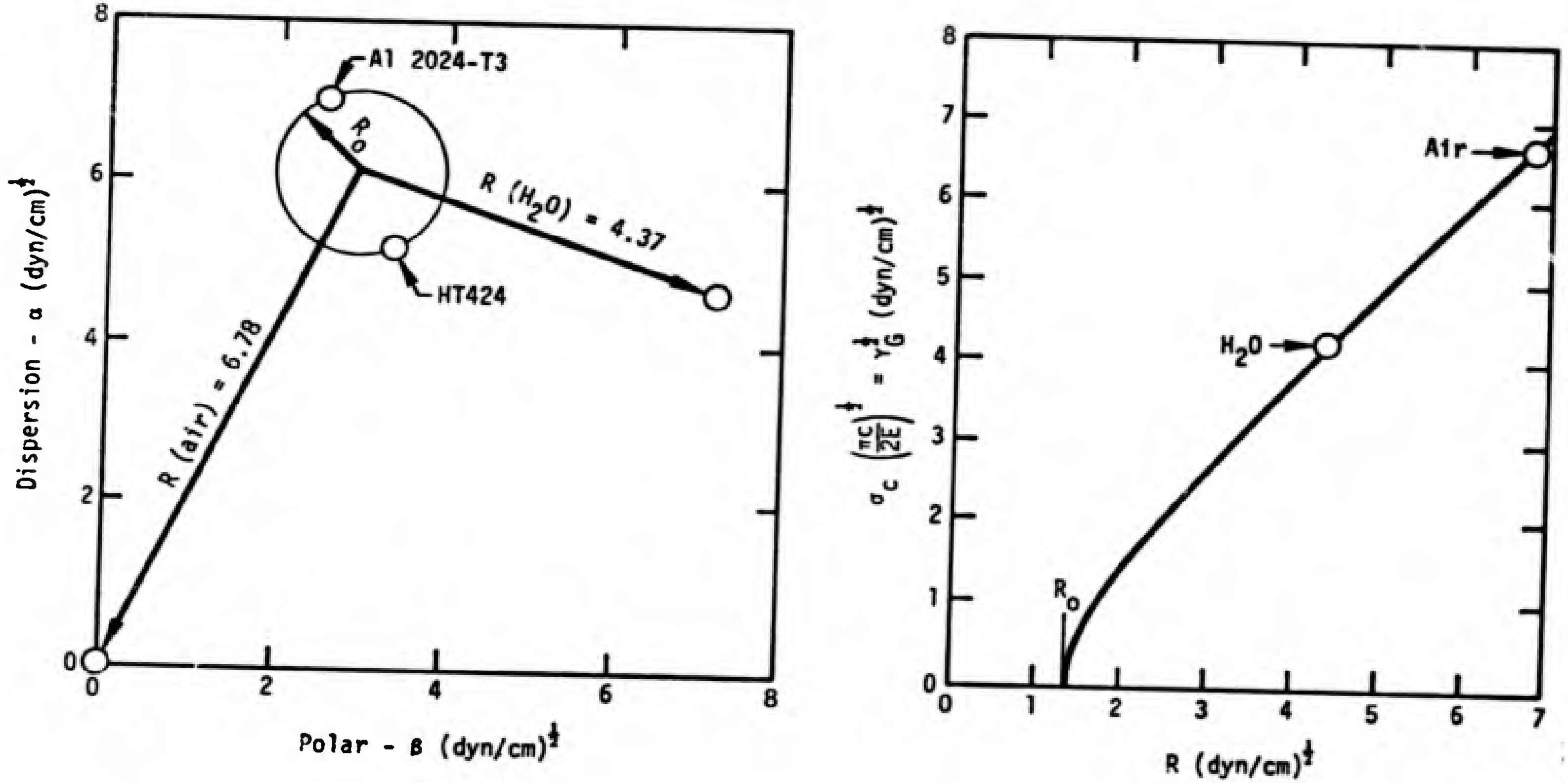

Fig. 48. Modified Griffith analysis of the effect of H_2O immersion in reducing critical failure stress σ_I for interfacial failure between HT424 and etched Al 2024-T3 ($\phi_I = 1 = \phi_c = 1.0$).

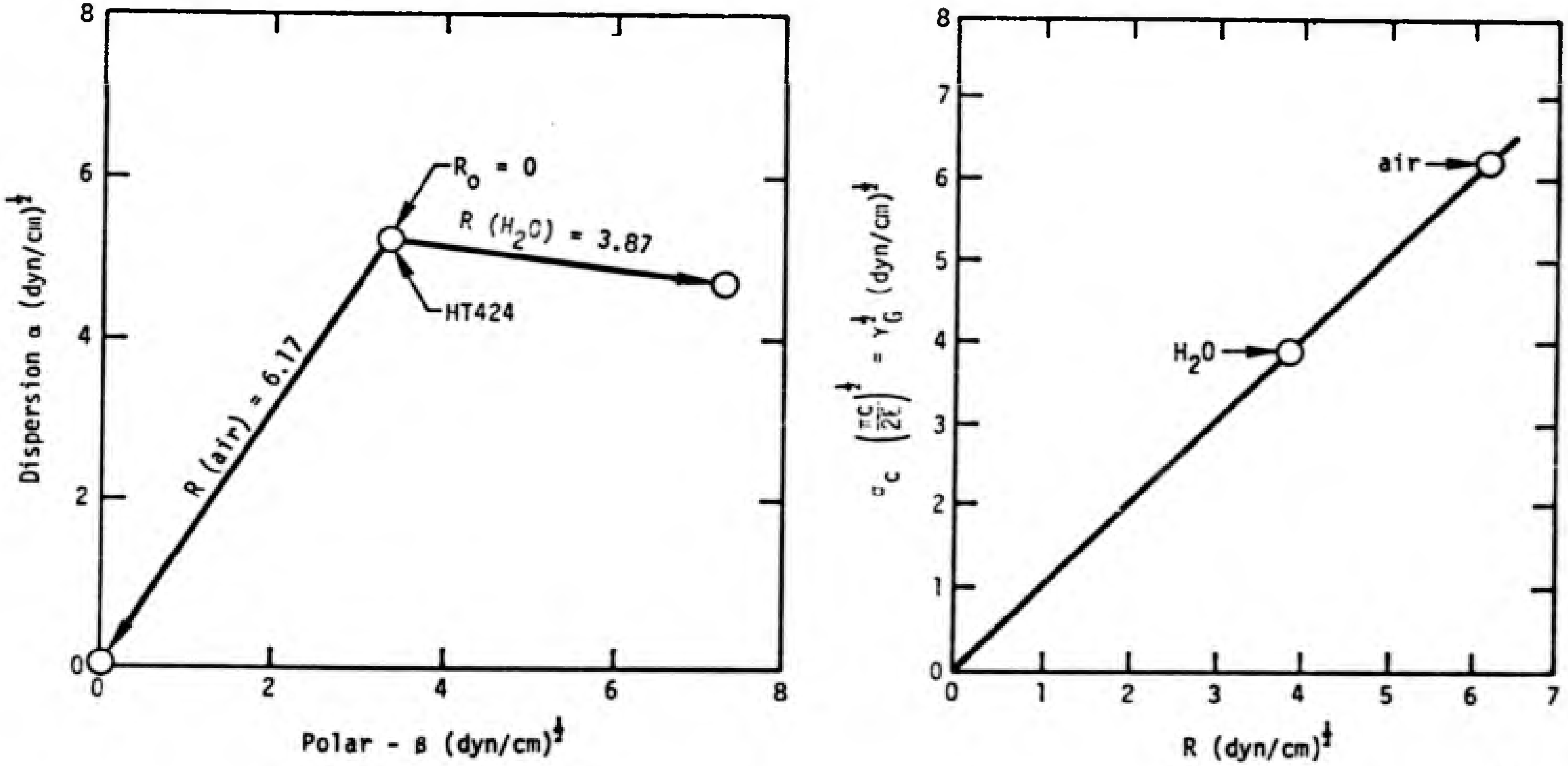

Fig. 49. Modified Griffith analysis of effect of H_2O immersion in reducing critical failure stress σ_c for cohesive failure in HT424 ($\phi_c = 1 - \phi_I = 1.0$).

from Eq. 14 of Section II.B.6 for $R_0 = 0$. For cohesive failure in HT424 the calculated ratio is as follows:

$$\frac{\sigma_c\ (H_2O)}{\sigma_c\ (air)} = 0.63 \tag{25}$$

The close similarity between Eq. 24 and Eq. 25 indicates that a water environment should not preferentially promote interfacial failure and that a distinction cannot be made as to the expectation of interfacial vs cohesive failure from the wettability analysis. However, a comparison of predicted values of $\sigma_i\ (H_2O)/\sigma_i(air)$ and $\sigma_c(H_2O)/\sigma_c(air)$, calculated from the wettability analysis, can be compared with observed joint degradation in the next section.

3. Joint Aging (BET) Effects

Al 2024-T3 samples were given the FPL etch and bonded at SET = 0 and SET = 20 hrs. They were then fractured after various lengths of time in a humidity chamber at 95% R.H. and 54°C. The experimental results are given in Tables 24, 25 and 26, and the average values of σ_b and ϕ_c are plotted in Fig. 50. The effect of bond exposure causes σ_b to decrease and then level off after about 200 hrs. At about 700 to 800 hrs σ_b decreases some more. The σ_b values for SET = 20 hrs correspond to the lower values expected from Fig. 36. The fraction of the surface ϕ_c that failed cohesively remains almost constant with BET and also shows the expected decrease at SET = 20 hrs (from Fig. 36). Since ϕ_c remains almost constant at about 0.8, it is concluded that degradation during BET is mainly due to weakening of the adhesive rather than degradation at the interface.

Finally, Fig. 51 shows a profile of the SET and BET response surface for lap shear bond strengths of 2024-T3 aluminum and HT424 adhesive. It should be noted that the initial and final values of BET, bond strengths $\sigma_b \approx 3200$ psi and $\sigma_b \approx 2200$ psi correlate closely with the work of others (see ref. 38, Table 15, page 74) for the Al-HT424 system.

It is interesting to note that the predicted ratio $\sigma(H_2O)/\sigma(air) \sim 0.64$ for interfacial or cohesive degradation is in close agreement with the experimental ratio of σ_b at SET = 0 hr, BET = 0 hr, to that of σ_b at SET = 20 hr and BET = 1000 hrs (Fig. 51)

$$\frac{\sigma_b\ (20\text{ hr SET, }1000\text{ hr BET})}{\sigma_b\ (0\text{ hr SET, }0\text{ hr BET})} \approx \frac{2250\text{ psi}}{3250\text{ psi}} = 0.69 \tag{26}$$

TABLE 24: Compilation of Lap Shear Test Data for Sulfuric-Chromate Etched Al 2024-T3 with Bond Exposure Time (BET) at 54°C and 95% R.H. (all bonds fabricated with SET = 0 hr)

Test No.	σ_b (psi)	ϕ_I	ϕ_c	σ_b/ϕ_I	ϕ_c/ϕ_I	BET (hr)
1	3260	.30	.70	10867	2.33	0
2	3190	.35	.65	9114	1.86	
3	3520	.20	.80	17600	4.00	
4	3170	.30	.70	10567	2.33	
5	3330	.25	.75	13320	3.00	
6*	3120	.20	.80	15600	4.00	
1	2560	.20	.80	12800	4.00	165
2	2310	.25	.75	9240	3.00	
3	2710	.15	.85	18066	5.67	
4	2680	.15	.85	17866	5.67	
5	2450	.30	.70	8167	2.33	
6	2670	.25	.75	10680	3.00	
1	2330	.30	.70	7767	2.33	449
2	2130	.30	.70	7100	2.33	
3	2640	.15	.85	17600	5.67	
4	2790	.20	.80	13950	4.00	
5	2520	.30	.70	8400	2.33	
6	2560	.20	.80	12800	4.00	
1	2510	.25	.75	10040	3.00	621
2	2470	.20	.80	12350	4.00	
3	2590	.10	.90	25900	9.00	
4	2520	.20	.80	12600	4.00	
5	2390	.40	.60	5975	1.50	
6	2430	.30	.70	8100	2.33	
1	2270	.25	.75	9080	3.00	808
2	1830	.45	.55	4066	1.22	
3	2070	.20	.80	10350	4.00	
4	2410	.20	.80	12050	4.00	
5	2480	.20	.80	12400	4.00	
6	2140	.20	.80	10700	4.00	
1	2470	.25	.75	9880	3.00	1023
2	2190	.25	.75	8760	3.00	
3	2600	.20	.80	13000	4.00	
4	2430	.20	.80	12150	4.00	
5	1970	.30	.70	6567	2.33	
6	1850	.30	.70	6166	2.33	

TABLE 25: Compilation of Lap Shear Test Data for Sulfuric-Chromate Etched Al 2024-T3 with Bond Exposure Time (BET) at 54°C and 95% R.H. (all bonds have 20 hr SET at 54°C and 95% R.H.)

Test No.	σ_b (psi)	ϕ_I (visual)	ϕ_c	σ_b/ϕ_I	ϕ_c/ϕ_I	BET (hr)
1	2920	.55	.45	5309	0.82	0
2	2700	.55	.45	4909	0.82	
3	2790	.55	.45	5073	0.82	
4	2970	.55	.45	5400	0.82	
5	2600	.55	.45	4727	0.82	
6	2950	.55	.45	5364	0.82	
1	2500	.25	.75	10040	3.00	171
2	2150	.45	.55	4778	1.22	
3	2310	.35	.65	6600	1.86	
4	2160	.35	.65	6170	1.86	
5	2270	.35	.65	6486	1.86	
6	2180	.35	.65	6229	1.86	
1	2520	.35	.65	7200	1.86	333
2	2250	.45	.55	5000	1.22	
3	2480	.45	.55	5511	1.22	
4	2170	.45	.55	4822	1.22	
5	1940	.50	.50	3880	1.00	
6	2400	.35	.65	6857	1.86	
1	2200	.30	.70	7333	2.33	669
2	2240	.35	.65	6400	1.86	
3	2250	.40	.60	5625	1.50	
4	2230	.40	.60	5575	1.50	
5	2290	.40	.60	5725	1.50	
6	24.0	.35	.65	6886	1.86	
1	2260	.40	.60	5650	1.50	983
2	2070	40	.60	5175	1.50	
3	2440	.40	.60	6100	1.50	
4	2030	.45	.55	4511	1.22	
5	1940	.40	.60	4850	1.50	
6	2220	.40	.60	5550	1.50	

TABLE 26: Brief Summary of SET and BET Effects at 54°C and 95% R.H. Upon Lap Shear Bond Strength of HT424 Adhesive and Etched Al-2024-T3

SET (hr)	BET (hr)	$\sigma_b \pm \delta_b$ (psi)	Number of Test Specimens
0	0	3250 ± 300	3
6	0	2950 ± 47	3
20	0	2780 ± 50	3
43	0	2930 ± 180	3
119	0	2830 ± 320	3
0	0	3085 ± 250	6
2	0	3120 ± 240	6
21	0	2850 ± 170	6
48	0	2740 ± 380	6
92	0	2850 ± 180	6
0	0	3263 ± 107	6
0	165	2563 ± 123	6
0	449	2495 ± 177	6
0	621	2485 ± 55	6
0	808	2200 ± 187	6
0	1023	2252 ± 248	6
20	0	2822 ± 125	6
20	171	2263 ± 100	6
20	333	2293 ± 173	6
20	669	2270 ± 53	6
20	983	2162 ± 147	6
120	1009	2290 ± 123	6

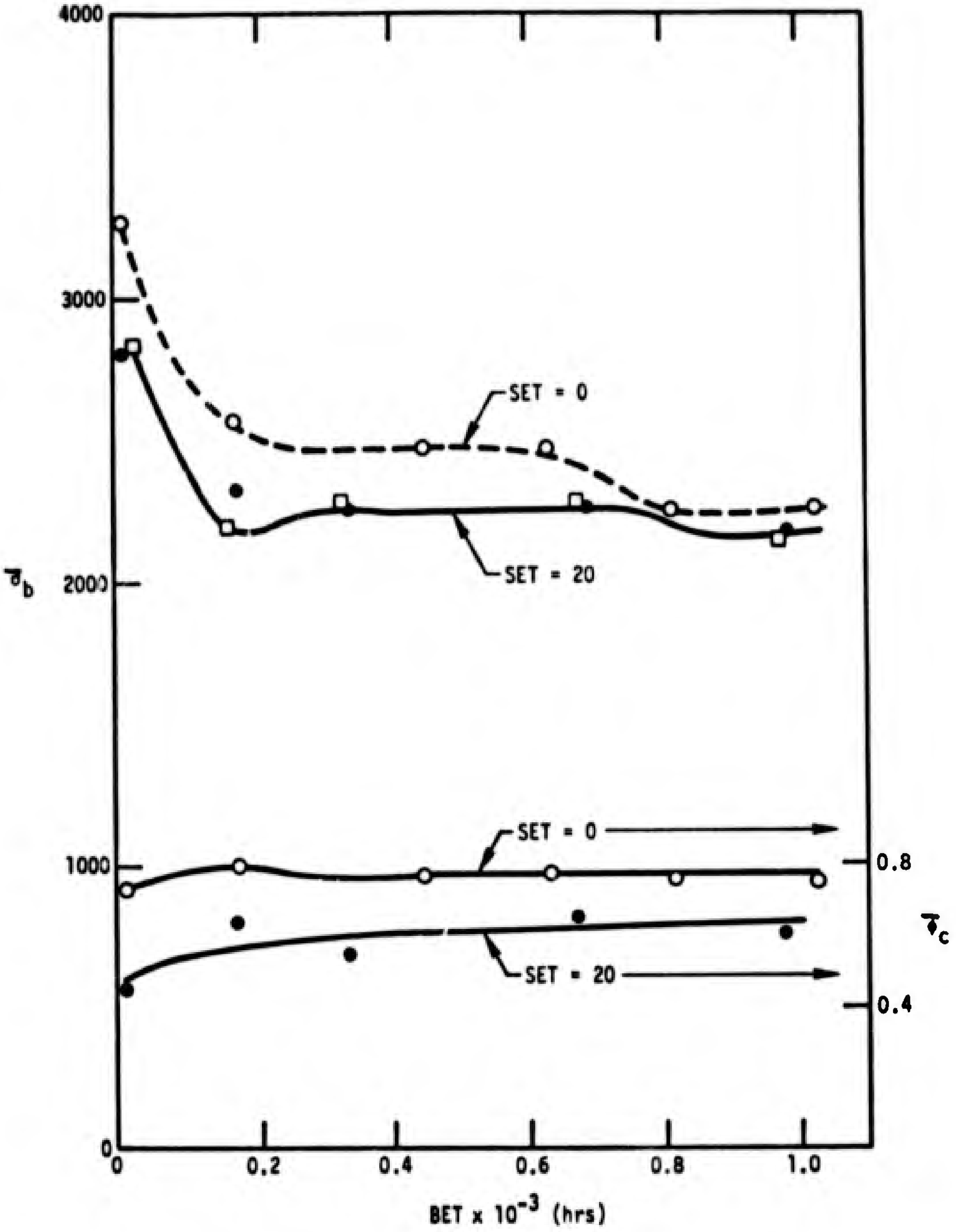

Fig. 50. Plot of σ_b and ϕ_c vs BET at 54°C, 95% R.H. SET = 0 and 20 hrs.

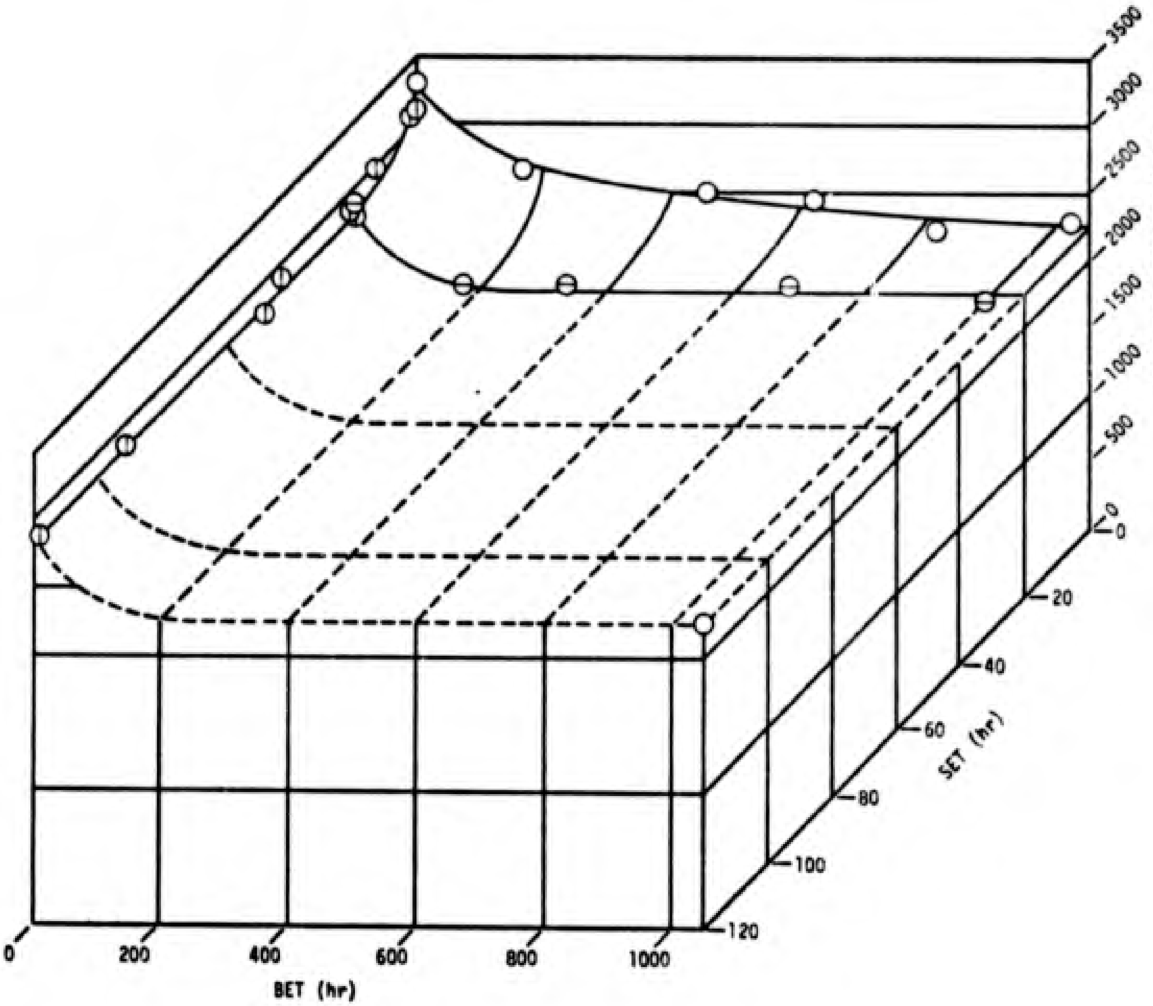

Fig. 51. SET and BET response surface for lap shear bond strength for Al 2024-T3-HT424

B. Titanium Adherends

1. Surface Character vs. Joint Strength

a. Ellipsometry

Ellipsometry results for phosphate-fluoride films on Ti-6Al-4V are reported in Table 27. The values of n_f and d on the right of Table 27 are the refractive index and film thickness computed for a range of values of the absorption coefficient κ_f. For ion sputtering experiments the film is removed in about 12.5 minutes (see Table 28). Sputter removal for other oxides have proved to be about 10 to 15 Å/min in our system. If the sputter rate is the same for the phosphate-fluoride film on Ti-6-4 the film is of the order of 200 Å thick. This value corresponds with the ellipsometer results if $n_f = 2.8$, $\kappa_f = 0.1$ (no solution was found for $\kappa = 0$). Since the refractive index of titanium dioxide is reported(18) to be about $n_f = 2.6$ to 2.9 and $\kappa_f = 0$ and since values of $n_f = 1.5$, $\kappa_f = 0.8$ for d ~ 500 Å, seem to be unreasonable, a value of about 200 Å may be more correct. To check the ellipsometer measurements, the thickness of the film was measured by means of the reflection interference microscope. In this technique, the film was picked up on a glass slide and examined in reflection using a thallium light source (λ = 5400 Å). One beam is reflected off the glass slide while the other is reflected off the top of the film; the fringe displacement in the image of the combined beams is a measure of the film thickness. Figure 52 shows a piece of the phosphate-fluoride film on a glass slide. The displacement due to the film is about 0.2 of the fringe distance. Therefore, the film thickness is about 0.2 x 5400/2 = 540 Å. Since the interference microscope measurement is an absolute measurement, independent of the refractive index, it is concluded that the film removed from the Ti-6-4 and placed on a glass slide is indeed ~ 540 Å but that the removal process has increased its thickness. This appears even more likely when considering the observations made during the film removal.

The film that is removed from Ti-6-4 is yellow-brown with the oxide layer on top. When this film is washed with water the yellow-brown layer appears to dissolve leaving the oxide layer on the microscope slide. This same observation was made by Hamilton and Lyerly(13) (personal communication). Two things could make the oxide films appear too thick in the interference microscope, an air gap between the film and the slide, or some of the yellow-brown layer was

TABLE 27

Ellipsometric Results for the Phosphate-Fluoride Film on Ti-6-4

λ = 6328 Å, Angle of Incidence = 70°, $n = 3.09\,(1 - i\,1.11)$

Δ	ψ	Computer Solutions		
		κ	n	d (Å)
72.24	27.86	0	----	----
		.1	2.85	200
		.2	2.46	256
		.3	2.16	310
		.4	1.93	356
		.5	1.75	397
		.6	1.65	428
		.7	1.58	464
		.8	1.52	514
Interference Microscope				540

TABLE 28

Ellipsometry and Sputter Time for Ti-6Al-4V with Various Surface Treatments (Angle of Incidence 70°)

Surface Treatment	λ	Δ	ψ	n_f	κ_f	Film Thickness Å	Sputter time min	Sputter rate Å/min
Phosphate-fluoride	6328	72.86	27.86	2.84	0.1	200	12.5	16
Nitric Acid-fluoride	5461	100.04	30.88	2.10	0.0	130	10	13
TURCO	5461	88.10	24.34	2.80	0.3	184	12.5	15

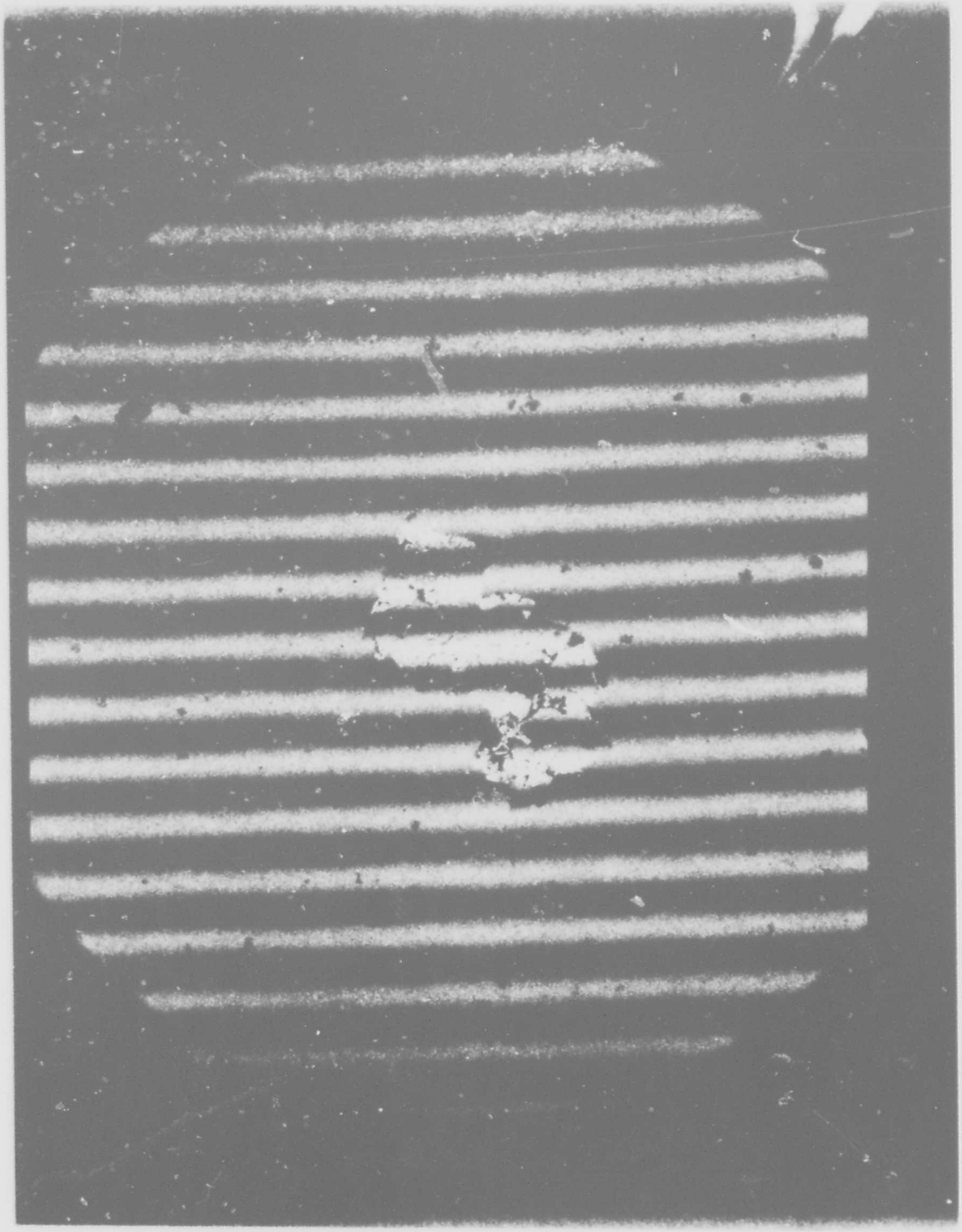

Fig. 52. Photograph from reflection interference microscope ($\lambda = 5400$ Å)

not removed by the water. As for the aluminum surface after the FPL etch, the titanium surface after the phosphate-fluoride treatment is very rough. If the film is removed with the same topography as it has on the metal, the distance between a plane touching points along the bottom of the film and a plane touching points along the top would be much larger than the actual film thickness. Aside from effects of roughness of an order much less than the wave length of the light used, ellipsometry does not suffer from this problem. Only light reflected from facets with the proper angle of incidence is accepted by the analyzer; light from all other facets of the rough surface are scattered away from the detector. It appears that the phosphate-fluoride films formed on Ti-6-4 by the Gillette researchers were quite different from ours. Their films were reported to be of the order of 3000 Å as compared to our 200-500, their films were crystalline - ours amorphous and their films contained fluorine - ours may not have.

It is believed that the differences may be due to the differences in phosphate-fluoride treatment used at Gillette as compared to that at the Science Center or to the oxide film removal process. Table I of Appendix B shows the step by step treatment at Gillette(13) and General Dynamics(41) to compare with our Table 2. Although each process is referred to as the phosphate-fluoride process, each has slightly different conditions. In a recent report(42) Alexander (at L.A. Div. of NR) points out the large effect slight differences in the detail steps can have. He used the Battelle formulation and found that 80°F gave a completely different film (with respect to SEM) as compared to that found at 185°F. He also found that the rinse time was critical as to the film formed and the bonding characteristics. Both the Gillette workers and Alexander found fluorine in their films, whereas we found that if F was present it was masked by an Fe peak. This effect may be similar to our not observing chromium on FPL etched aluminum. A 24 hr period in our vacuum system may have removed the fluorine.

b. Auger Spectroscopy

Figure 53 is an example of an Auger electron spectrogram for a Ti-6Al-4V sample. The spectrogram was performed after the phosphate-fluoride treatment but prior to ion sputtering. The surface elements present are the alloy elements (see Table 4) Ti, Al, V, Fe, C, N and O as well as surface contamination P, Ni, S, and Cu. If F is present it is masked by the Fe (650 eV)

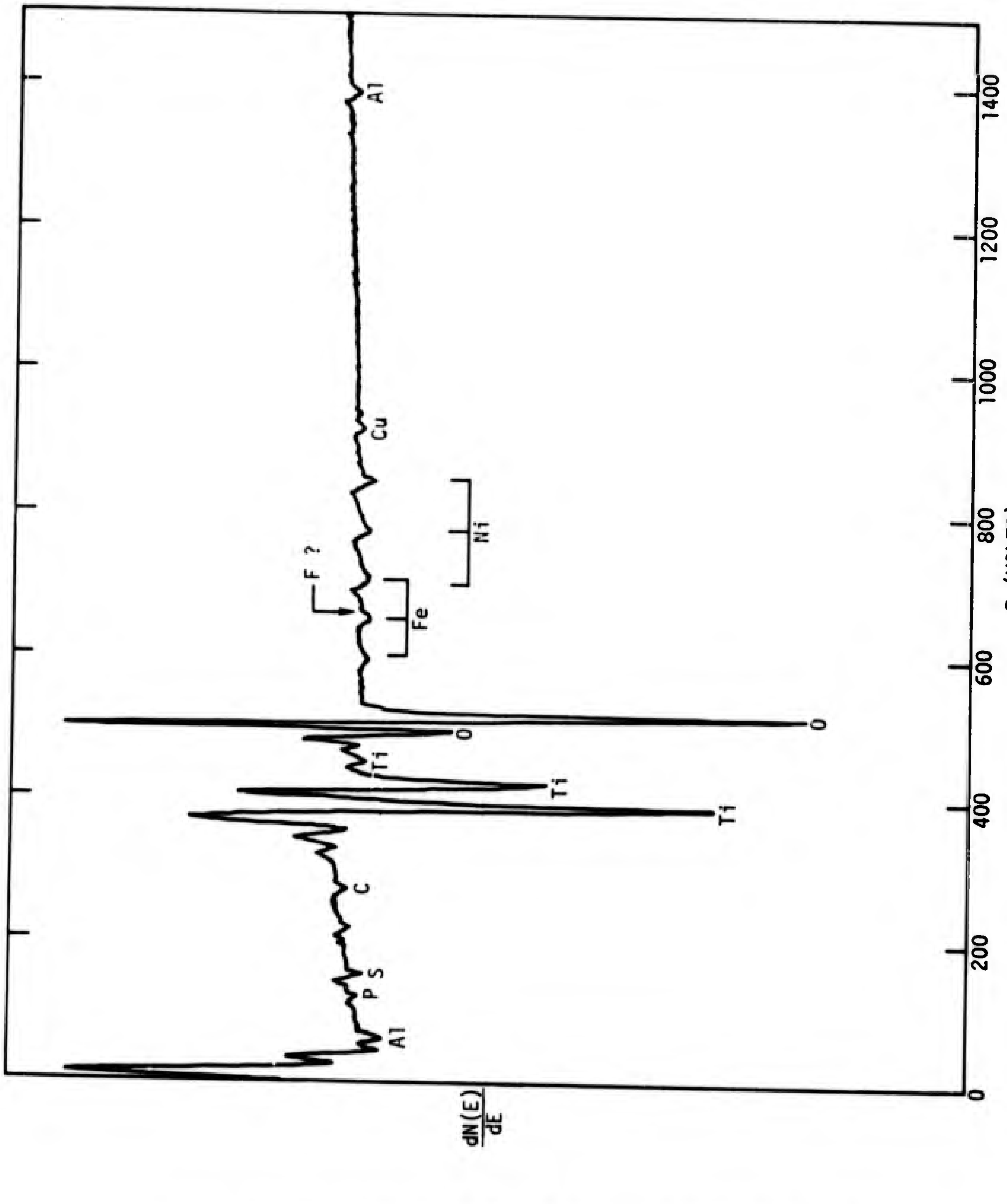

Fig. 53. AES for Ti-6Al-4V after the phosphate-fluoride treatment.

peak. Figure 54 shows the AES after 40 minutes of Ar ion sputtering. The surface contamination has been greatly reduced but of course the alloy elements are still present. The APPH values prior to ion bombardment for surfaces prepared by the phosphate-fluoride, nitric acid-fluoride and TURCO treatment are compared in Table 29.

c. Chemical Profiles

Figures 55, 56 and 57 are chemical profiles for films formed on Ti-6Al-4V by the phosphate-fluoride, the nitric acid-fluoride and TURCO surface treatments, respectively. An interesting feature of Figures 55, 56 and 57 and Table 29 is that the surface phosphate-fluoride treatment with the least surface contamination produced the strongest bonds. In Figure 57 for TURCO treated Ti-6Al-4V the oxygen APPH increases during the initial sputtering as the carbon contamination is removed. These chemical profiles give a qualitative analysis of the elements that are in the chemical films.

d. Surface Potential Difference

The SPD for three different surface treatments are recorded in Table 29. There seems to be no correlation between SPD and bond strength or any of the other surface parameters.

e. Microscopy

Figures 58 and 59 show SEM photographs at X1000 and X4000 for the phosphate-fluoride, TURCO, nitric acid-fluoride and PASA JELL surface treatment of Ti-6Al-4V. The surfaces that result from the nitric acid-fluoride and the PASA JELL treatment (Fig. 59) look very much alike and are very similar to SEM pictures reported by Lively(43) at LTV Aerospace Corp. and Rauch and Reddy(44) at American Cyanimide. The SEM photographs for the TURCO treatment are quite different than for the nitric acid-fluoride or PASA JELL treatment and are similar to pictures reported by Alexander[42] at the Los Angeles Division of Rockwell International.

The most controversial SEM results are for the phosphate-fluoride treatment. Alexander demonstrated that what was considered to be minor changes in the phosphate-fluoride procedure could cause dramatic changes in the surface morphology. Although for this report we used the NR phosphate-fluoride treatment (per ST0610LA0004, see Table 2) recommended by Alexander, our micrographs

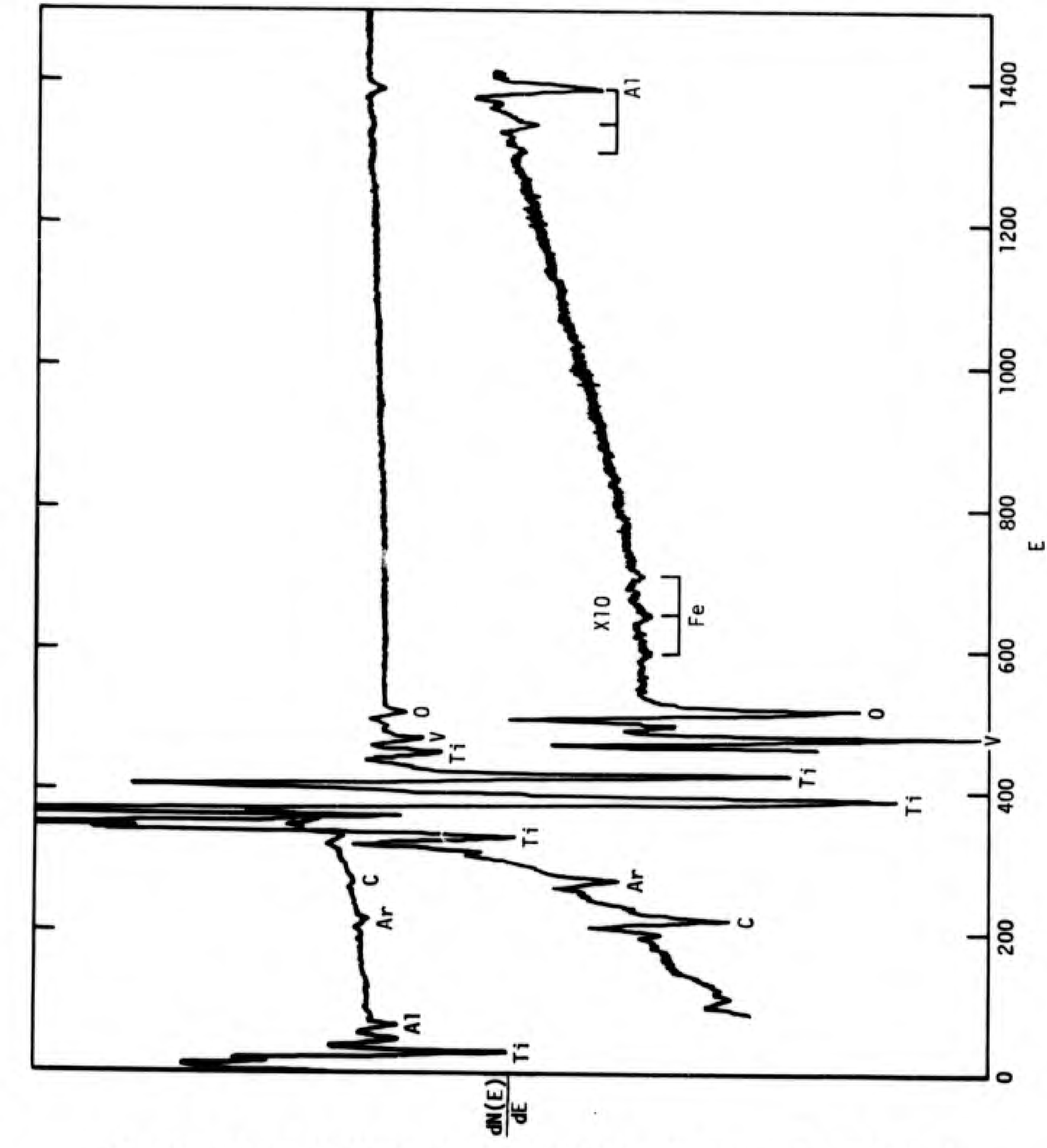

Fig. 54. AES for Ti-6Al-4V after phosphate-fluoride treatment and 40 minutes of Ar^+ bombardment.

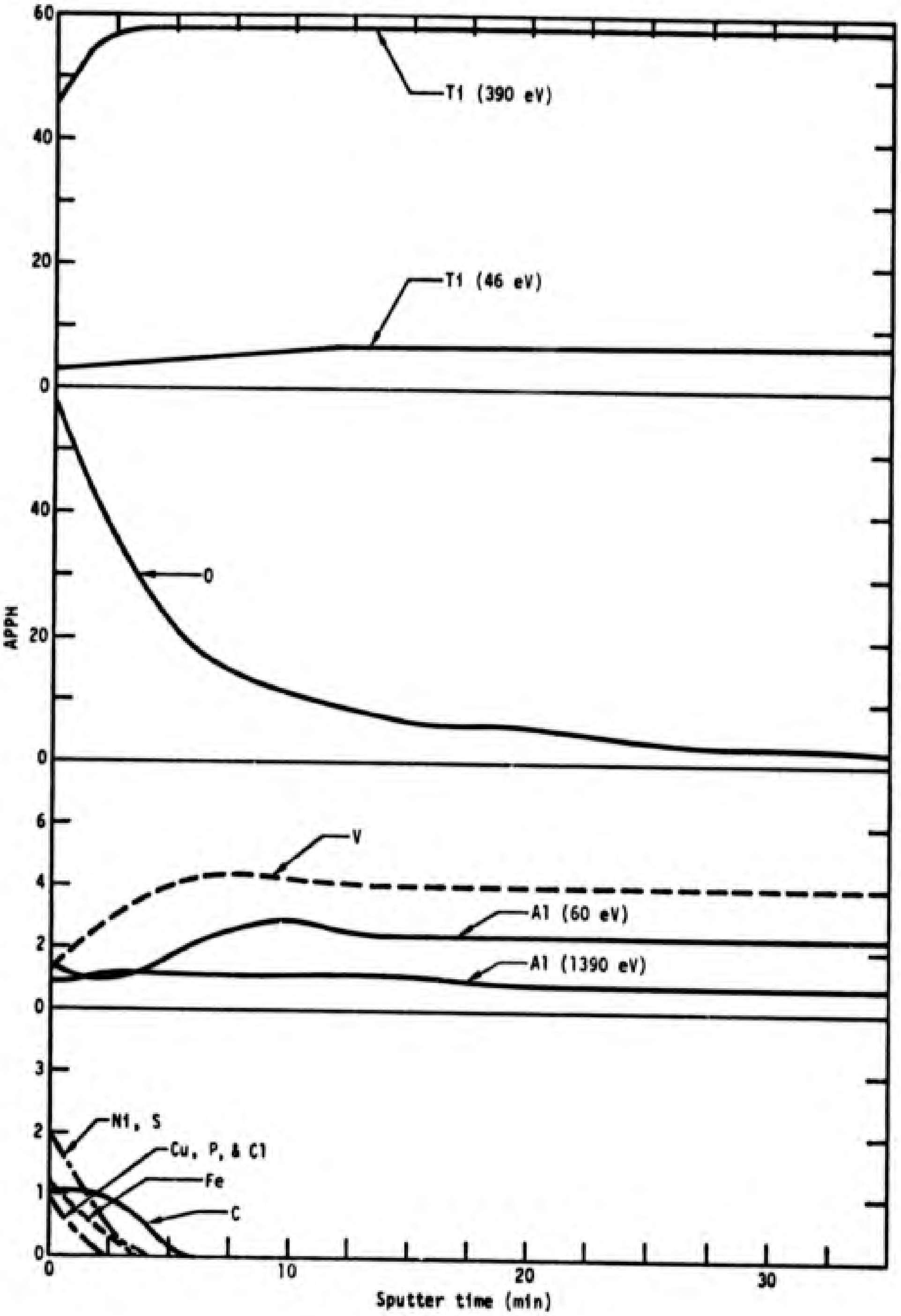

Fig. 55. Chemical profile of film on Ti-6Al-4V after the phosphate-fluoride treatment.

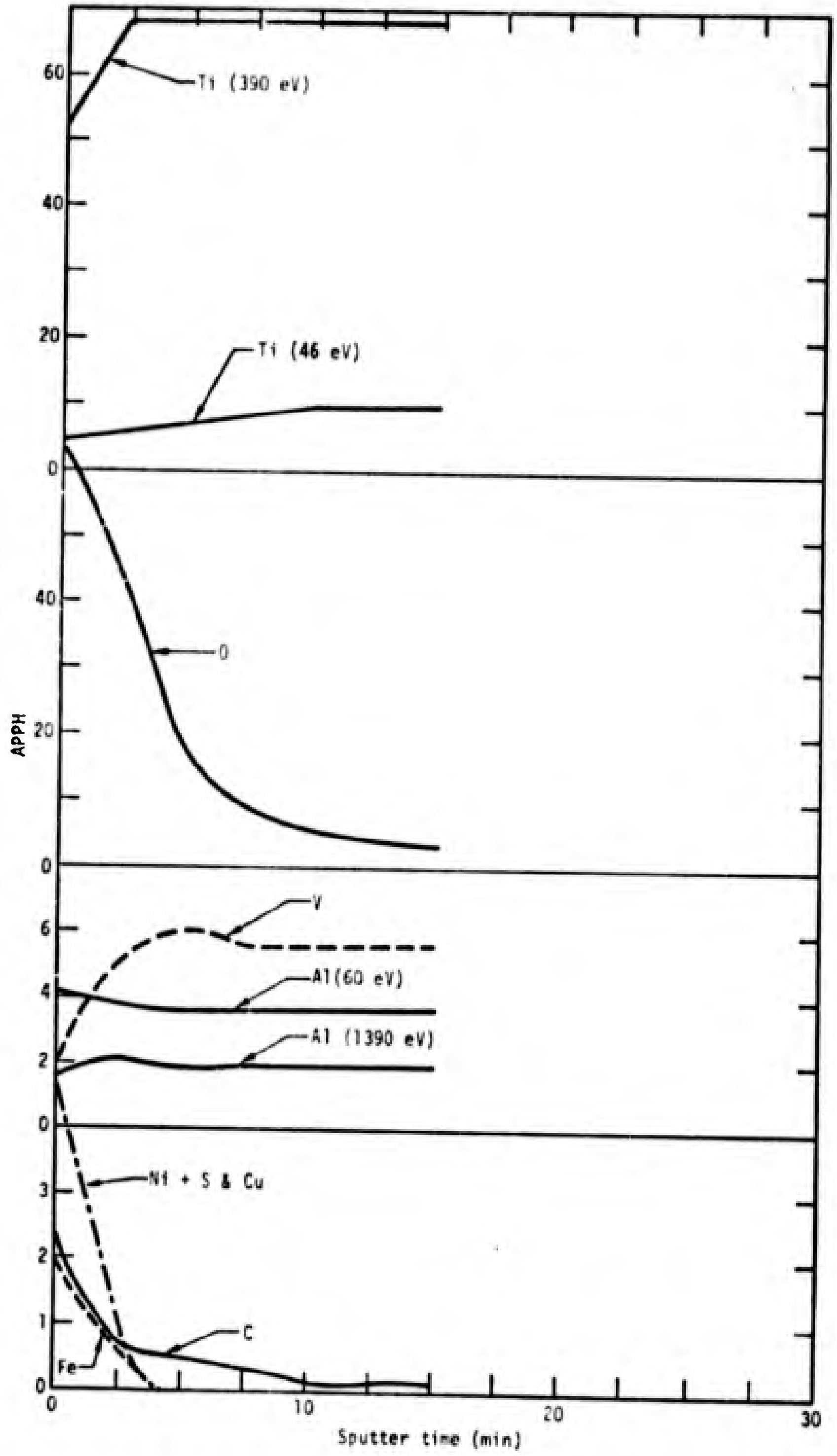

Fig. 56. Chemical profile of film on Ti-6Al-4V after the nitric acid-fluoride treatment.

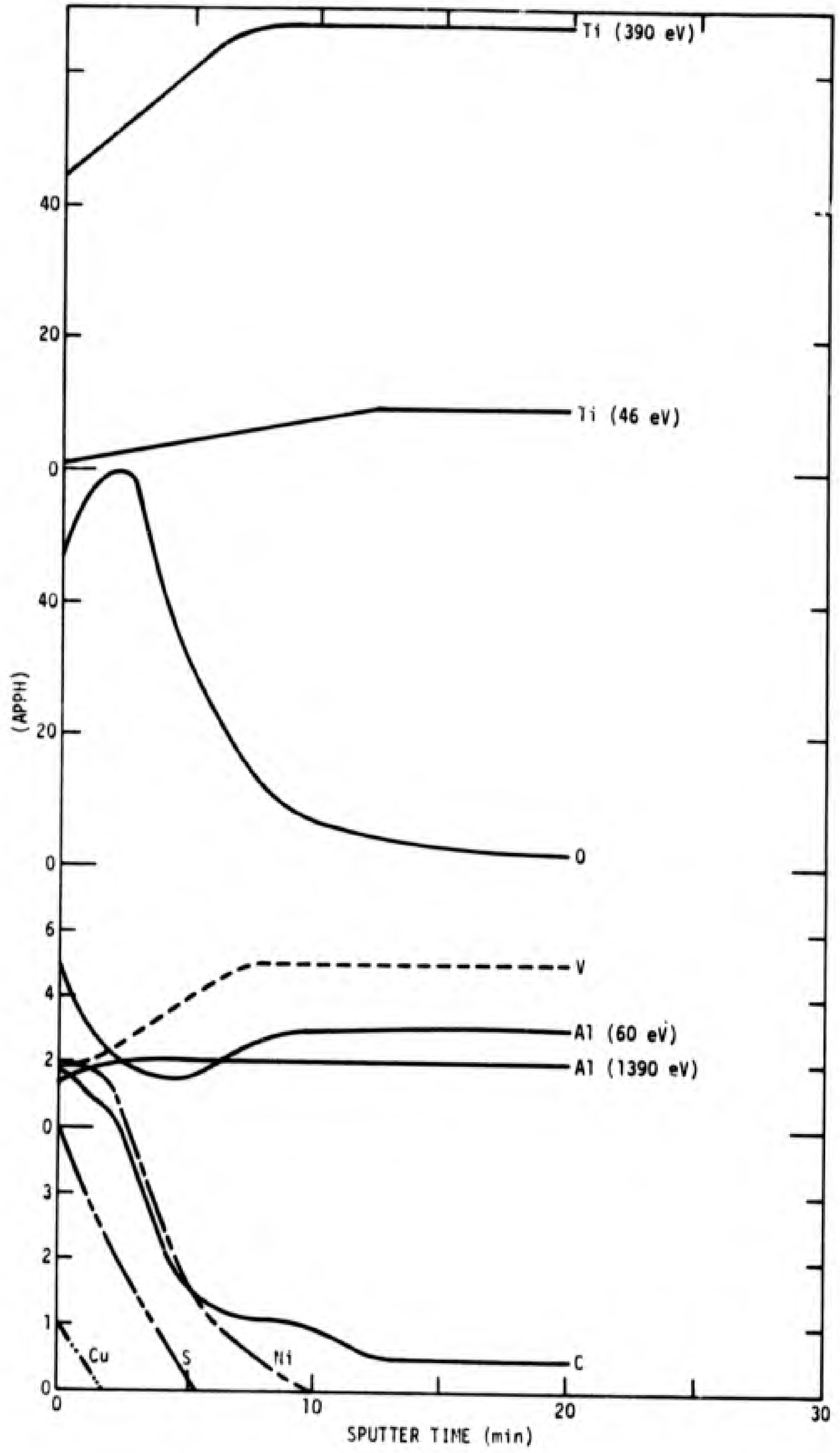

Fig. 57. Chemical profile on film on Ti-6Al-4V after the TURCO treatment.

TABLE 29

Surface Characterization of Ti-6Al-4V Samples and Bond Strength for Various Surface Preparations - Adhesive HT424

Surface Treatment	Ellipsometry			SPD	γ_{SV}	Auger Spectroscopy (APPH)											Bond Strength Psi (avg. of 9 bonds)
	Film Thickness (Å)	n_f	κ_f			Ti	Al	V	Cu	Ni	Fe	C	O	F	S	P	
Phosphate-Fluoride	200	2.84	0.1	0.38	66	47	1.5	1.5	1	2	1.2	1	58	?	2	1	3400 ± 300
TURCO	160	2.80	0.3	0.04	66	47	5	2	1	5	0	5	47	0	4	0	3100 ± 400
Nitric acid fluoride	100	2.8	0.0	0.34	66	52	4.2	2	4.8	4.8	2	2.3	65	0	4.8	0	2400 ± 300

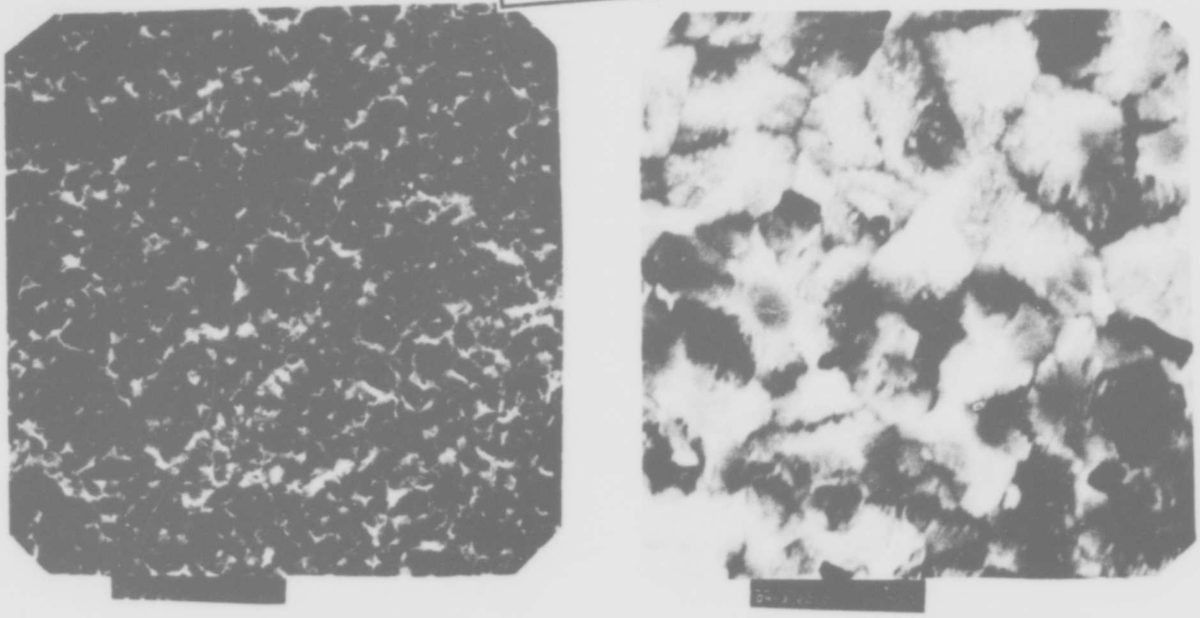

(a) 1000X Phosphate-fluoride Ti-6Al-4V (b) 4000X

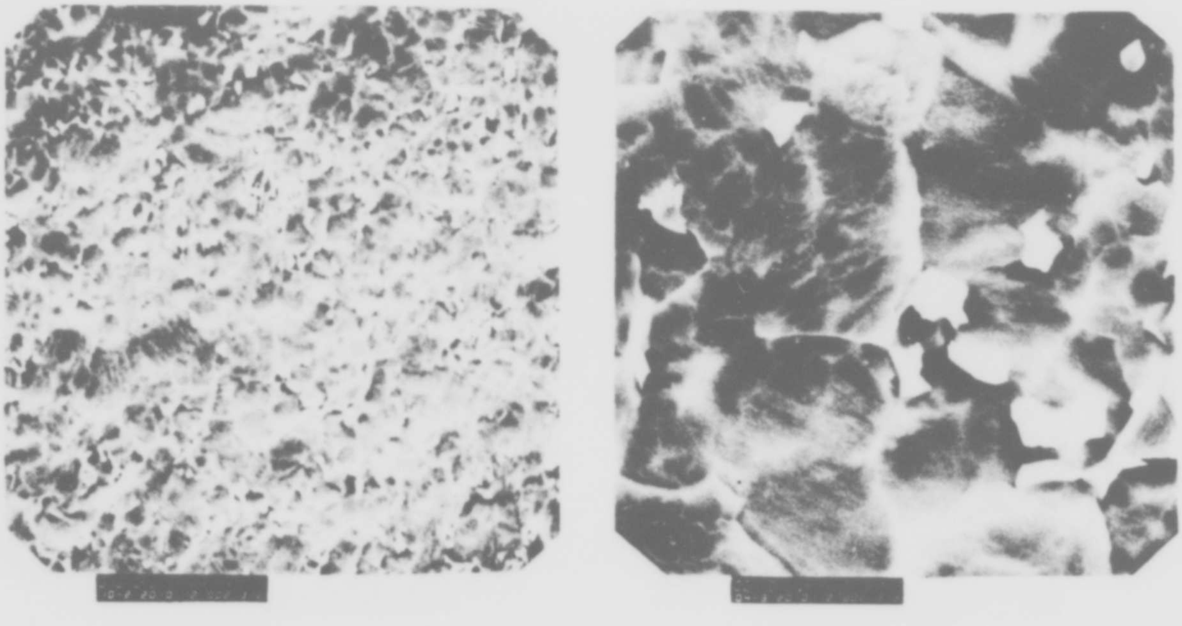

(c) 1000X Turco Ti-6Al-4V (d) 4000X

Fig. 58. SEM of a Ti-6Al-4V surface after the phosphate-fluoride (c and d) treatments.

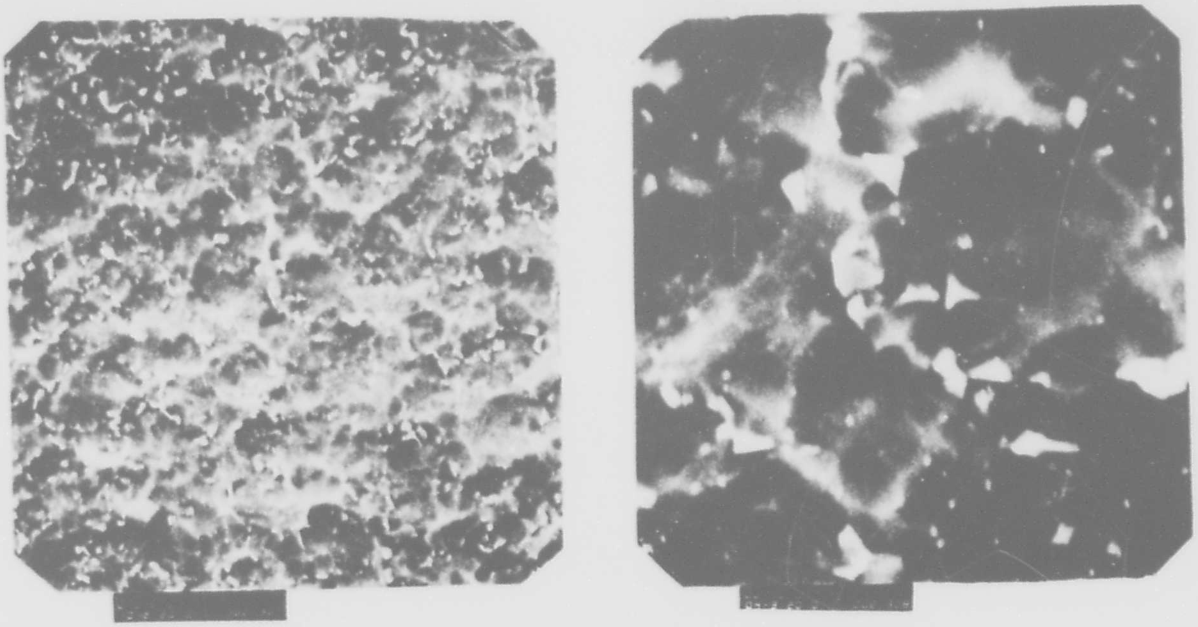

(a) 1000X Nitric acid-fluoride Ti-6Al-4V (b) 4000X

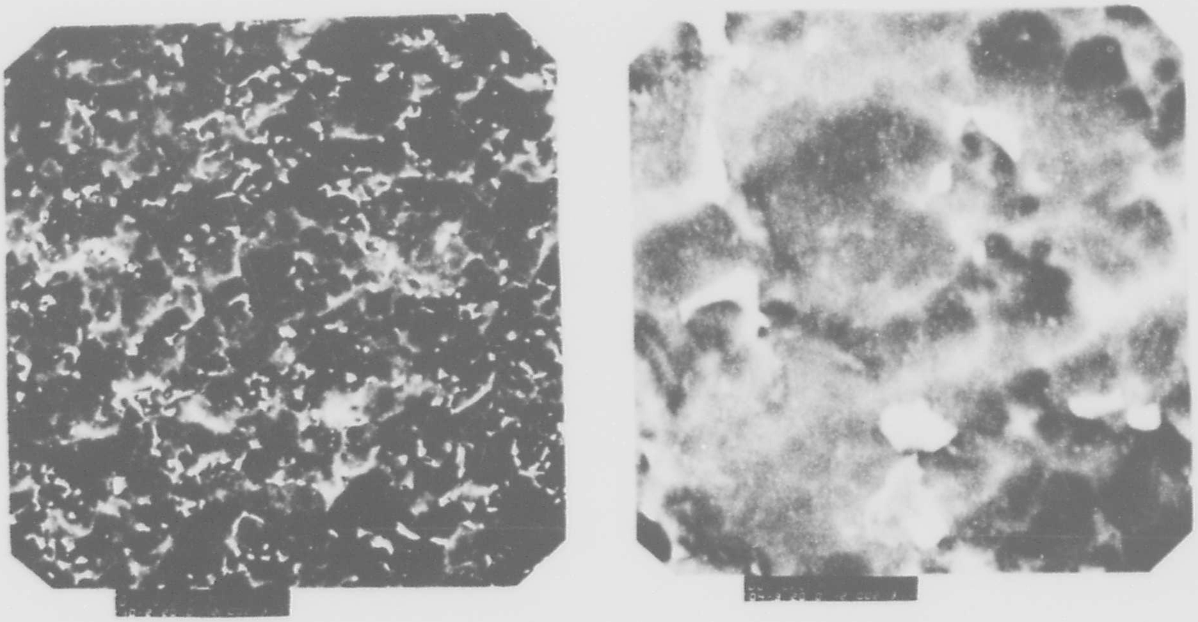

(c) 1000X Pasa Jell Ti-6Al-4V (d) 4000X

Fig. 59. SEM of a Ti-6Al-4V surface after the nitric acid (a and b) and PASA JELL (c and d) treatments.

do not look like those reported by him(42) for the same treatment. The SEM pictures for the phosphate-fluoride treatment in Fig. 58 look more like those reported by Alexander (ref. 42, Fig. 2) for the Battelle 185°F phosphate-fluoride treatment, but with less pronounced drystallite growth. There is some resemblance to the photographs reported by Hamilton and Lyerly(13) which show sharp grain boundaries but much less crystallite growth. A comparison of the details for the phosphate-fluoride treatment is given in Appendix B. It will be observed that slight differences in procedure do exist and may account for the differences in SEM results.

Microscopic examination of fractured bonds for Ti-6Al-4V and HT424 adhesive, reveals the natural porosity of the adhesive as was found in the Al study. Figure 60a shows photographs of two halfs of a fractured bond that failed cohesively. About 50% of the bond area is void although a layer of adhesive is attached to the metal over the entire bond area. Figure 60b shows photographs of two matching halfs of a bond that failed interfacially in the center portion and cohesively at the top and bottom. The natural porosity is noticeable in the areas that failed cohesively. The picture on the right of Fig. 60b shows the oxide-primer interface between the glass fiber net. The picture on the left shows the matching adhesive surface. Contrary to photographs of Al 2024-T3 - HT424 fracture surfaces, the bright areas are adhesive surface, the dull metal-oxide surface. Although the distinction is not easily determined from the photographs, there is no question when observing under the microscope which area is adhesive and which is metal.

The SEM photographs in Fig. 61 show fracture surfaces after a tensile test of a Ti-6Al-4V - HT424 lap shear joint. Figure 61a is a low magnification picture (X20) showing the top of the adhesive (left side), glass fibers and metal-oxide interface (central). Considerable adhesive or primer adheres to the oxide as seen in Figure 61b (X200). Figure 61c is a high magnification (X4000) of the oxide surface and Figure 61d is the mating adhesive surface which replicates the oxide. The oxide surface after bonding and fracture (Fig. 61c) is similar to that prior to bonding (Fig. 60b) except the surfaces in each grain appear more rounded. There does not appear to be any oxide particles adhering to the adhesive surface in Fig. 61d, indicating failure to be at the primer-oxide interface in this region.

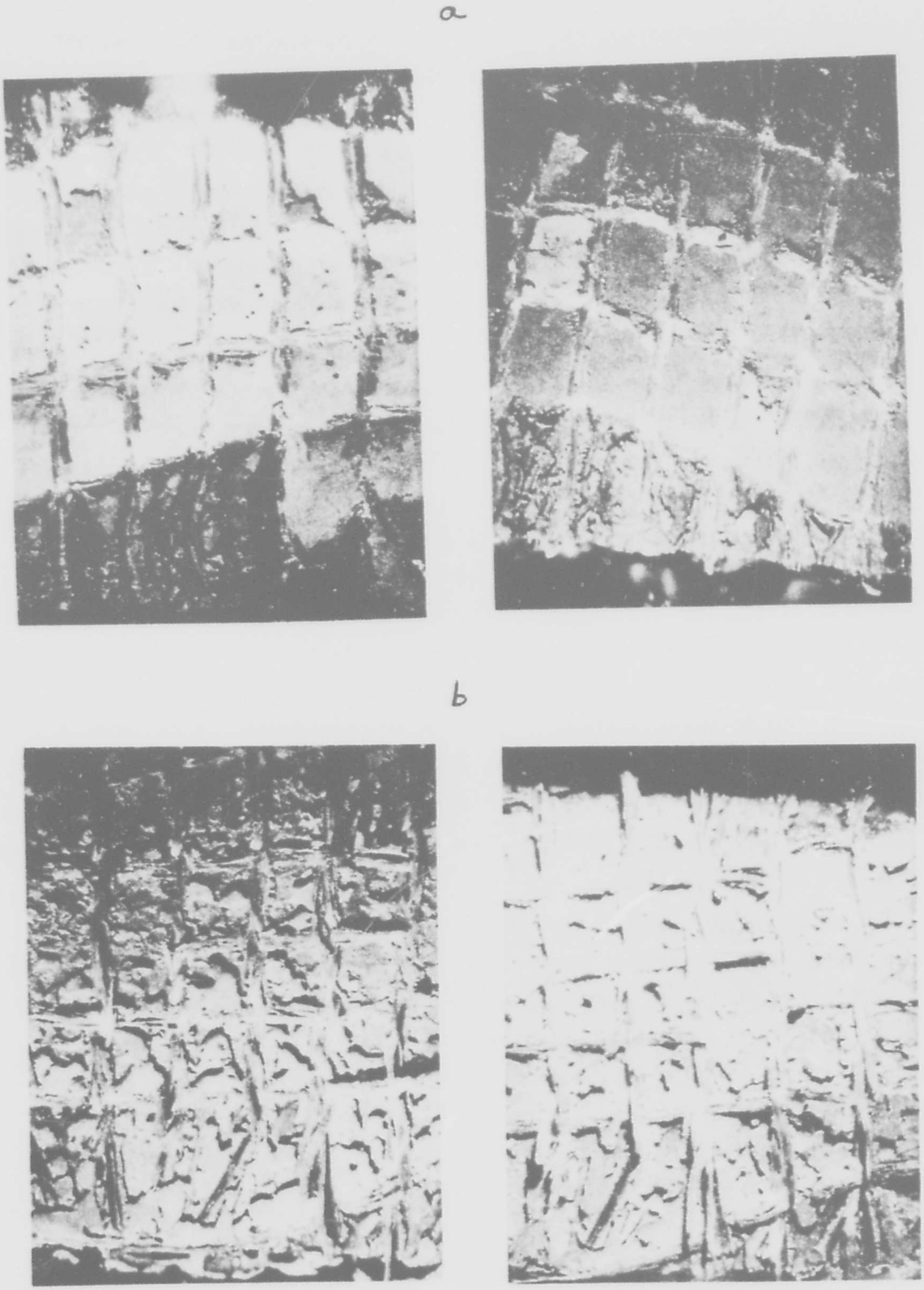

Fig. 60. Photographs of bond fracture areas for Ti-6Al-4V - HT424. a) cohesive failure, b) adhesive failure.

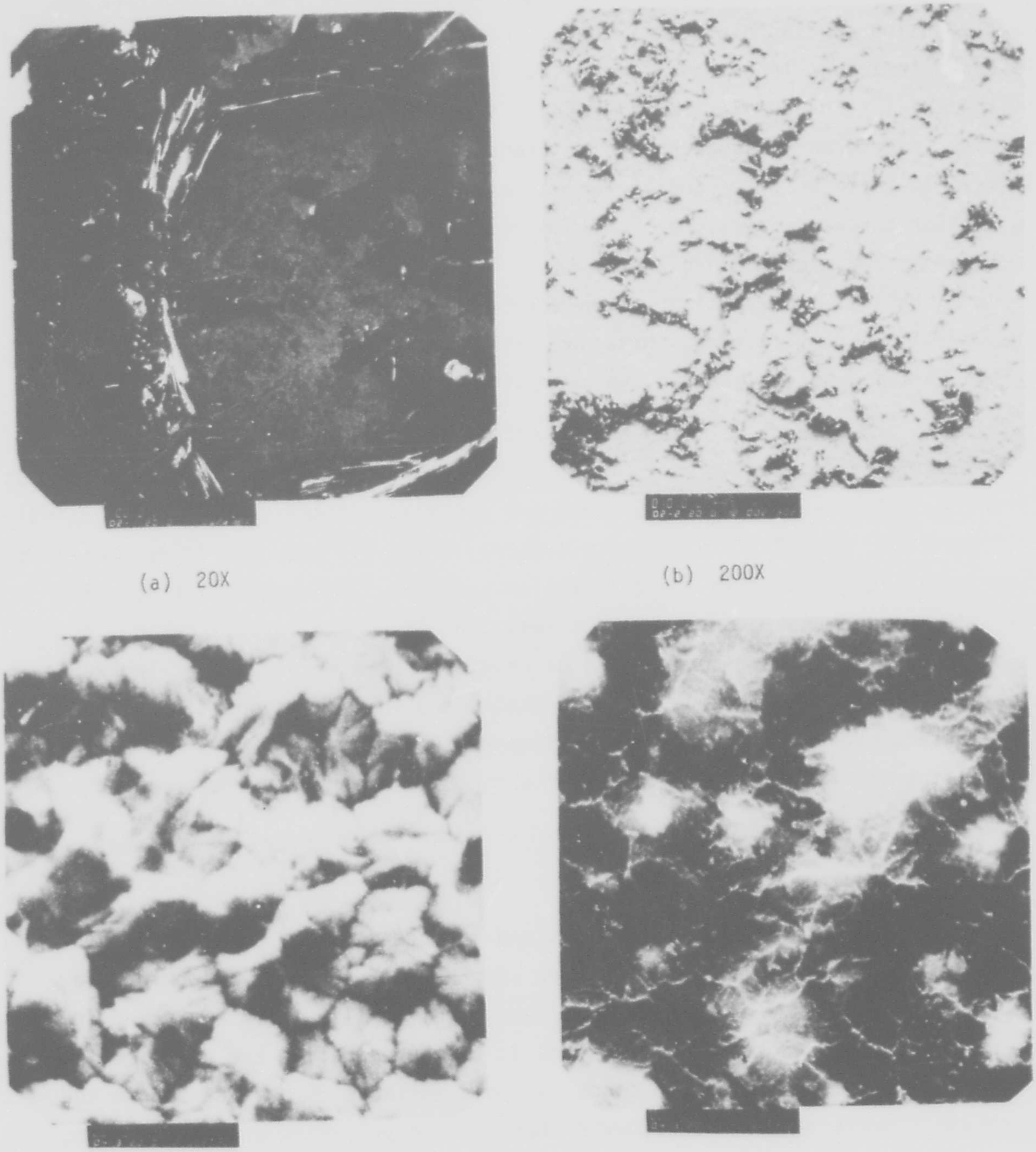

(a) 20X (b) 200X

(c) 4000X (d) 4000X

Fig. 61. SEM of Ti-6Al-4V surface after bonding with HT424 and fracture.

The film on a phosphate-fluoride treated sample of Ti-6Al-4V was removed using the technique described by Hamilton and Lyerly(13) in Gillette Research Institute Technical Report 4185. One segment of the film was examined in the Philips EM-300 electron microscope and another segment was examined with a Zeiss interference microscope. The transmission electron micrograph in Figure 62 reveals that the film roughly reproduces the underlying metal structure and is similar to that reported by Hamilton and Lyerly(13) (see their Fig. 8). There are regions 2-3 microns in diameter which likely are replications of primary alpha particles. In addition, there are many undulations in the film superimposed upon this structure; these undulations are apparently characteristic of the film and not related to the microstructure of the Ti-6-4.

A typical selected area electron diffraction pattern from the film is shown in Figure 63; the very diffuse rings indicate that the film is amorphous. In addition to the diffuse rings there are discrete reflections appearing faintly in Figure 63. Dark field electron microscopy (Fig. 64) show particles that give rise to the reflections in the diffraction pattern. The crystalline material (bright spots in Figure 64) represents less than 1% of the surface layer. A crystal pattern of the minute amount of crystalline material was not indexable as any form of titanium oxide and is probably due to impurity particles. Although Hamilton and Lyerly report that their removed phosphate-fluoride films were crystalline anatase, Lively(43) found theirs to be amorphous as we report here.

f. Contact Angles

Contact angle measurements and surface energy analysis were conducted on cast films of the BR-34 Primer and FM34B-32 Adhesive (Bloomingdale Div., American Cyanamide). Both primer and adhesive films were evaluated in the uncured and cured states. The steps in film preparation are detailed in Table 30. The film preparation steps outlined in Table 30 provide smooth and homogeneous surfaces of the polymeric phase of the polyimide adhesive bonding system for wettability study. Steps (4) and (5) of Table 30 utilize a dry N_2 blanket over the specimen in order to minimize hydrolytic or oxidative degradation at the film free surfaces. The results of wettability measurements and surface energy analysis are compiled in Table 31 through Table 33. The typical Zisman plots of cosine of liquid-solid contact angle cos θ versus liquid surface tensions γ_{LV} are graphed in the upper curves of Figure 65 through Figure 68.

Fig. 62. Transmission electron micrograph of phosphate-fluoride film from Ti-6Al-4V.

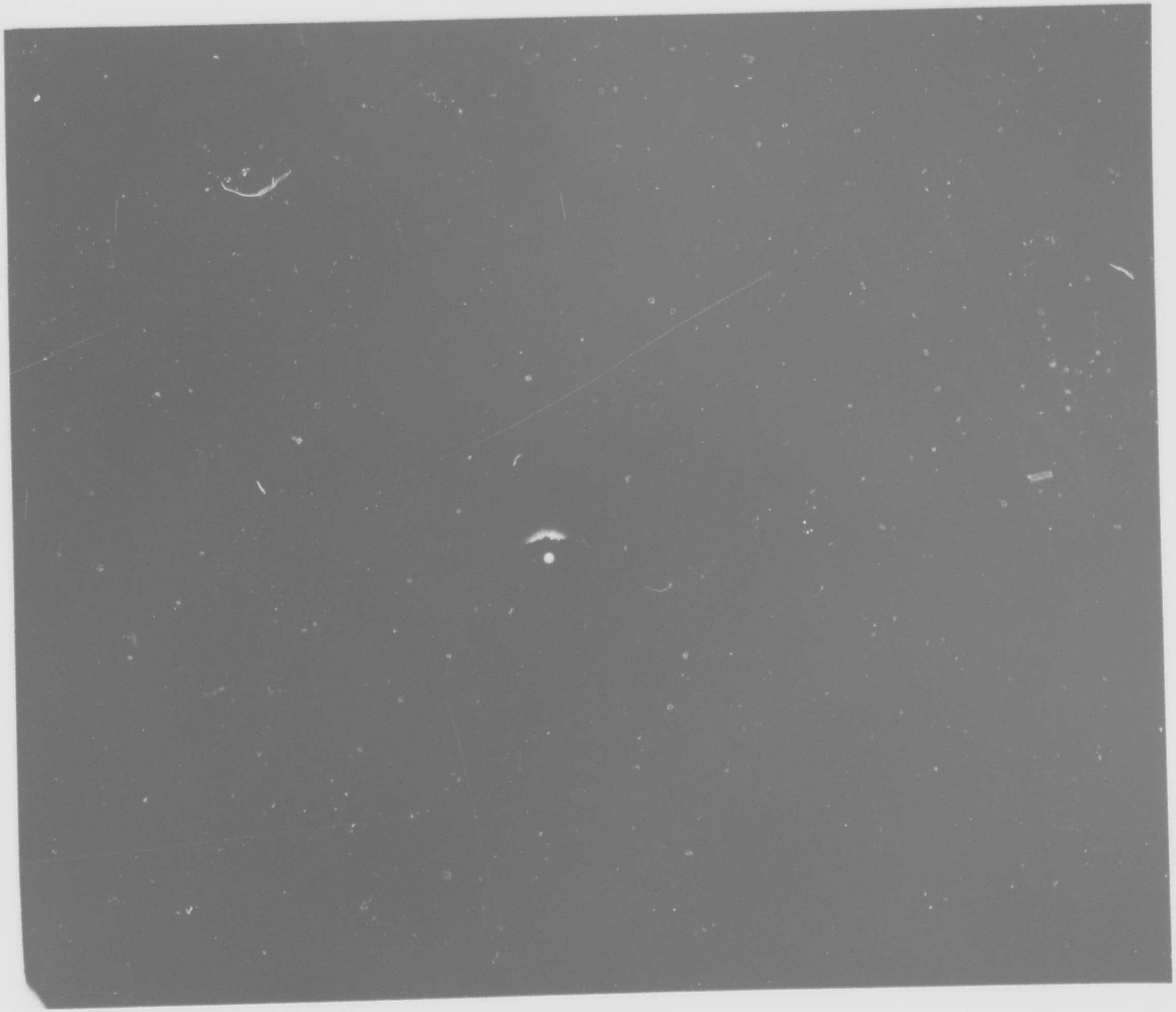

Fig. 63. Typical electron diffraction pattern of phosphate-fluoride film from Ti-6Al-4V.

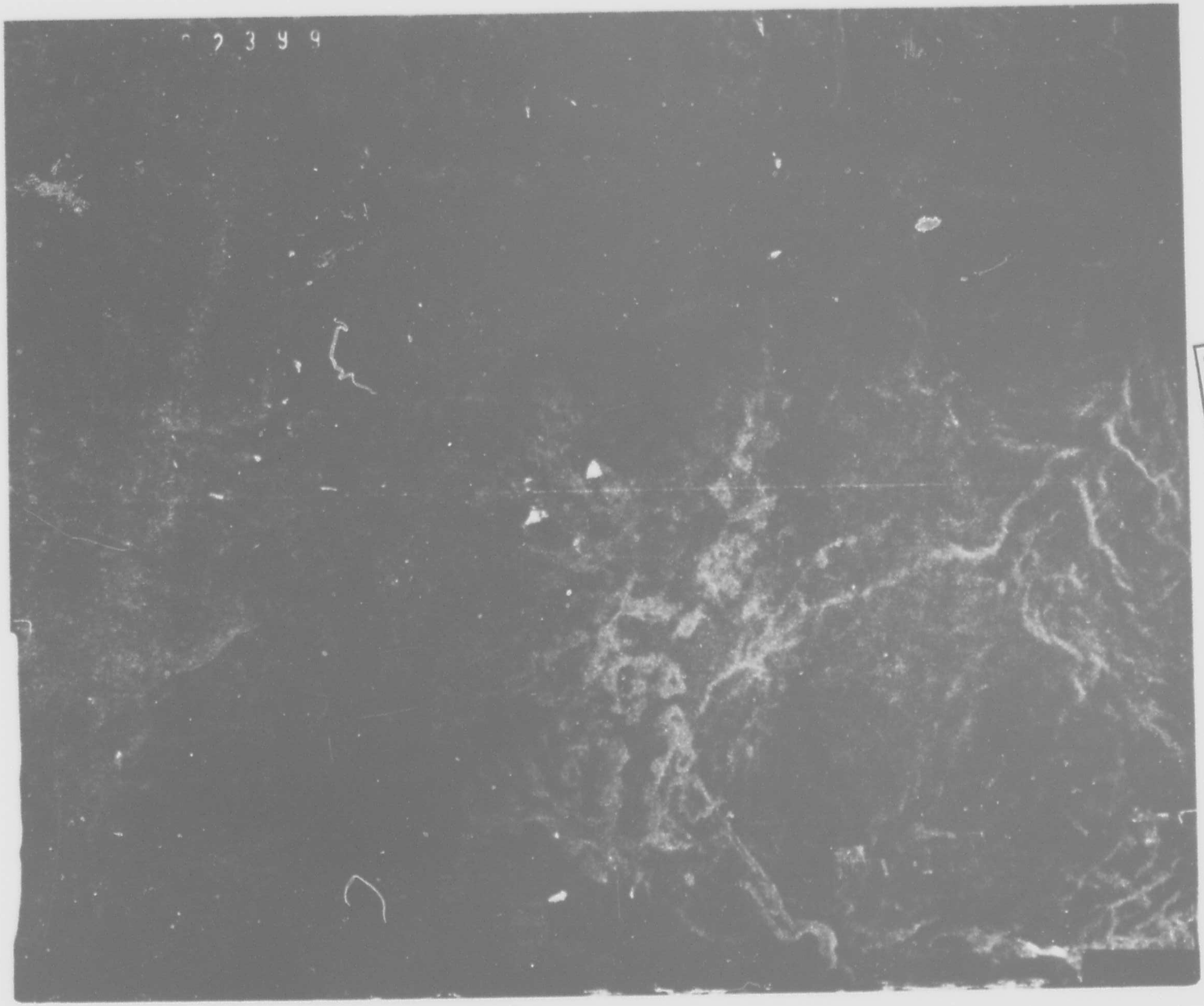

Fig. 64. Dark field electron micrograph of phosphate-fluoride film from Ti-6Al-4V.

TABLE 30: Film Preparation for Wettability Analysis

BR-34 Primer

1) 1 part primer diluted with 5 parts BR34-2 thinner.
2) Coated on glass slide by dipping.
3) 30 minute air dry.
4) 30 minute oven dry at 104°C in dry N_2 atmosphere.
5) 60 minute oven dry at 210°C in dry N_2 atmosphere.
6) Uncured samples given 20 hour air dry and 5 hour vacuum dry.

FM 34B-32 Adhesive

1) Film dissolved in MEK.
2) Coated on glass slides.
3) Given 2 hour vacuum dry.
4) Cured for 90 minutes at 550°F in dry N_2 atmosphere.
5) Uncured samples given only the vacuum dry.

TABLE 31: Cosine of Liquid-Solid Contact Angle of Test Liquids on Uncured and Cured Films of BR-34 Primer and FM 34-B32 Adhesive

Test Liquid	γ_{LV} (dyn/cm)	BR-34 Primer (1)uncured $\cos\theta$	BR-34 Primer (2)cured $\cos\theta$	FM 34B-32 Adhesive (3)uncured $\cos\theta$	FM 34B-32 Adhesive (4)cured $\cos\theta$
water	72.8	-.0523	0.000	.707	.574
glycerol	64.0	.485	.438	.588	.629
ethylene glycol	48.3	.829	.616	.819	.755
1-br.-napthalene	44.6	.956	.951	.985	.998
PG-E-200	43.5	.891	.799	.927	.982
tricresyl phosphate	40.9	.961	.934	.990	.990
hexadecane	27.6	----	.9994	.999	.999

TABLE 32: Analysis of Liquid-Solid Interactions

γ_L (dyn/cm)	$2\alpha_L$ $(\mathrm{dyn/cm})^{\frac{1}{2}}$	β_L/α_L	(1)	(2)	(3)	(4)
			$W_a/2\alpha_L$ $(\mathrm{dyn/cm})^{\frac{1}{2}}$			
72.8	9.34	1.53	7.39	7.79	13.31	12.27
64.0	11.66	.94	8.15	7.90	8.72	8.94
48.3	10.83	.81	8.16	7.21	8.11	7.83
44.6	13.36	0.0	6.53	6.51	6.63	6.67
43.5	10.62	0.74	7.75	7.37	7.89	8.12
40.9	12.52	.21	6.41	6.32	6.50	6.50
27.6	10.51	0.0	----	5.25	5.25	5.25

TABLE 33: Calculated Solid-Vapor Surface Tension Properties by the Determinant Method

	$\gamma_{SV}^{d} \pm \delta^{d}$	$\gamma_{SV}^{p} \pm \delta^{p}$	$\gamma_{SV} \pm \delta$
BR-34 Primer			
1) uncured	49.7 ± 5.8	3.1 ± 0.8	52.8 ± 5.4
2) cured	38.6 ± 2.6	2.8 ± 0.7	41.4 ± 2.1
FM 34B-32 Adhesive			
3) uncured	29.1 ± 3.6	20.4 ± 4.8	49.5 ± 2.1
4) cured	30.9 ± 2.9	15.2 ± 2.7	46.1 ± 1.2

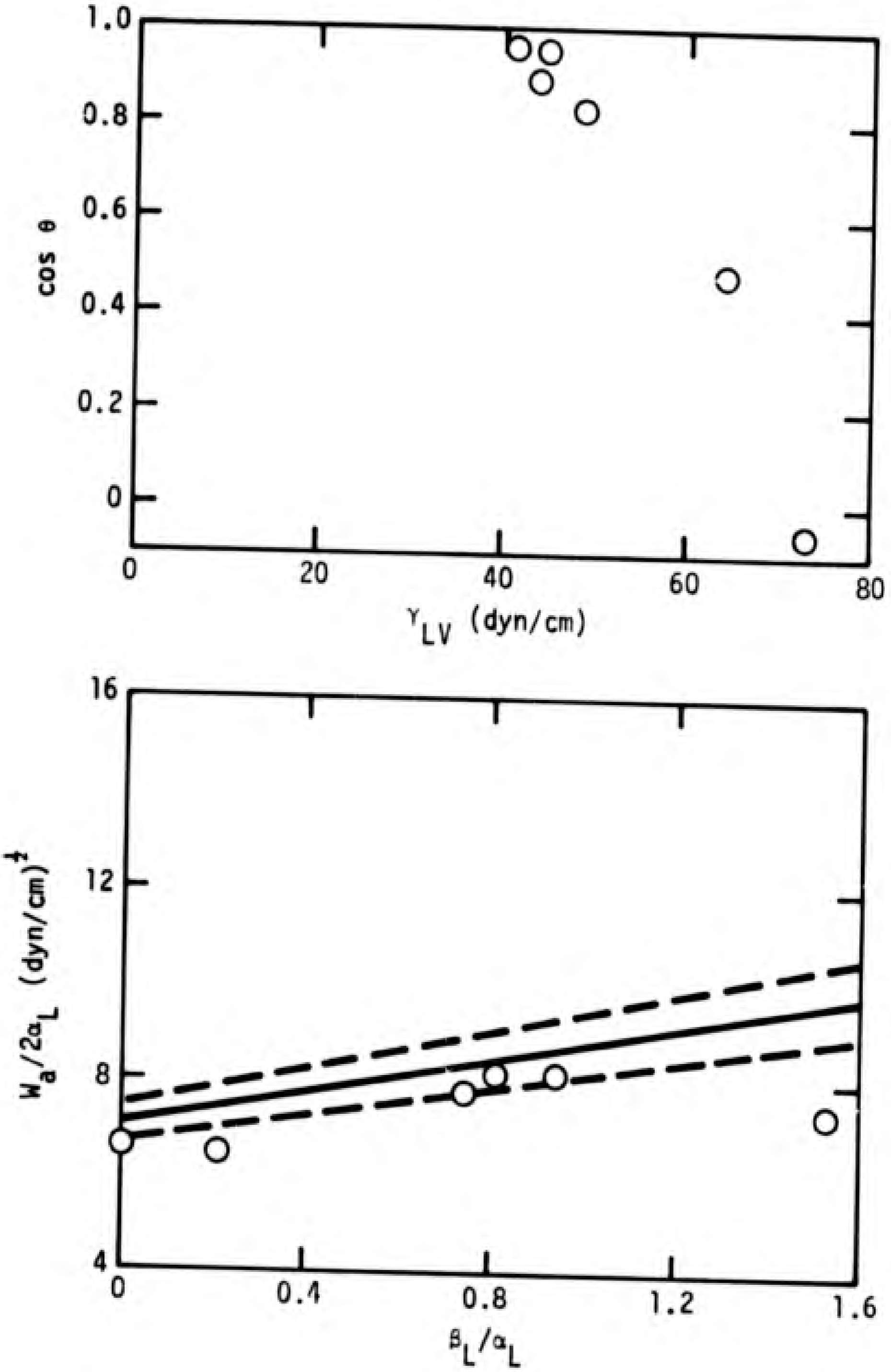

Fig. 65. Graphical presentation of wettability data for uncured BR-34 primer.

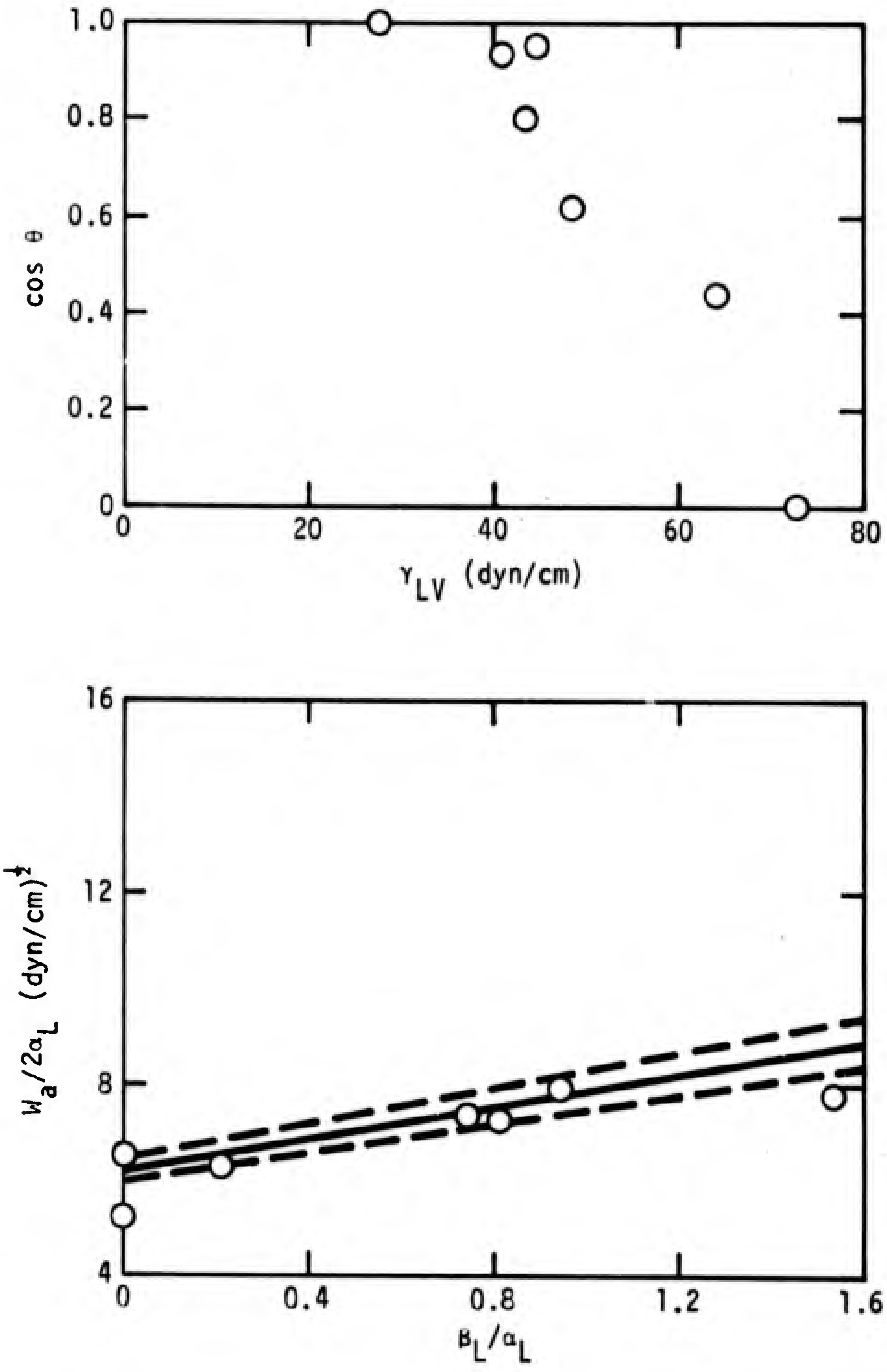

Fig. 66. Wettability data for cured BR-34 primer.

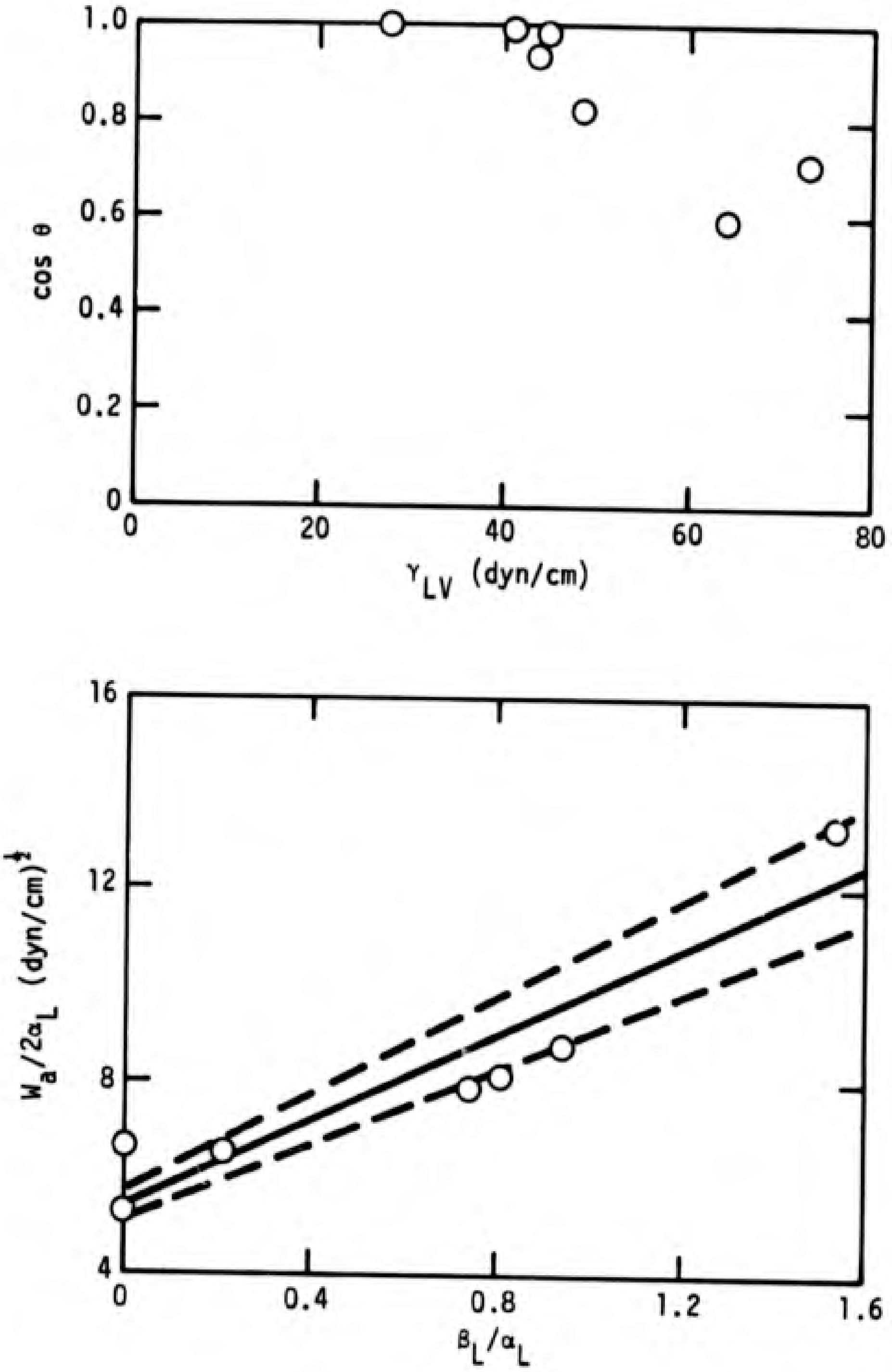

Fig. 67. Wettability data for uncured FM34B-32 adhesive.

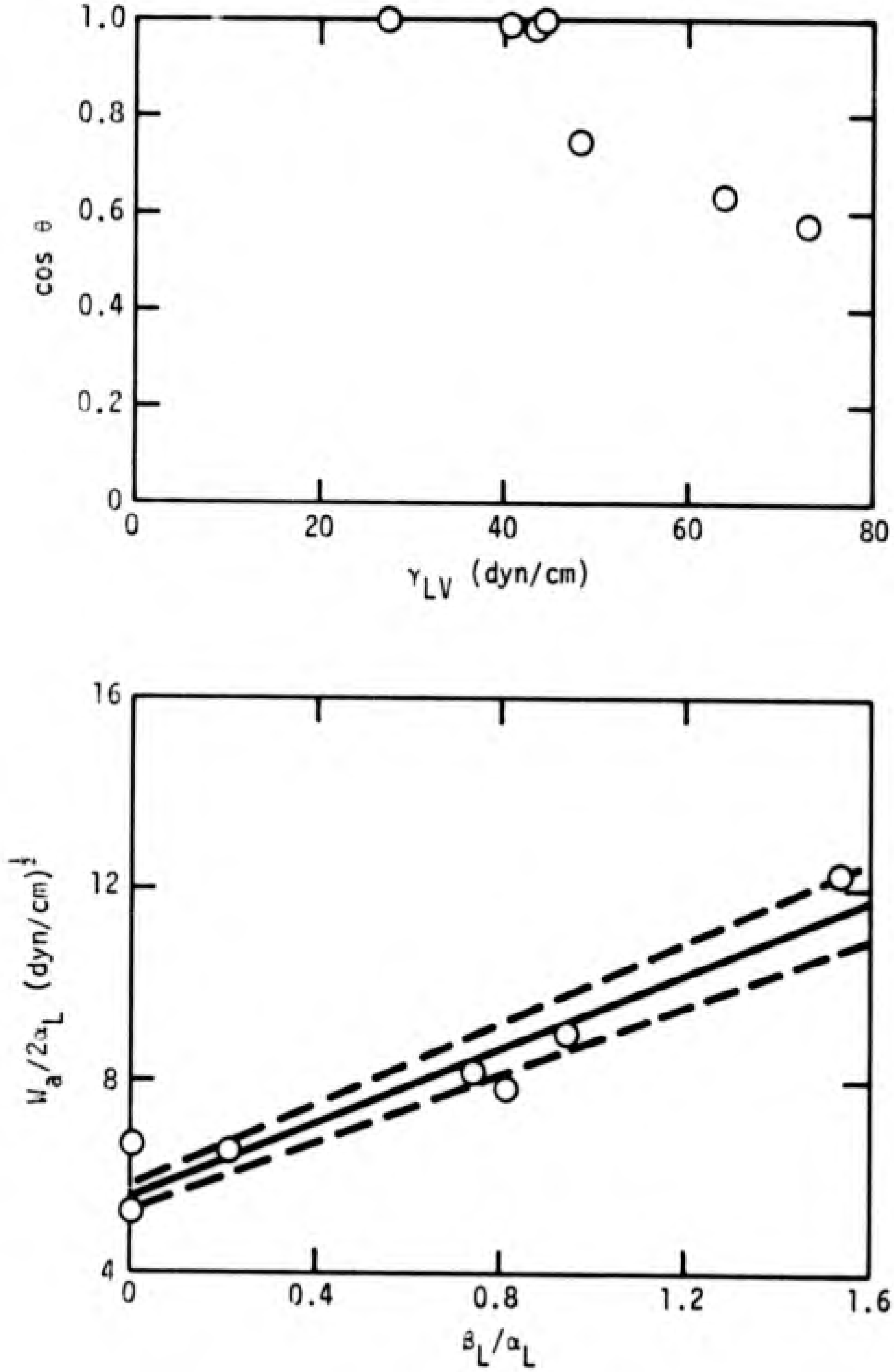

Fig. 68. Wettability data for cured FM34B-32 adhesive.

The lower curves of Figure 65 through Figure 68 present the data in the format defined by Eq. 9 of Section II.B.6. The summary of solid surface tension properties presented in Table 33 shows that adhesive primer BR-34 displays significantly higher values γ_{SV}^{d} and lower values of γ_{SV}^{p} than the FM34B-32 adhesive in both the uncured and cured state. These results would imply that the BR-34 primer and FM34B-32 display differences in surface chemistry and also that the interface between primer and adhesive will display non-optimum interfacial bonding. The wettability envelopes for BR-34 primer are shown in Figure 69.

Wettability studies for Ti-6Al-4V alloy were initiated using the surface treatments recommended by the adhesive manufacturer for the FM34B-32 adhesive system. Table 2 outlines the detailed steps for the metal surface treatments utilized in these experiments.

The predictions from Figure 69, is that poor bonding will result between the BR-34 primer and the FM34B-32 adhesive. Figure 70 shows the wettability envelope for freshly prepared nitric acid-fluoride which is essentially identical to the phosphate-floride treated surfaces of Ti-6Al-4V. The prediction is poor bonding between BR-34 primer and either of the treated surfaces.

In order to test the predictions developed by the wettability envelope analysis of Figures 69 and 70 a series of lap shear joints were prepared and tested, as indicated in Table 34. These single lap shear bonds all showed low bond strength and dominant interfacial failure as preducted from the wettability envelope analysis. The lower set in Table 34 shows that low bond strength also result when no primer is used.

To test whether extraneous stresses imposed by differential thermal expansion during cure, influence bond strength, a Ti-6Al-4V bonding jig was constructed to replace the Al jig and applied in bonding studies for lap shear strength of Ti-6Al-4V adherends primed with BR34B-32 primer and bonded with FM34B-32 adhesive. In this experiment three sets of six adhesive joints were prepared using a different metal surface treatment for each set of six bonds. The results of these experiments are summarized in Table 35.

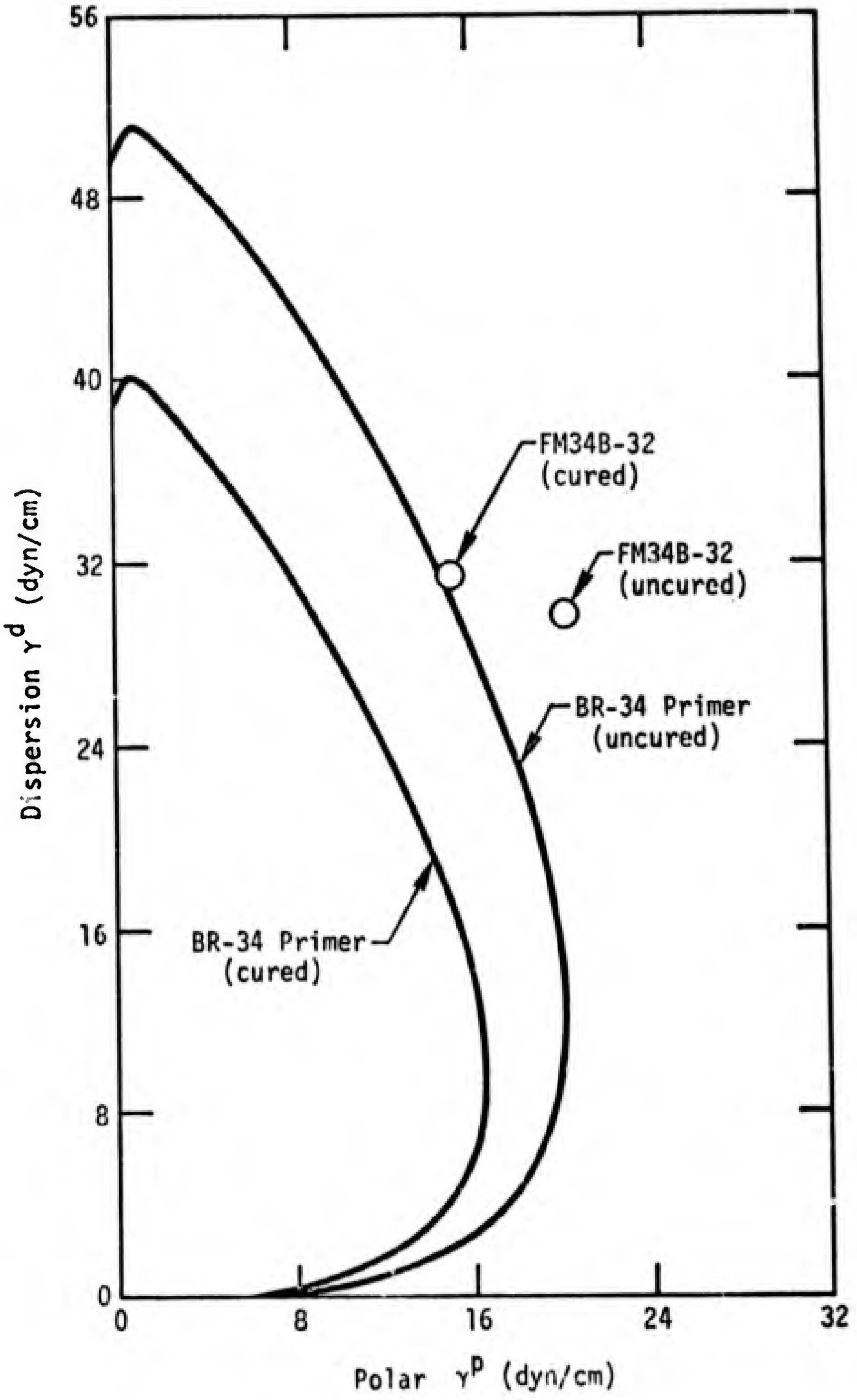

Fig. 69. Wettability envelopes for uncured and cured BR-34 primer.

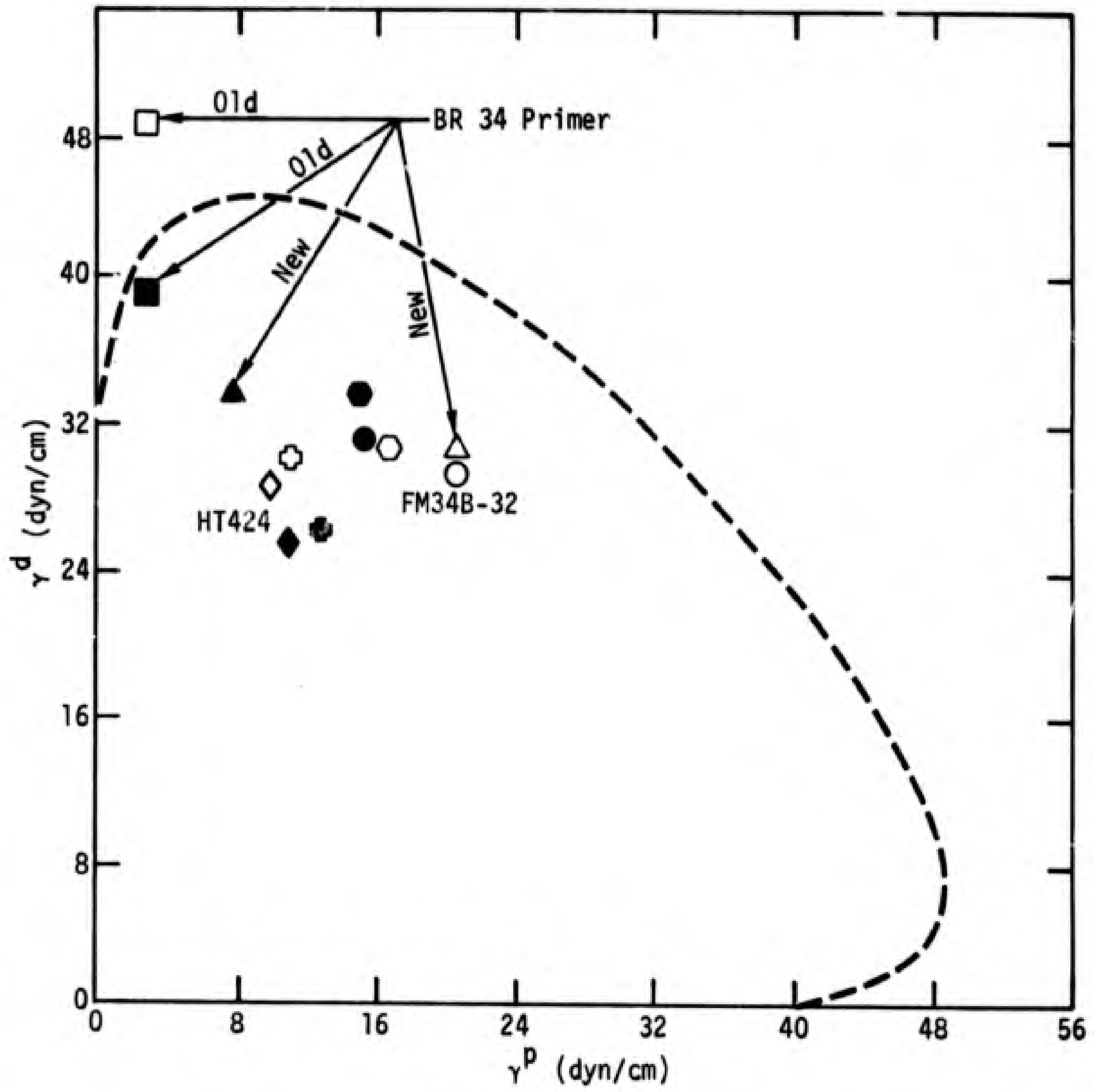

Fig. 70. Wettability envelopes for Nitric Acid-fluoride and Phosphate-fluoride Treatment of Ti-6Al-4V.

BR-34 Primer	Old	Uncured	□
		Cured	■
	New	Uncured	△
		Cured	▲
FM34B-32	Old	Uncured	○
		Cured	●
	New	Uncured	⬡
		Cured	⬢
HT424		Uncured	◇
		Cured	◆
HT424 Primer		Uncured	✥
		Cured	✚

TABLE 34: Results of Preliminary Study of Lap Shear Tests

metal = Ti-6Al-4V
primer = Br-34 (American Cyanimid)
adhesive = FM-34B-32 " "

Bond #	Surface Treatment	σ_b Bond Strength	average σ_b	type of failure
1	1) Alkaline cleaned 2) Br-34 Primered (Primer tended to bead up)	1052 psi	872 ± 211 psi	~ 95% interfacial
2		728		
3		604		
4		908		
5		652		
6		1288		
1	1) Alkaline cleaned 2) HNO_3-HF etched 3) Br-34 Primered (primer tended to bead up)	870	970 ± 100	~ 95% interfacial
2		1070		
3		broke in jig		
4		↓		
5				
6				
1	1) Alkaline cleaned 2) HNO_3-HF etched 3) PASA Jell 107 treated 4) No primer	930	807 ± 231	~ 50% interfacial
2		1030		
3		460		
4		broke in jig		

TABLE 35: Summary of Simple Lap Shear Bond Tests of BR-34B-32 Primer/FM-34B-32 Adhesive to Surface Treated Ti-6Al-4V Adherends Using a Ti-6Al-4V Bonding Jig and Tested at 23 ± 1°C and 50 ± 5% R.H.

1) PASA-JELL Treatment

Bond No.	σ_b (psi)	ave. σ_b	ave. dev.	Type of Failure
1	1220	1420	± 557	~ 50-100% at primer-metal interface
2	1300			
3	1970			
4	2000			
5	70			
6	1960			

2) TURCO Titanium Treatment

Bond No.	σ_b (psi)	ave. σ_b (psi)	ave. dev. (psi)	Type of Failure
1	840	1278	± 419	100% at primer-metal interface
2	460			
3	2020			
4	1540			
5	1300			
6	1510			

3) Phosphate-Fluoride Treatment

Bond No.	σ_b (psi)	ave. σ_b (psi)	ave. dev. (psi)	Type of Failure
1	1960	1965	± 92	~ 75% at primer-metal interface
2	1970			
3	1760			
4	2200			
5	1900			
6	2000			

The low values of lap shear strength reported in Table 35 for several standard surface treatments for Ti-6Al-4V using the Ti-6Al-4V alignment jig tend to reinforce the conclusion that poor wetting between BR34B-32 primer and adhesive or primer and Ti-6Al-4V described by the wettability envelopes of Figures 69 and 70 is the primary cause of low joint strength.

Experimental observations show that the BR34-32 thinner supplied by American Cyanamide-Bloomingdale Division for use with BR34B-32 primer produced an autophobic reaction to surface treated Ti-6Al-4V adherends. This phenomena is characterized by initial wetting and spreading, followed by spontaneous retraction of the liquid film to form drops of finite liquid-solid contact angles. BR34-32 thinner shows autophobic effect with contact angle going from $\theta = 0$ degree to $\theta = 12$ degrees in 10 to 20 seconds after contact with phosphate-fluoride etched Ti-6Al-4V as monitored in the NRL goniometer at 23 ± 1°C. Figure 71a shows the riverlet pattern produced on HNO_3/HF etched Ti-6Al-4V by the dried film of BR34B-32 primer as a consequence of the autophobic wetting effect which leaves an uneven distribution of primer on the metal surface. Figure 71b shows the two fracture surfaces from the lap shear joint prepared from these incompletely primed surfaces in which substantial failure is evidenced at the primer-adhesive interface as predicted by the wettability study. It was conconcluded that the BR-34B-32 primer was from a bad lot and a new supply of primer and adhesive were purchased. Figure 72 shows the wettability envelopes for the new BR34B-32 primer. The wettability parameters for the FM34B-32 adhesive falls within the envelope for the uncured primer. Figure 70 shows that the parameters for the new adhesive and primer fell within the envelopes for the metal surface. It is predicted that strong bonds will result between the new primer, adhesive and Ti-6Al-4V adherends.

The bond strengths for five lap shear joints with the new adhesive and primer are reported in Table 36. The bond strength values fall within the range reported by the manufacturer for this system and correlate well within the average value of 3121 psi reported by Lively[43]. The primer did not bead up and form a riverlet pattern as in Figure 71a. It is concluded that the first batch of primer was bad and that the wellability analysis revealed the fault.

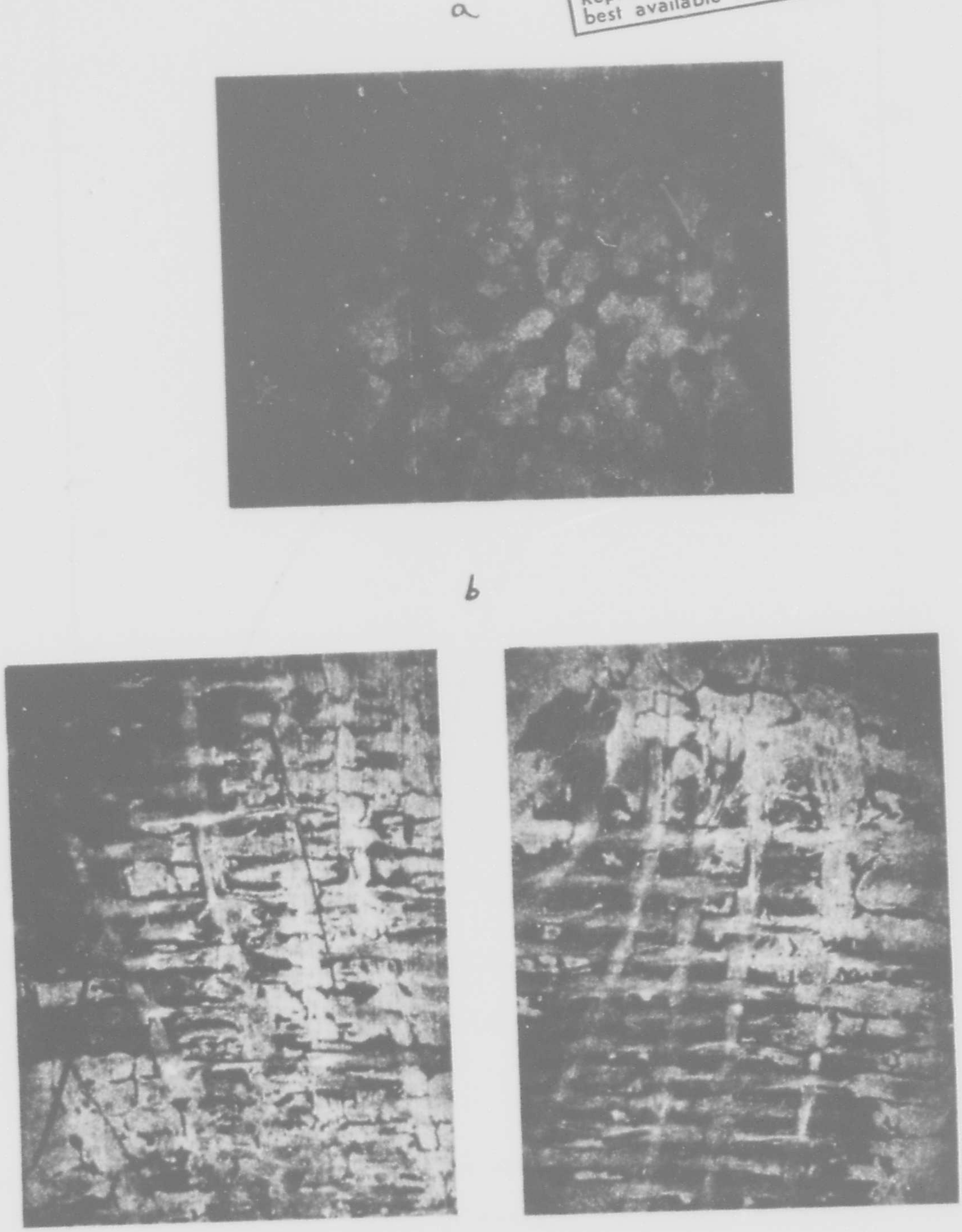

Fig. 71. (a) Riverlet pattern of FM34B-32 primer on HNO_3/HF etched Ti-6Al-4V due to autophobic wetting-dewetting.

(b) Fracture surfaces of FM34B-32 primed Ti-6Al-4V bonded to FM34B-32 adhesive showing failure at the primer-adhesive interface.

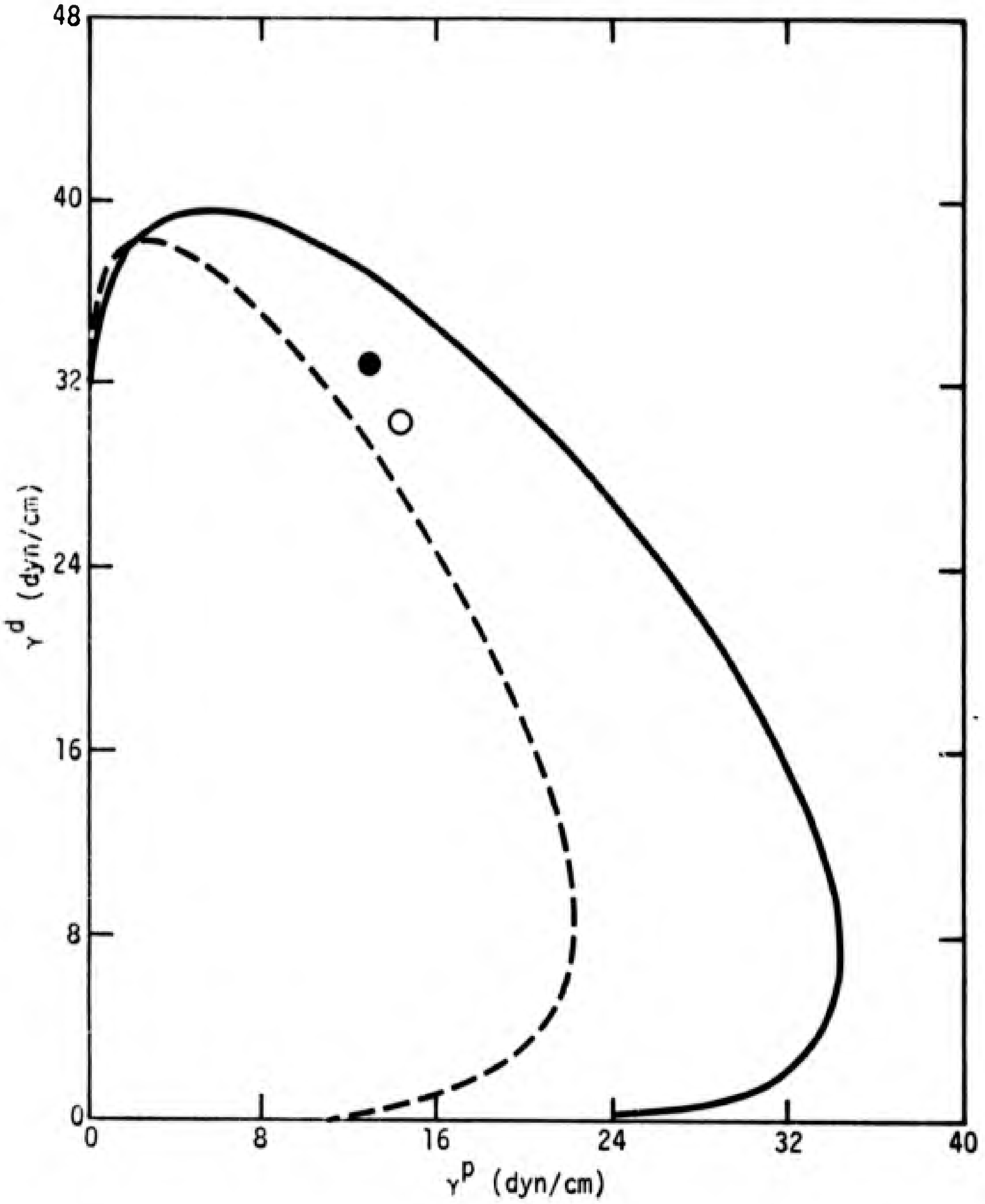

Fig. 72. Wettability Envelopes for New BR34-32 Primer, Uncured (Solid Line) Cured (Dashed Line).
New FM34B-32 Adhesive Uncured ○
Cured ●

TABLE 36: Adhesive Bonding of Ti-6Al-4V (phosphate-fluoride) with a new batch of FM34B-32 adhesive and BR-34B-32 primer. Lap shear joint.

Sample	Bond Strength psi
1	3500
2	2440
3	2940
4	3080
5	3380
	Avg 3068 ± 300

The surface tension properties of HT424 adhesive and primer fall well within the wettability envelope in Figure 70. Strong bonds are expected from the wettability analysis. The bond strengths reported for Ti-6Al-4V-HT424 system in Table 37 average 3358 ± 352 psi and in Table 38 they average 3143 ± 533 psi for TURCO treatment, in accordance with the wettability analysis.

2. Surface Aging Effects

a. Effect of Humidity and Time

Figure 73 shows σ_b vs ϕ_c for various SET aging experiments. Although there is large scatter due to an unknown uncontrolled parameter, the trend is towards $\sigma_I \approx 0$ and $\sigma_b \sim 5000$ psi. These results are interpreted as failure of a weak boundary layer ($\sigma_I \sim 0$) at the oxide primer interface (as concluded from the SEM study) and failure in the adhesive of $\sigma_c \sim 5000$ psi. The average values of ϕ_c and σ_b ($\bar{\phi}_c$ and $\bar{\sigma}_b$) for six bonds at each of the various values of SET are given in Table 47 and plotted in Figure 74. Within experimental scatter it appears that surface aging of the Ti-6Al-4V at 54°C and 95% R.H. has no effect upon either $\bar{\phi}_c$ or $\bar{\sigma}_b$. Ellipsometric measurement of unbonded side of the samples after fracture revealed that negligible changes had occurred during SET ($\Delta = 72.5 \pm 0.8$, $\psi = 29.6 \pm 0.8$ after SET as compared to $\Delta = 72.9$, $\psi = 27.9$ prior to SET).

b. Effect of SET on Contact Angles

Samples of Ti-6Al-4V sheet 0.063" x 1" x 2" were given the nitric acid-fluoride surface treatment. Wettability experiments were conducted on these etched surfaces subsequent to increasing surface exposure time (SET) at 23°C and 50 ± 5% R.H. The results are compiled in Table 39 for the contact angle θ measurements with test liquids of varied surface tension γ_{LV} at four levels of ambient SET = 2.5 hr to 35 hr. Figure 75 shows the downward shift in cos θ versus γ_{LV} which results from increasing ambient SET from 2.5 hr to 35 hr and represents diminished wettability with increased SET. These results of one surface treatment of Ti-6Al-4V alloy display the same trends shown by earlier studies of Al 2024-T3 subsequent to the FPL etch treatment. The initial exploratory results were reconfirmed in more detailed studies involving the same surface treatment followed by seven levels of ambient SET (23 ± 0.5°C, 50 ± 5% R.H.).

TABLE 37: Preliminary Examination of Phosphate-Fluoride Treatment of Ti-6Al-4V

- Phosphate-Fluoride Treatment

metal = Ti-6Al-4V
primer = HT-424 parts A&B (American Cyanimid)
adhesive = HT-424

Results: (single lap shear bond strength)

Bond #	σ_b	average σ_b	average deviation
1	3550 psi		
2	3830		
3	3040	3358	± 352 psi
4	2760		
5	3220		
6	3750		

TABLE 38: Preliminary Examination of TURCO Treatment for Ti-6Al-4V

- TURCO Treatment

metal = Ti-6Al-4V
primer = HT-424 parts A & B (American Cyanimid)
adhesive = HT-424

Results: (single lap shear bond strength)

Bond #	σ_b	average σ_b	average deviation
1	3710 psi		
2	2720		
3	3730	3143	± 533 psi
4	2320		
5	2790		
6	3590		

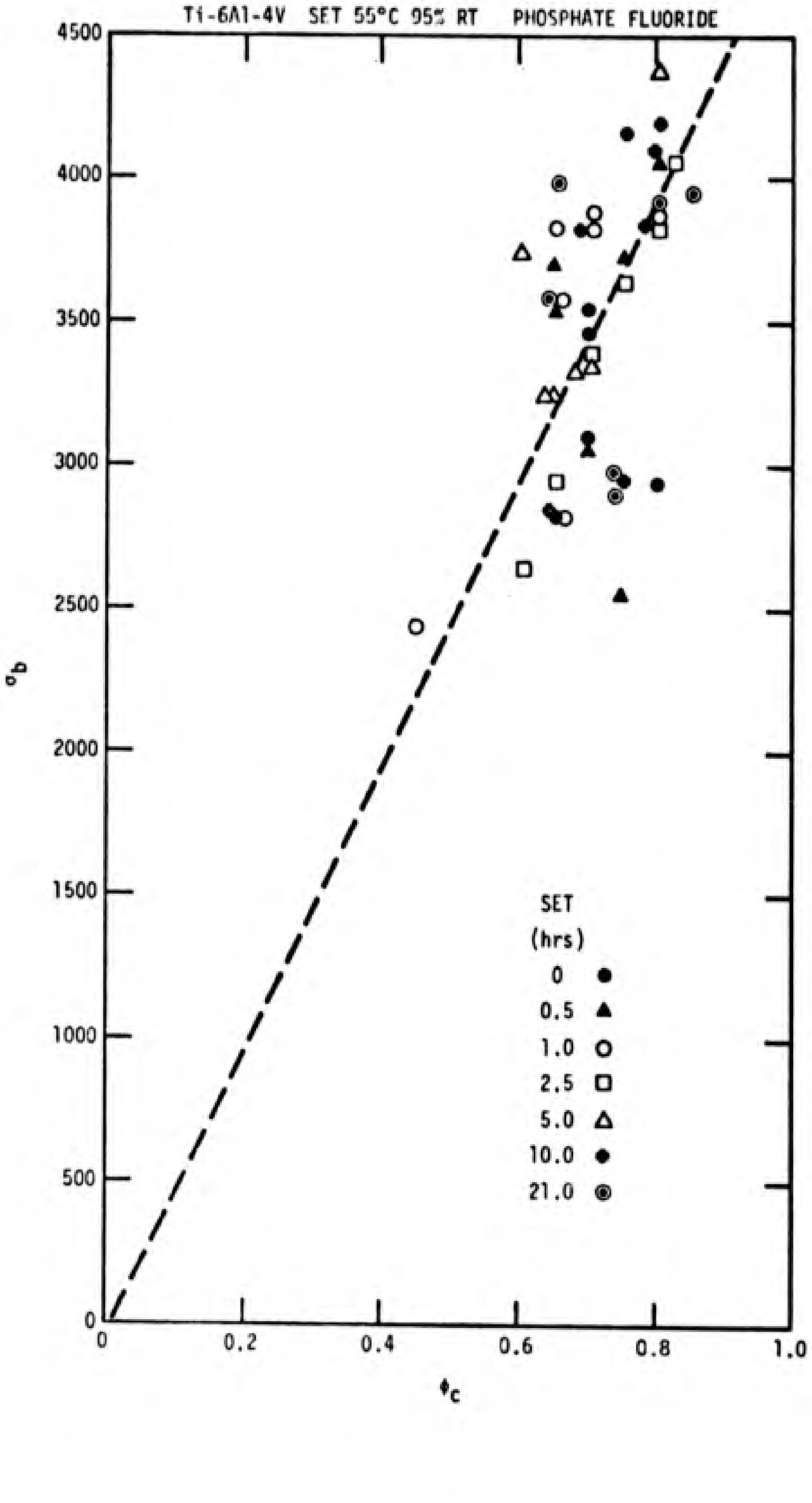

Fig. 73. Plot of σ_b vs ϕ_c for SET, 54°C, 95% R.H., phosphate-fluoride treated Ti-6Al-4V - HT424.

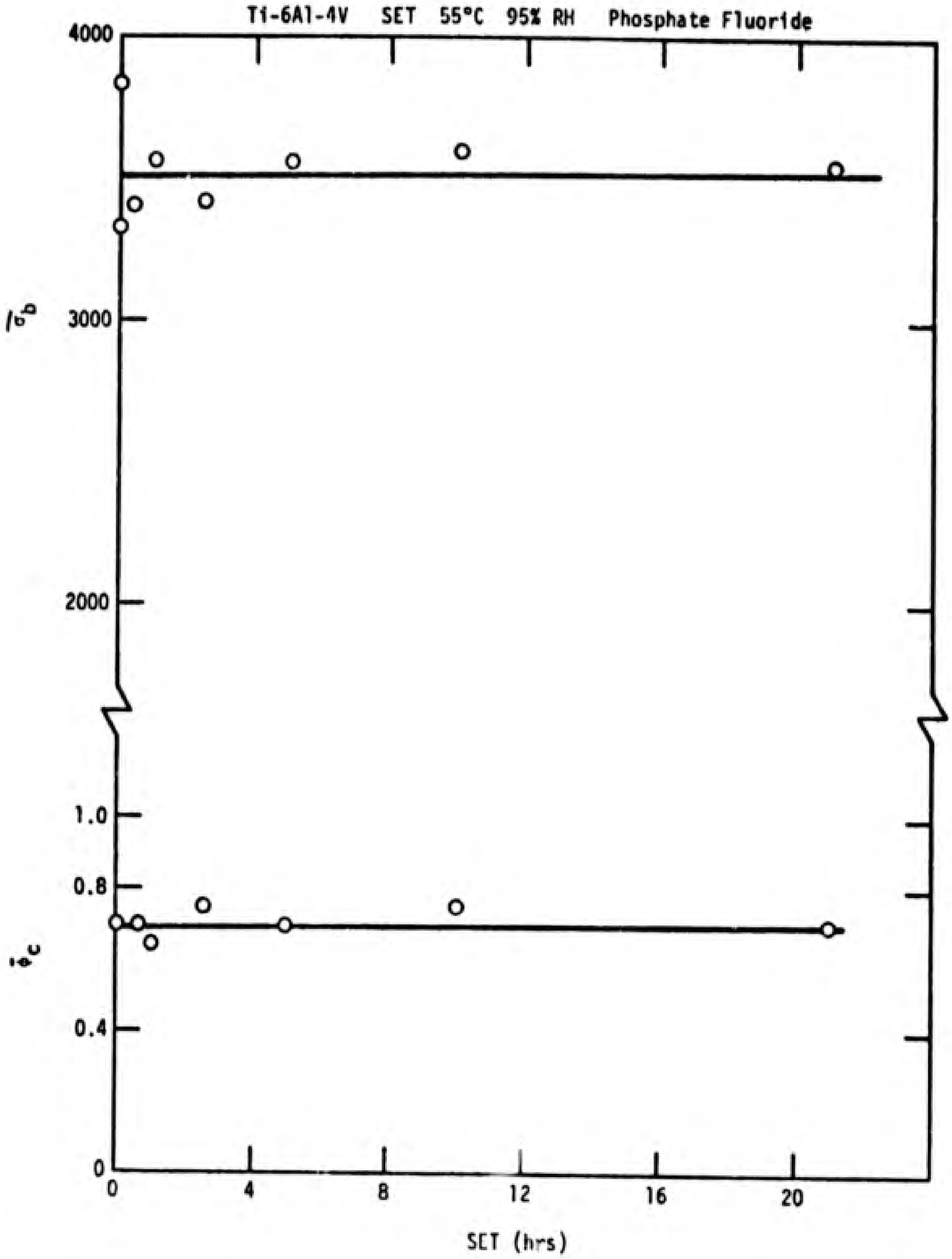

Fig. 74. Plot of $\bar{\sigma}_b$ and $\bar{\phi}_c$ vs SET at 54°C, 95% R.H., for Ti-6Al-4V - HT424 with phosphate-fluoride treatment.

TABLE 39: Cosine of Liquid-Solid Contact Angle θ of Acid-Etched Ti-4V-6Al (nitric acid-fluoride) at various SET conditions (23°C and 50 ± 5% R.H.)

SET (hr)		2.5	5.0	23	35
Test Liquid	γ_{LV} (dyn/cm)	$\cos\theta$	$\cos\theta$	$\cos\theta$	$\cos\theta$
water	72.8	.839	.848	.454	.438
glycerol	64.0	.839	.788	.755	.438
formamide	58.3	.974	.875	.809	.875
ethylene glycol	48.3	1.00	.921	.857	.731
1-br. napthalene	44.6	1.00	1.00	1.00	.996
P.G. E-200	43.5	1.00	.777	.985	.927
tricresy phosphate	40.9	1.00	.990	.996	.996
P.G. P-1200	31.3	.999	.996	.992	.992
hexadicane	27.6	1.00	1.00	1.00	1.00

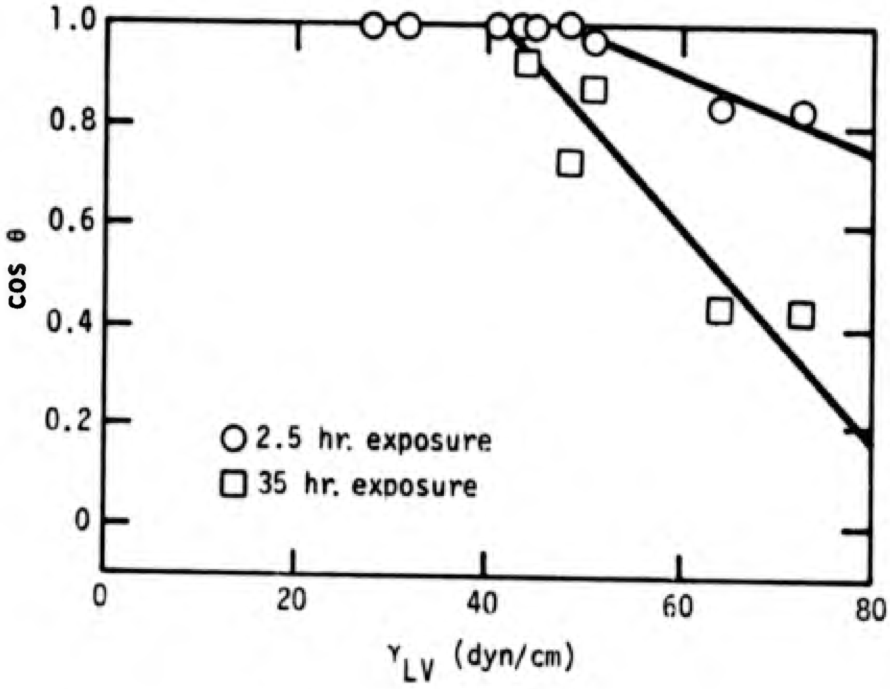

Fig. 75. Effects of SET (23°C, 50 ± 5% RH) upon the values of cos θ *vs* γ_{LV} for acid etched Ti-6Al-4V

The results of this more detailed study, increasing ambient SET upon measured values of advancing liquid-solid contact angle, on HNO_3/HF treated Ti-6Al-4V are summarized in Table 40. Liquid-solid interactions which provided $\theta > 0$ and $\cos \theta < 1.0$ were further analyzed by the dispersion-polar interaction relations. The summary results of this surface energy analysis as provided by the determinant calculation for mean values of dispersion γ_{SV}^d and polar γ_{SV}^p components of solid-vapor surface tension $\gamma_{SV} = \gamma_{SV}^d + \gamma_{SV}^p$ and the respective standard deviations $\pm\delta^d$, $\pm\delta^p$, and $\pm\delta$ are presented in Table 41. The data of Table 41 indicate that surface energy analysis provides a significant resolution of ambient SET effects upon the dispersion and polar character of the surface treated Ti-6Al-4V alloy. Figure 76 presents the mean values of γ_{SV}^d, γ_{SV}^p and γ_{SV} plotted as functions of SET. The curves of Figure 76 show that HNO_3/HF etched Ti-6Al-4V alloy displays a regular time dependent transition in surface properties with major changes during initial surface aging at SET = 0 - 24 hr at 23°C and 50 ± 5% R.H.

The results shown in Figure 76 for surface treated Ti-6Al-4V may be compared with those previously reported for the FPL etched Al 2024-T3 in Figure 42. Whereas Al 2024-T3 showed approximately stable surface properties from SET = 0 to 50 hr at 23°C and 50 ± 5% R.H., followed by changes to ~ 300 hrs, it is evident that immediate changes occur with surface treated Ti-6Al-4V alloy. This initial instability prevented meaningful wettability measurements on surface treated Ti-6Al-4V at times where SET < 2.5 hr. The net effects of SET in reducing γ_{SV}^p and increasing γ_{SV}^d are similar for both Ti-6Al-4V and Al 2024-T3 surfaces. The consistent shift of the values of $\alpha_s = \gamma_{SV}^{d\,\frac{1}{2}}$ versus $\beta_s = \gamma_{SV}^{p\,\frac{1}{2}}$ properties of HNO_3/HF treated Ti-6Al-4V are shown in Figure 77 and these closely follow similar plots shown previously for the FPL etched Al 2024-T3 (Figure 48).

The wettability envelope for the HNO_3/HF etched Ti-6Al-4V surfaces at varied levels of ambient SET covered by Table 40 and Table 41 are displayed by the curves of Figure 78. It may be recalled that if the surface tension

TABLE 40: Effects of ambient surface exposure time (SET) at 23°C and 50 ± 5% R.H. on the wettability of HNO_3/HF acid etched Ti-6Al-4V at 20°C

SET (hr)	2.5	5	23	48	72	144	192	γ_{LV}
Test Liquid	Advancing Contact Angle θ							(dyn/cm)
water	33	32	63	64	74	65	69	72.8
glycerol	33	38	41	64	59	57	52	64.0
formamide	13	29	36	29	29	40	40	58.3
ethylene glycol	0	23	31	43	41	34	38	48.3
α-bromonapthalene	0	0	0	5	5	16	7	44.6
polyglycol E-200	0	39	10	22	29	31	17	43.5
tricresyl phosphate	0	8	5	5	5	10	5	40.9
polyglycol P-1200	3	5	7	7	5	5	7	31.3
hexadecane	0	0	0	0	0	0	0	27.6

TABLE 41: Surface Energy Analysis for Ambient SET Effects (23°C and 50 ± 5% R.H.) on HNO_3/HF Etched Ti-6Al-4V at 20°C

SET (hr)	$\gamma_{SV}^{d} \pm \delta^{d}$ (dyn/cm)	$\gamma_{SV}^{p} \pm \delta^{p}$ (dyn/cm)	$\gamma_{SV} \pm \delta$ (dyn/cm)	α_s $(dyn/cm)^{\frac{1}{2}}$	β_s $(dyn/cm)^{\frac{1}{2}}$
2.5	7.18 ± 3.1	69.8 ± 11.2	77.0 ± 8.6	2.68	8.35
5	15.9 ± 4.3	47.6 ± 8.0	63.5 ± 3.9	3.99	6.90
23	27.3 ± 4.0	22.9 ± 5.9	50.1 ± 2.9	5.22	4.79
48	31.9 ± 3.6	15.1 ± 4.4	47.0 ± 2.6	5.65	3.89
72	36.5 ± 3.9	11.5 ± 4.3	47.9 ± 3.3	6.04	3.39
144	31.2 ± 2.9	13.6 ± 3.0	44.8 ± 1.4	5.59	3.69
192	34.0 ± 2.9	12.4 ± 3.2	46.4 ± 1.4	5.83	3.52

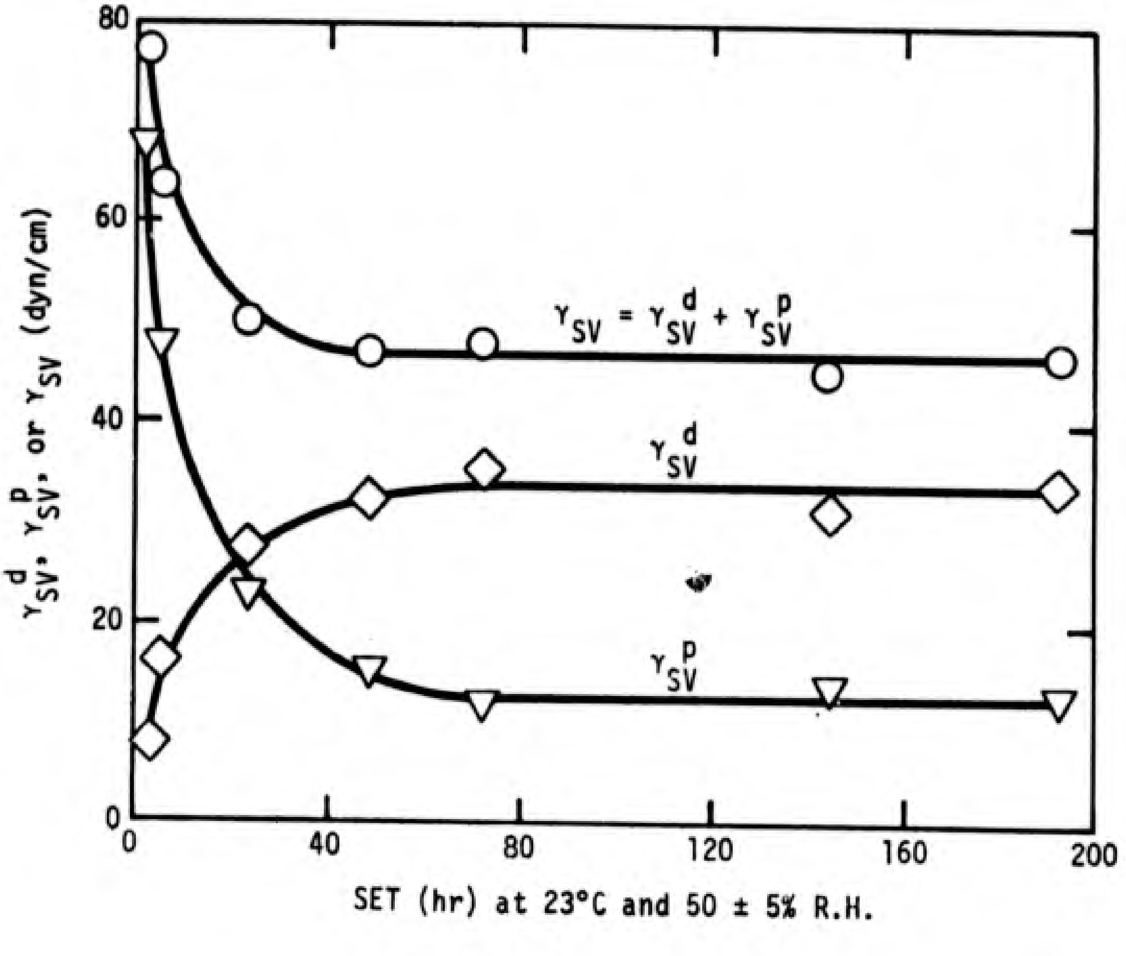

Fig. 76. Effect of ambient SET at 23°C, 50 ± 5% R.H. on calculated average values of γ_{SV}^d, γ_{SV}^p and γ_{SV} for HNO_3/HF etched Ti-6Al-4V.

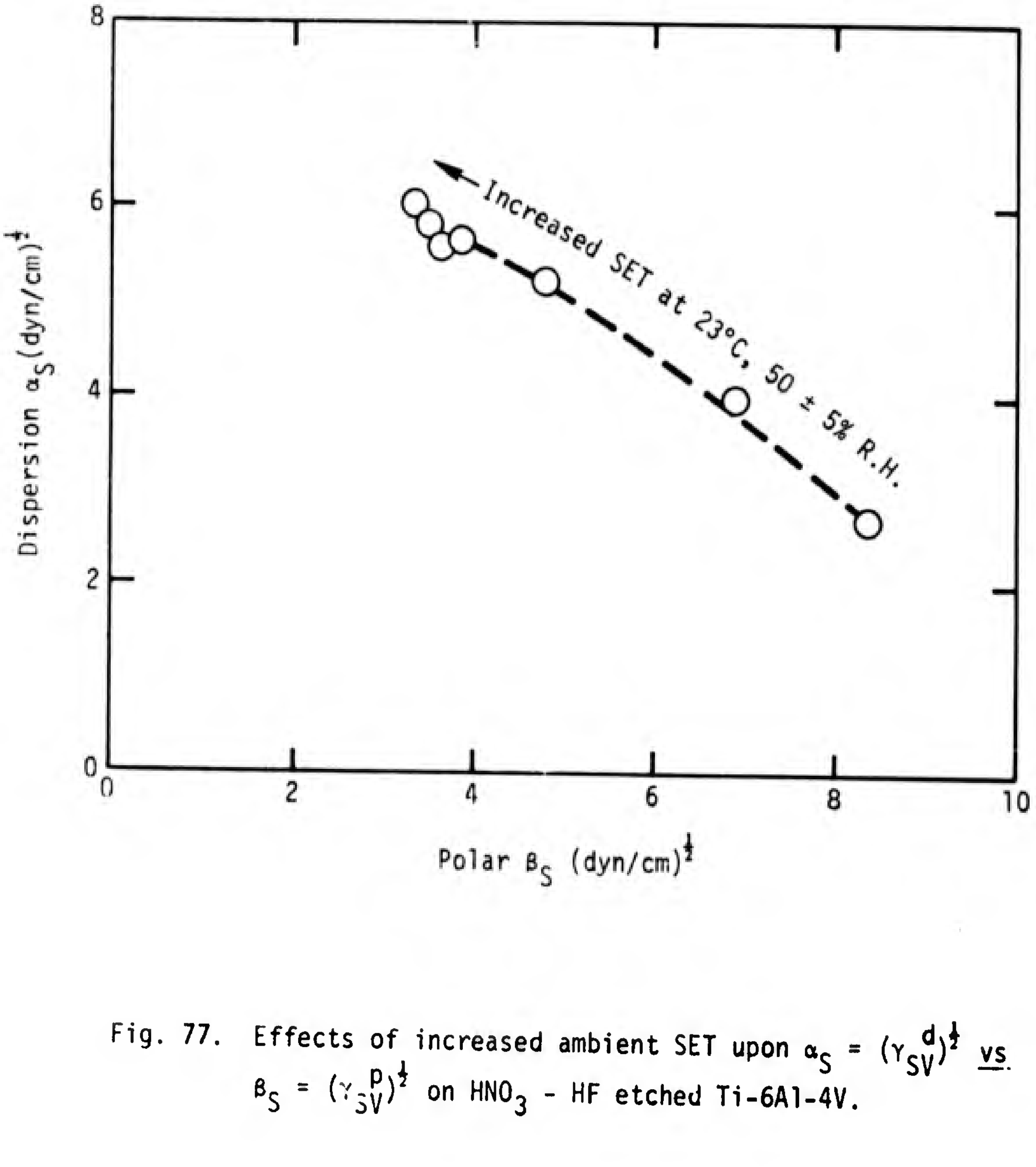

Fig. 77. Effects of increased ambient SET upon $\alpha_S = (\gamma_{SV}^d)^{\frac{1}{2}}$ vs. $\beta_S = (\gamma_{SV}^p)^{\frac{1}{2}}$ on HNO_3 - HF etched Ti-6Al-4V.

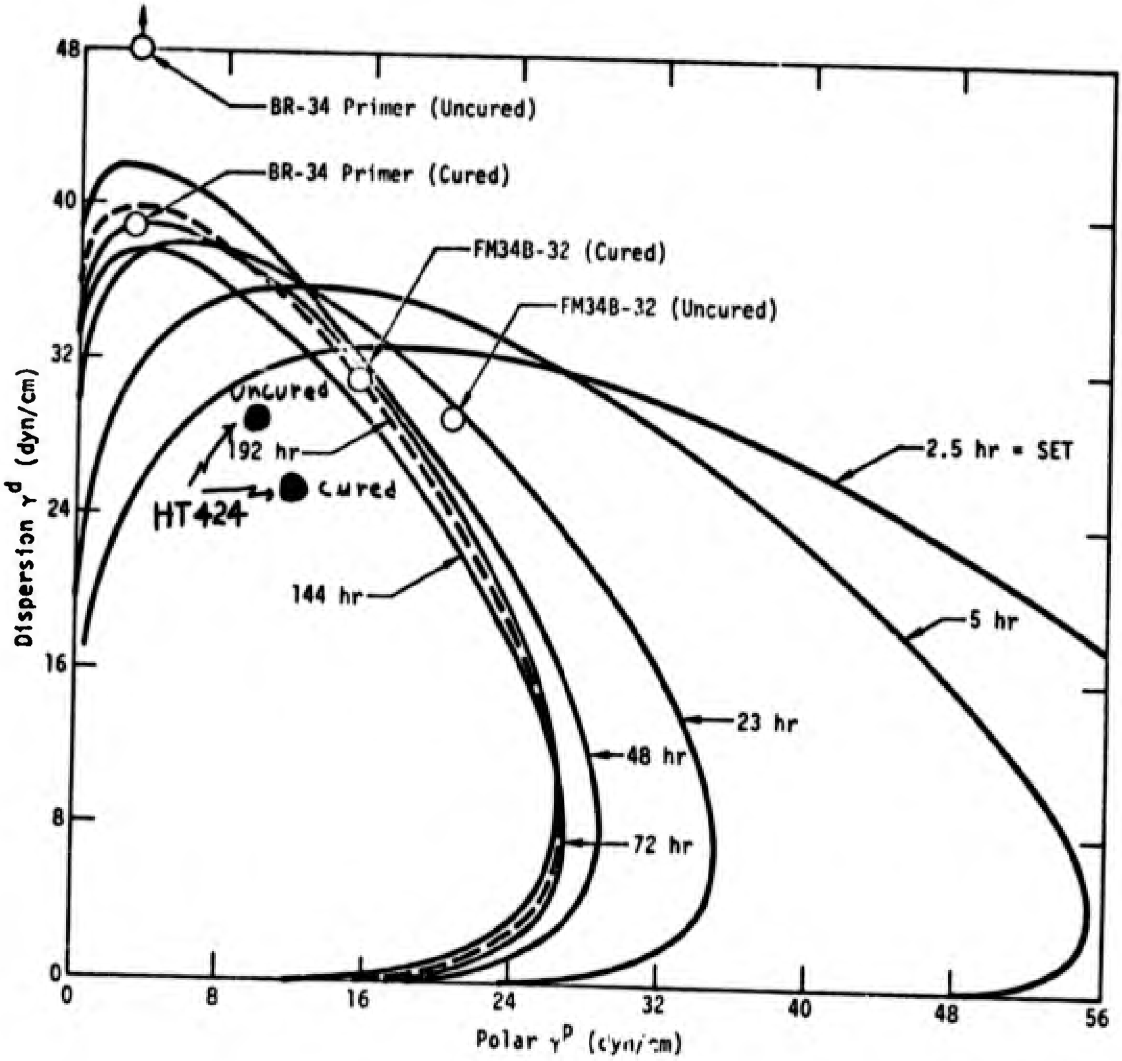

Fig. 78. Wettability envelopes for HNO_3/HF etched Ti-6Al-4V at various SET.

properties of a simple liquid or adhesive material fall within the region between the origin $\gamma_{SV}^d = \gamma_{SV}^p = 0$ and the curve defining the wettability envelope spontaneous spreading is predicted in the absence of rheological restraints. The data points on Figure 78 represent the surface tension properties of the bad batch of polyimide primer BR-34 and adhesive FM-34B-32. It is seen in Figure 78 that SET can only make a bad situation even worse as far as bondability is concerned. Table 42 gives contact angle data for the phosphate-fluoride treatment of Ti-6Al-4V. Table 43 presents the analysis of liquid-solid interactions. Table 44 summarizes the results of calculations for average values of γ_{SV}^d, γ_{SV}^p, γ_{SV} and the respective standard deviations $\pm\delta^d$, $\pm\delta^p$, $\pm\delta$ based on the determinant method. The experimental variation in $W_a/2\alpha_L$ versus β_L/α_L is shown by the data points of Figure 79 for phosphate-fluoride treated Ti-6Al-4V with SET $\leqslant$ 0.5 hr. The linear solid curve of Figure 79 represents the average values $\gamma_{SV}^d = 28.4$ dyn/cm and $\gamma_{SV}^p = 35.3$ dyn/cm while the dashed curves represent the uncertainties defined by $\delta^d = \pm 3.6$ dyn/cm and $\delta^p = \pm 6.8$ dyn/cm.

The plots of γ_{SV}^d and γ_{SV}^p shown in Figure 80 indicate that γ_{SV}^d appear to maximize at SET $\approx$ 16 hr while γ_{SV}^p minimizes at SET = 20 to 30 hr. These results differ from γ_{SV}^d and γ_{SV}^p data for HNO_3/HF etched Ti-6Al-4V shown previously in Figure 76. These results of surface energy analysis of the phosphate-fluoride treated Ti-6Al-4V panels do indicate that ambient SET effects at short times SET = 0 to 24 hr produce significant variations in wettability and should effect adherence to polymeric adhesives.

The wettability envelopes for phosphate-fluoride treated Ti-6Al-4V developed from the γ_{SV}^d and γ_{SV}^p values tabulated in Table 44 are displayed in Figure 81. It may be recalled from Eq. 13 of Section II.B.6 that if the surface tension properties of a simple liquid or adhesive material fall within the region between the origin $\gamma_{LV}^d = \gamma_{LV}^p = 0$ and curve defining the wettability envelope spontaneous spreading is predicted in the absence of rheological restraints. The surface tension properties of uncured and cured HT424 adhesive are seen to fall well within the wettability envelopes for phosphate-fluoride

TABLE 42

Cosine of Liquid-Solid Contact Angle θ of Phosphate-Fluoride Treated Ti-6Al-4V at Various SET Conditions (23° and 50 ± 5% R.H.)

Surface Exposure Time (hr)		0-0.5	8	16	25	30	52
Test Liquid -	γ_{LV} (dyn/cm)	cos θ					
water	72.8	.9994	.5736	-.3420	.0175	.0349	.4067
glycerol	64.0	.9976	.7547	.4695	.3907	.3746	.0000
ethylene glycol	48.3	.9986	.7660	.4540	.7660	.5446	.7193
poly glycol E-200	43.5	.9926	.7314	.9336	.8387	.9205	.6820
tricresyl phosphate	40.9	.9945	.9903	.9962	.9976	.9511	.9613
α-bromonaphthalene	44.6	.9999	.9986	.9986	.9994	.9962	.9976
hexadecane	27.6	.9999	.9994	.9994	.9994	.9994	.9994

TABLE 43

Analysis of Liquid-Solid Interactions

Surface Exposure Time (hr)			0-0.5	8	16	25	30	52
γ_{LV} -	$2\alpha_L$	β_L/α_L	$W_a/2\alpha_L$ $(dyn/cm)^{\frac{1}{2}}$					
72.8	9.34	1.53	15.58	12.27	5.13	7.93	8.07	10.96
64.0	11.66	.94	10.96	9.63	8.07	7.63	7.54	5.49
48.3	10.83	.81	8.91	7.88	6.48	7.88	6.89	7.67
43.5	10.62	.74	8.16	7.09	7.92	7.53	7.87	6.89
40.9	12.52	.21	6.52	6.50	6.52	6.53	6.37	6.41
44.6	13.36	.00	6.68	6.67	6.67	6.67	6.66	6.67
27.6	10.51	.00	5.25	5.25	5.25	5.25	5.25	5.27

TABLE 44

Calculated Solid-Vapor Surface Tension
Properties by the Determinant Method

Surface Exposure time (hr)	$\gamma^d_{SV} \pm \delta^d$ (dyn/cm)	$\gamma^p_{SV} \pm \delta^p$ (dyn/cm)	$\gamma_{SV} \pm \delta$ (dyn/cm)
0 - 0.5	28.4 ± 3.6	35.3 ± 6.8	63.7 ± 4.0
8	31.4 ± 3.1	15.3 ± 3.2	46.6 ± 1.6
16	52.4 ± 9.5	5.6 ± 1.8	58.0 ± 10.9
25	40.3 ± 2.6	3.2 ± 0.9	43.5 ± 2.0
30	37.9 ± 2.4	3.1 ± 0.9	41.1 ± 1.9
52	31.7 ± 3.2	12.8 ± 5.6	44.5 ± 4.1

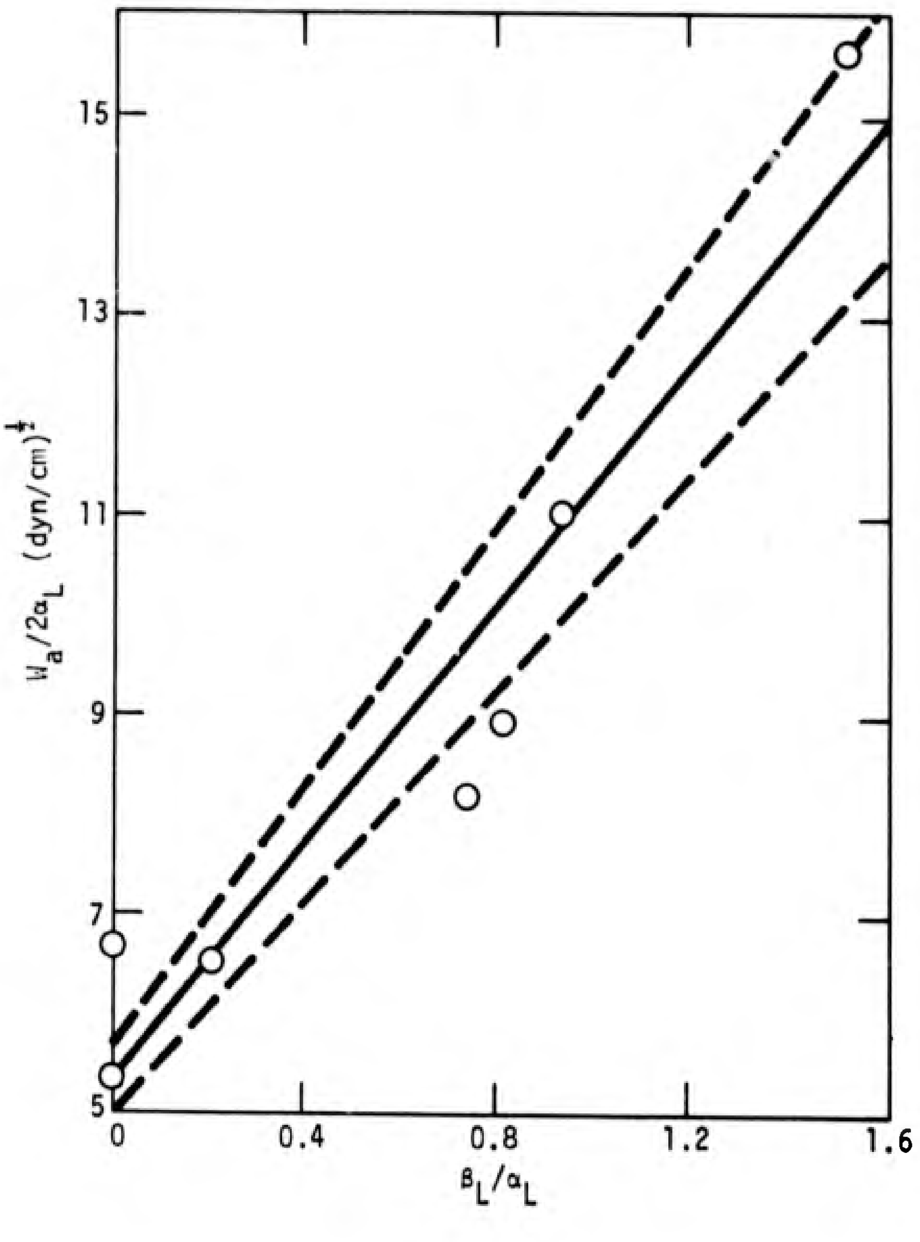

Fig. 79. Variation in $W_a/2\alpha_L$ versus β/α_L for phosphate-fluoride treated Ti-6Al-4V with 0 to 0.5 SET in ambient air.

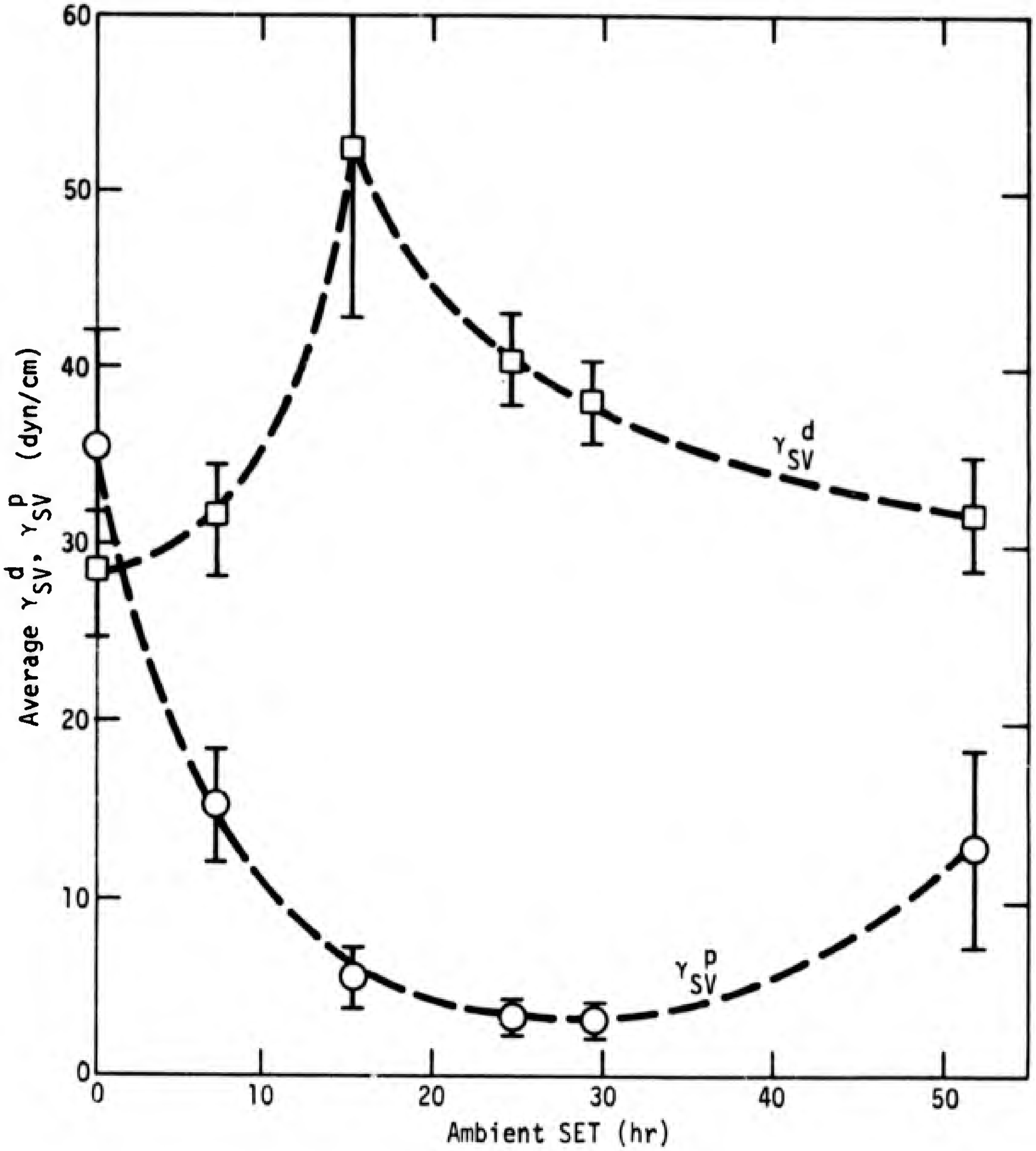

Fig. 80. Effect of ambient SET at 23°C, 50 ± 5% R.H. on calculated average values for γ_{SV}^{d} and γ_{SV}^{p} for phosphate-fluoride treated Ti-6Al-4V.

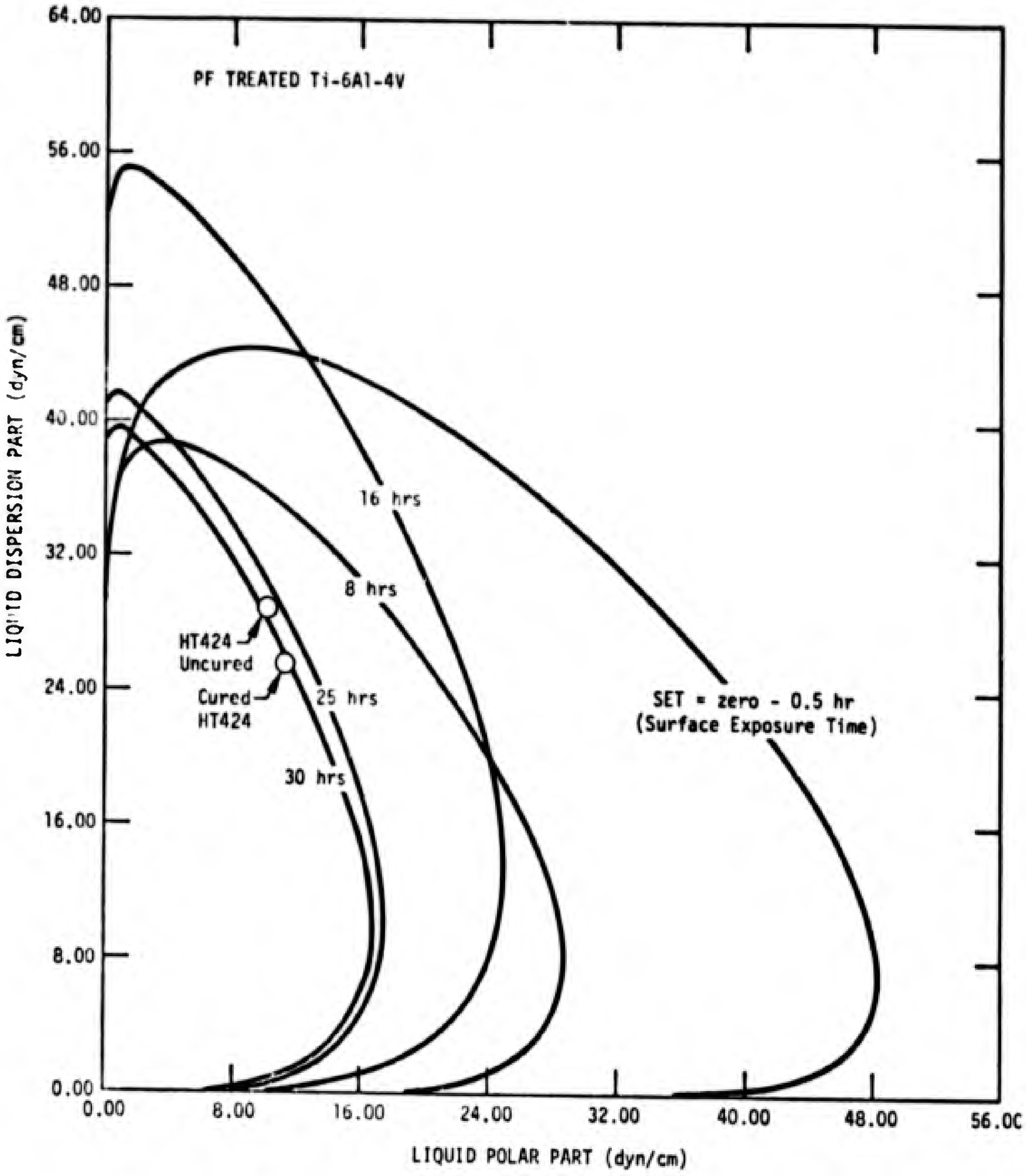

Fig. 81. Wettability envelopes for Ti-6Al-4V, phosphate-fluoride treated and SET 23°C, 50 ± 5% R.H. ambient air.

treated Ti-6Al-4V for ambient SET = $\leq$ 0.5 hr, 8 hr, and 16 hr and to fall near the boundary of the envelopes for SET = 25 hr and 30 hr. As seen in Figure 74 the average bond strength remains high to SET = 21 hr in accord with the wettability analysis.

Wettability measurements and surface energy analysis methods were applied to a detailed study of phosphate-fluoride treated surfaces of Ti-6Al-4V under accelerated aging conditions of 54 ± 1°C and 95% R.H. surface exposure. Subsequent to surface treatment the surface exposure condition (SET) at 54 ± 1°C and 95% R.H. was applied for varied periods and the surfaces characterized by wettability measurements with the test liquids identified in Table 45. The measured values of contact angle θ for five test liquids and 12 levels of surface exposure time (SET) are compiled in Table 45.

The results of the standard determinant analysis of wettability data is presented in Table 46 which tabulates the calculated average values of γ_{SV}^{d}, γ_{SV}^{p}, γ_{SV} and the associated standard deviations δ^{d}, δ^{p}, δ. The curves of Figure 82 illustrate the rapid degradation of surface energy properties for phosphate-fluoride treated Ti-6Al-4V due to SET effects. Figure 83 presents related information on surface energy degradation in terms of the rapidly diminishing wettability envelopes with increased SET. Inspection of Figure 83 shows the wettability envelopes for Ti-6Al-4V enclose the surface energy properties of uncured and cured HT424 epoxy-phenolic adhesive for all SET conditions covering SET = 0 to 24 hr indicative of a wettable surface. The wettability analysis indicates that weak bonds should result for SET > 24 hrs.

The averaged values of γ_{SV}^{d}, γ_{SV}^{p}, γ_{SV} for phosphate-fluoride treated Ti-6Al-4V at SET (23°C, 50% R.H.) and SET (54°C, 95% R.H.) are combined on a single master curve in Figure 84. A dimensionless time-humidity shift factor:

$$a_{TC} = \frac{\text{SET (23°C, 50\% R.H.)}}{\text{SET (54°C, 95\% R.H.)}} \cong 3.5$$

TABLE 45: Contact angles θ of test liquids on phosphate-fluoride etched Ti-6Al-4V at various SET conditions (54 ± 1°C and 95% R.H.)

Surface Exposure time (SET) hr		0	.25	.75	1.12	1.83	3.33
Test Liquid	γ_{LV} (dyn/cm)	θ	θ	θ	θ	θ	θ
water	72.8	2	10	47	43	50	60
glycerol	64.0	4	14	41	45	41	55
ethylene-glycol	48.3	3	4	12	14	18	15
polyglycol E-200	43.5	7	5	6	6	6	9
1-bromonapthalene	44.6	1	2	2	2	2	3
tricresyl phosphate	40.9	6	7	7	7	7	6

SET (hr)	5.37	7.47	10.47	12.97	23.6	47.5
γ_{LV} (dyn/cm)	θ	θ	θ	θ	θ	θ
72.8	75	73	83	84	96	97
64.0	56	66	62	70	77	79
48.3	31	34	49	44	56	61
43.5	7	9	12	18	30	38
44.6	4	5	4	5	4	4
40.9	7	9	10	8	8	6

TABLE 46 : Calculated solid-vapor surface tension properties by the determinant method for 54 ± 1°C and 95% RH SET

SET (hr)	$\gamma_{SV}^{d} \pm \delta^{d}$ (dyn/cm)	$\gamma_{SV}^{p} \pm \delta^{p}$ (dyn/cm)	$\gamma_{SV} \pm \delta$ (dyn/cm)
0	28.7 ± 5.0	37.3 ± 9.0	66.0 ± 4.8
.25	28.6 ± 5.0	36.4 ± 8.8	65.0 ± 4.6
.75	32.0 ± 3.7	19.6 ± 3.7	51.7 ± 1.4
1.12	30.7 ± 4.3	22.1 ± 5.0	52.8 ± 1.7
1.83	32.8 ± 3.4	17.8 ± 3.2	50.6 ± 1.3
3.33	34.6 ± 3.0	12.4 ± 2.1	47.1 ± 1.2
5.37	40.7 ± 1.4	5.7 ± 0.7	46.4 ± 0.8
7.47	37.5 ± 2.5	6.4 ± 1.2	43.9 ± 1.5
10.47	42.2 ± 2.0	3.0 ± 0.7	45.2 ± 1.6
12.97	41.4 ± 2.0	2.7 ± 0.7	44.0 ± 1.7
23.6	44.9 ± 2.5	0.8 ± 0.4	45.6 ± 2.5
47.5	43.6 ± 1.9	0.4 ± 0.2	44.0 ± 1.8

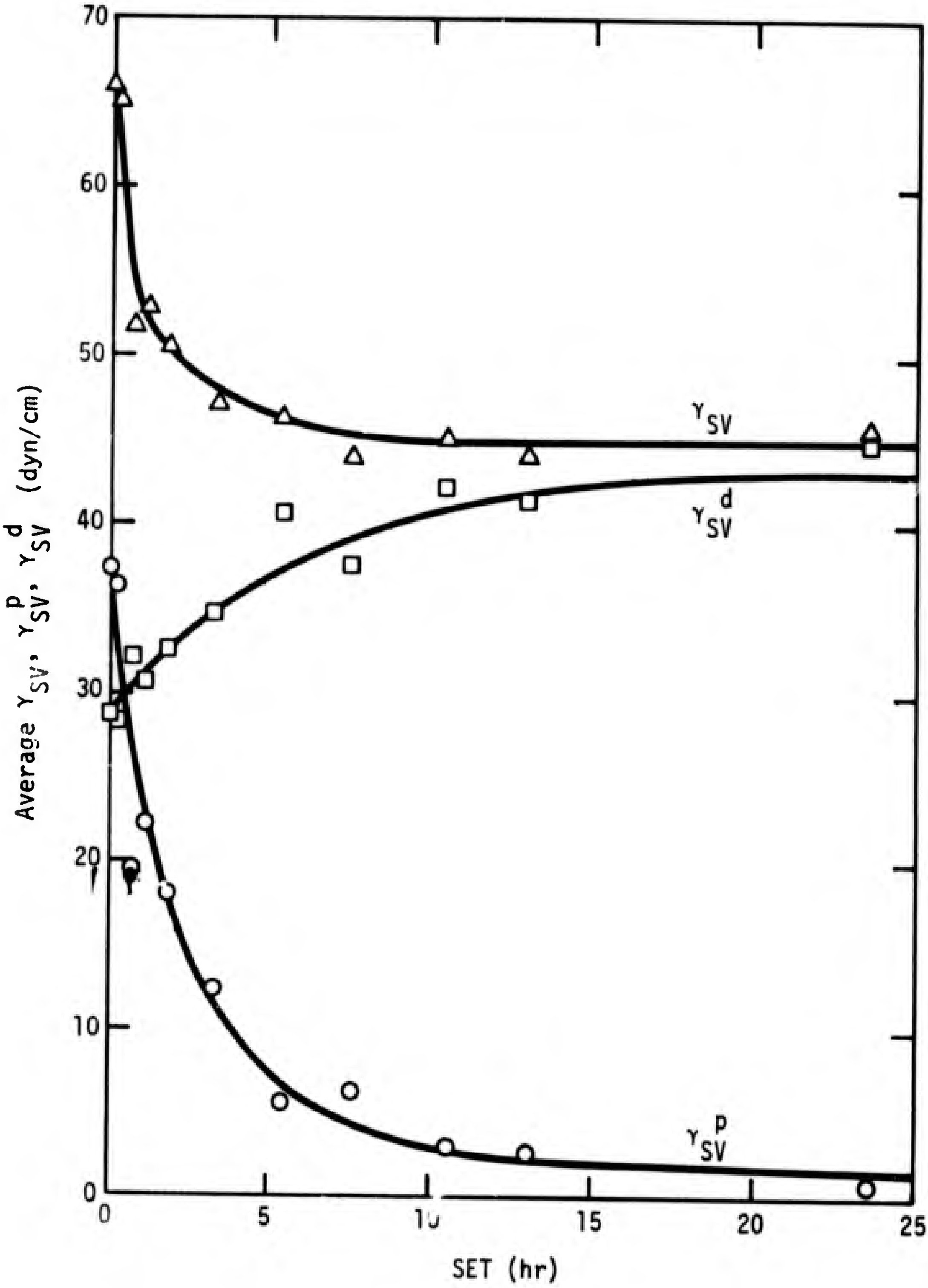

Fig. 82. Effect of SET at 54 ± 1°C, 95% R.H. on calculated average values for γ_{SV}^d, γ_{SV}^p and γ_{SV} for phosphate-fluoride treated Ti-6Al-4V.

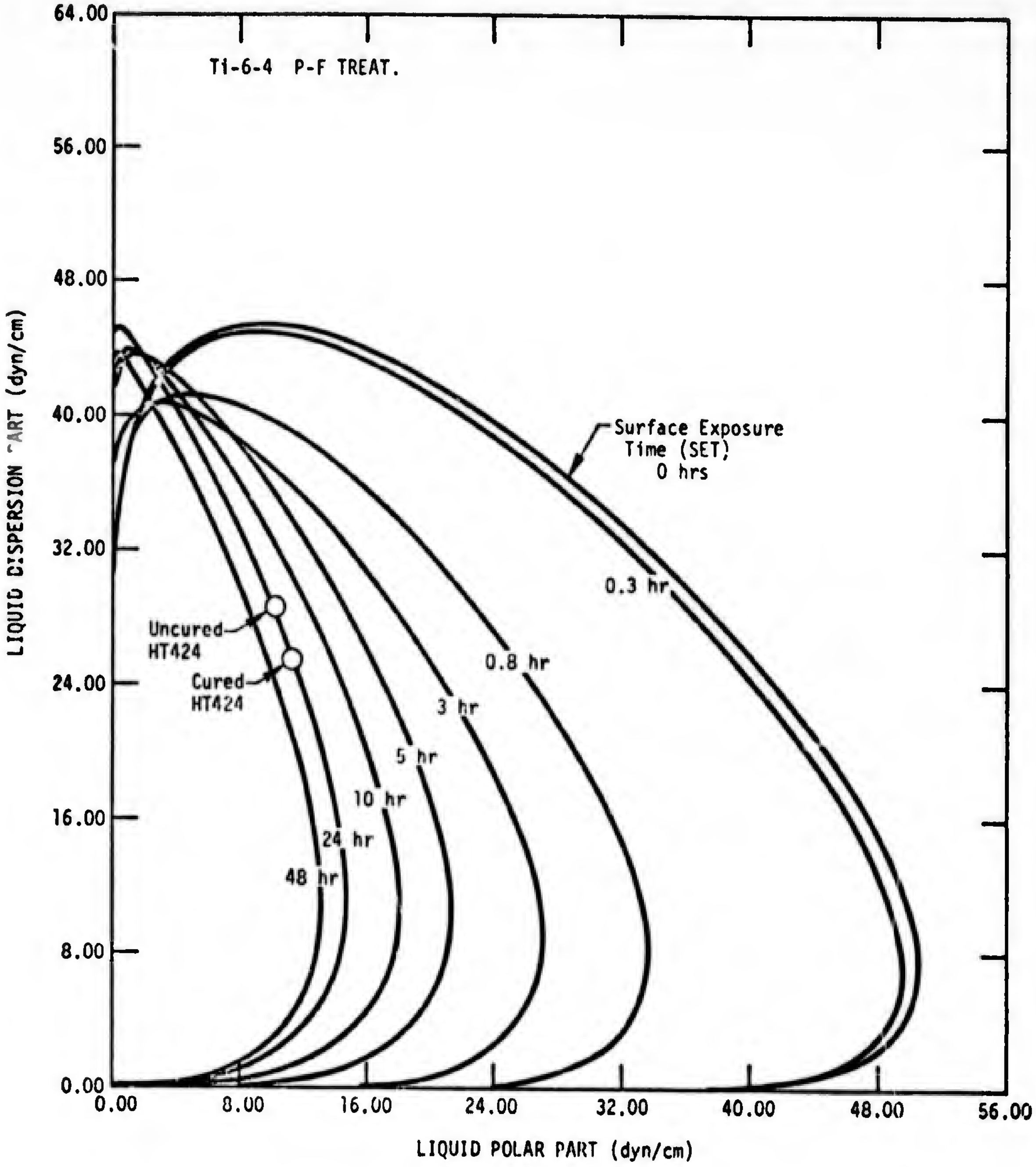

Fig. 83. Wettability envelopes for Ti-6Al-4V phosphate-fluoride, SET 54°C, 95% R.H.

is applied to the surface energy data of Table 44 and Table 46 to achieve the master curves of Figure 84. The earlier discussion of SET effects on the surface properties of the FPL etched Al 2024-T3 provides a substantially higher time shift factor:

$$a_{TC} = \frac{\text{SET (23°C, 50\% R.H.)}}{\text{SET (55°C, 95\% R.H.)}} \cong 58.5$$

The master curves of $\gamma_{SV} = \gamma_{SV}^{d} + \gamma_{SV}^{p}$ shown by Figure 84 provide a compact means of combining the effects of time, temperature, and humidity effects.

The surface energy diagram of Figure 85 illustrates the shift in dispersion (α) versus polar (β) components which are displayed by phosphate-fluoride treated Ti-6Al-4V with surface exposure time SET. The averaged surface energy properties of HT424 (α_1 = 5.21, β_1 = 3.31) are included in Figure 85.

3. Joint Aging (BET) Effects

Figure 86 shows the bond strength σ_b versus ϕ_c for bond exposure times (BET) from 0 to 1016 hrs at 54°C and 95% R.H., Figure 87 is for SET = 21 hrs. The dashed lines in Figures 86 and 87 have the same slope and intercept as for Figure 73. The average values of ϕ_c and σ_b ($\bar{\phi}_c$ and $\bar{\sigma}_b$) at a particular value of SET and BET are plotted in Figures 88 and 89. As for the SET data, BET has little effect on $\bar{\phi}_c$ but contrary to the SET data BET causes degradation of bond strength $\bar{\sigma}_b$.

Table 47 gives the average values of σ_b and ϕ_c for various BET and SET conditions and these data are plotted as a SET vs BET response surface in Figure 90.

The modified Griffith failure criteria defined by Eq. 14 through Eq. 18 of Section II.B.6 can be applied to evaluate water immersion effects on the critical failure stress σ_I of the HT424 to Ti-6Al-4V interfacial bond. The surface properties of HT424 are represented by α_1 = 5.21 $(\text{dyn/cm})^{\frac{1}{2}}$ and

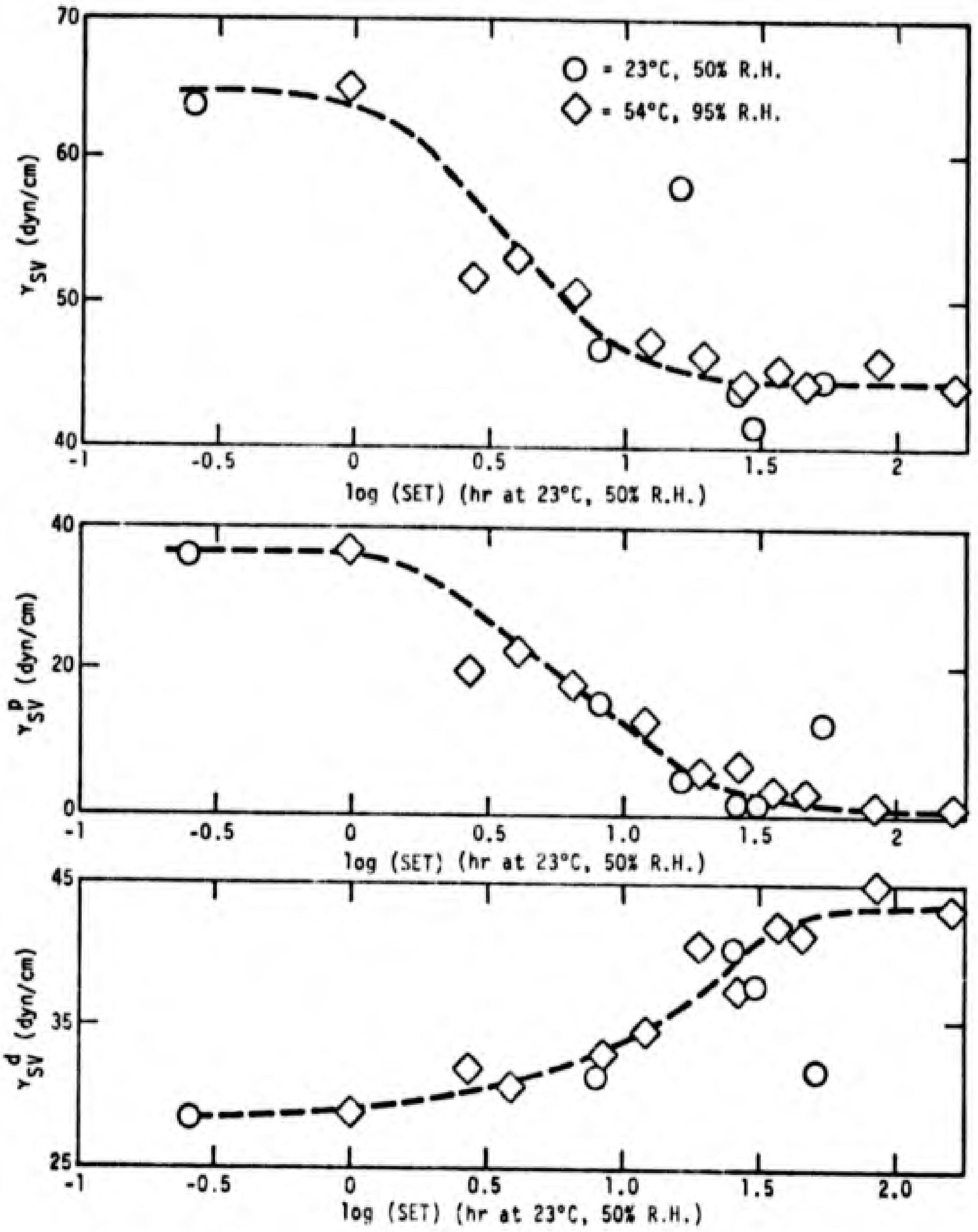

Fig. 84. Combined master curve for average values of γ_{SV}^d, γ_{SV}^p and γ_{SV} for phosphate-fluoride treated Ti-6Al-4V, SET 23°C, 50% R.H. and for 54°C, 95% R.H.

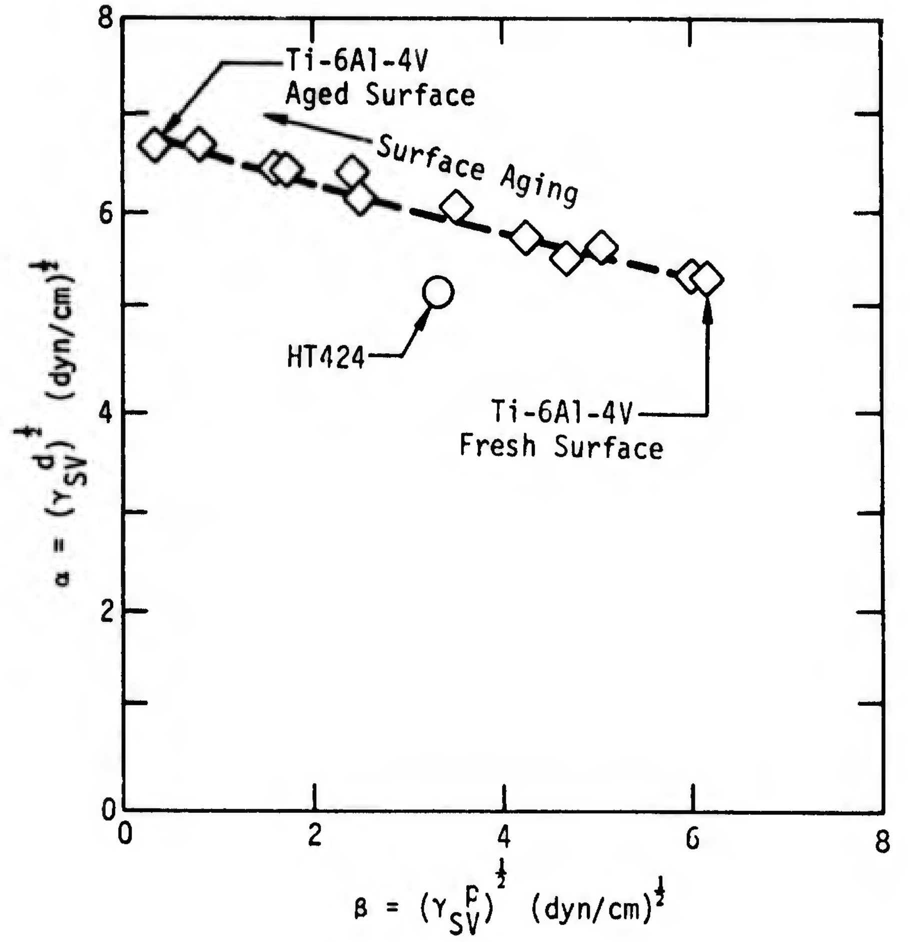

Fig. 85. Effects of SET on the shift of α_S vs β_S for phosphate fluoride treated Ti-6Al-4V.

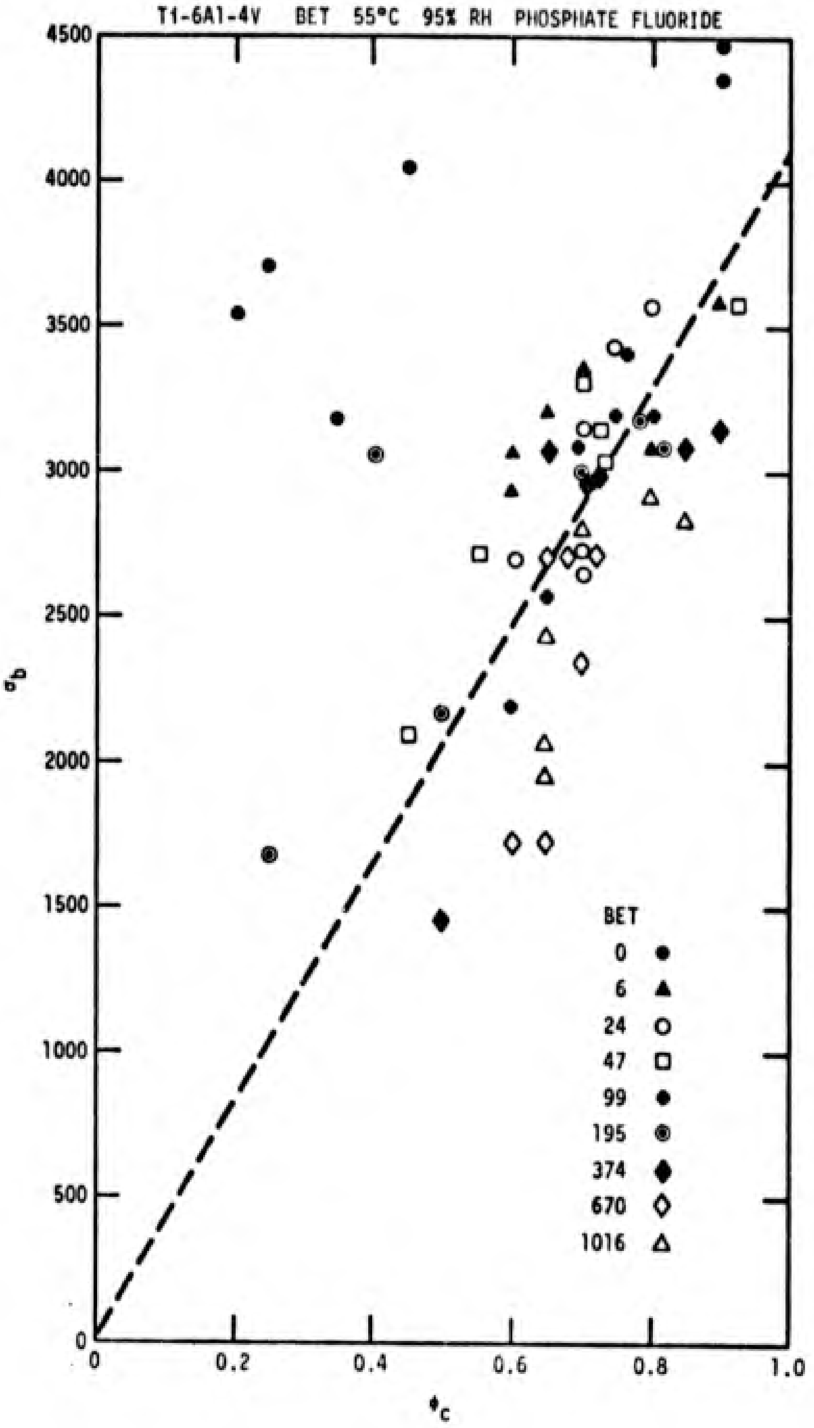

Fig. 86. Plot of σ_b vs ϕ_c for BET 54°C, 95% R.H., phosphate-fluoride treated Ti-6Al-4V - HT424.

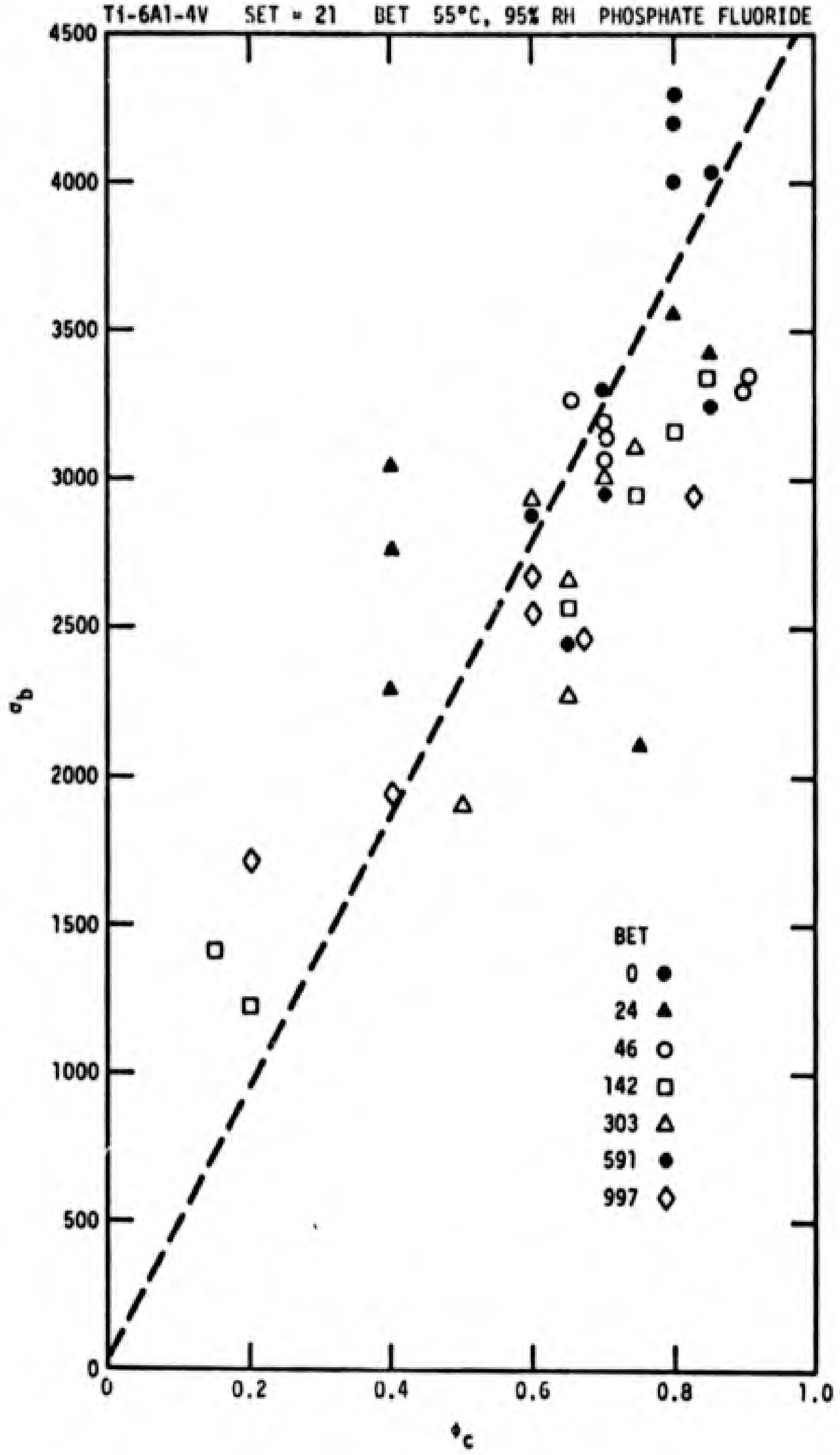

Fig. 87. Plot of σ_b vs ϕ_c for SET = 21 hrs and BET 55°C, 95% R.H. phosphate-fluoride treated Ti-6Al-4V - HT424.

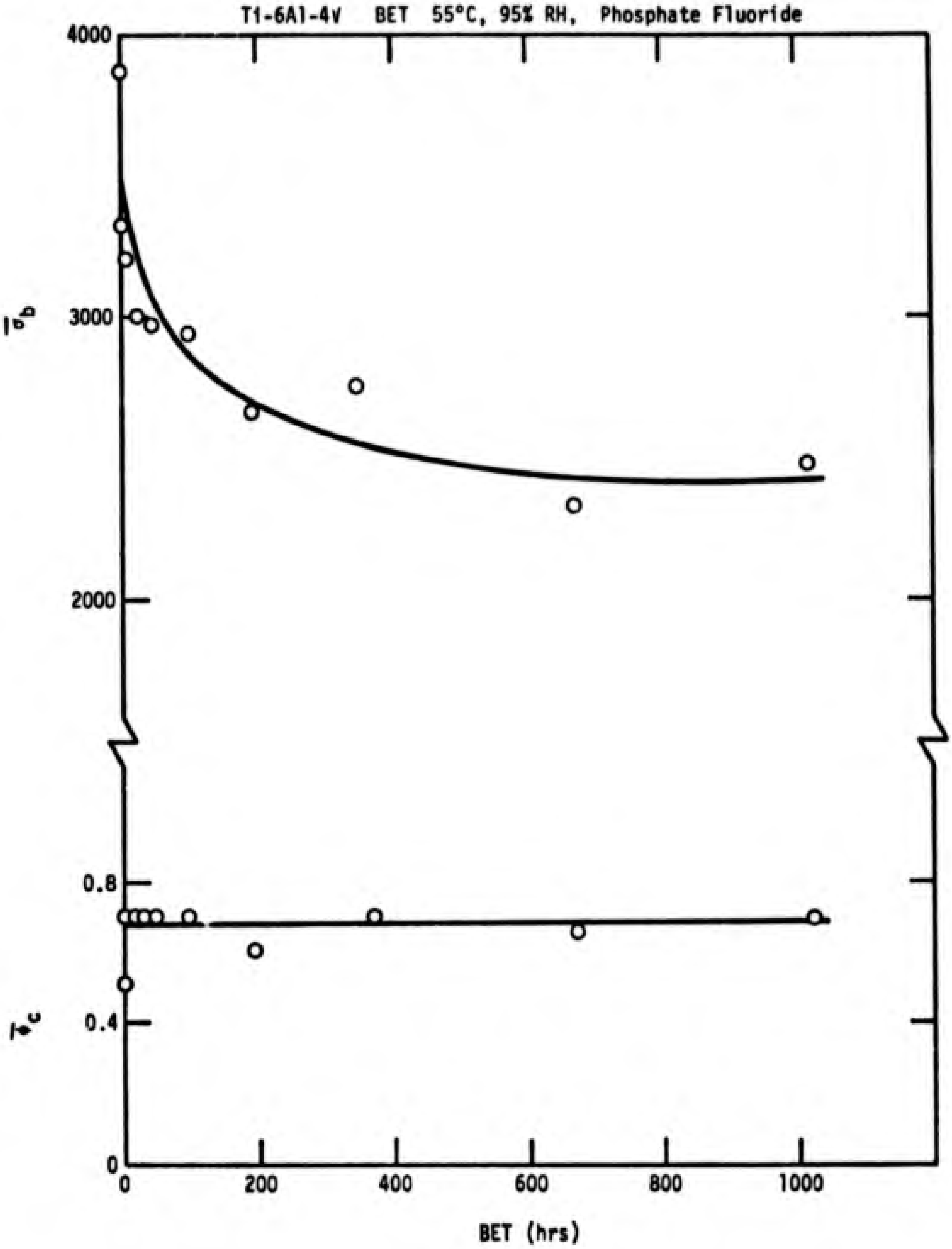

Fig. 88. Plot of $\bar{\sigma}_b$ and $\bar{\phi}_c$ vs BET at 54°C, 95% R.H. for Ti-6Al-4V - HT424.

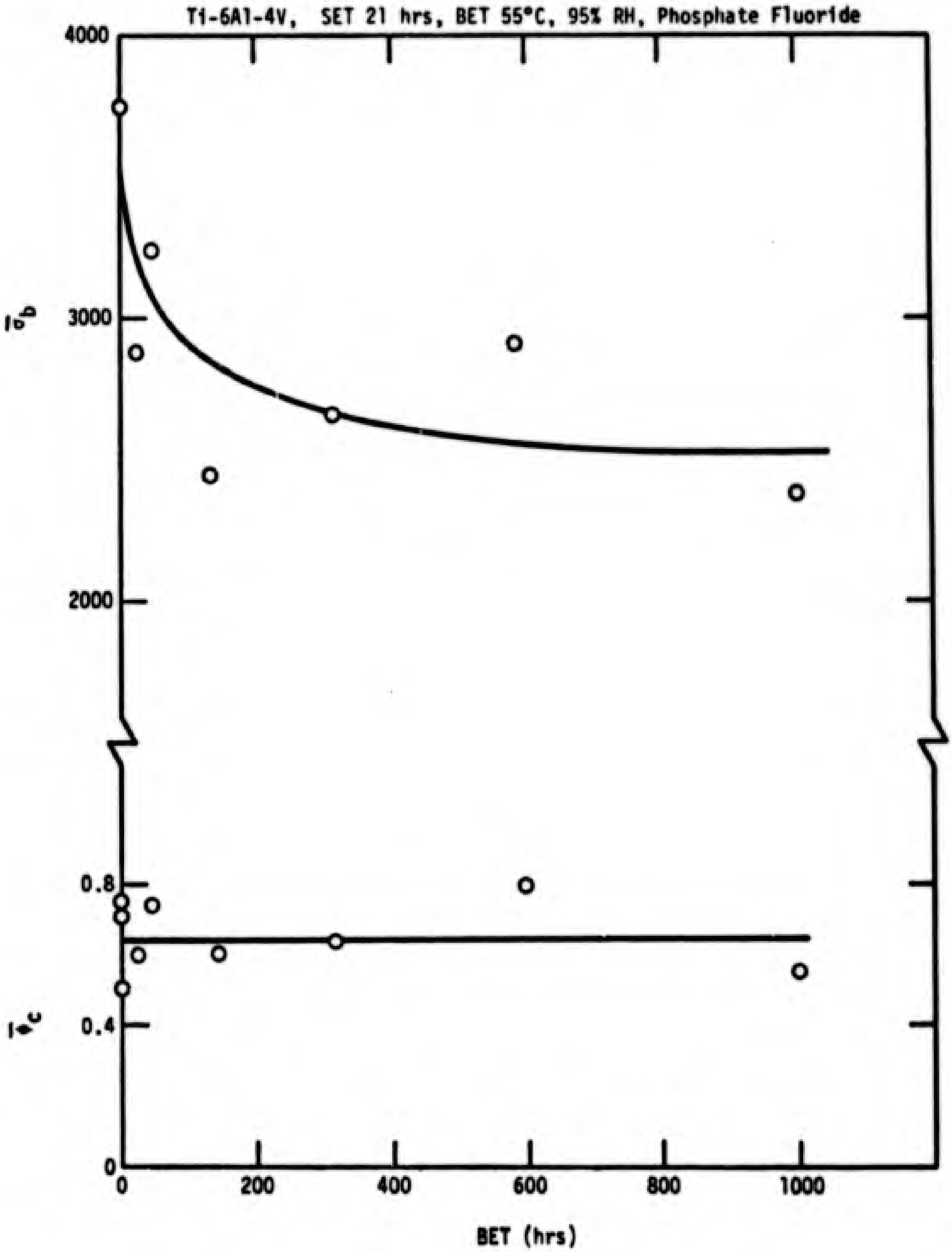

Fig. 89. Plot of $\bar{\sigma}_b$ and $\bar{\phi}_c$ vs BET at 54°C, 95% R.H. for Ti-6Al-4V - HT424 with SET = 21 hrs.

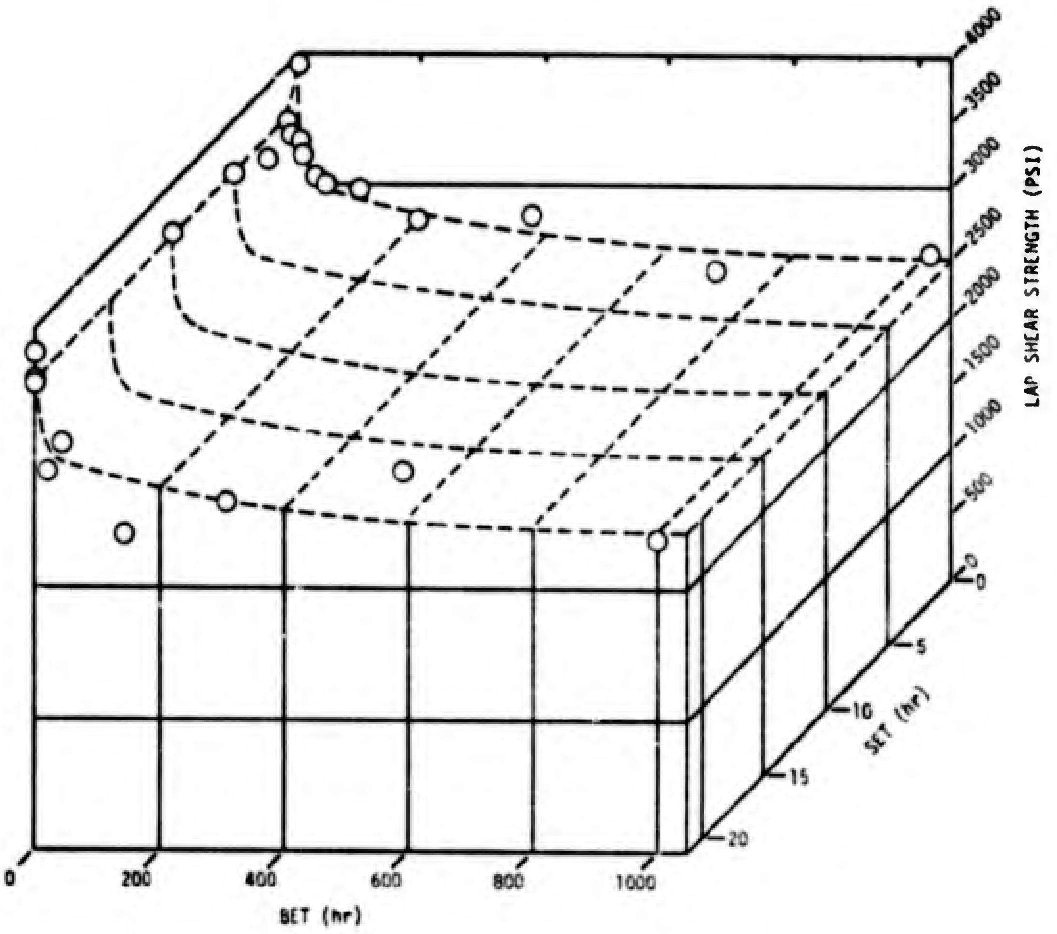

Fig. 90. SET vs BET response surface for lap shear bond strength for Ti-6Al-4V - HT424.

TABLE 47: Brief Summary of Combined SET - BET Effects at 54°C and 95% R.H. upon lap shear strength of HT424 adhesive and phosphate-fluoride etched Ti-6Al-4V

SET (hr)	BET (hr)	$\bar{\sigma}_b \pm \delta_b$	$\bar{\phi}_c$	Number of test specimen
0	0	3333 ± 387	0.70	6
0.5	0	3438 ± 432	0.70	6
1.0	0	3572 ± 384	0.60	6
2.5	0	3412 ± 425	0.75	6
5.0	0	3557 ± 332	0.70	6
10	0	3610 ± 493	0.75	6
21	0	3547 ± 414	0.70	6
0	0	3882 ± 412	0.50	6
0	6	3210 ± 163	0.70	6
0	24	3030 ± 367	0.75	6
0	47	2980 ± 380	0.70	6
0	99	2937 ± 371	0.70	6
0	194	2677 ± 508	0.60	6
0	374	2758 ± 449	0.70	6
0	670	2340 ± 393	0.67	6
0	1016	2490 ± 330	0.70	6
21	0	3777 ± 471	0.75	6
21	24	2880 ± 477	0.60	6
21	46	3243 ± 80	0.75	6
21	142	2435 ± 747	0.60	6
21	303	2653 ± 396	0.64	6
21	591	2922 ± 274	0.80	6

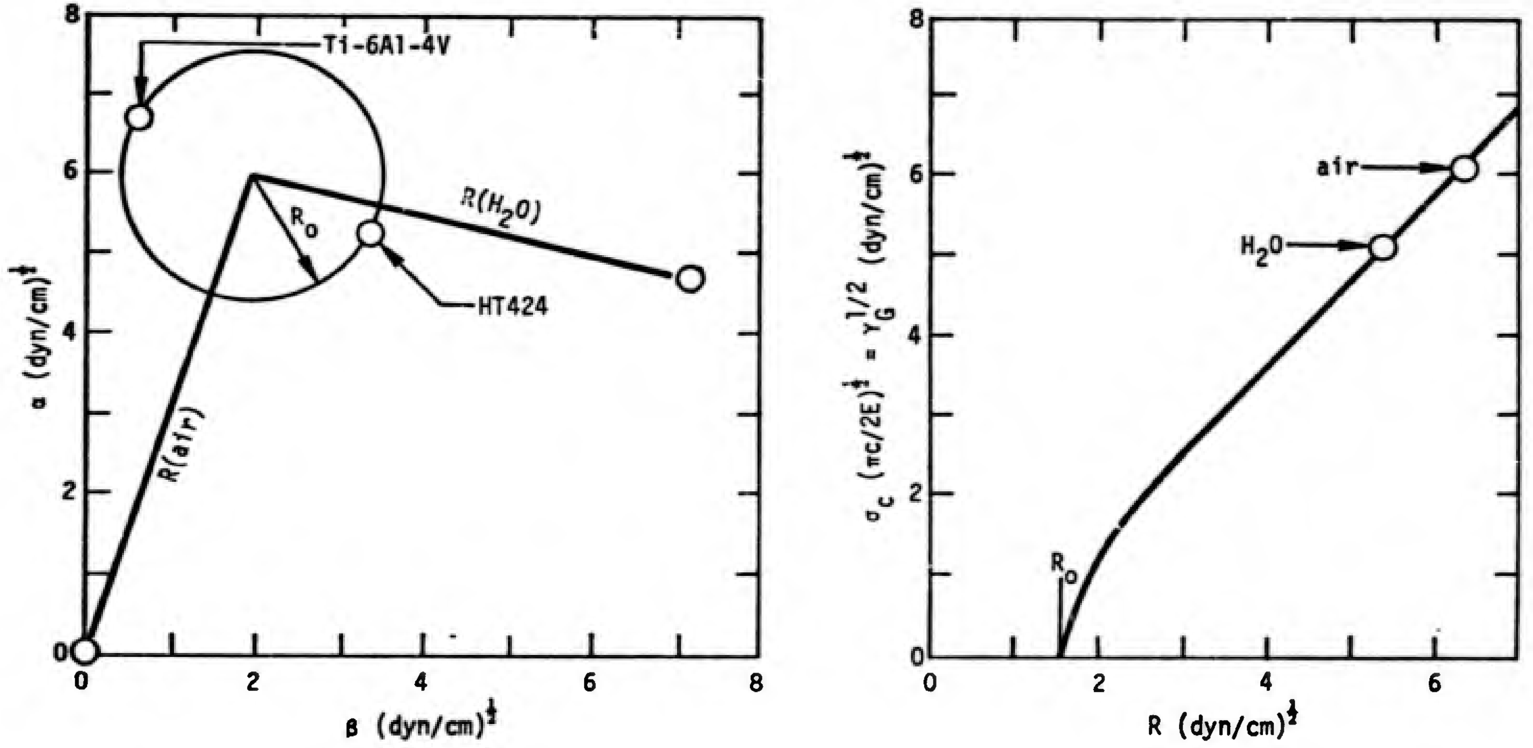

Fig. 91. Modified Griffith analysis of the effect of H_2O immersion in reducing critical failure stress σ_I for interfacial failure between HT424 and phosphate-fluoride treated Ti-6Al-4V, ($\phi_I = 1 - \phi_c = 1.0$).

$\beta_1 = 3.31$ (dyn/cm) . The surface properties of surface aged phosphate-fluoride etched Ti-6Al-4V are represented by $\alpha_3 = 6.61$ (dyn/cm) and $\beta_3 = 0.60$ (dyn/cm) as described by averaged values for SET = 23.6 hr and 47.5 hr in Table 46 characteristic of long term surface exposure. These surface energy values for HT424 and Ti-6Al-4V are indicated in the α vs β diagram of Figure 91. The point H = 5.91 and K = 1.96 (dyn/cm) defined by Eq. 17 and Eq. 18 of Section II.B.6 provides the locus for the vectors R_0, R(air), and R(H_2O) where $\alpha_2 = \beta_2 = 0$ for air and $\alpha_2 = 4.67$ (dyn/cm) and $\beta_2 = 7.14$ (dyn/cm) for H_2O. The right view of Figure 91 presents the function of γ_G ($\propto \sigma_c$)versus R for interfacial failure, where $\phi_I = (1-\phi_c) = 1.0$, between HT424 and Ti-6Al-4V. The prediction from the Griffith analysis is that:

$$\frac{\sigma_I(H_2O)}{\sigma_I(\text{air})} = 0.84$$

A previous calculation for the effect of water immersion on the critical Griffith stress ratio for cohesive failure of HT424 provided a ratio:

$$\frac{\sigma_c(H_2O)}{\sigma_c(\text{air})} = 0.63$$

Inspection of the SET vs BET response surface in Figure 90 yields:

$$\frac{\sigma_b\ (1000\text{ hr BET})}{\sigma_b\ (0\text{ hr SET, BET})} \simeq \frac{2500}{4000} = 0.63$$

in good agreement with the Griffith critical stress ratio for cohesive failure. This indicates that aging of Ti-6Al-4V-HT424 joints causes degradation mostly in the adhesive rather than at the interface.

4. Surface Mapping

We have prepared Ti-6-4 adhesive couples with the phosphate fluoride surface treatment, followed by deliberate contamination in certain areas. This was done to see if the contaminated areas could be detected by mapping with respect to surface potential difference (SPD) and ellipsometry and the effect contamination would have on bond strength. It was demonstrated that failure areas on Al caused by humidity aging could be predicted in advance of bonding. It is demonstrated here that failure areas caused by contamination can be predicted in advance for Ti-6-4.

Table 48 gives the ellipsometric parameters Δ and ψ as a function of position on various samples prior to bonding. Table 49 gives the SPD map of the samples prior to bonding and Table 50 gives the ϕ_I map after bonding fracture.

Figures 92, 93 and 94 are maps of ellipsometric parameters Δ and ψ, and surface potential difference (SPD) that were made after the phosphate-fluoride treatment but prior to bonding Ti-6-4 couples with HT424 adhesive. The map position along the abscissa corresponds with the position indicated on the schematic representation of the samples. After bonding and tests to failure on an Instron tensile tester the surfaces were examined under a low power microscope to estimate the fraction ϕ_I of each map position square that failed at the metal-adhesive interface. Values of ϕ_I are also mapped in the figures.

Figures 92, 93 and 94 are control experiments for which no contamination was introduced. Values of Δ and SPD are fairly constant with the respect to position indicating films of constant thickness and outer surface dielectric properties. The average value of Δ is 71.1 ± 1.6, $\psi = 28.3 \pm 0.9$ and SPD is 0.06 ± 0.04 volts. Values of ψ and ϕ_I show unrelated patterns with respect to position. Variations of ψ probably reflect slight changes in substrate or film optical properties due to sample preparation. Interfacial failure, ϕ_I, proves to be essentially zero for positions 1, 2, 3 and 4 (the outer edge) but increases to about 0.3 for positions 5, 6, 7 and 8 (inner adhesive zone). The

TABLE 48 Ellipsometric Mapping of Ti-6-4 Prior to Bonding
λ = 6328 Å Angle of Incidence 70°

	Position on Sample							
Sample	1	2	3	4	5	6	7	8
1161A	75.2 28.0	65.0 34.1	66.8 33.6	73.5 28.1	72.7 27.9	69.3 34.9	66.8 34.2	73.7 27.9
1161B	75.4 26.7	66.5 32.8	61.5 33.9	71.8 28.1	74.2 28.0	66.6 31.8	65.9 31.2	70.4 27.5
1162A	73.5 27.0	72.6 27.0	73.0 27.7	58.0 31.7	58.0 33.0	68.9 27.9	68.4 27.2	67.8 28.6
1162B	51.5 41.0	61.0 39.2	75.5 28.4	72.6 27.8	70.2 29.2	69.3 29.6	54.8 39.3	68.8 39.4
1163A	74.2 27.5	3.7 26.0	55.2 32.9	67.7 29.6	71.2 28.8	2.7 24.6	1.4 23.3	69.7 28.3
1163B	69.8 27.5	68.7 27.9	71.0 26.1	21.3 25.8	69.8 27.4	70.7 27.6	72.7 28.0	73.8 27.2
1164A	71.2 27.9	70.0 28.4	71.8 26.8	70.7 27.0	71.9 27.6	70.4 28.4	68.6 28.7	70.6 28.5
1164B	77.7 26.4	75.8 25.3	74.5 25.9	74.4 25.6	69.2 26.1	69.0 26.1	74.4 26.4	74.0 27.9
1165A	71.2 28.3	67.0 28.7	68.6 27.9	68.5 27.0	67.7 28.7	67.2 29.9	66.8 29.8	68.0 28.5
1165B	74.2 28.2	70.4 28.6	73.2 28.4	69.3 27.3	68.8 29.3	71.0 29.5	73.7 28.1	73.4 28.3
1166A	66.8 30.5	71.9 30.3	69.6 30.4	68.0 28.0	65.7 29.4	71.7 31.1	72.3 32.2	71.4 30.8
1166B	71.1 29.0	73.7 28.9	72.3 28.4	71.4 27.4	72.0 27.4	72.2 29.7	74.4 29.2	74.4 28.0

TABLE 49 Surface Potential Difference
Mapping of Ti-6-4 Prior to Bonding

Sample	SPD (volts) Position on Sample							
	1	2	3	4	5	6	7	8
1161A	+.162	+.36	+.336	+.175	+.12	+.325	+.3	+.044
1161B	+.17	+.395	+.395	+.215	+.15	+.36	+.34	+.075
1162A	+.145	+.13	+.185	+.27	+.245	+.055	+.045	+.05
1162B	+.438	+.405	+.11	+.08	+.055	+.07	+.265	+.375
1163A	+.162	+.343	+.38	+.2	+.325	+.481	+.415	+.065
1163B	+.085	+.04	+.037	+.35	+.025	-.075	-.08	-.02
1163B	+.0135	-.038	-.05	+.32	-.045	-.105	-.11	-.17
1164A	+.11	+.05	+.06	+.05	+.06	+.12	+.11	+.05
1164B	+.162	+.13	+.162	+.14	+.395	+.41	+.235	+.195
1165A	+.021	-.034	-.025	-.019	-.085	-.13	-.15	-.12
1165B	+.085	+.08	-.005	-.13	-.11	-.04	-.038	+.02
1166A	+.09	+.065	+.042	+.019	+.019	+.022	+.016	+.034
1166B	+.125	+.1	+.075	+.065	+.05	+.05	+.035	+.034

TABLE 50 Mapping of Ti-6-4 With Respect to ϕ_I After Bonding and Fracture

	Position on Sample							
Sample	1	2	3	4	5	6	7	8
1161A	.02	.08	.02	.01	0.5	0.6	.3	.2
1161B	0.02	0	.02	.02	0.2	0.4	0.2	.1
1162A	0.1	0.03	0.1	0.1	0.2	0.0	0.0	0.0
1162B	0.0	0.1	0.1	0.07	0.2	0.2	0.2	0
1163A	0.2	0.3	0.3	0.6	0.2	0.8	0.8	0.3
1163B	0.2	0	0	0.7	0.4	0.2	0.2	0.2
1164A	0	0	0	0	0.3	0.3	0.3	0.2
1164B	0	0	0	0	0.3	0.3	0.3	0.2
1165A	0	0	0	0	0.2	0.4	0.5	0.5
1165B	0	0	0	0	0.3	0.6	0.6	0.6
1166A	0.02	0.02	0	0.02	0.3	0.2	0.3	0.1
1166B	0.05	0.05	0.05	0	0.2	0.3	0.3	0.2

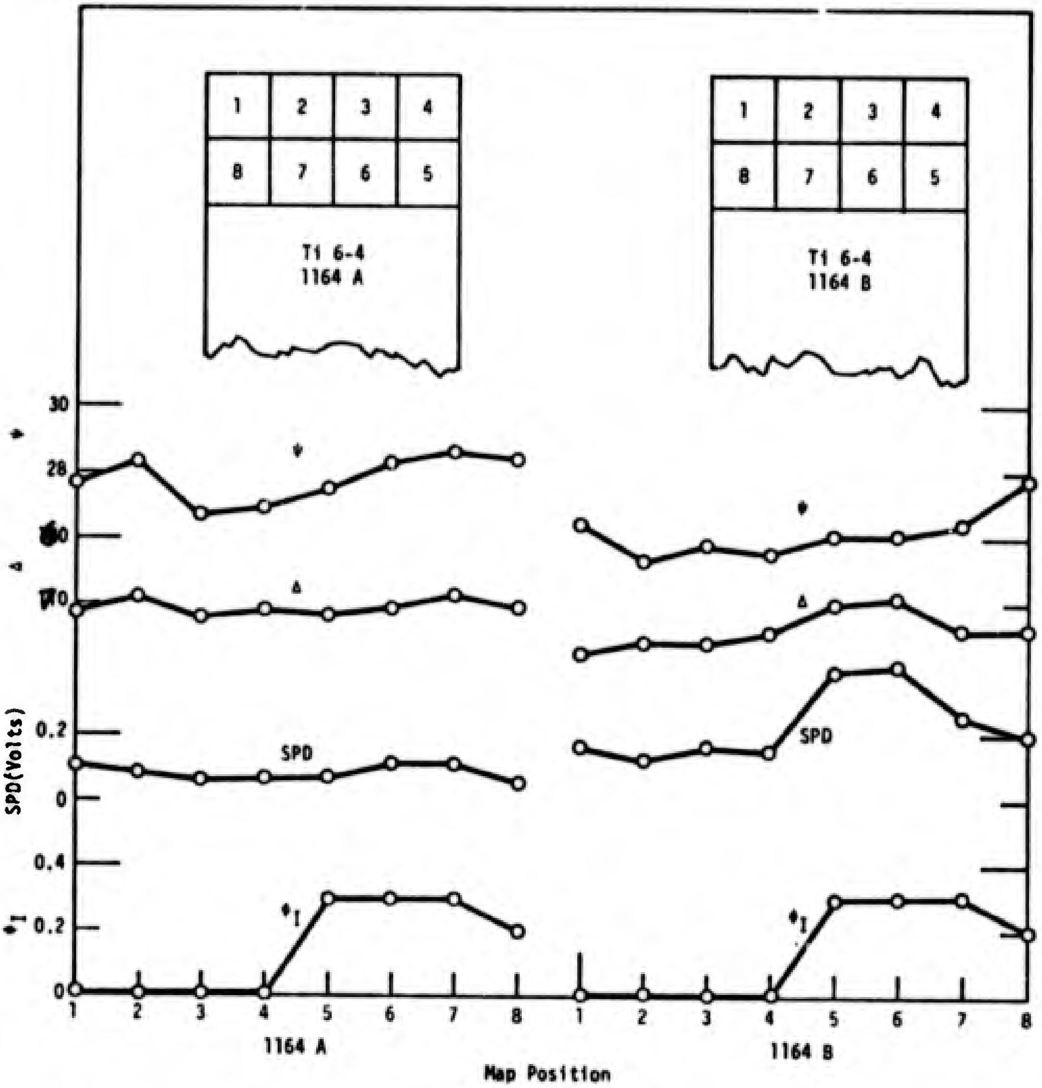

Fig. 92. Prebond surface character map, Δ, ψ, SPD as compared to post bond ϕ_I map for control test bond, 1164.

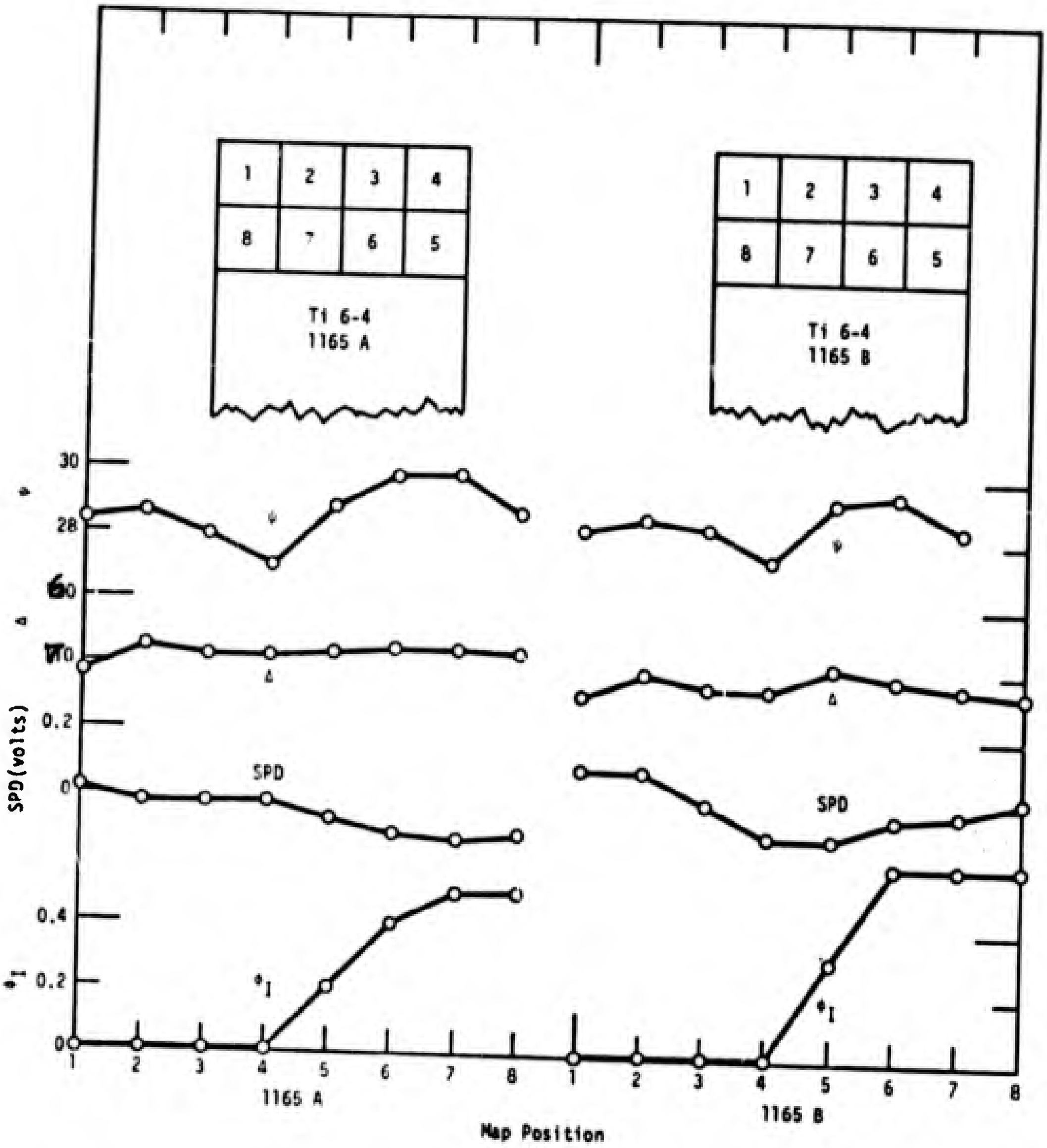

Fig. 93. Prebond surface character map, Δ, ψ, SPD as compared to post bond ϕ_I map for control test bond, 1165.

higher values of ϕ_I in zone 5-8 are not caused by variations in surface properties but are caused by higher stress levels in zone 5 to 8 as the lap shear joints tend to bend slightly in tension (see Figure 18).

Figure 94 is a map for specimens that were deliberately contaminated, by a finger print after wetting the finger with sweat from the forehead, in the areas indicated by the hatch (position 1, 2 for 1162A and 1, 2, 7, 8 for 1162B). A map of the contaminated areas is indicated at the top of the figure by giving a value of 1 for contamination and zero for no contamination. Values of ϕ_I for sample 1162 shows that interfacial failure was greater at the contaminated outer edge (position 1-4) and that in each case Δ, ψ and SPD reflect the ϕ_I curve. The finger print map at the top of Figure 95 for 1162B is identified by Δ, ψ and SPD and show that for 1162B contamination is much greater in the areas that were deliberately contaminated, but ϕ_I for both 1162A and B indicate that contamination has spread to the other areas.

Figure 96 shows the position of contaminants for 1161A and B and 1163A and B. Samples 1161A and B were contaminated by a dry finger. Samples 1163A and B were contaminated by smearing vacuum grease on a finger, rubbing the grease off and then pressing the finger on the sample. Figure 97 shows that the dry finger print is clearly identified by Δ, ψ and SPD and that ϕ_I increased above the average control values, except for positions 2 and 3 of 1161B. Figure 98 shows that the grease smudges are identified in the extreme by Δ, ψ and SPD. Note that the pattern of ψ is inverted from that for other contamination (Figures 95-97). This indicates that ellipsometry can be used to identify the type of contamination as well as its degree. The values of ϕ_I are much larger in the contaminated areas. The dashed SPD line for 1163B shows the reproducibility of the SPD scan. Average values of Δ, ψ and SPD ($\overline{\Delta}$, $\overline{\psi}$, $\overline{\text{SPD}}$) corresponding to different average values of ϕ_I ($\overline{\phi}_I$) from Tables 48, 49 and 50 are plotted in Figure 99. A correlation exists between $\overline{\text{SPD}}$, $\overline{\Delta}$ and $\overline{\phi}_I$. $\overline{\psi}$ does not show the same correlation because of the different types of contamination.

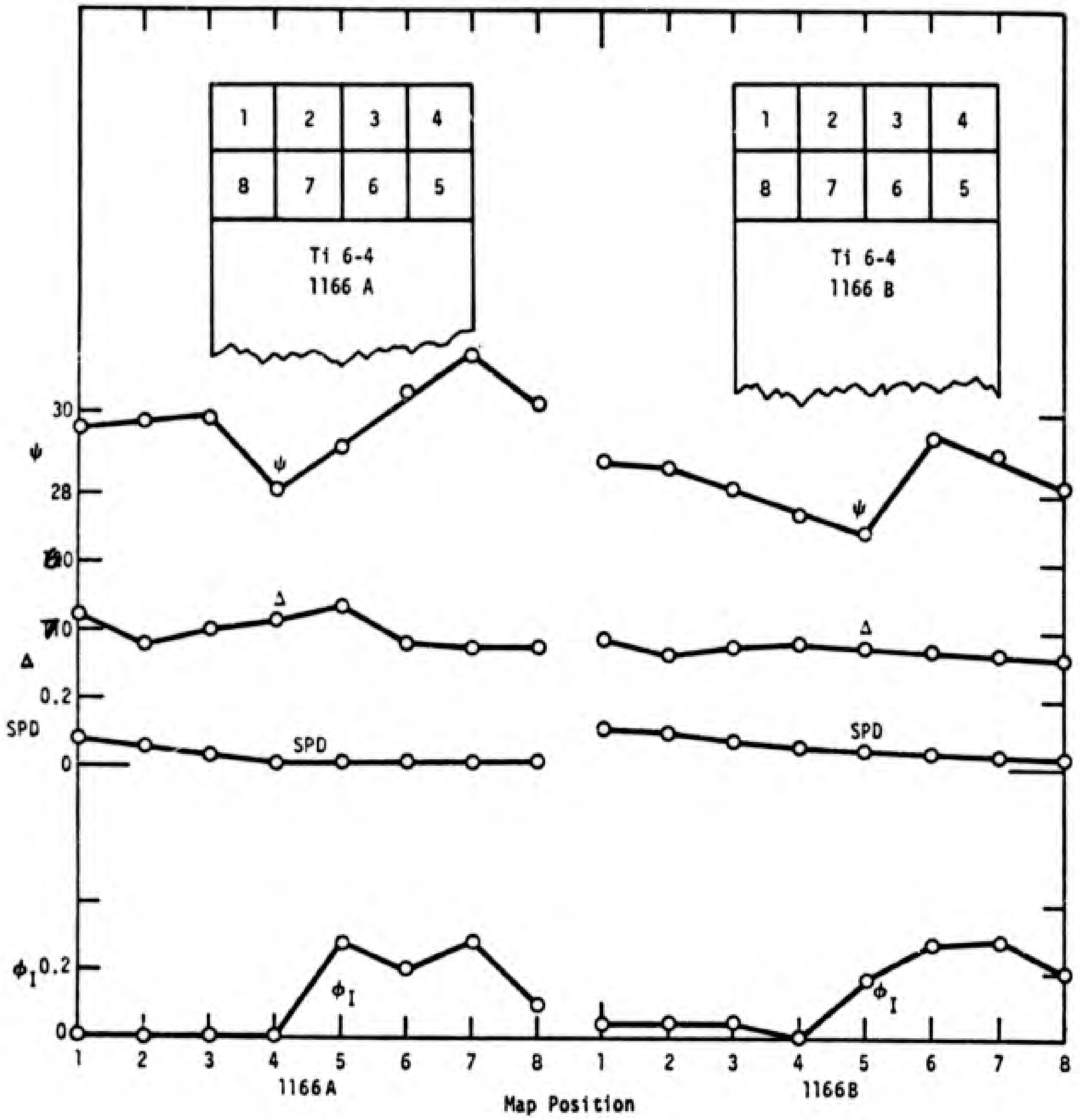

Fig. 94. Prebond surface character map, Δ, ψ, SPD as compared to post bond ϕ_I map for control test bond, 1166.

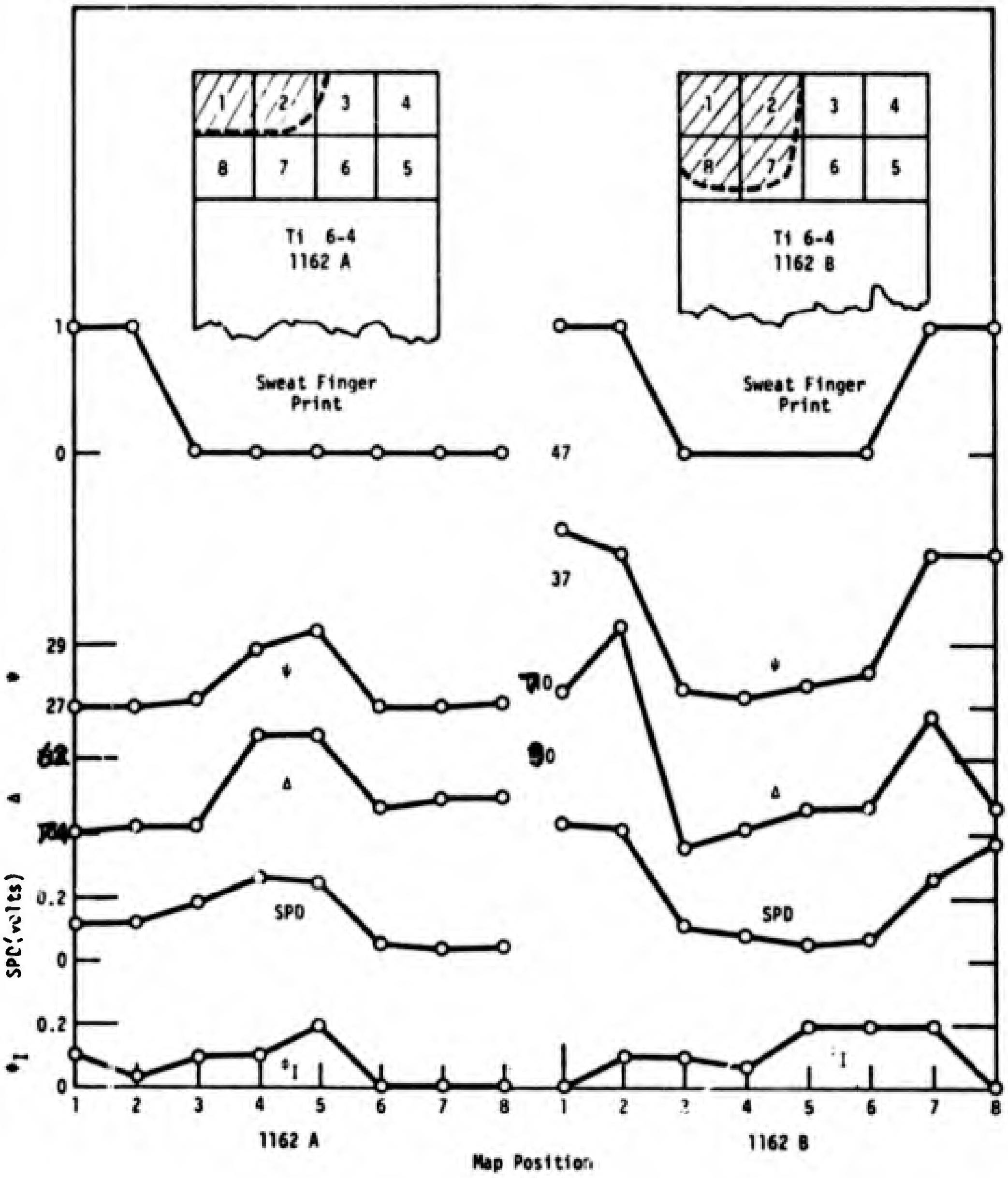

Fig. 95. Prebond surface character map, Δ, ψ, SPD as compared to post bond ϕ_I map for a Ti-6Al-4V contaminated sample 1162.

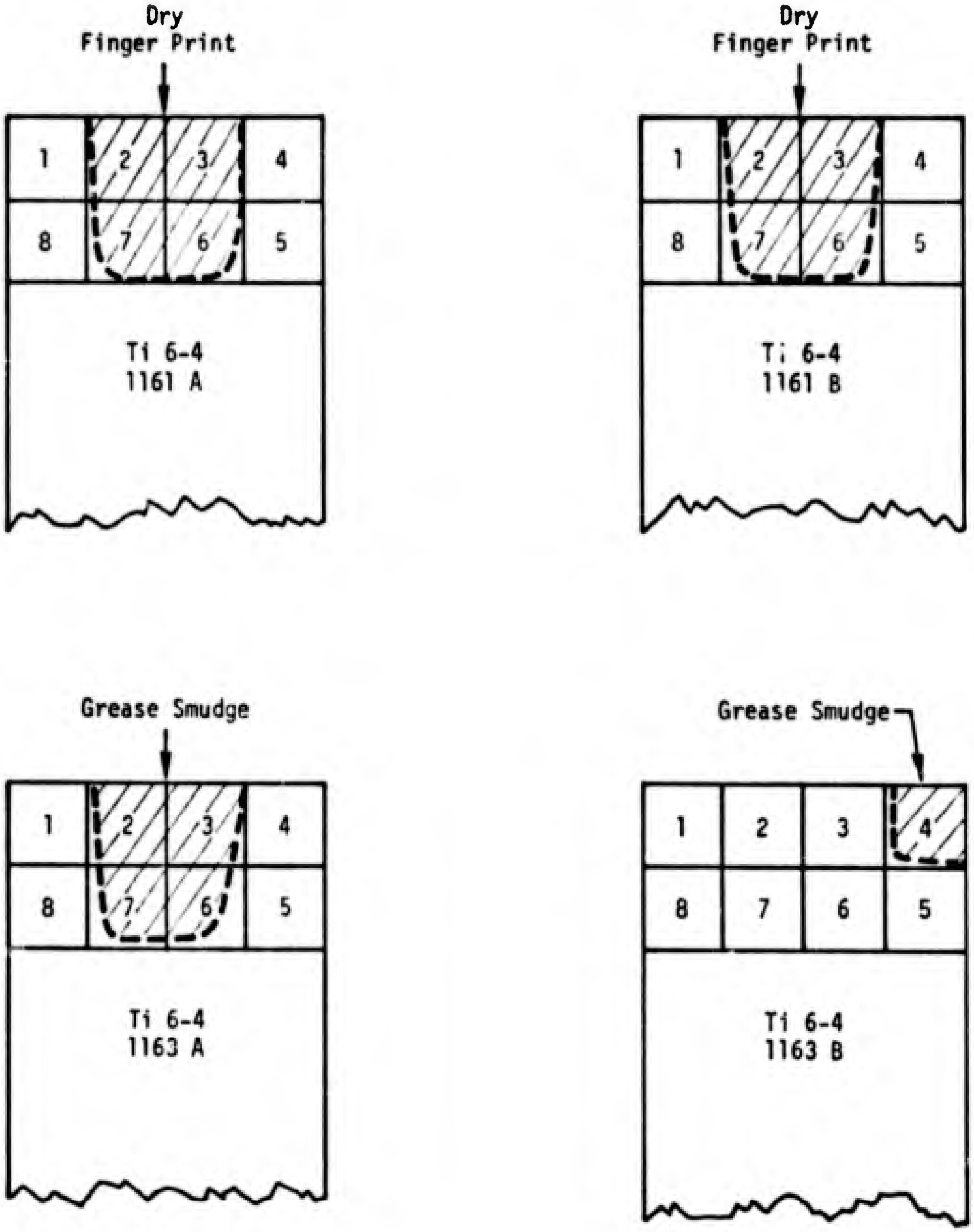

Fig. 96. Prebond surface character map, Δ, ψ, SPD as compared to post bond ϕ_I map for a Ti-6Al-4V contaminated sample.

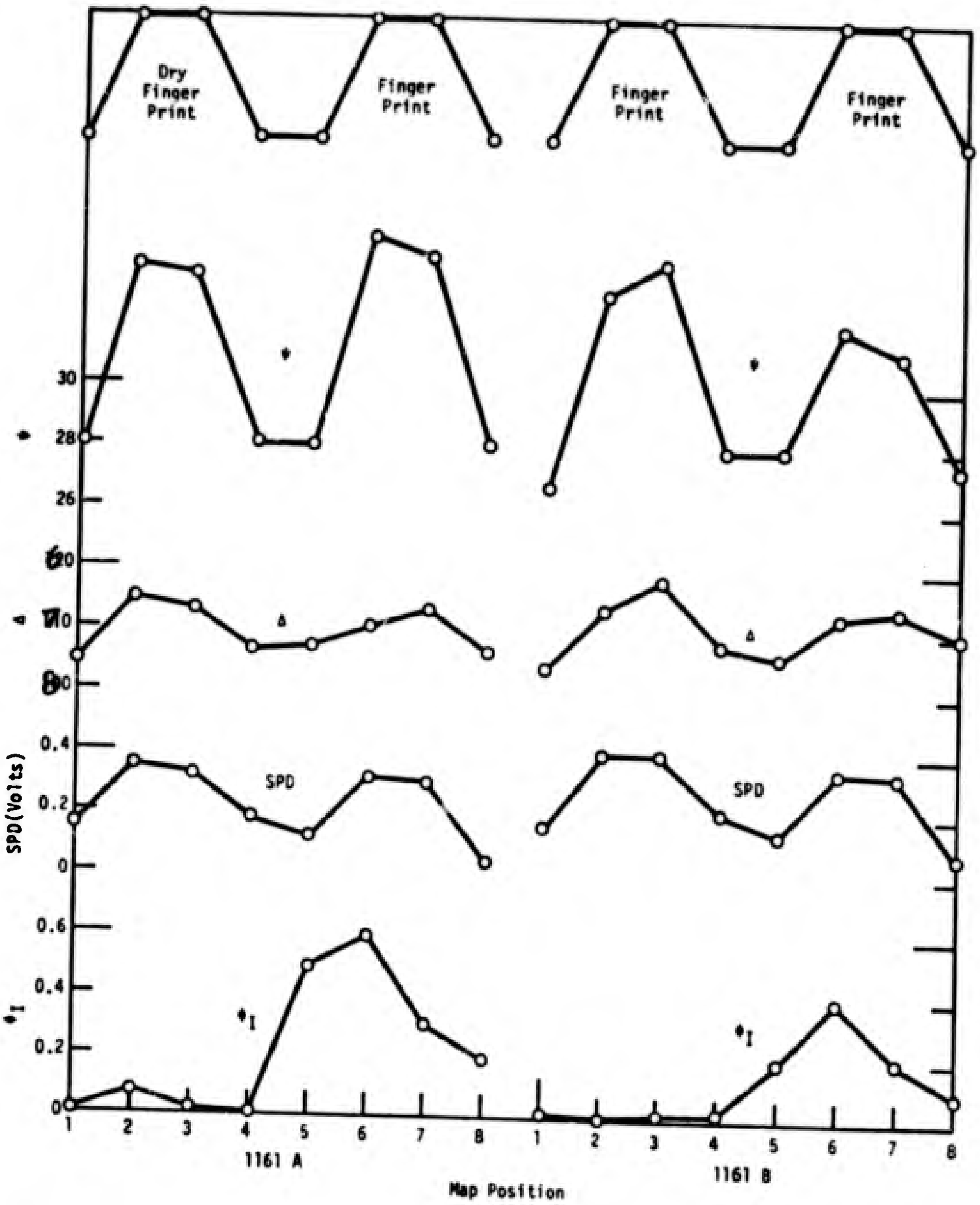

Fig. 97. Prebond surface character map, Δ, ψ, SPD as compared to post bond ϕ_I map for a Ti-6Al-4V contaminated sample 1161.

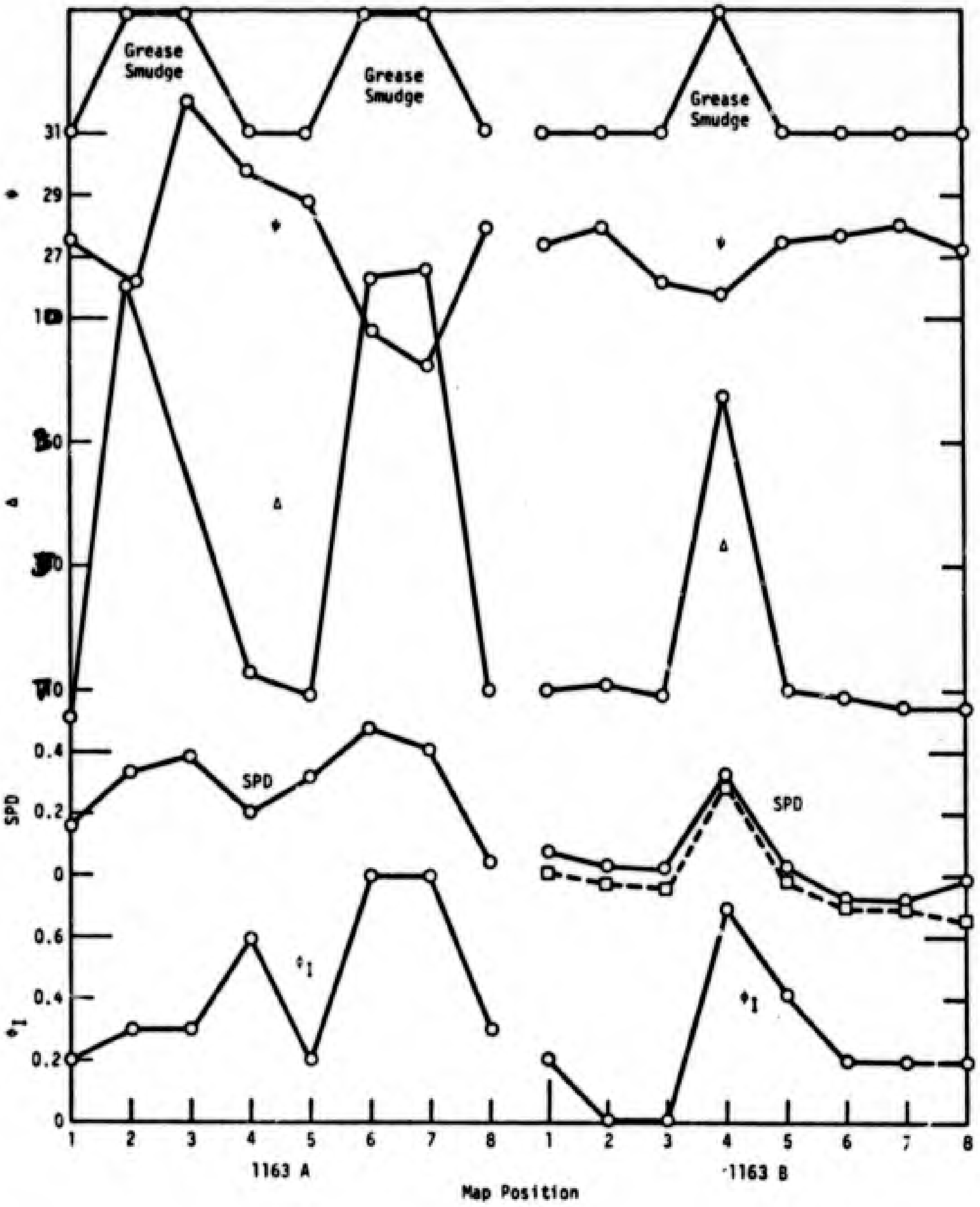

Fig. 98. Prebond surface character map, Δ, ψ, SPD as compared to post bond ϕ_I map for a Ti-6Al-4V contaminated sample 1163.

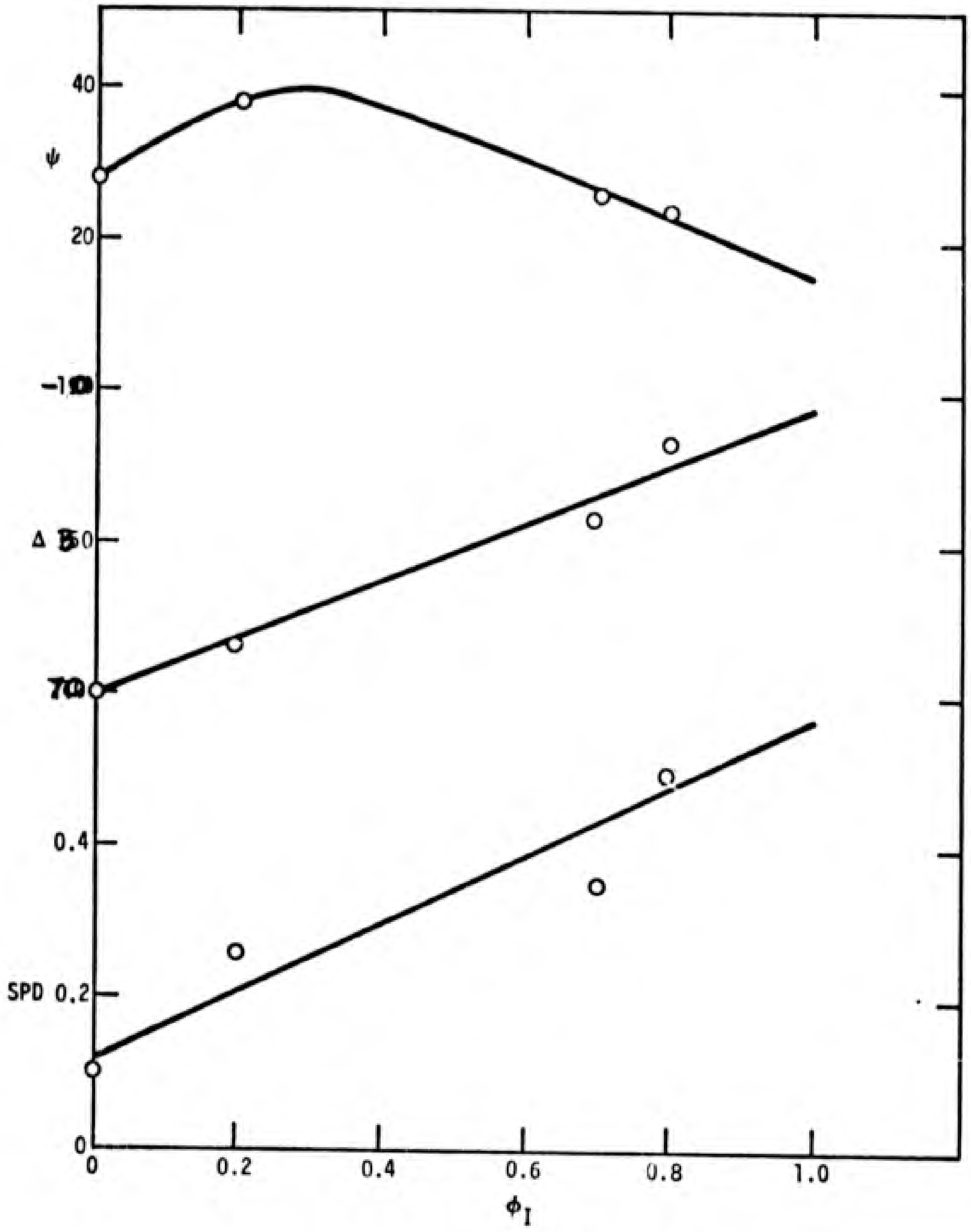

Fig. 99. Plot of $\overline{SPD}$, $\bar{\Delta}$ and $\bar{\psi}$ vs $\bar{\phi}_I$.

Table 51 is a table of bond strength σ_b and values of $\bar{\phi}_I$ for each bond couple. Comparison of average bond strength σ_b, $\bar{\phi}_I$ and $\bar{\phi}_c$ for different contamination reveals that the dry finger print bond is about the same as the control bonds even though the print could be detected by the surface tools. The grease smudge produced more interfacial failure and lower bond strength than the controls. Surprisingly, although the sweat finger print gave the lowest value of $\bar{\phi}_I$ it also gave the lowest bond strengths. It is concluded that either SPD or ellipsometry could be used to locate inadvertent contamination of Ti-6Al-4V surfaces after preparation but prior to bonding.

C. Summary of Results

With respect to the Al 2024-T3-HT424 and Ti-6Al-4V-HT424 systems, the following important observations have been made:

1. After surface preparation of Al 2024-T3 with the FPL etch, ellipsometry reveals that the oxide film varies in thickness and structure across the surface. The average thickness is of the order of 200Å with refractive index of $n_f \sim 1.8$ close to that for α alumina ($n_f \sim 1.7$) but with an effective absorption index much larger ($\kappa_f \sim 0.3$) than for α alumina ($\kappa_f \sim 0$). The effective absorption index may be related to the surface roughness as well as the true absorption index. After surface preparation of Ti-6Al-4V with the phosphate fluoride treatment, the oxide is rather uniform across the surface. The average thickness is also about 200Å with $n_f \approx 2.8$ close to TiO_2 ($n_f \approx 2.85$) but with effective absorption index also larger ($n_f \approx 0.1$) than the bulk oxide ($\kappa_f \sim 0$). Ellipsometry of FPL etch surfaces prior to and after bonding and fracture indicates that interfacial failure is in the oxide film.

2. Auger spectroscopy and ion-sputter-etching give semi-qualitative chemical profiles of the films formed during surface preparation. Other than the aluminum and oxygen, Cu, C and S were detected on the 2024-T3 aluminum after the FPL etch. If chromium was present it was removed by the vacuum system before analysis was begun. Iron segregates to the outer surface of the oxide. Copper segregates into the oxide with a maximun concentration near the central region of the oxide. Nickel segregates to higher concentration in the oxide than in the metal. Silicon is not observed in the FPL etch surface but was markedly noticeable in an area of interfacial fracture. Auger analysis on the

TABLE 51: Bond Strength and Average $\bar{\phi}_I$ and $\bar{\phi}_c$ for Ti-6-4 (HT-424 Adhesive)

Sample Couple	Contamination	σ_b (psi)	$\bar{\phi}_I$	$\bar{\phi}_c$
1166A-B	non	4040	0.13	0.87
1165A-B	non	3220	0.23	0.77
1164A-B	non	3800	0.14	0.86
1161A-B	Dry Finger Print	3800	0.16	0.84
1163A-B	Grease Smudge	2780	0.34	0.66
1162A-B	Sweat Finger Print	2600	0.08	0.92

adhesive surface that had mated with the FPL etch oxide revealed a large carbon peak as expected but also revealed Al, O, N, Cu and traces of Fe and Mg also indicating transfer of oxide to the adhesive and thus failure in the oxide.

Auger analysis and profiles of Ti-6Al-4V with the phosphate-fluoride treatment revealed Ti, Al, V, Fe, C, N and O as well as surface contamination P, Ni, S and Cu. If F is present it is masked by one of the Fe peaks. The concentration of O, Cu, Ni, Fe, S and C is larger in the oxide than in the metal. The concentration of Ti, Al and V are lower in the oxide than the metal.

3. Microscopy reveals that the FPL etch leaves an aluminum surface with very high density of pit holes with a large spectrum of dimensions. Primer flows into these holes and probably increases adhesion by the hook and latch effect. Failure is observed in the adhesive, in the glass carrier, in the primer and in the primer-metal interface (shown to be in the oxide). Considerable natural porosity is observed in the adhesive.

Similar failure modes are observed for Ti-6Al-4V-HT424 with the exception that interfacial failure appears to occur at the oxide-primer interface. These observation indicate that the bond strength for a lap shear joint is the sum of the strengths in particular areas, i.e. the surface is not of uniform strength.

Aluminum oxide film formed by the FPL etch could not successfully be removed but titanium oxide film from the phosphate-fluoride treatment could. The oxide film from the phosphate-fluoride proved to be amorphous with maximum thickness ~ 540Å. The larger thickness measurement for the removed oxide (measured by interferometry) with respect to the insitu film (measured by ellipsometry) is probably due to the very rough nature the film must have (revealed by SEM).

4. Contact angle measurements provide data for wettability envelopes, which showed that freshly etched 2024-T3 aluminum alloy and the phosphate-fluoride Ti-6Al-4V are wettable by the HT424 adhesive and primer. Aging these

surfaces in humidity chambers reducesthe wettability but not sufficent to cause weak bonds. One batch of FM34B-32 adhesive and BR-34 primer had wettability parameters that indicated non wetting of the Ti-6Al-4V with varying surface preparations and therefore formed weak bonds. A new batch of FM34B-32 and primer proved to have proper wettability parameters and did form strong bonds. It is apparent that the wettability parameters, viz the polar part of the solid surface tension γ^p and the dispersion part γ^d relate directly to the thermodynamic ability of the surface to form strong or weak bonds. Although one would expect these parameters to be related to the state of the surface with respect to organic contamination, they may also be related to the physical and chemical nature of the oxide film. These relationships have yet to be explored.

5. Surface mapping of 2024-T3 aluminum and Ti-6Al-4V with respect to ellipsometry and SPD have revealed that these instruments can be used as non destructive testing tools to predict the probable loci of weak bonding prior to the bonding process.

6. Surface aging of 2024-T3 aluminum in humidity chambers causes degradation of the surface (oxide growth and contamination) with associated changes in the ellipsometry, SPD and wettability parameters. The surface degradation results in bond strength degradation. This fraction of the total bond area (ϕ_I) increases and the associated bond strength σ_I decreases with SET. Surface aging of Ti-6Al-4V with the phosphate-fluoride treatment does not affect the oxide thickness and negligible changes in ellipsometry parameters are noted. The fraction of the surface that fails at the interface remains essentially constant with SET as does the bond strength. The wettability parameters do degrade with SET but not sufficient to cause weak bonds.

7. Joint exposure in a humidity chamber causes degradation of the HT424 adhesive and therefore degradation of bonds for 2024-T3 aluminum HT424 and Ti-6Al-4V-HT424 joints. The Griffith critical stress analysis from the contact angle and wettability parameters, faithfully predicted that joint exposure in a humidity chamber will cause degradation of the adhesive and interface for the aluminum system but only the adhesive for the titanium system.

Section IV

DISCUSSION AND CONCLUSIONS

To improve adhesive joints, the investigator concentrates his efforts on the weakest link. If failure occurs primarily in the adhesive, emphasis is placed on a search for a stronger adhesive. If failure occurs primarily at a weak boundary layer due to contamination or in the oxide, emphasis is placed on cleanliness or surface preparations. Since new applications demand stronger and stronger adhesive joints, the tendency will be to continue improvement of the weakest link as it shifts from one locus to another. It is concluded, therefore, that the development of tools, such as described in this report, for identifying the weak regions is of importance now and will continue to be of prime importance in the development of stronger adhesive joints.

The most significant results of this research impacts on two important areas, one has to do with nondestructive testing (NDT) of surfaces prior to bonding, the other has to do with understanding failure mechanisms in the Al 2024-T3-HT424 and Ti-6Al-4V-HT424 systems.

It has been demonstrated that surface regions that will result in a poor adhesive bond can be identified prior to bonding by ellipsometry and/or SPD. The potential of such NDT techniques is most significant for two reasons. First, suppose a completely satisfactory adhesive bonding procedure is developed in the laboratory for a particular application, inadvertant problems can arise on a factory assembly line that may cause deviations from the necessary processing parameters. Examples of these problems include contaminated processing solutions, contamination of atmospheric ambient, malfunction of process equipment, etc. Even though it may be impractical to survey every part or every region of every part by the NDT equipment, spot checks could be valuable for taking corrective action on the assembly line before too many parts had been bonded. Second, to improve on a given adhesive system, it is necessary to identify those parameters that are causing weakness.

Comparison of surface properties for various surface treatments, with bond strengths, as in Tables 6 and 29, does not reveal conclusive correlations. Proper surface preparations yield strong bonds with mostly cohesive failure as for the FPL etch and plasma treatment in Table 6 and for the phosphate-fluoride and TURCO process in Table 29. The low bond strengths for the vapor degrease process in Table 6 may relate to the large carbon contaminant revealed in the Auger analysis and the resultant low wettability revealed by the low solid surface tension γ_{SV}. Table 29 reveals that high bond strengths are obtained with the phosphate-fluoride and TURCO treatments but that low bond strengths result from the nitric acid fluoride treatment. The only surface properties for the nitric acid-fluoride treatment that differ from both the TURCO and the phosphate fluoride treatments (see Table 29) are the larger concentration of copper within the oxide film and the smaller film thickness. In fact, there is almost a linear relation between film thickness and bond strength in Table 29. It is believed that this relationship is only coincidental or indirect in nature. The SEM pictures (Figs. 58 and 59) show that the surface roughness increases in the same order as the bond strength, i.e. nitric acid-fluoride, TURCO and phosphate fluoride. For a properly prepared surface, (uncontaminated), the effect of surface treatment to bond strength is probably mechanical, by increasing surface area and/or producing a hook and latch property. However, this report demonstrates that there is a relationship between physical and chemical surface properties and bond strength for aged or contaminated surfaces.

A. Aluminum

Failure of an adhesive joint between Al 2024-T3 and HT424 can occur at the metal-oxide interface, in the oxide layer, in the primer or adhesive, at voids between primer and adhesive, or in the glass carrier. A schematic representation of half of a bond is given in Fig.100. The area of any given bond can be subdivided into small regions or patches that have failed in one of the above mentioned loci. The dashed line

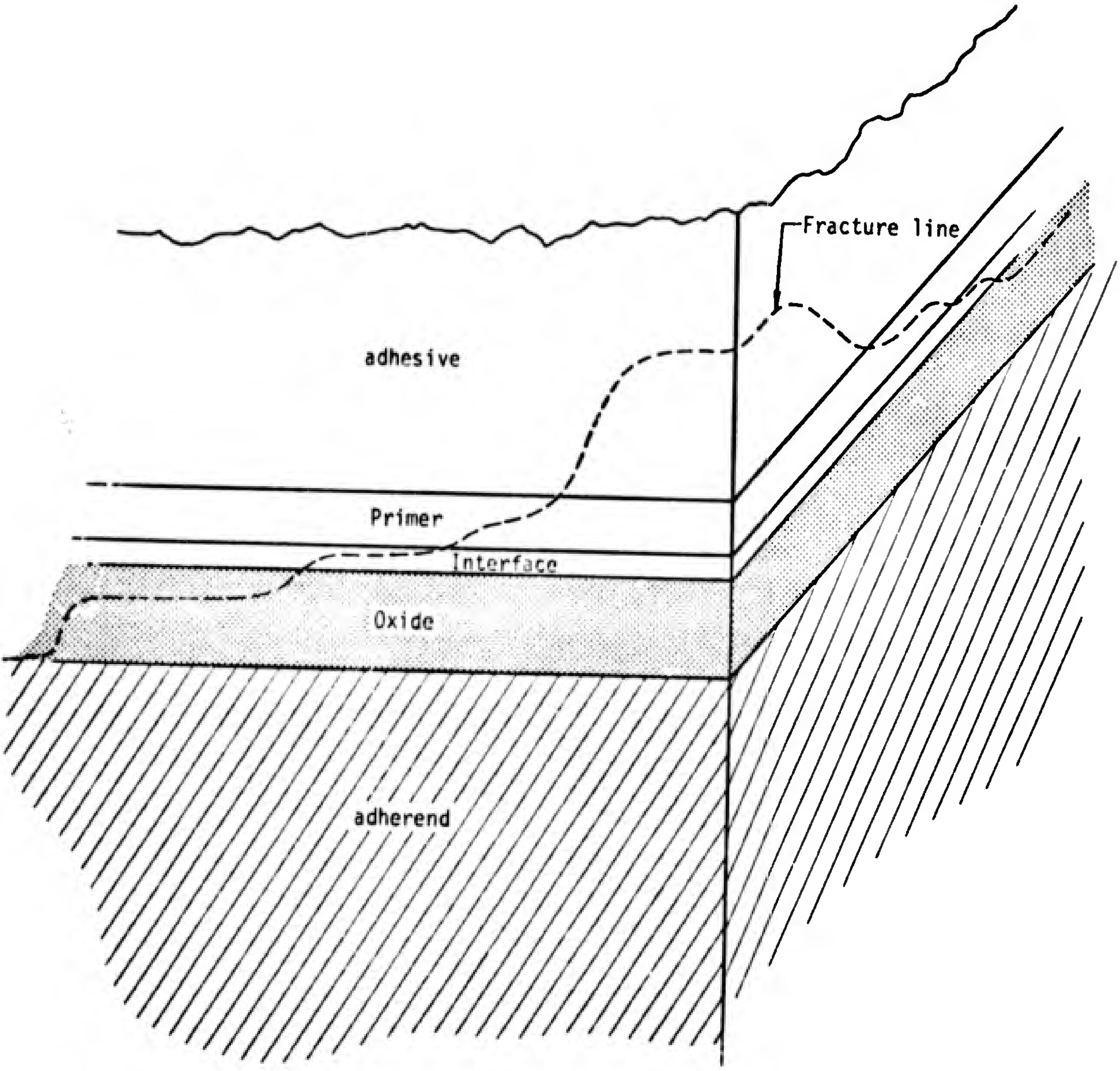

Fig. 100. Schematic representation of bond region with hypothetical fracture line.

in Fig. 100 represents the line of fracture that might occur. In spite of the attempt to prepare surfaces with uniform character, the result was always a nonuniform surface with respect to surface properties and localized bond failure mode. Let the fraction of the surface that failed at the interface be ϕ_I, and the corresponding average bond strength be σ_I, the fraction that failed in voids between primer and adhesive be ϕ_v ($\sigma_v = 0$), the fraction that failed in the adhesive be ϕ_c' with corresponding average bond strength σ_c' and the fraction that failed in the glass be ϕ_g with σ_g. The total bond strength σ_b can be expressed

$$\sigma_b \approx \phi_I\sigma_I + \phi_c'\sigma_c' + \phi_g\sigma_g \tag{32}$$

where

$$\phi_I + \phi_c' + \phi_v + \phi_g = 1 \tag{33}$$

Then

$$\sigma_b \approx \phi_c'(\sigma_c' - \sigma_I) + \sigma_I(1 - \phi_v - \phi_g) + \phi_g\sigma_g \tag{34}$$

Except in a few instances (such as for Fig. 19) fracture in the glass was cohesive and since the glass matrix was always the same ϕ_g and σ_g are constants with ϕ_g estimated to be about 0.3. If for a set of experiments σ_I, σ_c', ϕ_v and ϕ_g are constants, then plots of σ_b <u>vs</u> ϕ_c' will yield a straight line with $\sigma_b = \sigma_I(1-\phi_v-\phi_g) + \phi_g\sigma_g$ at $\phi_c' = 0$ and $\sigma_b = \sigma_c'$ at $\phi_c' = 1$. If however any of the parameters σ_g, σ_I, σ_c', ϕ_v and ϕ_g are not constant a straight line will not result from a plot of σ_b <u>vs</u> ϕ_c'. In our experiments we have made the approximation that $\sigma_g \sim \sigma_c'$ and $\phi_v \approx 0$ so that Eq. 34 reduces to a form of Eq. 19,

$$\sigma_b \approx \phi_c(\sigma_c - \sigma_I) + \sigma_I \;. \tag{35}$$

Where $\phi_c = \phi_g + \phi_i$

though considerable number of data cluster around a straight line as in Figs. 31 and 32, it is not surprising that there is large scatter such as in Fig. 33. If σ_c is constant but σ_I or ϕ_v is not constant for a set of experiments, then a plot of σ_b *vs* ϕ_c will not fall on a straight line but will fan out from $\phi_c = 1$, $\sigma_c \approx 3800$ psi, as observed in Fig. 33. Values of σ_I can be calculated with Eq. 35 for each set of values of σ_b and ϕ_c as seen in Fig. 36. It becomes obvious that results from the common practice of measuring σ_b as a function of experimental variables such as humidity, temperature time, etc. is difficult to interpret in terms of physical characteristics and mechanisms unless the various parameters σ_c', σ_g, σ_I, ϕ_I, ϕ_g ϕ_c and ϕ_v are separated. Each of these parameters may relate in a different way to a physical characteristic, such as oxide film thickness, oxide optical constants, work function (SPD) or chemical composition. Figures 16 and 17 also reveal that for lap shear joints the stress is not constant over the bond area. Failure tends to occur as shown in Fig. 19 from a paper by Bolger.(38)

In spite of all of these unknowns we have demonstrated that in certain circumstances (Figs. 28, 29 & 30) ϕ_I, ϕ_c and σ_I are related to the oxide thickness and optical properties. As the oxide thickens the work function increases as reflected in the SPD. The increase in interfacial failure with oxide thickness is shown to be failure in the oxide and is interpreted in the simple terms, that the probability of the presence of a defect that can propagate under stress is directly proportional to the quantity of oxide (i.e. oxide thickness). The strength of the oxide σ_I is related to the oxide structure and is reflected in the optical properties. It follows that to discover more about the mechanism of bond failure for a particular adhesive system it is necessary to measure σ_I, ϕ_I, σ_c, ϕ_c, ϕ_v, σ_g and ϕ_g in order to discover the relation between these variables and the physical and chemical properties within the bond. For example, chemical analysis by Auger spectroscopy has revealed that silicon contamination is in the oxide in the region of oxide failure but is not present in the oxide in the non bonded region. This indicates that in addition to regions of the thicker oxide the surface that was contaminated with silicones or glass may also produce weakened areas.

Aging surfaces at various temperatures and relative humidity (SET) degrades the bond. The change in the physical and chemical properties associated with this degradation are not fully understood as yet, but it is clear that further research with ellipsometry, SPD, Auger spectroscopy, SEM and electron diffraction is likely to reveal the details. Thus far it appears that during aging (SET) a structural transformation occurs in the oxide that is produced by the FPL etch. This is reflected in the optical properties. Simultaneous with oxide growth and structural transformation surface contamination may occur with resultant decrease in the polar nature (wettability) of the surface. Figures 21 and 28 show that at 95% RH and 54°C both σ_I and ϕ_c decrease during SET whereas σ_c remains essentially constant. On the other hand, during BET degradation is mostly restricted to the adhesive. During BET ϕ_c (and ϕ_I) remain essentially constant and σ_c decreases.

B. Titanium

As for aluminum, titanium fails via the various modes illustrated in Fig. 100 for the lap shear joint. However, interfacial failure proves to be at the oxide-primer interface rather than in the oxide. The phosphate-fluoride treated titanium does degrade with respect to wettability, probably due to surface contamination. Degradation of the adhesive, and thus bond-strength, will occur when exposed to humidity chambers as for aluminum.

C. Conclusions

The original purpose of this study has been fulfilled in that a better understanding of the physical and chemical properties of surfaces after various surface preparations has been obtained; the various fracture modes have been revealed and the important parameters of Eq. 34 are separated. It has been demonstrated in the case of FPL etched aluminum that σ_I and ϕ_I are related to oxide thickness and structure (optical properties). Further study of the relationship between fracture parameters, σ_I, ϕ_I, σ_c, ϕ_c etc. and physical and chemical properties will be useful and hopefully will lead to an understanding of those properties that must be designed into surface preparations, primers and adhesives to obtain high strength and durable joints.

REFERENCES

1. O. Kubaschewski and B. E. Hopkins: Oxidation of Metals and Alloys, 2nd Ed., Butterworth, London, 1962.
2. T. Smith: J. Electrochem. Soc. 112, 560 (1965).
3. P. Kofstad: High Temperature Oxidation of Metals, John Wiley & Sons, New York, 1966.
4. J. C. Bolger and A. S. Michaels in Interface Conversion for Polymer Coatings, ed. P. Weiss, G. Dale Cheever, American Elsevier Publishing Co., New York, 1969, Ch. 1.
5. F. Keller, M. S. Hunter, D. L. Robinson: J. Electrochem. Soc. 101, 335 (1954).
6. F. Liechti and W. D. Treadwell: Helv. Chim. Acta 30, 1204 (1947).
7. R. A. Harrington and H. R. Nelson: Trans. AIME, 137, 62 (1940).
8. H. W. L. Phillips: Inst. Met. Monograph and Report Series No. 13, 237 (1952).
9. W. G. Burghers, A. Claasen, and J. Zernike: Z. Phys. 74, 593 (1932).
10. S. Yamaguchi: J. Electrochem. Soc. 108, 302 (1961).
11. B. Rivolta: Met. Ital. 50, 173, 255 (1958).
12. A. M. Brusilavskii, B. E. Boguslauskaya, and E. G. Nasavich: Trudy Inst. Lakov i Krasok 2, 23-35 (1939). C.A. 34:21427.
13. W. C. Hamilton and G. A. Lyerly: Tech. Report 4185, Picatinny Arsenal Contract DAAA-21-70C-0434, Gillette Research Institute, Rockville, Maryland, March 1971.
14. N. J. DeLollis, Adhesives for Metals, Industrial Press, Inc., New York (1970), p. 35.
15. F. L. McCrackin, E. Passaglia, R. R. Stromberg, and H. L. Steinberg, J. Res. Nat. Bur. Std. A67, 363 (1963).
16. F. L. McCrackin, NBS Technical Note 479, April, 1969.
17. C. A. Fenstermaker and F. L. McCrackin, Sur. Sci. 16, 85 (1969).
18. H. H. Landholt and R. Bornstein, Zchlenwert und Funktronen (Springer-Verlage, Berlin, 19237 Vol. II, Part 8.

    M. Kayama, Chem. Abstracts 62:12572e

    Rikagaka Kenkyuosho Hokoka, 39, 121 (1963)

    D. L. Johnson and L. C. Tao, Surf. Sci.; 16, 390 (1969).

19. M. A. Barret and A. B. Winterbottom "First International Congress on Metallic Corrosion", London 1961, Butterworths 1962.
20. G. W. Simmons, J. Colloid and Interface Science **34**, 343 (1970).
21. M. P. Seah, Surf.Sci. **32**, 703 (1972).
22. M. Klasson, J. Hedman, A. Berndtsson, R. Nilsson, C. Nordling and P. Melnik, Physica Scripta **5**, 93 (1972)
23. M. L. Tarng and G. K. Wehner, J. App. Phys. **44**, 1534 (1973).
24. J. T. Grant, T. W. Hass, and J. E. Houston, accepted by Physics Letters A.
25. D. T. Quinto and W. D. Robertson, Surf. Sci., **27**, 645 (1971)
26. H. Shimizu, M. Ono, and K. Nakayama, Sur. Sci. **36**, 817 (1973).
27. J. R. MacDonald and C. A. Barlow, Jr., J. Chem. Phys. **39**, 412 (1963); 40, 1535 (1964); 43, 2575 (1965).
28. J. R. MacDonald and C. A. Barlow, Jr., Sur. Sci. **4**, 381 (1966).
29. R. V. Culver and F. C. Thompkins, Advan. Catalysis **11**, 74 (1959).
30. J. E. Boggio and R. C. Plumb, J. Chem. Phys. **44**, 1081 (1966).
31. W. A. Zisman, *Adhesion and Cohesion*, P. Weiss, ed., Elsevier, Amsterdam, (1962), pp. 176-208.
32. D. H. Kaelble, *Physical Chemistry of Adhesion*, Wiley, New York (1971), Charp. 5 and 12.
33. D. H. Kaelble, J. Macromol. Sci.-Reviews Macromol. Chem. **C6**(1), 85 (1971).
34. D. H. Kaelble, "Adsorption and Interdiffusion Mechanisms of Bonding in Polymer Composites", Proc. 23rd Int. Cong. of Pure and Appl Chem., Vol. 8, Butterworths, London (1971), pp. 265-301.
35. American Cyanamide Co. Bloomingdale Department, Havre DeGrace, Maryland 21028
36. S. Tajima, Adv. Corr. Sci. and Tech. **1**, 234 (1970) Ed. by M. G. Fontana and R. W. Staehle, Plenum Press, New York.
37. B. B. Bowen, Northrop Corporation (personal communication).
38. R. L. Patrick, *Treatise on Adhesion and Adhesives*, Marcel Dekker, Inc. (1973), p. 177.

39. D. H. Kaelble and E. H. Cirlin, J. Polymer Sci. Part C, 35 79 (1971).

40. E. H. Cirlin and D. H. Kaelble, J. Poly-Sci., Polymer Physics Ed. 11, 785 (1973).

41. W. E. Johnson, et al, Final Report AMC-59-7-618, Vol. 3, Contract AF33(600)-34392, Nov. 1959.

42. E. L. Alexander, MA-71-545, July 1971.

43. G. W. Lively, Tech. Report AFML-TR-73-270, Jan. 1974.

44. F. C. Rauch and T. B. Reddy, Tech. Report, AFML-TR-73-215, Nov. 1973.

APPENDIX A

Determination of Adhesive/Cohesive Failure Areas

Although ϕ_I can be estimated by visual observation, a more quantitative estimate is needed. The most quantitative estimate thus far is made by photographing the fracture bonds and placing a fine grid (20 lines per inch) on cellophane over the bond area. The grid squares that cover the area that broke interfacially (metal color) were counted. The top lines of Table 1A compare the visual estimate of observer (a) with the photographic technique (observer b). The mean percent deviation of the visual values from the photo values is 55%. The second set of observations compares the photo-technique by observer (b) with the same technique by observer (c). The mean percent deviation of the values obtained by (b) from those by (c) is 12%. A third set of observations by observer b was made visually and photographically, however, the visual observations were made by comparing the specimen with three samples that had been estimated by the photographic technique for comparison standards. By using the standards the mean percent deviation of the visual observations from the photo-observations is 4% in the region of 70°C 80% adhesive failure.

It would be advantageous if a technique could be found for measuring ϕ_I directly that would be rapid and accurate. A number of electrical methods were attempted. Measurement of the capacitance of the samples after putting lacquer on all areas except the bond area, proved useless in that no reproducible result could be obtained; both sodium chloride aqueous solution and mercury were used. The last set of values in Table 1A shows the estimates of ϕ_I by measuring the hydrogen evolution current, with a potentiostat, at a fixed time interval after placing a constant voltage between the sample and a reference electrode in a 3% sodium chloride solution. This technique does give a correlation between I_{H_c} and ϕ_I estimated by the photo-technique as seen in Fig. 1A, but the mean deviation of the electrochemical from the photo-technique is 34%. The fractional value of $¢_I$ was obtained for the electrochemical measurement by dividing the current for a given specimen that had not been bonded but was masked except for the area where the bond would be (i.e. 0.5 sq. inches). To see if a correlation exists between bond strength σ_b and cohesive failure areas as determined by the electrochemical technique σ_b is plotted vs $¢_c$ in Fig. 2A. Since the scatter is worse than that determined by the photo-technique (see Fig. 32) the electrochemical technique was abandoned.

TABLE 1A

Comparison of Estimates of Φ_I by Various Techniques

		Φ_I									%
a	Visual	0.16	0.18	0.18	0.24	0.24	0.25	0.28	0.39	0.45	55
b	Photo	0.15	0.25	0.10	0.20	0.40	0.35	0.60	0.65	0.70	
b	Photo	0.01	0.03	0.09	0.13	0.25	0.35	0.43	0.77	0.78	12
c	Photo	0.01	0.03	0.12	0.17	0.34	0.41	0.51	0.77	0.78	
b	Photo	0.72	0.76	0.74	0.75	0.76	0.81				4
b	Visual	0.70	0.70	0.75	0.76	0.80	0.80				
b	Photo	0.18	0.18	0.25	0.24	0.49	0.39	0.45	0.97	0.97	34
d	Electro	0.11	0.20	0.16	0.37	0.33	0.52	0.21	0.76	1.3	

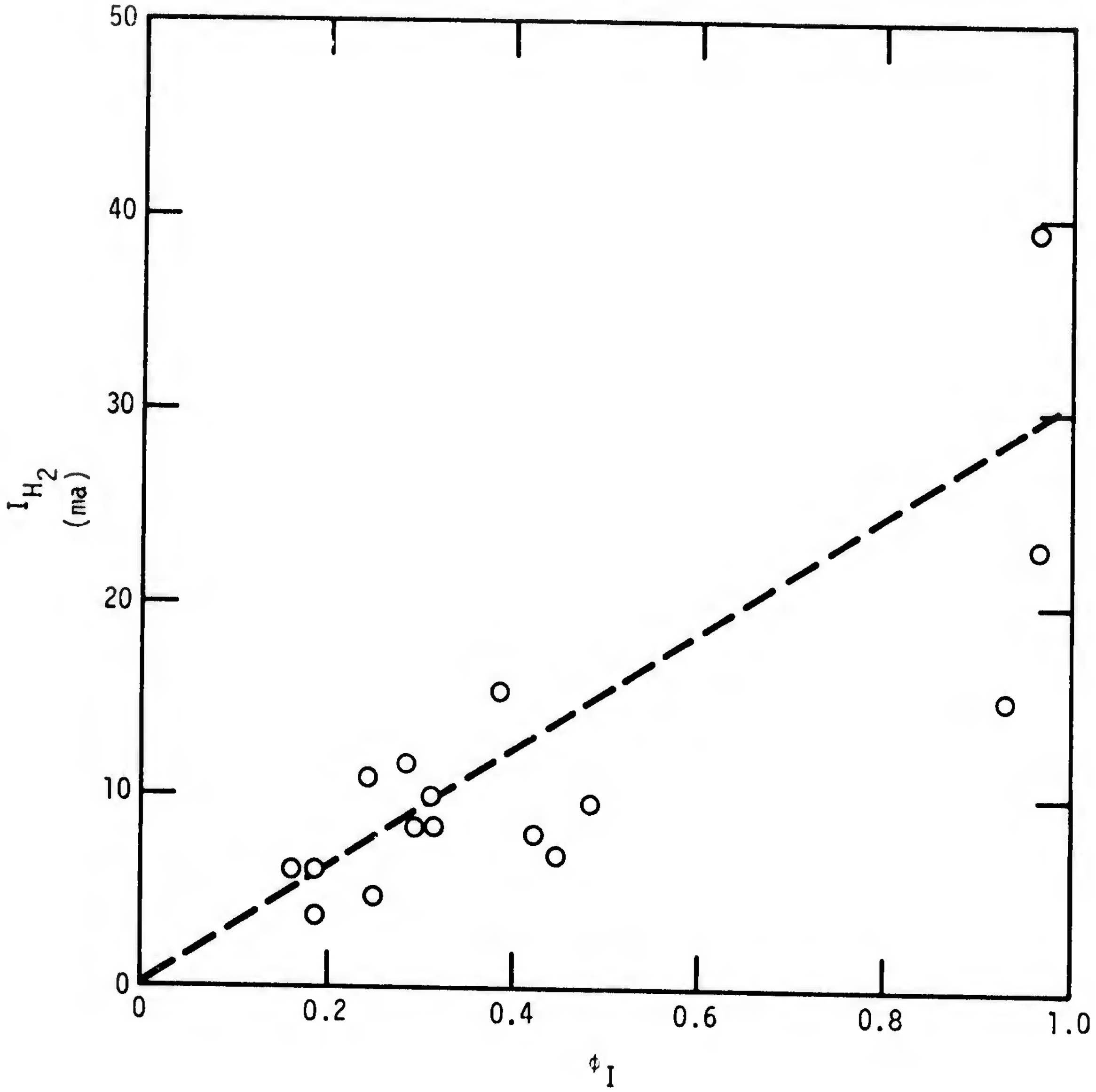

Fig. 1A. Plot of hydrogen current I_{H_2} vs the fraction of the bond area that failed interfacially ϕ_I.

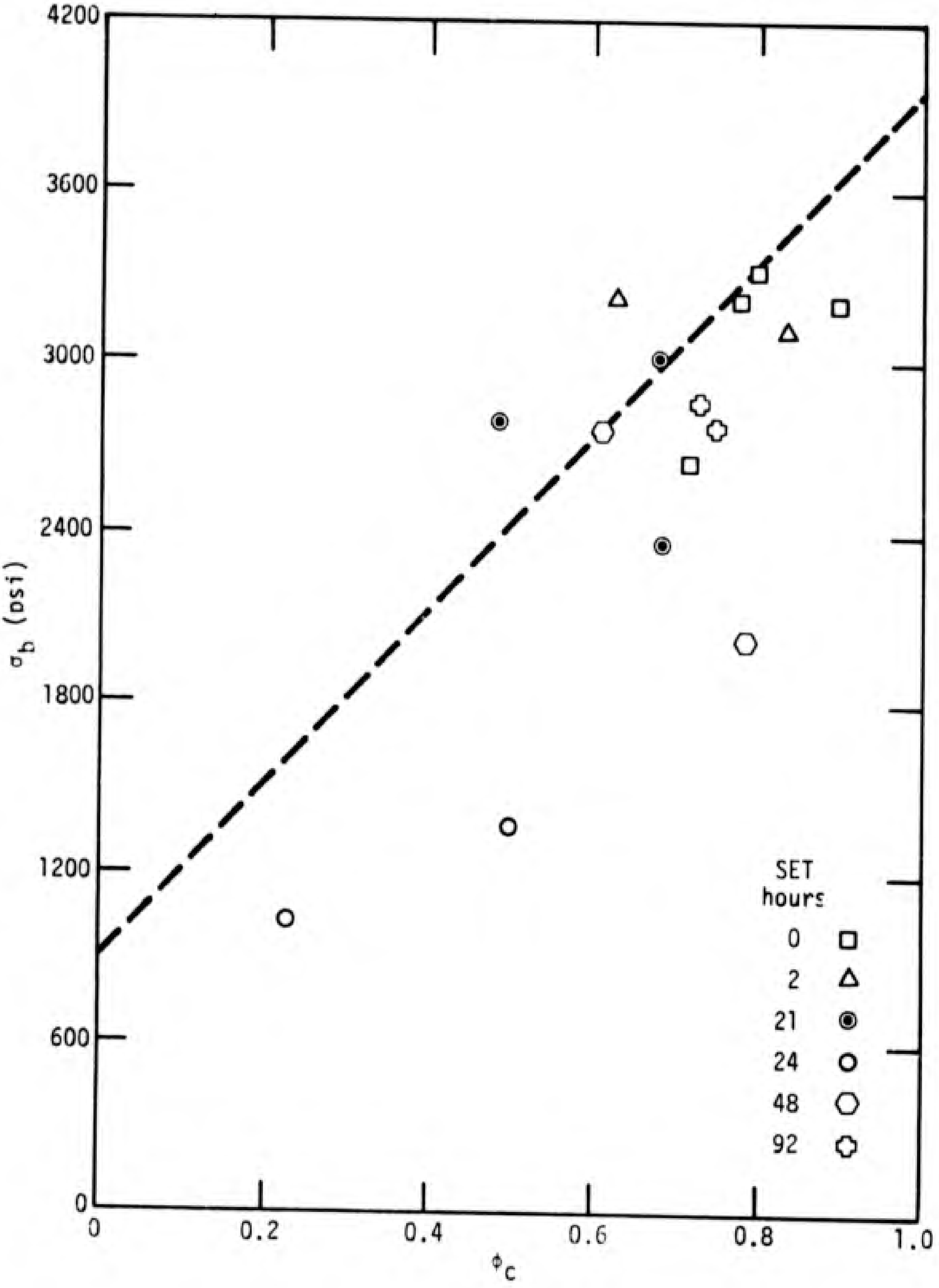

Fig. 2A. Plot of σ_b vs ϕ_c, ϕ_c determined with the electrochemical technique.

APPENDIX B

Gillette

Bell process FW-4352, Rev. E, Phosphate-Fluoride Treatment

1) Degrease.
2) Alk. clean 5-15 min. 140-180°F.
3) Rinse.
4) Pickle - 2.0-3 oz/gal HF
   40-50 oz/gal HNO_3
5) Rinse.
6) Phosphate-Fluoride 2 min max, RT
   6.5 - 7.0 oz/gal Na_3PO_4
   2.5 - 3 oz/gal KF
   2.2 - 2.5 fluid oz/gal (70%) HF
7) Rinse RT
8) Hot water soak 145-155°F 15 min.
9) Final rinse (quick spray) RT - 160°F .3 to 1 min.
10) Dry air RT - 160°F.

General Dynamics (Battelle formulation)

1) Methyl ethyl ketone wipe.
2) Trichloroethylene-vapor degrease.
3) Pickle in the following water solution at room temperature for 30 sec:

   Nitric acid - 15 percent by volume of 70 percent HNO_3 solution
   Hydrofluoric acid - 3 percent by volume of 50 percent HF solution.
4) Rinse in tap water at room temperature.
5) Immerse in the following water solution* at room temperature for 2 min:

   Trisodium phosphate - 50 grams/liter of solution
   Potassium fluoride - 20 grams/liter of solution
   Hydrofluoric acid (50 percent solution) - 26 milliliters/liter of solution

---

*This bath composition was developed at the Battelle Memorial Institute and is protected by U.S. Patent 2,864,732. Licensing arrangements can be obtained from the Battelle Development Corporation, Columbus, Ohio.

6) Rinse in tap water at room temperature.
7) Soak in 150°F tap water for 15 min.
8) Spray with distilled water and air-dry.

☆U.S.Government Printing Office: 1975 — 657-020/493